Experiments and simulations on wormlike micelles : photo-responsive behavior and applications

Qizhou Chen

Thèse de doctorat

NNT : 2021UPASP146

Experiments and simulations on wormlike micelles: photo-responsive behavior and applications

Expérimentations et simulations sur des micelles wormlike : comportement photo-réactif et applications

Thèse de doctorat de l'université Paris-Saclay et de East China University of Science and Technology

École doctorale n°564 : physique de l'Ile-de-France (PIF)
Spécialité de doctorat : Physique
Unité de recherche : Université Paris-Saclay, CNRS, Laboratoire de Physique des Solides, 91405, Orsay, France
Graduate School : Physique. Référent : Faculté des sciences d'Orsay

Thèse présentée et soutenue à Paris-Saclay, le 17 décembre 2021, par

Qizhou CHEN

Composition du Jury

Giuseppe FOFFI Professeur, Université Paris-Saclay, LPS	Président
Aixin SONG Professeur, Shangdong University, School of Chemistry and Chemical Engineering	Rapporteur & Examinatrice
Maria SAMMALKORPI Docteur, Aalto University, Department of Chemistry and Materials Science	Rapporteur & Examinatrice
Aihua ZOU Professeur, Shanghai Normal University, College Of Chemistry and Materials Science	Examinatrice
Laurence TALINI Docteur, CNRS, UMR 125	Examinatrice
Qibin CHEN Professeur, East China University of Science and Technology, School of Chemistry and Molecular Engineering	Examinateur

Direction de la thèse

Anniina SALONEN Docteur, Université Paris-Saclay, LPS	Directrice de thèse
Yazhuo SHANG Professeur, East China University of Science and Technology, School of Chemistry and Molecular Engineering	Directrice de thèse

université PARIS-SACLAY | ÉCOLE DOCTORALE Physique en l'Île-de-France (PIF)

Titre : Expérimentations et simulations sur des micelles wormlike : comportement photo-réactif et applications

Mots clés : micelle en forme de ver photosensible; simulation de dynamique moléculaire; fluide viscoélastique; ascension de la bulle

Résumé : Les matériaux souples réactifs sont un sujet de recherche actif depuis des décennies. Parmi les différents types de matériaux, les systèmes de micelles ressemblant à des vers photosensibles construits par des tensioactifs avec une morphologie d'auto-assemblage contrôlable et des propriétés rhéologiques réglables ont attiré une large attention. De tels systèmes d'auto-assemblage photosensibles peuvent non seulement être faciles à concevoir, propres et sans pollution, mais il est également possible d'ajuster et de contrôler avec précision le temps de réponse et la localisation du stimulus. C'est pourquoi de tels systèmes présentent des perspectives d'application prometteuses dans la libération de médicaments, l'industrie pétrochimique, la catalyse commutable, la modification de surface, la bio-ingénierie, les matériaux photosensibles intelligents et le domaine de l'optique. L'un de ces systèmes est composé de molécules photosensibles à base de cinnamate et de tensioactifs Gemini. Il montre une riche zoologie de morphologies d'auto-assemblage, y compris des micelles sphériques, des micelles vermiformes, des vésicules, des cristaux liquides, un système aqueux à deux phases, etc. Ces auto-assemblages présentent tous un excellent comportement photosensible. Cependant, en raison de l'échelle microscopique des auto-assemblages, la question de savoir comment ils s'assemblent et ce qui entraîne le changement de morphologie sous irradiation UV est encore ouverte. Les méthodes de simulation informatique à l'échelle atomique et moléculaire suscitent notre intérêt en raison du succès de la modélisation du comportement d'auto-assemblage. Avec l'amélioration rapide des performances des ordinateurs et les progrès des méthodes théoriques, les méthodes de simulation et de calcul sur ordinateur sont devenues une méthode indispensable dans la recherche théorique. Dans cette thèse, pour construire les micelles wormlike photosensibles, les cinnamates, représentés par l'o-méthoxycinnamate (OMCA), avec différents ortho-substituants en position méta-, para ont été sélectionnés comme molécules photosensiblesà introduire dans la solution de tensioactif Gemini. Grâce à des méthodes expérimentales telles que la rhéologie et la cinétique de réaction, combinées à une simulation de dynamique moléculaire (DM), des calculs quantitatifs, le processus de transformation morphologique sous la lumière UV, la cinétique de réaction de photo-isomérisation, la différence de molécules photosensibles et le mécanisme de transformation morphologique de cette système font l'objet d'une enquête approfondie.

La rhéologie des micelles vermiformes en fait un fluide modèle intéressant pour l'amincissement par cisaillement. Le comportement collectif des bulles dans les fluides fluidifiants par cisaillement est courant dans les procédés industriels tels que le traitement des eaux usées, l'extraction du pétrole et la flottation par mousse. En raison du comportement rhéologique complexe des fluides viscoélastiques, les recherches sur le comportement ascendant des bulles dans le fluide sont rares. Nous avons étudié la montée de bulles dans un système micellaire vermiforme classique (composé de CTAB/NaSal) dans des liquides bulleux avec une fraction gazeuse de 5% à 30% et montrons que la montée des suspensions concentrées de bulles dans les fluides newtoniens est bien décrite en utilisant l'équation de Richardson-Zaki. Cependant, pour les solutions d'amincissement par cisaillement, la relation de Richardson-Zaki ne s'applique plus. Le regroupement des bulles entraîne des vitesses de montée plus rapides et une dépendance plus faible de la fraction volumique des bulles. Nous discutons de ces résultats en termes de processus de flottation, où ils peuvent aider à concevoir des expériences de flottation plus efficaces pour les fluides fluidifiants par cisaillement.

Notre recherche aidera à comprendre l'influence de la structure des molécules photosensibles sur le comportement photosensible des micelles de type ver photosensibles ainsi que la montée des bulles dans le fluide non newtonien, ce qui fournit en outre des orientations théoriques pour les applications industrielles telles que fluide photo-rhéologique, séparation gaz-liquide, flottation de mousse etc.

université PARIS-SACLAY | ÉCOLE DOCTORALE Physique en l'Île-de-France (PIF)

Title: Experiments and simulations on wormlike micelles: photo-responsive behavior and applications

Keywords: photo-responsive wormlike micelle; molecular dynamics simulation; viscoelastic fluid; bubble rise

Abstract: Responsive soft materials have been an active research topic for decades. Among the different types of materials photo-responsive wormlike micelle systems constructed by surfactants with controllable self-assembly morphology and adjustable rheological properties have attracted widespread attention. Such photo-responsive self-assembly systems can not only be easy to design, clean and pollution-free, but it is also possible to precisely adjust and control the response time and localization of the stimulus. This is why such systems show promising application prospects in drug release, petrochemical industry, switchable catalysis, surface modification, bioengineering, smart photosensitive materials and optics field. One such system is composed of cinnamate-based photosensitive molecules and Gemini surfactants. It shows a rich zoology of self-assembly morphologies, including spherical micelles, wormlike micelles, vesicles, liquid crystals, an aqueous two-phase system and so on. These self-assembly structures all show excellent photo-responsive behavior. However, owing to the microscopic scale of the self-assemblies, the question of how they assemble and what drives the morphology change under UV irradiation is still open.

With the rapid improvement of computer performance and the progress of theoretical methods, computer simulation and calculation methods have become an indispensable method in theoretical research. In this thesis, to construct the photo-responsive wormlike micelles, the cinnamates, represented by o-methoxycinnamate (OMCA), with different ortho-substituents in meta- or para-position were select as the photosensitive molecules to introduce into Gemini surfactant solution. Through experimental methods such as rheology and reaction kinetics, combined with molecular dynamics (MD) simulation, quantitative calculations, the morphological transformation process under the UV light, photo-isomerization reaction kinetics, the difference in photosensitive molecules and the mechanism of morphology transformation of this system are comprehensively investigated.

The rheology of wormlike micelles makes them an interesting shear thinning model fluid. The collective behavior of bubbles in shear thinning fluids is common in industrial processes such as sewage treatment, oil extraction, and froth flotation. Because of the complex rheological behavior of viscoelastic fluids, the research on the rising behavior of bubbles in the fluid is scarce. We studied the rise of bubbles in a classic wormlike micelle system (composed of CTAB/NaSal) in bubbly liquids with a gas fraction of 5%-30% and show that the rise of the concentrated suspensions of bubbles in the Newtonian fluids is well described using the Richardson-Zaki equation. However, for the shear thinning solutions, the Richardson-Zaki relation no longer applies. Bubble clustering leads to faster rise velocities and a weaker dependence on the bubble volume fraction. We discuss these results in terms of the flotation process, where they can help design more efficient flotation experiments for shear thinning fluids.

Our research will help understanding of the influence of the structure of photo-sensitive molecules on the photo-responsive behavior of photo-responsive wormlike micelles as well as the bubbles rise in non-Newtonian fluid, which further provides theoretical guidance for industrial applications such as photo-rheological fluid, gas-liquid separation, foam flotation, etc.

université PARIS-SACLAY | ÉCOLE DOCTORALE Physique en l'Île-de-France (PIF)

标题: 光响应蠕虫状胶束的光响应行为和应用的实验和计算机模拟

关键词: 光响应蠕虫状胶束；剪切稀化粘弹性流体；气泡上升；分子动力学模拟

摘要: 近些年来，响应型软物质材料一直是科研人员的研究热点，其中由表面活性剂参与构建的光响应自组装体引起了广泛的关注。该刺激响应型自组装体系不仅具有丰富的自组装形态和不同的自组装尺度，包括球形胶束、蠕虫状胶束、囊泡、液晶等，而且易于设计，清洁无污染。这些优势使其在药物释放、石油化工、可切换催化、表面改性、智能光敏材料和器件等领域中有巨大的应用价值。其中，由肉桂酸酯类光敏分子和 Gemini 表面活性剂组成的光响应体系表现出了丰富的自组装形态，包括球形胶束、蠕虫状胶束、囊泡、液晶、双水相等。这些自组装都表现出出色的光响应行为。然而由于表面活性剂自组装体的微观尺度，表面活性剂是如何自组装的以及该自组装体在紫外线照射下是如何发生形态变化的问题仍然悬而未决。随着计算机性能的迅速提高和理论方法的进步，计算机模拟和量化计算已成为理论研究中不可缺少的方法。

本论文选择了以邻甲氧基肉桂酸酯（OMCA）为代表的含有不同的邻位、间位和对位取代基的肉桂酸类的光敏小分子引入 Gemini 表面活性剂溶液中来构建光响应性蠕虫状胶束。通过流变学和反应动力学等实验方法，结合分子动力学（MD）模拟、量化计算等理论计算方法系统地研究了这些光响应蠕虫状胶束在紫外光照下的光响应行为，和光响应行为的反应动力学和微观机理以及肉桂酸酯光敏小分子之间的分子结构与性质差异。蠕虫状胶束的流变性使它们成为一种典型的剪切稀化粘弹性流体。剪切稀化粘弹性流体中气泡的聚集上升行为在污水处理、石油提取和泡沫浮选等工业过程中非常常见。由于剪切稀化粘弹性流体复杂的流变行为，目前对与该流体中气泡上升行为的研究寥寥无几。我们研究了气体分数在5%到30%的蠕虫状胶束（由 CTAB/NaSal 组成）气泡液中的中气泡的上升行为，并发现 Richardson-Zaki 方程可以很好的描述牛顿流体中气泡的上升行为。然而，对于剪切稀化液体，Richardson-Zaki 方程不再适用。气泡的聚集加快了气泡上升速度并削弱了和气泡体积分数之间的相关性。此外，我们预测在剪切稀化粘弹性流体最大面积通量处的气体体积分数比在牛顿流体更高，这对剪切稀化粘弹性流体中的泡沫浮选过程具有重要的意义。

我们的研究将有助于理解光敏分子的结构对光响应蠕虫状胶束光响应行为的影响以及剪切变稀粘弹性流体中气泡的上升行为，这为剪切变稀粘弹性流体在工业上进一步的发展和应用如光流变液、气液分离、泡沫浮选等，提供了理论指导。

Contents

Chapter 1 Introduction

1.1 The self-assemblies of surfactants

Surfactants are amphiphilic molecules composed of a hydrophilic head group and a hydrophobic tail chain. The hydrophilic head group is usually a polar group, and the hydrophobic tail chain is usually a non-polar hydrophobic hydrocarbon chain. They can be orientated and arranged at interfaces, reducing surface tension.

Surfactants adsorb at air/liquid interfaces. At low concentrations, surfactants exist as monomers in aqueous solution. When the concentration increases to a certain concentration, the surfactant molecules will start to self-assemble into various aggregates in solution. This critical concentration is called CMC (critical micelle concentration). There are many types of surfactant self-assembly. As shown in Fig. 1.1, common ones include spherical micelles, wormlike micelles, vesicles and so on.

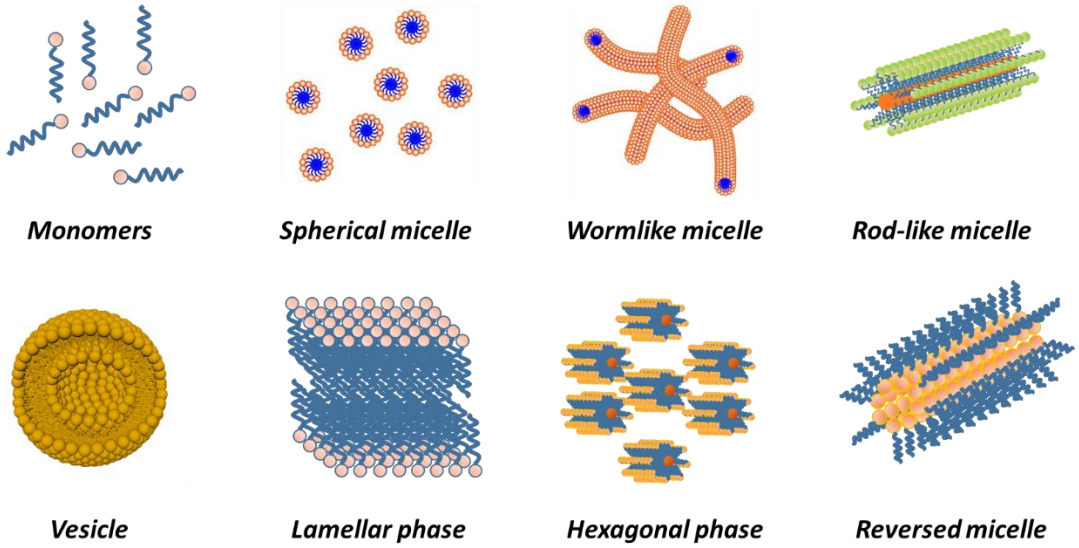

Fig. 1.1 The morphologies of the self-assembly formed by surfactant

1.1.1 Critical packing parameter of surfactants

The molecular structure of surfactants and solvent environment have a significant effect on the shape and size of micelles. According to the concept of critical packing parameter proposed by Israelachivili [2], the geometric shape of the aggregate can be predicted by the formula: $P = v/a_0 l$, where v is the volume of the hydrophobic chain of the surfactant; l is the maximum effective length of the hydrophobic chain, and a_0 is the effective area of the hydrophilic head group in the cross section. P characterizes the molecular interface packing parameter, and different packing patterns present different aggregate morphologies. As shown

in Fig. 1.2, when $P \leq 1/3$, the morphology of surfactant is expected to self-assemble into spherical micelles; when $1/3 \leq P < 1/2$, it is rod-like or wormlike micelles; when $1/2 \leq P < 1$, the aggregates are tubular or vesicles; when $P = 1$, they usually form lamellar structures. However, P is also affected by the external environment, such as surfactant concentration, temperature, pH, and ionic strength as this changes the interactions between the surfactants.

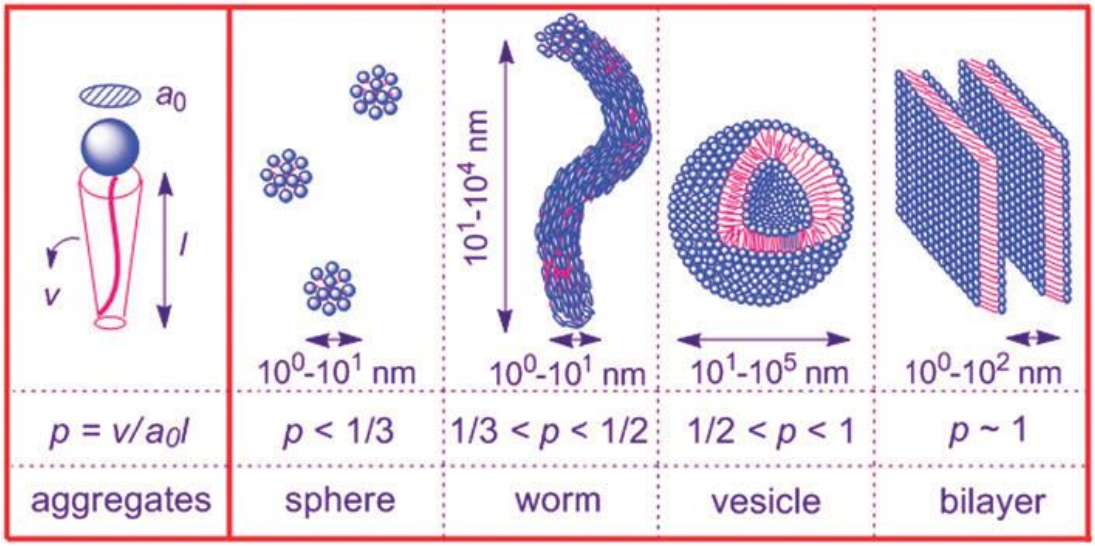

Fig. 1.2 Relationship between the critical packing parameter P and the morphology of self-assemblies predicted by Israelachivili [2-3]

1.1.2 Spherical micelles

Spherical micelles are the most common type of micelle structure. For most surfactants, when the concentration is above CMC, the surfactant will self-assemble to form spherical micelles in the aqueous solution. In the process of self-assembly, a permanently charged surfactant (positively or negatively) in an aqueous solution faces at least two opposite forces: (1) the associative force due to the hydrophobic effect; (2) The repulsive force due to the same charge of the polar head group [4]. The interaction between surfactant molecules allows them to spontaneously form micelles in aqueous solution.

1.1.3 Rod-like or wormlike micelles

After increasing the surfactant concentration or adding other additives to the surfactant system, due to the adjustment of the molecular arrangement, the morphology of the aggregates will change from small spherical micelles to larger micelles accordingly. In most cases, spherical micelles grow in one-dimension, forming cylindrical or rod-like micelles. As the concentration of surfactants or the amount of added additives continues to increase, short rod-like micelles will grow in length to form elongated wormlike micelles (WLMs) [5].

1.1.4 Vesicle

In water, surfactants with lower spontaneous curvate arrange in bilayers, formed of two layers of surfactants with hydrophobic groups facing inwards and hydrophilic groups facing outwards. When the bilayer is closed on itself, vesicles are formed. The structure of vesicles is similar to the structure of primitive biological cells and their size distribution is usually from 50nm to 200nm. Vesicles are of great significance in many fields, such as controlled drug release, bioseparation, and sensor [6]. The existence of surfactant vesicles greatly facilitates the study of bilayers, and play a significant role in the study of simulating biofilms and expanding the application of surfactants in biomedicine.

1.1.5 Other self-assemblies

In addition to spherical micelles, wormlike micelles and vesicles, Surfactants can aggregate into a whole variety of structures such as a gels [7], lyotropic liquid crystalline phases [8-9], and aqueous multi-phase systems which are organized at macroscopic length-scales [10-13]. These surfactant self-assembly strucutres have a wide range of applications in gene therapy, drug carriers, chemical reactions, daily chemicals, nanomaterials, etc.

1.2 Rheological properties of surfactant solutions

Surfactant solutions exhibit complex rheological behavior. The rheological properties of surfactant solutions depend on the self-assembly structures formed, which in turn is affected by the concentrations of the surfactant and counter ion, temperature, and the presence of added salts. Understanding the relationships between the self-assembly morphology and rheological behavior of surfactant solution are of great importance to numerous applications.

1.2.1 Spherical and short rod-like micelles

Spherical micelles at low concentrations are Newtonian fluids at a low shear rates. At high shear rates, the solution exhibits shear thickening behavior due to the shear-induced structures [14]. With the increase of surfactant concentration, the spherical micelles grow in one direction and become short rod-like micelles. The solution still maintains the same properties as the spherical micelles except for an increased viscosity.

1.2.2 Wormlike micelles

When the concentration of surfactant exceeds the critical overlapping concentration of wormlike micelles (C^*), the wormlike micelles begin to entangle with each other to form a dynamically reversible three-dimensional network structure. This structure remains in a dynamic equilibrium and can be continuously broken and reorganized, endowing the system

with significant viscoelasticity, similar to "living" polymers [15]. At low shear rate, the three-dimensional network structure of wormlike micelles is stable and the viscosity of them is considerable and nearly unchanged with the increase of the shear rate. The wormlike micelles undergo a shear-induced transition from a state of entangled, weakly oriented micelles to a state of highly aligned micelles above a certain critical shear rate after which shear thinning behavior is observed [16]. Once the degree of cross-linking and branching of the wormlike micelles is high enough, an elastic gel is formed. For the gel structure formed by surfactants, the shear thinning behavior also occurs due to the breakage of the network structure [17].

The widely accepted model used to describe the viscoelastic behavior of wormlike micelles was proposed by Cates and his colleagues [18]. This model is mainly composed of two characteristic relaxation times: one is the breaking time τ_b, which is used to characterize the time for the micelle to break into two parts; the other is the reptation time τ_{rep}, which is to characterize the micelle destruction and reptation time. The dynamic viscoelastic behavior of wormlike micelles attracts interest for both basic research and technical applications. When $\tau_b >> \tau_{rep}$, the dissociation and repacking of micelles is a slow process. At this time, the dominant stress relaxation mechanism is reptation. The wormlike micelles behave similarly to polydisperse, non-fractured polymers and have a certain non-exponential relaxation time $\tau_R = \tau_{rep}$. When $\tau_{rep} >> \tau_b$, the micelles are in a process of continuously rapid fracture and reorganization. The wormlike micelles formed by surfactants usually have this characteristic behavior which follows the Maxwell model [19]. The long-term behavior of stress relaxation can be described by a single exponential decay, and the corresponding relaxation time calculation formula is

$$\tau_R = (\tau_{rep}\tau_b)^{1/2} \tag{1-1}$$

This single exponential viscoelastic system has simple linear rheological behavior. For this Maxwell-compliant fluid, its viscoelasticity can be characterized by the following formula [20]:

$$G'(\omega) = G_0 \frac{\omega^2\tau_R^2}{1+\omega^2\tau_R^2} \tag{1-2}$$

$$G''(\omega) = G_0 \frac{\omega\tau_R}{1+\omega^2\tau_R^2} \tag{1-3}$$

G_0 is the elastic plateau modulus obtained by the extrapolation method; τ_R is the relaxation time; G' is the elastic modulus; G'' is the viscous modulus; when $G'' > G'$, the system mainly shows viscosity. When $G' > G''$, the system mainly shows elasticity.

The Cole-Cole rule [21] is an effective method to check whether a fluid conforms to the Maxwell fluid model. The corresponding formula is as follows:

$$G'' + (G' - \frac{G_0}{2})^2 = (\frac{G_0}{2})^2 \tag{1-4}$$

For fluids conforming to the Maxwell model, the *G'-G"* curve should be a semicircle, and the diameter of the semicircle should be G_0. However, due to the Rouse relaxation modes, the sample curve may deviate from the standard semicircular curve at high frequency.

Obviously, the viscoelastic behavior of the wormlike micelles can be studied by rheological methods. The characteristic parameters of the wormlike micelles can be estimated and characterized by the rheological properties of the system. The wormlike micelles formed by surfactants have been widely used in the industry due to their dynamic viscoelasticity. For example, in the process of oil recovery, the traditional polymer drilling mud will leave many holes of uneven size in the wellbore after the drilling process, reducing the efficiency of oil recovery. However, the surfactant-type drilling mud can be completely restored after the drilling process and it does not cause any damage to the system [22]. Therefore, more in-depth research on wormlike emicelles can help them better apply in various fields.

1.2.3 Other self-assembly structures

For the self-assembled vesicle structure of surfactant, when the vesicle concentration is low, the vesicle is a double-layer structure and the solution exhibits a Newtonian fluid behavior [23]. When the vesicle concentration is high enough, multilamellar vesicles were formed. The viscosity of the solution increases and the solution shows a shear thinning behavor without the zero-shear viscosity [24].

1.3 Gemini surfactant

Oligomeric surfactants are a type of surfactant developed in recent years. Such molecules are composed of two or more amphiphilic chains, and the amphiphilic chains are connected together by linking groups. Gemini surfactants are typical oligomeric surfactants, consisting of two hydrophobic tails and two hydrophilic head groups connected by a spacer. Bunton et al. first reported the synthesis of this type of a surfactant, which was named "Gemini" by Menger and Littau [25]. Compared with traditional single-chain surfactants, Gemini surfactants have the advantages of extremely low critical micelle concentration (CMC), low interfacial tension, good solubilization ability and strong self-assembly ability and richer aggregate morphologies, etc. Because of these unique properties, Gemini surfactants are considered to be the "next generation" high-quality surfactants and are widely used in various research fields [26-28].

1.3.1 The structure of Gemini surfactant

Gemini surfactants are composed of two hydrophobic tails, two hydrophilic head groups, and a spacer group which links the two head groups, as shown in Fig. 1.3. The molecular structure of most Gemini surfactants is symmetric: two identical polar head groups and two

hydrophobic tail chains with the same chain length. However, there are also some studies on the synthesis and self-assembly behavior of asymmetric Gemini surfactants [29-32].

Gemini surfactants can be divided into different subcategories according to the length and composition of the hydrophobic chain, the flexibility (rigid/flexible) and structure (length and polarity) of the spacer group, and the chemical structure of the polar head group (cationic/anionic/nonionic). The hydrophobic tails of Gemini surfactants are usually composed of alkyl chains with adjustable length. The types of polar head groups and spacer groups are also rich. The polar ion head groups can be cationic quaternary ammonium salts, amine ions or anionic phosphoric acid groups, sulfate ester groups, carboxylic acid groups, and sulfonic acid groups. The polar nonionic head group can be polyether or sugar. The spacer group can be a rigid chain (short chain composed of methylene, stilbene, etc.) or a flexible chain (long hydrocarbon chain), and it can also be a polar group (polyether) or non-polar group (aliphatic, aromatic, etc.). By changing the structure or length of the hydrophobic tail chains, polar head groups and the spacer group, we can adjust the hydrophilicity, the charge and other properties of Gemini surfactants, thereby enabling Gemini surfactants to have a rich variety, unique physical and chemical properties and adaption to a variety of specific applications [28].

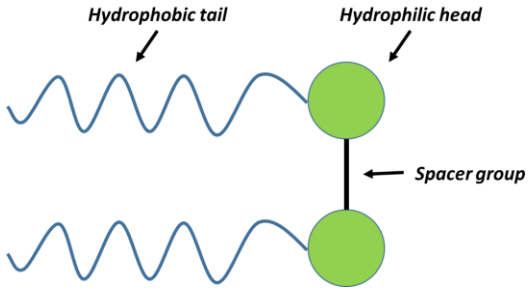

Fig. 1.3 Schematic structure of Gemini surfactant

1.3.2 Classification of Gemini surfactants

Gemini surfactants are classified according to their charge in aqueous solution. They can be classified into four types: cationic, anionic, zwitterionic and nonionic Gemini surfactants. Among them, cationic surfactants play an important role in the field of self-assembly and quaternary ammonium salt Gemini surfactants are main cationic surfactants. This Gemini surfactant has a simple structure which is easy to synthesize and has excellent performance. And because of the special structure of its head group, it presents many unique properties, such as sterilization, anti-corrosion, antistatic, etc., which cannot be replaced by other types of Gemini surfactants. Quaternary ammonium salt cationic Gemini surfactants are composed of a quaternary ammonium salt ion head group and a linear hydrocarbon tail chain, which can be expressed as *m-s-m*, where m and s respectively represent the number of carbon atoms in the

alkyl tail chain and the number of carbon atoms of the spacer. Their molecular structure is shown in Fig. 1.4. Quaternary ammonium salt cationic Gemini surfactants have greater flexibility than the corresponding single-chain surfactants. For example, the quaternary ammonium Gemini surfactant C_{12}-s-C_{12}·2Br^- (s = 2, 4, 6...20), as the methylene chain(s) grows, aggregates with different morphologies such as wormlike micelles, spherical micelles and vesicles can appear in the solution [33]. Zana's group has carried out a lot of research work on the synthesis and properties of quaternary ammonium cationic Gemini surfactants, which has promoted the development of Gemini surfactants [34].

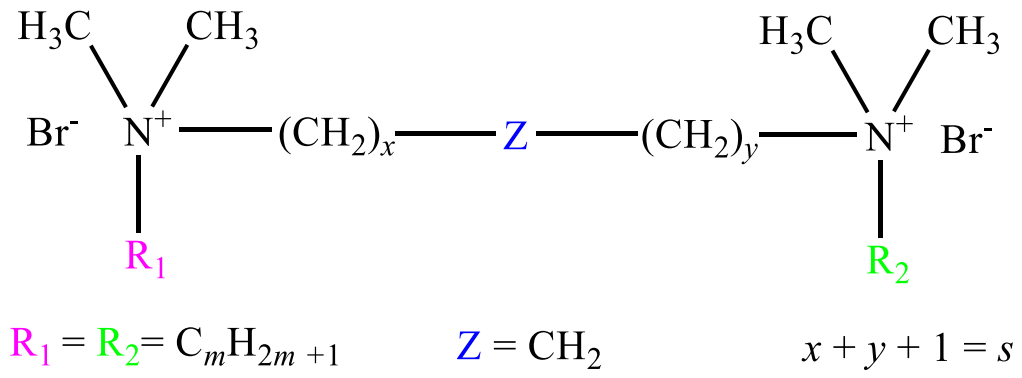

Fig. 1.4 Schematic structure of quaternary ammonium cationic Gemini surfactants *m-s-m* [34]

1.3.3 Properties of Gemini surfactants

Traditional surfactants have to maintain a certain distance between the molecules due to the electrostatic repulsion between their polar head groups. For Gemini surfactants, two polar head groups are connected by chemical bonds, thereby the two head groups are very tightly connected together. On the one hand, this connection greatly weakens the electrostatic repulsion between the two polar head groups. On the other hand, due to the proximity of the two alkyl chains, a strong interaction is generated between the hydrophobic tails, thereby greatly enhancing the hydrophobic binding force, which promotes the adsorption on the interface and the self-polymerization in the solution. Therefore, Gemini surfactants have many advantages over traditional surfactants [27-28, 34].

1.3.3.1 Excellent interfacial activity

Owing to the existence of the spacer group, Gemini surfactants can overcome the separation tendency of traditional surfactants due to the electrostatic repulsion between polar ion head groups. The CMC of Gemini surfactants is usually one to two orders of magnitude lower than the corresponding single-chain surfactants. In addition, there are more efficient in reducing the surface tension at gas/water and oil/water interfaces than traditional single-chain surfactants [35-36].

1.3.3.2 Stronger self-assembly ability and richer aggregation behavior

Compared with traditional surfactants, Gemini surfactants have a stronger tendency to aggregate and more readily form self-assemblies with low curvature in solution. In addition, Gemini surfactants have a rich aggregation morphology due to the packing pattern affected by their special molecular structure. The micelles in some Gemini surfactant solutions even self-assemble into unusual shapes, such as hollow cylinders (tube), ring, disk etc. [37-38]. The aggregate morphology of Gemini surfactant micelles depends not only on the molecular structure of the surfactant, but as all surfactants, also on external conditions, including the concentration of the solution, temperature, ionic strength, etc.

Chen [39] observed the microstructure of the aggregates of Gemini surfactant *m*-3-*m* (*m* = 16, 18) at different temperatures using a transmission electron microscope, and found that the aggregation morphology of 18-3-18 in aqueous solution changes from spherical micelles to rod-like micelles and to wormlike micelles with the increase of temperature. The micelle morphology can be restored to the original structure when the temperature is lowered. However, traditional surfactants hardly exhibit such complex microstructure changes with temperature changes.

1.3.3.3 Rheological properties

The aggregate structure of surfactant molecules in aqueous solution has a direct impact on the rheological properties of the system. The self-assembly of Gemini surfactant is special and arrives at lower concentrations, therefore the rheology follows. Compared with traditional surfactants, Gemini surfactants have higher viscosity when the concentration is lower, and the viscosity and concentration are positively correlated within a certain concentration range. Zana [40] studied the rheological properties of Gemini surfactant 12-s-12 (s = 2, 3, 4) and found that when the concentration of the 12-2-12 solution exceeds 2%, an entangled wormlike micelles form is produced. The solution exhibits viscoelasticity, endowing the surfactant solution rheological properties similar to the polymer solution. However, compared with polymer solutions, the wormlike micelles formed by surfactant molecules are in a dynamic equilibrium process, so they have better shear resistance. In addition, due to their special structure, the position and properties of the spacer group of Gemini surfactants is easy to adjust, so as to control the micelle type and the rheological properties of the system.

1.3.3.5 Other advantages

In addition, compared with single chain surfactants, Gemini surfactants also have better synergistic effect, water solubility and wettability, foaming ability, more complex phase behavior with polymers and other surfactants, stronger solubilization and emulsification capabilities, and lower Krafft points. These excellent properties of Gemini surfactants make it

have broad application prospects in the fields of chemical flooding, skin care, material synthesis, biomedicine, etc [41].

1.4 Responsive self-assembly system constructed by surfactants

In the previous sections we saw that surfactants can self-assemble in aqueous solutions to form a wide variety of ordered aggregates. In some fields such as, material synthesis from surfactant templates, drug delivery and release systems in pharmaceutics, and gene transfer in biological sciences, the conversion of aggregates between different structures would be interesting [42]. For example, when a vesicle formed by surfactants is used as a drug delivery carrier, in order to improve the release efficiency of the drug at the target site the structure and morphology of the vesicle needs to be adjusted appropriately [43]. Small changes in external environmental conditions (such as pH, CO_2, temperature, light, electric field and magnetic field, etc.) can stimulate changes in the molecular structure of the surfactant system, thereby affecting the interfacial properties of the system and the structure of the self-assembled aggregates. Stimulation can also be used to make the system transition between different microstructures Such changes are accompanied by changes in the physical and chemical properties of the system on the macro scale, such as viscosity [44]. The research and application of stimulus-responsive materials constructed by surfactants has become a topic of increasing interest to scientists [45-47].

These stimuli can be divided into physical and chemical, as shown in Fig. 1.5. Chemical stimuli require that the responders are directly added to the system to adjust the interaction between the surfactant and the solvent molecules on the molecular scale, including redox, pH and CO_2 response. The physical signal response is to adjust the self-assembly morphology of the system from outside the system by changing the kinetics and thermodynamics of the system or the interaction between molecules at specific positions, by using physical signals such as temperature, light, and electromagnetic fields [48-49]. Therefore, we can control and adjust physical and chemical properties by changing the environmental conditions in the responsive self-assembly system (pH value, ionic strength, etc.) or applying external stimuli (temperature, light, magnetic field, electric field, etc.), so as to expand application of this system in the functional material preparation, printing and dyeing, catalysis, biomedicine, micro-control sensing [50-52].

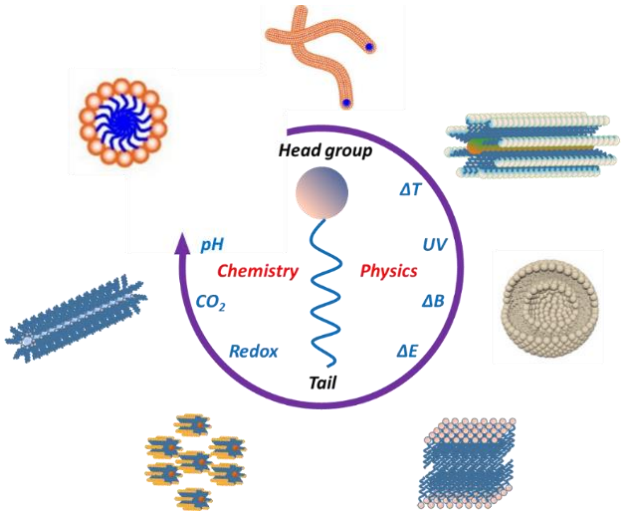

Fig. 1.5 Responsive self-assembly system constructed by surfactants

There are two main ways for surfactants to participate in the construction of intelligent responsive self-assembly systems: one is to introduce stimulus-responsive functional groups into the molecular structure of surfactants, that is, to synthesize new functional surfactants; the other is to introduce environmentally responsive components into the surfactant system, and construct an environmentally responsive system by the synergistic effect between the responsive components and surfactant molecules. The pros and consof the former are obvious. The system contains only one single component and no other additives are needed. The operation is simple and convenient. However, such surfactants often require complex synthesis, which is time-consuming and labor-intensive, and cannot effectively form ordered aggregates. Surfactants in the latter type of system are easy to synthesize and inexpensive. Based on the non-covalent interactions between surfactants and the response molecules, including van der Waals forces, hydrogen bonds, hydrophobic/hydrophilic interactions, electrostatic forces, π-π stacking and metal-ligand coordination complexes, the self-assembly in such system is easy to adjust and control [53-55]. In this dissertation, we are interested in the stimulus responsive system constructed through the synergy between surfactants and additives, which is why I will concentrate on describing such systems in the following.

1.4.1 Chemical signal responsive self-assembly system

Chemical signal responsive self-assembly refers to the surfactant self-assembly systems that respond to changes in chemical components or chemical properties of the system through adding extra substance into the system. The stimulus depends on a certain chemical reaction, and the responsive behavior of the system is adjusted by controlling the direction and degree of the reaction. Common chemical signal responsive self-assembly system includes the pH-responsive, CO_2-responsive, redox-responsive self-assembly and so on.

1.4.1.1 pH-responsive

pH-responsive self-assembly refers to adjusting the morphology and physicochemical properties of aggregates in the system by changing the pH value in the solution. Surfactant molecules in such systems or their additives contain pH-responsive groups (such as -COOH, -NH_2, -ArOH, -OPO_3H_2, and -PO_3H_2, etc.). They can change the molecular structure and the driving force for the formation of aggregates by interacting with H^+ or OH^- and further affect the physical and chemical properties of the solution on the macroscopic level [56].

A pH responsive system can be constructed by adding pH-sensitive molecules to the surfactant system. As shown in Fig. 1.6, Feng's research group [57] prepared a pH-responsive wormlike micelle system by simply mixing the amphiphilic molecule N-erucamidopropyl-N, N-dimethylamine with the pH-responsive molecule maleic acid (UC22AMPM). It was found that when the pH of the system increased from 6.20 to 7.29, the zero-shear viscosity of the wormlike micelles decreased by five orders of magnitude.

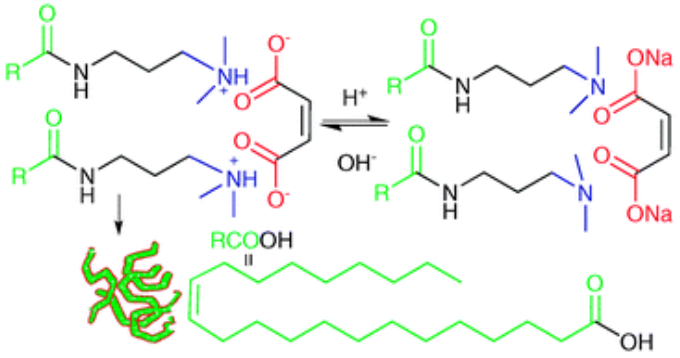

Fig. 1.6 pH-responsive self-assemblies constructed by surfactants [57]

1.4.1.2 CO_2-responsive

Another chemical stimulus is CO_2, which has excellent biocompatibility and reproducibility, and does not contaminate products. When the absorbed CO_2 is replaced by an inert gas, there is also no accumulation in the system. The CO_2 response shows more advantages than the pH response [58]. For mixed systems, the additives or surfactants containing tertiary amine groups are usually used to construct a CO_2-responsive self-assembly system. Feng [59] developed a CO_2-responsive wormlike micelle system based on the anionic surfactant sodium dodecyl sulfate (SDS) and N, N, N', N'-tetramethyl-1,3-propanediamine (TMPDA) in a ratio of 2:1. As shown in Fig. 1.7, when CO_2 is introduced into the mixed solution, the TMPDA molecule is protonated into a quaternary ammonium salt. Every two SDS molecules and a protonated TMPDA molecule are bridged together by non-covalent electrostatic attraction, forming a "pseudo" Gemini surfactant. At this time, a wormlike micelle with viscoelasticity is constructed in the system. After N_2 is introduced into the system to remove CO_2, the quaternized molecules are deprotonated into tertiary amines, which destroys the bridge of "pseudo" Gemini

surfactant. They return to the traditional SDS molecules and reassemble into low-viscosity spherical micelles. This reversible spherical-wormlike micelle conversion can still have good CO_2 responsiveness after several repeated cycles.

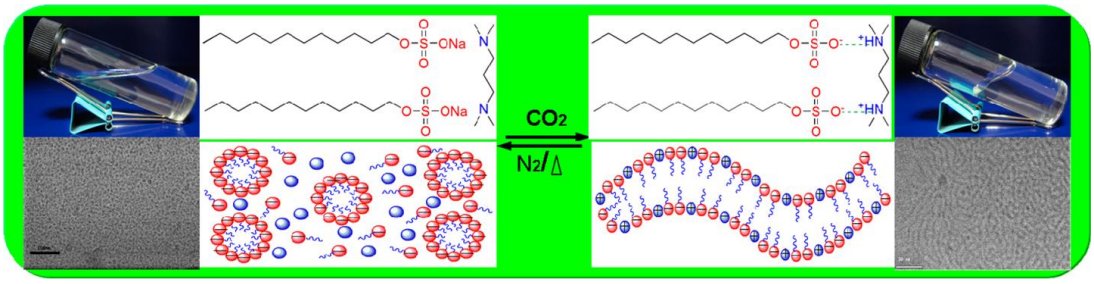

Fig. 1.7 CO_2-responsive self-assemblies constructed by surfactants [59]

1.4.1.1 Redox-responsive

In the physiological environment redox processes are widespread, which is why the redox self-assembly system has important research value. Usually, self-assembled systems with redox response contain ferrocene, sulfur atoms and other groups in their surfactants or additives. By controlling and changing the molecular redox state, the microstructure of the self-assembled body and the macroscopic properties of the system can be adjusted. Abe's group [60] developed a redox fluid based on cationic ferrocene-based surfactant (11-ferrocenylundecyl) trimethylammonium bromide (FTMA) and sodium salicylate (NaSal). As shown in Fig. 1.8, initially, FTMA and NaSal self-assemble to form wormlike micelles. The redox active ferrocene group at the end of alkyl tail chain of FTMA can control of its chemical structure by switching between the reduced and oxidized states: the reduced ferrocene group is hydrophobic, and the oxidized ferricinium cation is hydrophilic. Therefore, the wormlike micelles are transformed into rod-like micelles after oxidization, resulting in a sharp decrease in the viscosity of the system and the loss of elasticity. Based on the control of the hydrophilic-lipophilic balance of FTMA through redox stimulation, a smart material that can switch between wormlike micelles and short rod-like micelles can be constructed.

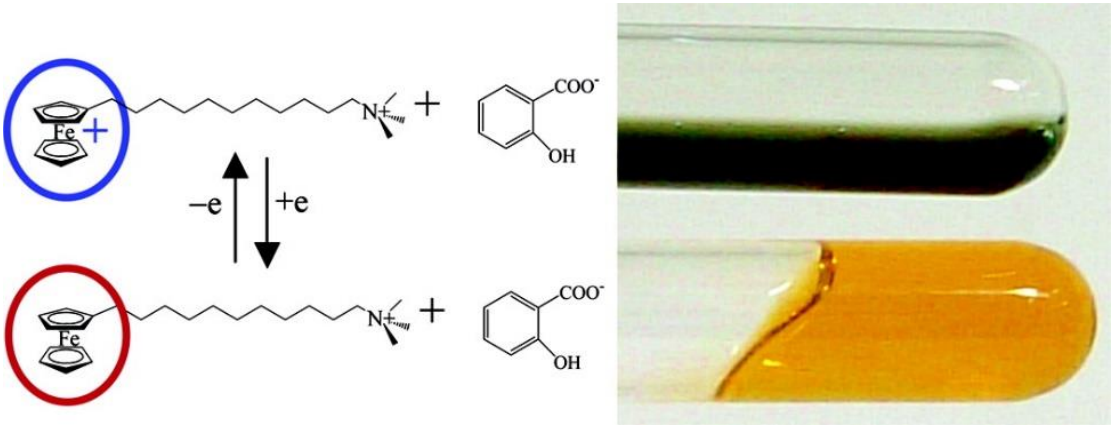

Fig. 1.8 Redox-responsive self-assemblies constructed by surfactants [60]

1.4.2 Physical signal responsive self-assembly system

Physical stimuli can be simple, convenient, environmentally friendly and effective methods to regulate the formation and performance of aggregates. We start with a short section on temperature-responsive systems, before describing photo-responsive systems in more detail.

1.4.2.1 Temperature-responsive

The most widely used temperature-responsive surfactant system is that of temperature-responsive fluids, i.e., systems whose flow properties change with temperature. People divide the fluids formed into two types: thermal thinning (the viscosity of the system decreases with temperature) and thermal thickening (the viscosity of the system increases with temperature). Following the Arrhenius law, the length of the micelle decays exponentially with the increase of temperature, which leads to an exponential drop in the zero-shear viscosity of the system. Since the thermal thinning of wormlike micelles is a very common phenomenon, surfactant self-assemblies with thermal thickening have been the focus of many researchers [61]. The thermal thickening behavior is mainly caused by the transformation of low-viscosity spherical micelles or vesicles into wormlike micelles with high viscosity, and the transformation of viscoelastic wormlike micelles into elastic gels. Raghavan [62-63] developed a thermal thickening micelle system (Fig. 1.9) by simply mixing cetyl trimethylammonium bromide (CTAB) and 5-methyl salicylic acid (5MS). As the temperature increases, the self-assembly system transforms from vesicles to wormlike micelles, and the zero-shear viscosity increases by more than 1000 times. When they are heated, some anions at the aggregate/water interface are transferred to the bulk phase because heating hinders the weak physical adsorption. This desorption changes the geometry of the molecules, thereby reducing the interfacial curvature of the aggregates, resulting in a transformation of the aggregate structure.

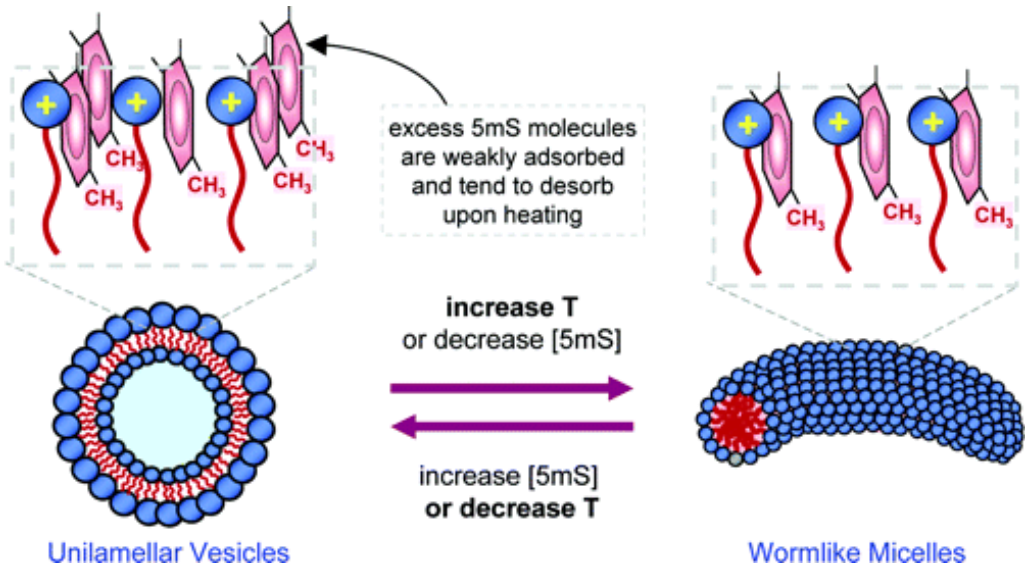

Fig. 1.9 Temperature-responsive self-assemblies constructed by surfactants [63]

1.4.2.2 Photo-responsive self-assembly system

Photo-responsive self-assembly of surfactants requires that a component involved in the self-assembly will undergo photo-isomerization, photo-polymerization, or photo-degradation under stimulation of a specific wavelength of light, which causes a change of the structure or polarity of the photo-sensitive group. This change will affect the interaction between molecules, which will regulate their self-assembly behavior (the microstructure of the self-assembly, the phase behavior and rheology of the macroscopic system) [64].

Compared to the stimuli introduced in the previous section, photo stimulus has many advantages. First, light is a non-invasive trigger which avoids direct contact with the sample, thereby avoiding changes in system components and in temperature. Second, light provides a wide range of adjustable parameters (such as wavelength, intensity, and duration) to manipulate the self-assembly behavior of the photo-responsive system. Third, compared with redox reagents, pH changes, salinity, etc., light is a mild, inexpensive and easily available energy source. Compared with electricity and ultrasound, light can be finely positioned in time and space. This is especially valuable in nanoscience and nanotechnology: such as sensor systems, nano-electronics, microfluidics, information storage and MEMS devices [65]. In Fig.1.10, common photo-responsive additives are shown, these include azobenzene molecules, cinnamic acid molecules, and spiropyran molecules. They all have in common, that under irradiation of ultraviolet light, they absorb the energy of the excited photon, and then undergo electronic transitions and the transformation of molecular structure. These changes affect the packing pattern of the surfactant molecules in the aggregates, thereby regulating the self-assembly behavior of the system. In the next section the different types of systems will be described in more detail.

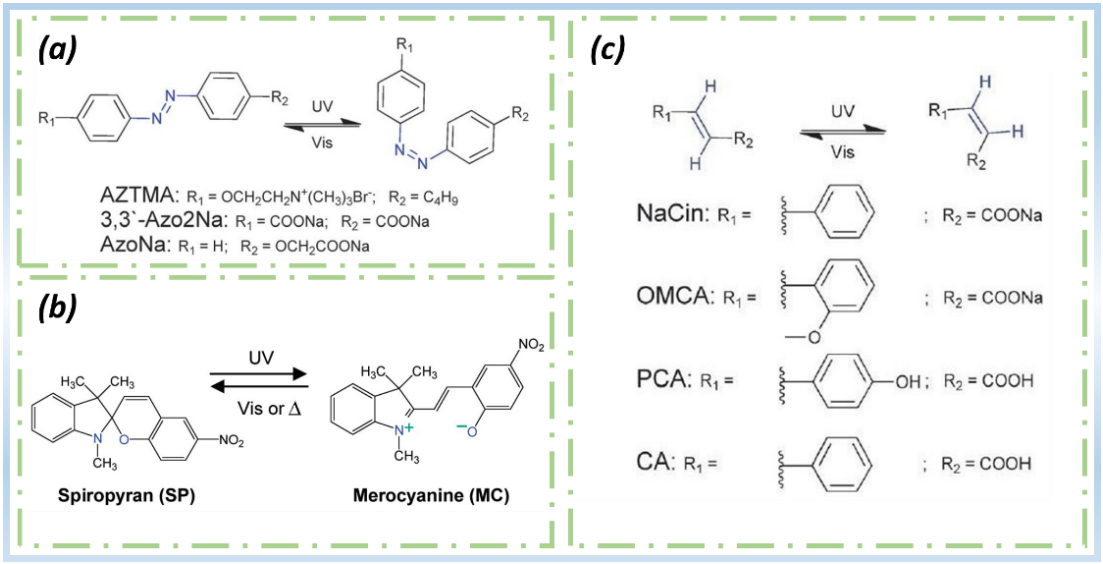

Fig. 1.10 Common photo-sensitive molecules (a) Azobenzene (b) Spiropyran (c) Cinnamic acid [66]

Photo-responsive self-assemblies constructed by azobenzene

The azophenyl group is one of the typical photo-induced isomerization groups. The trans to cis isomerization of the azophenyl group in ultraviolet-visible light can be repeated many times without decomposition [67]. As shown in Figure 1.11, Raghavan [68] used 4-azobenzene carboxylic acid (ACA) and a cationic surfactant bis(2-hydroxyethyl)methyl ammonium chloride (EHAC) to prepare a new type of photo-responsive fluid. It was found that initially ACA and EHAC self-assembled to form unilamellar vesicles. These vesicles are well dispersed in the solution, so the sample has a lower viscosity. After being exposed to ultraviolet light, the vesicles transform into wormlike micelles. The flexible chains of long wormlike micelles entangle with each other in the aqueous solution, so the sample exhibits an extremely high viscosity, which is nearly 1 million times higher than that of the vesicle solution. The self-assembly constructed by the azobenzene molecules can be switched back and forth between ultraviolet light and visible light, so that the sample can reversibly cycle between the low-viscosity state and the high-viscosity state.

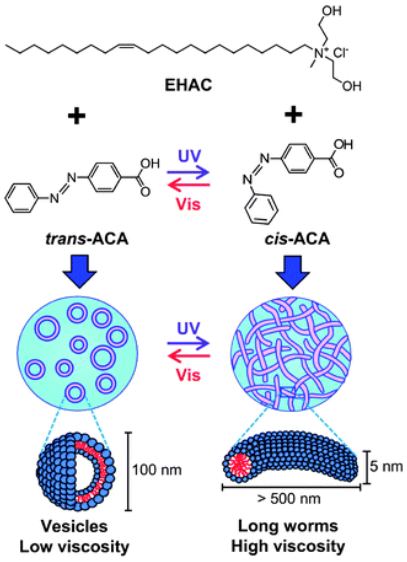

Fig. 1.11 Photo-responsive behavior of the EHAC–ACA system [68]

Besides the photo-thickening behavior, a large number of photo-thinning fluids that transform from relatively viscous wormlike micelles into aggregates with relatively low viscosity after exposure to ultraviolet light have also been reported. Huang's group [69] established a photo-controllable and adjustable polymorphic multi-scale binary self-assembly system by adding azobenzene sodium (AzoNa) to the traditional surfactant CTAB (Fig. 1.12). With the extension of ultraviolet light irradiation time, the isomerization state of azobenzene can regulate the self-assembly from long flexible wormlike micelles to vesicles, lamellae, rod-like micelles and small spherical micelles. Therefore, the properties of the solution change significantly on a macroscopic scale. The photo-induced changes in the dipole moment and

geometric configuration of the azophenyl cause the transition of the self-assembly in multi-state multi-scale. This kind of photo-regulated multi-state and multi-scale self-assembly system expands the industrial applications of photo-responsive self-assembly system, such as molecular devices, logic gates and sensors.

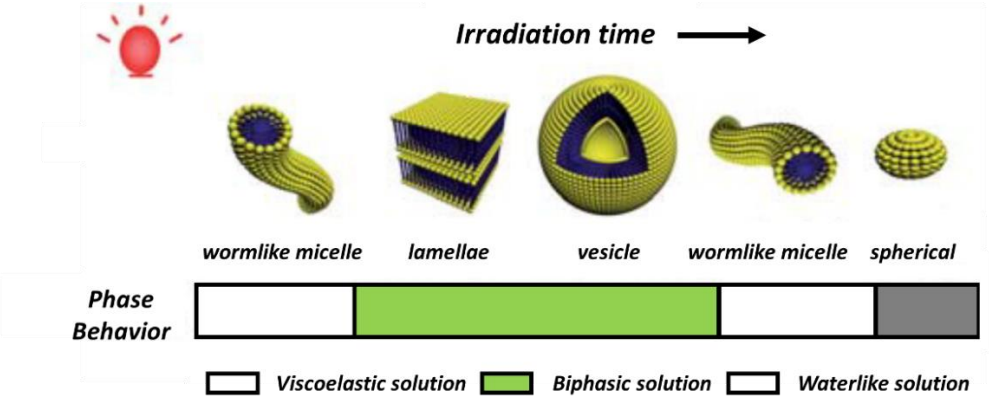

Fig. 1.12 Photo-responsive behavior of the AzoNa/CTAB system [69]

Photo-responsive self-assemblies constructed by spiropyran

Spiropyran (SP) is a well-known photochromic compound that can undergo photo-isomerization between the colorless SP form and the open merocyanine (MC) under different wavelengths of light irradiation. The closed SP is a non-ionic hydrophobic molecule, while the open MC form is an ionic hydrophilic molecule. The different properties before and after the light cause the difference in the interaction between the surfactant molecules and two photo-isomers [70-71]. In Fig. 1.13, Raghavan [72] incorporated the SP into lecithin/sodium deoxycholate (SDC) reverse micelles to obtain a photo-responsive rheological fluid. Under ultraviolet light, SP is isomerized to MC, reducing the fluid viscosity by 10 times. Furthermore, Sakai [73] studied the adsorption behavior of spiropyran-modified cationic surfactants on the silica/water solution interface and the photo-responsive properties of the assembled molecules on the interface after adsorption. Hanley [74] synthesized a series of surfactants with SP as the head group, and discussed the influence of the length of the hydrophobic tail chain on its physical and chemical properties and the behavior of the liquid crystal matrix, which paves the way for a stimulus response element for ultraviolet light.

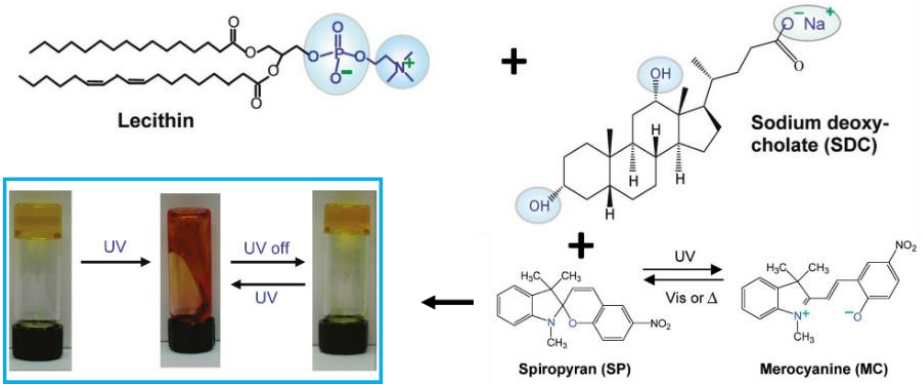

Fig. 1.13 Photo-responsive behavior of photorheological fluids constructed by the lecithin/SDC reverse micelles and SP [72]

Photo-responsive self-assemblies constructed by cinnamic acid

Cinnamic acid molecules are also a common photo-responsive additive. In the absence of ultraviolet light irradiation, the cinnamic acid group exists stably in *trans* structure. When the cinnamic acid group is irradiated with ultraviolet light (wavelength around 365nm), the cinnamic acid is isomerized from the *trans* structure to the *cis* structure. This structure change can lead to an increase or decrease in solubility, as will be discussed in Chapter 3. The small changes in the photo-responsive molecular structure lead to changes in the microstructure of the aggregates of the system and the macroscopic physical and chemical properties. Compared with azobenzene molecules, cinnamic acid molecular additives have better solubility, so they can be directly compounded with surfactants, and do not need to be improved by further synthesis like azobenzene additives. It is simpler and more convenient. Compared with azobenzene additives, cinnamic acid additives have lower cost, better biocompatibility, and rich morphologies. And they are relatively stable under visible light, and are colorless and transparent. Therefore, cinnamic acid additives are an excellent choice for studying the photo-responsive self-assembly system constructed by surfactants although their response is irreversible.

(1) Photo-responsive wormlike micelles constructed by cinnamic acid

Raghavan's group has done a lot of work on the photo-responsive wormlike micelles constructed by the cinnamic acid additive/surfactant mixture system [72, 75-76]. As shown in Fig. 1.14, they [75] constructed wormlike micelles through the cationic surfactant CTAB and *trans*-o-methoxycinnamic acid (*trans*-OMCA) in alkaline solution, Under UV light, OMCA is isomerized from *trans*-OMCA to *cis*-OMCA, which changes the packing patterns of molecules at the micelle interface, resulting in the transformation of long wormlike micelles into shorter wormlike micelles or rod-like micelles. The rheological results show that the viscosity of the solution can be reduced by more than 4 orders of magnitude with the extension of the UV

irradiation time. The performance of the fluid can be adjusted by changing the composition of the system and the duration of ultraviolet light irradiation, thereby expanding its potential applications in sensors and microfluidic devices.

In addition to the aqueous system, Raghavan [77] also reported a photo-responsive system based on reverse micelles in non-polar solutions. Dai's research group has also done a lot of research in this area [78-79]. The photo-thinning fluid formed by wormlike micelles constructed by *trans*-OMCA and C_{16}mimBr in aqueous solution was systematically studied. They used N-cetyl-N-methylmorpholinium bromide (CMMB) and *trans*-cinnamic acid (*trans*-CA) to construct a new type of triple responsive (photo, pH and temperature responsive) wormlike micelles, which can be used as a good model of wormlike micelles with multiple responses to light stimulation. Their studies help to understand the mechanism of multiple responses and broaden its application range.

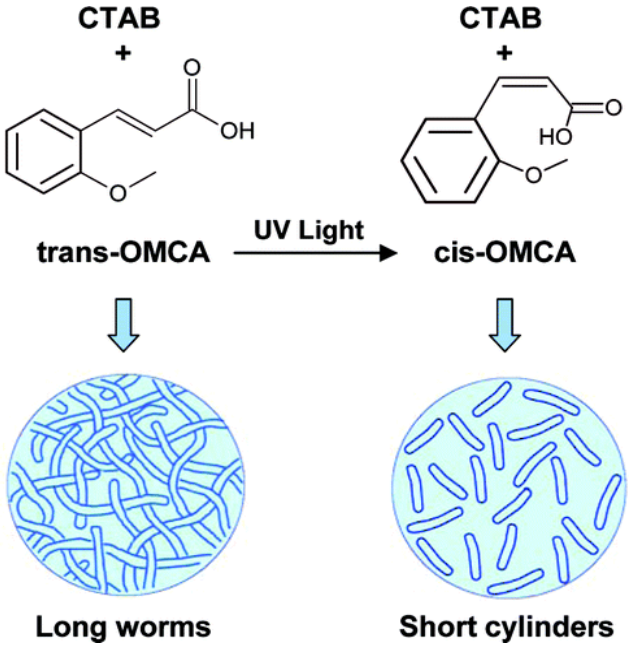

Fig. 1.14 Photo-responsive behavior of the CTAB/*trans*-OMCA wormlike micelle system [75]

(2) Photo-responsive vesicle constructed by cinnamic acid

Besides the reports of the photo-responsive wormlike micelles constructed by cinnamic acid salts, the photo-responsive behavior of vesicles has also been extensively studied. As shown in Fig. 1.15, Hao's group [21] studied the phase behavior and photo-responsiveness of the mixed system of tetradecyldimethylamine oxide (C_{14}DMAO) and para-coumaric acid (*trans*-PCA). Their study found that when the concentration of C_{14}DMAO in the mixed system was fixed, with the increase of PCA concentration, L_1 phase (micelle), two-phase L_1/L_a, L_a phase (vesicle) and L_a/precipitation appeared in sequence. By irradiating the area of the vesicles with ultraviolet light, the vesicles will be transformed into wormlike micelles.

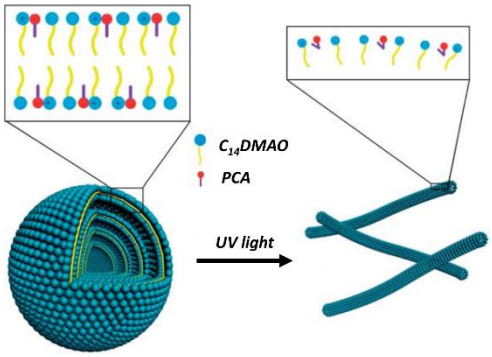

Fig. 1.15 Photo-responsive behavior of the C_{14}DMAO/*trans*-PCA vesicle-to-wormlike micelle system [21]

Li's group [80] studied the photo-responsive behavior of vesicles constructed by alkyldimethylamine oxide (C_mDMAO, *m* = 10, 12, 14) and *trans*-coumaric acid isomerides, including *trans*-ortho-coumaric acid (*trans*-OCA), *trans*-meta-coumaric acid (*trans*-MCA) and *trans*-para-coumaric acid (*trans*-PCA). The results show that multi-lamellar vesicles (MLV) appeared in certain areas in *trans*-PCA/C_{12}DMAO and *trans*-OCA/C_mDMAO systems. The molecular structures of C_mDMAO and *trans*-coumaric acid isomers significantly affects the region of MLV. The larger the *m*, the larger the MLV area. For the *trans*-OCA/C_mDMAO system, depending on the chain length of C_mDMAO and the ratio of *trans*-OCA to C_mDMAO, multi-lamellar vesicles can be transformed into a homogeneous and transparent micellar phase or two-phase system by ultraviolet light irradiation. This research is of great significance for the systematical understanding of the ratio and structure of surfactants on the photo-responsive behavior of self-assemblies in the system. Furthermore, the research on photo-responsive self-assembly constructed by surfactants of different chain lengths and photo-sensitive molecules of different structures provides basic data and theoretical guidance for expanding the application of smart materials.

(3) Photo-responsive lyotropic liquid crystal constructed by cinnamic acid

Apart from the nano-scale wormlike micelles and vesicles in the photo response research, the meso-scale lyotropic liquid crystals constructed by cinnamic acid derivatives also have important research value. Yu's group [81] combined two imidazole-based surface active ionic liquids (SAIL) with photo-responsive molecules (*trans*-CA; *trans*-PCA) to synthesize 1-dodecyl-3-methylimidazolium cinnamate ([C_{12}mim][CA]) and 1-dodecyl-3-methylimidazolium para-hydroxy-cinnamate ([C_{12}mim][PCA]), and studied their self-assembly behavior in aqueous solution. As shown in Fig. 1.16, hexagonal liquid crystal phase (H_1) and cubic liquid crystal phase (V_2) are constructed in [C_{12}mim][CA] aqueous solution. In contrast, the [C_{12}mim][PCA] / H_2O system displays a single hexagonal liquid crystal phase (H_1) in a wide concentration region. Under ultraviolet light, the photo-isomerization of cinnamate molecules causes the decrease of surface activity of the SAIL and the lattice parameters of the

formed liquid crystal phase. This work enriches the research on photo-responsive lyotropic liquid crystals, and expands the potential applications of smart-responsive liquid crystal materials in drug delivery, biochemistry, materials science, etc.

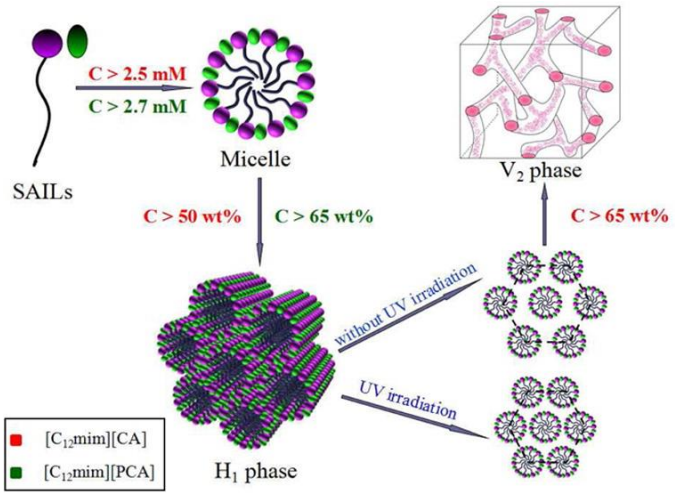

Fig. 1.16 Photo-responsive behavior of $[C_{12}mim][CA]/H_2O$ and $[C_{12}mim][PCA]/H_2O$ binary systems [81]

1.4.2.3 Applications of the photo-responsive self-assembly

As shown in Fig. 1.17, photo-responsive self-assemblies have a wide range of applications in the fields of smart fluids, material synthesis, drug delivery systems, and gene transfer in biological sciences. Tian [82] constructed a reversible solubilization system through the micelles formed by the photo-responsive surfactant AZTMA and the commercial non-ionic surfactant Tween 80 to solubilize the organic pollutants in the soil, thereby purifying the soil. This system overcomes some shortcomings of traditional surfactants in strengthening soil restoration, such as high cost and secondary pollution caused by washing agents and increases the commercial application value of photo-responsive self-assembly.

Surfactant wormlike micelle systems used for fluid drag reduction (DR) have poor heat transfer capabilities. Therefore, these fluids are only used in some circulation systems where heat exchange is not important. Based on this, Jacques [83] constructed a photo-responsive wormlike micelle system through the cationic surfactant oleyl bis(2-hydroxyethyl)methyl ammonium chloride (EO12) and *trans*-OMCA, which provided a potential solution for the above problems. Initially, these strong viscoelastic wormlike micellar fluids have a good drag reduction efficiency (DR efficiency up to 75%). After UV irradiation, OMCA undergoes photoisomerization from trans to cis. The liquid shows lower viscoelasticity and lower DR performance. However, its heat transfer performance is far better than the original fluid. This study highlights the possibility of cutting off DR (and thus enhancing heat transfer) at the inlet of the heat exchanger in the circulation system.

Huang [84] reported a bacterial-like vesicle system (C_4AG@2β-CD). The ultraviolet light will trigger the development of hair on the surface of the vesicle (similar to cilia extending from the surface of bacteria). The formation of cilia causes the encapsulated drug to be released from the vesicles. This bioinspired vesicle creates a novel type of photo-responsive nano-carrier which releases active ingredients through deformation rather than complete destruction.

The hydrated structure of hydrogel makes it attractive as a bio-friendly material. Therefore, hydrogels have various potential applications in the biomedical field, such as drug delivery and tissue engineering scaffolds. Alexander [85] reviewed the latest research progress of photo-responsive hydrogel systems. The transition from gel to sol under light irradiation makes photo-responsive hydrogel systems have a good application prospect in emerging biomaterials. Ehud [86] reported a new photo-responsive lyotropic liquid crystal system designed by the host-guest method. The system consists of monoolein (MO) and oleic acid (OA) as the host lipids and the active unit of azobenzene as the guest. The isomerization of the guest molecule is controlled by light, so as to achieve the precise control of the time, space and dosage of drug release. When a continuous release may be toxic, using this lipid biomaterial is a good alternative as an effective matrix in therapy.

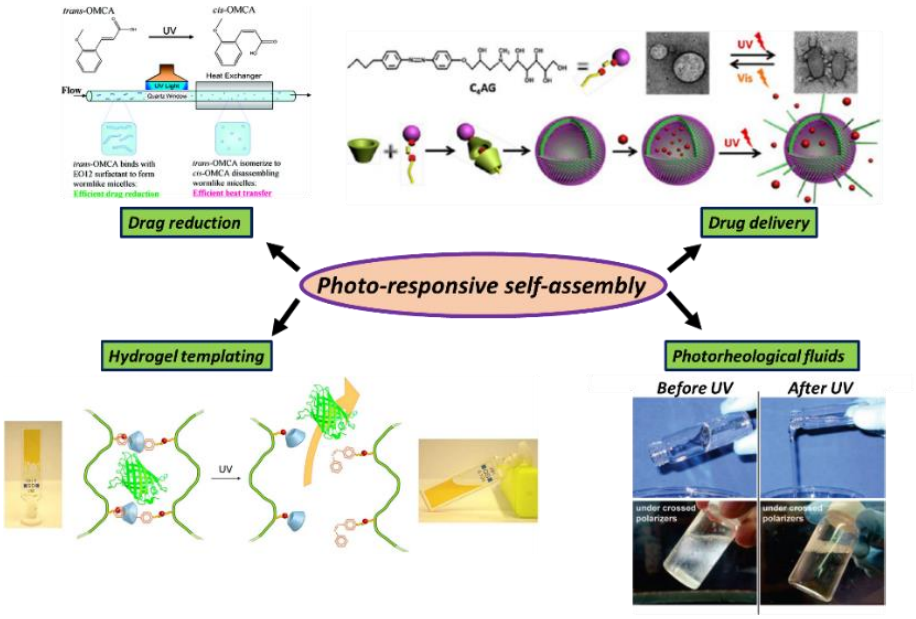

Fig. 1.17 Applications of photo-response self-assembly [83-86]

1.5 Bubble rise in wormlike micelles

Gas-liquid two-phase flow is widely present in chemical processes and when the gas phase dispersed in the continuous phase is in the form of bubbles it is an ideal contact method for heat and mass transfer. In typical gas-liquid contact equipment such as bubble columns, fluidized beds, and biochemical reactors, coalescence and collision of bubbles have an important impact

on the internal fluid mechanics, heat transfer, mass transfer, and reaction of the equipment [87]. A comprehensive understanding of bubble rising helps to optimize equipment structure and improve process efficiency

1.5.1 Bubbly liquid

As shown in Fig. 1.18, gas-liquid mixtures can be divided into different regions depending on the volume fraction of gas (φ_{gas}) single bubble ($\varphi_{gas} \approx 0$), bubbly liquid ($\varphi_{gas} < 64\%$), wet foam ($64\% < \varphi_{gas} < 85\%$) and dry foam ($\varphi_{gas} > 95\%$). When the gas fraction is below 64%, the bubbles can remain spherical, and such suspensions are called bubbly liquids. Bubbly liquids are unstable dispersions, as the bubbles rise rapidly because of gravity and turn it into a wet foam.

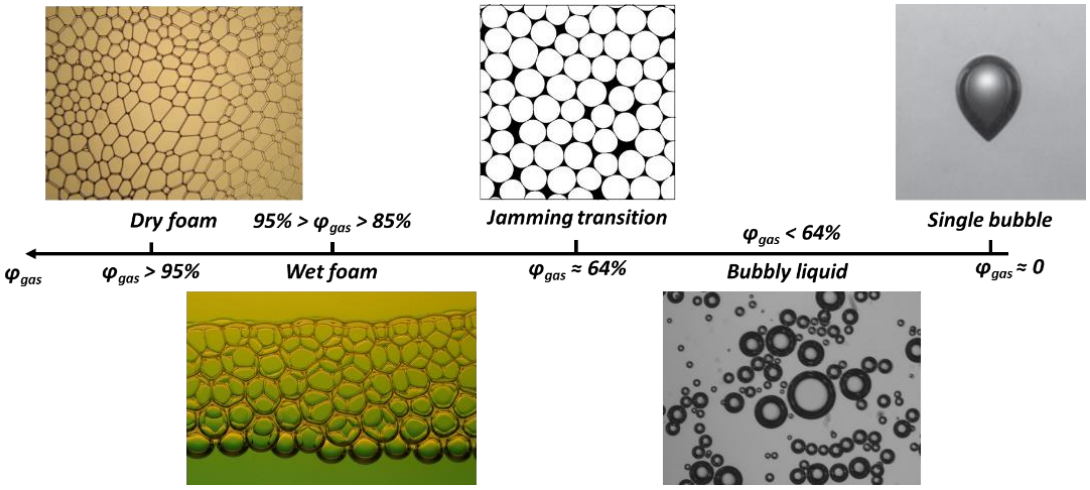

Fig. 1.18 Classification of bubbles in liquid

1.5.2 Single bubble rise velocity in Newtonian fluid

In order to understand bubble rise in concentrated bubble suspensions, we start by thinking about a single bubble first in a Newtonian fluid and then in non-Newtonian fluids, such as the wormlike micelle solutions of interest.

When a bubble is in a static fluid, the forces acting on it are shown in Figure 1.19. Under the assumption that the bubbles do not have any internal circulation and there is no slip at the boundary, we can define the final bubble rise velocity in Newtonian fluid from the Stokes' law:

$$v_s = \frac{\rho_c g d_e^2}{18\eta_c} \tag{1-5}$$

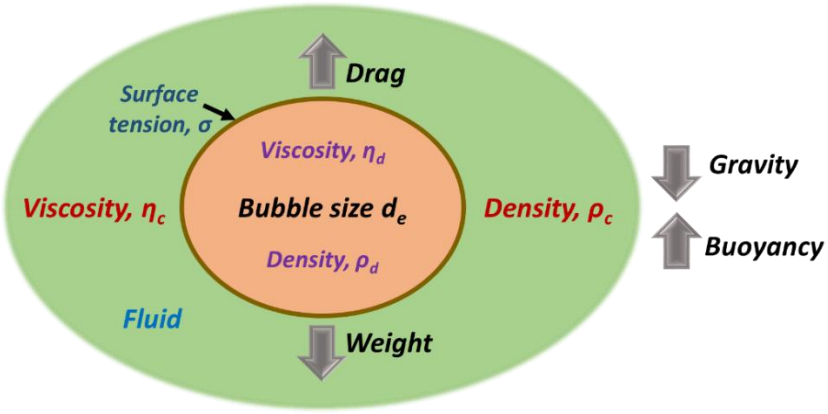

Fig. 1.19 A bubble of size d_e rising under the gravity and buoyancy in a static fluid of density ρ and viscosity μ.

Since the gas phase and the liquid phase are immiscible, the surface tension σ must be considered. For the bubble, η_d and ρ_d are practically zero. it is generally believed that when ignoring the wall effect, the shape of freely rising bubbles in the fluid mainly depends on the following dimensionless parameters:

$$Re = \frac{\rho_c v_s d_e^2}{\eta_c} \tag{1-6}$$

$$Eo = \frac{\rho_c g d_e^2}{\sigma} \tag{1-7}$$

$$Mo = \frac{g\eta_c^4}{\rho_c \sigma^3} \tag{1-8}$$

where, *Re* is the Reynolds number; *Mo* is the Morton number; *Eo* is the Eötvös number; ρ is the density; η is the viscosity; d_e is the bubble equivalent diameter; g is the acceleration of gravity; σ is the surface tension; the subscripts *c* and *d* represent the continuous phase and the dispersed phase, respectively; d_v and d_h are the diameter of the bubble in the vertical and horizontal directions.

Grace and Weber [88-91] summarized a large number of experimental data on bubble shape and velocity, and drew the bubble shape diagram in Newtonian fluids based on dimensionless parameters. Generally, the shapes of freely rising bubbles are divided into three categories: spherical, ellipsoidal, and spherical cap or ellipsoidal cap. When the aspect ratio of the bubble is within the range of 0.9-1.1 or the system is at low *Re*, *Eo* and *Mo* numbers, interfacial tension and viscous force dominate the bubble shape instead of inertial force, and the bubble shape basically maintains a spherical shape with little change (Fig. 1.20 (a)) [92]. The ellipsoidal bubbles appear in the range of high *Re* number and medium *Mo* number, with small aspect ratio and convex surface (Fig. 1.20 (b)). In the actual rising process, the viscosity of the liquid phase may cause the bubble to stretch in the horizontal direction, and the bubble shape may be an asymmetric ellipsoid. At the same time, the ellipsoidal bubble is usually accompanied by

oscillation or swing when it rises, which also causes the bubble shape to change continuously. When the *Re* and *Mo* are high, the bottom of the larger bubble is usually flat or jagged, which looks like a part cut from the upper part of the sphere. This shape is called a spherical cap shape or an ellipsoidal cap shape (Fig. 1.20 (c)). In addition to the three typical bubble shapes, other shapes such as bubbles with depressions at the bottom, skirt-like bubbles, and wobbling bubbles are also reported. These shapes can be seen as deformations of the three basic shapes mentioned above [92-93].

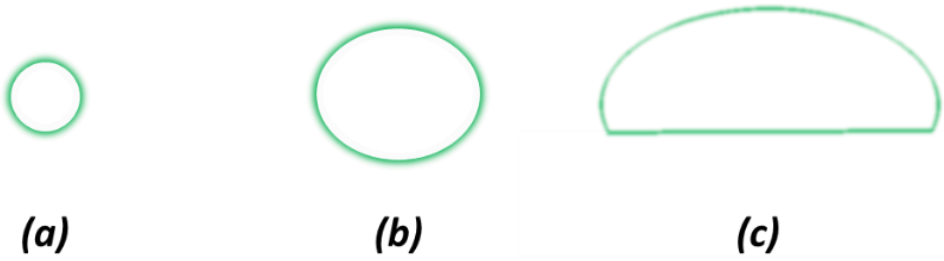

Fig. 1.20 Three representative shapes of the single bubble in Newtonian fluid (a) spherical, (b) ellipsoidal, (c) spherical cap

If the bubble is deformed, any shape change will affect its rise velocity. For correcting this, the drag coefficient C_D is used as a dimensionless parameter that characterizes the resistance of the fluid. Hadamard [94] was the first to theoretically derive the drag coefficient under low Reynolds number. For creeping flow in Newtonian liquids with the low Reynolds number, Hadamard ignored the inertial force and obtained the expression of drag coefficient with respect to Reynolds number:

$$C_D = \frac{24}{Re}\left(\frac{2+3(\eta_d/\eta_c)}{3+3(\eta_d/\eta_c)}\right) \tag{1-9}$$

For the gas-fluid system, because of the η_d is much smaller than η_c, C_D is close to $16/Re$, whereas for the case of solid-liquid system, $C_D \approx 24/Re$. And the bubble rise velocity after correction can be given by:

$$v_{HR} = \frac{\rho_c g d_e^2}{18\eta_c}\frac{3\eta_d+3\eta_c}{3\eta_d+2\eta_c} \tag{1-10}$$

which is called Hadamard-Rybczynski equation [95]. It can be seen from this equation that for a single bubble ($\eta_d \approx 0$), the v_{HR} will be close to 3/2 of the predicted value by the Stokes law velocity. Although formula (1-10) has strict theoretical significance, it is only applicable to the creeping flow state when the Reynolds number is very small ($Re \leq 1$). In the actual process, the Reynolds number is usually larger than 1, even hundreds or thousands, which is often accompanied by the deformation of the bubble. This causes the formula (1-10) to deviate greatly from the actual situation. For this reason, many researchers have made many amendments to the drag coefficient. Here, no more detailed will be discussed.

1.5.3 Single bubble rise velocity in non-Newtonian fluid

In non-Newtonian fluids, due to the complexity of rheological properties, bubbles show more diverse shapes [95-97]. As shown in Fig. 1.21, the shape of the bubble generally evolves with increasing bubble volume with the increasing volume from a spherical shape to an elongated teardrop shape, a flat teardrop shape and a pointed ellipsoid at the bottom, and finally becomes a spherical cap shape. The shape of the bubble generally evolves from a spherical shape to ellipsoidal shape and finally to spherical cap shape in shear-thinning inelastic fluid. And the unique shape of the bubble shape in the non-Newtonian fluid is the pointed tail, which usually exists in the non-Newtonian fluid with strong viscoelasticity [98-102]. Compared with Newtonian fluids, large-volume bubbles in non-Newtonian fluids are easier to maintain a spherical shape. However, due to the complexity of the rheological properties of different non-Newtonian fluids, it is currently difficult to accurately predict the shape of bubbles in non-Newtonian fluids.

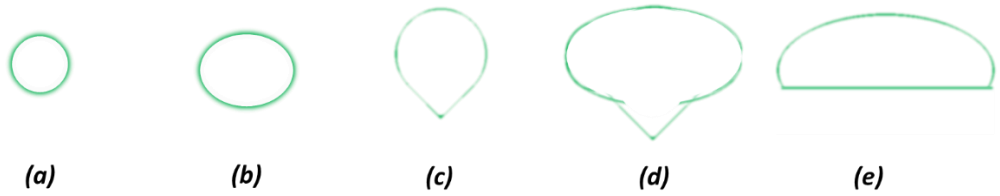

Fig. 1.21 Representative shapes of the single bubble in Newtonian fluid (a) spherical, (b) ellipsoidal, (c) teardrop shape, (d) flat teardrop shape with a pointed ellipsoid, (e) spherical cap.

When a bubble in a viscoelastic fluid rises, due to the shearing effect of the bubble and the shear thinning effect of the fluid, the viscosity around the bubble decreases, causing the bubble to rise faster than in Newtonian fluid under the same conditions. As we know, according to the Stokes' law, the bubble rise velocity increases with the bubble size continuously in a Newtonian fluid. However, there is a peculiar phenomenon when a bubble rises in a non-Newtonian fluid, that is, as the size of the bubble increases, the rising velocity of the bubble is discontinuous, and the velocity jumps at a certain critical size. The bubble diameter range of velocity jump is usually 3-6 mm, and the maximum velocity jump value can reach 6-10 times of the free ascent velocity [103]. There are many factors that may cause the bubble rise velocity jump, including bubble shape change, the reduction of the viscosity and the change of boundary condition. There is no unified theoretical explanation so far.

In the past few decades, researchers have conducted a lot of research on the free rise of bubbles in non-Newtonian fluids. For a single bubble in non-Newtonian fluid, Dewsbury [104] proposed the bubble drag coefficient. In a weakly shear thinning fluid, the correlation formula for the drag coefficient of a single (deformable) bubble is:

$$C_D = \frac{16}{Re}\left(1+0.173Re^{0.66}\right)+\frac{0.413}{1+16300Re^{-1.09}} \quad (1\text{-}11)$$

1.5.4 Bubble rise in Newtonian fluid

In industrial problems the bubbles are often encountered as multiple bubbles or bubble groups. The descriptions obtained from the study of single bubbles cannot be directly extrapolated to the case of bubble liquids as the interactions between the rising bubbles are far from trivial.

In a very dilute bubbly liquid (gas fraction less than 10^{-4}), bubbles can be evenly distributed in a static Newtonian fluid. At these concentrations the distance between the bubbles is very large. The separation of bubbles is larger enough to ignore the liquid velocity field induced by each bubble which decays as $(d_e/2)^{-1}$ and they can be assumed to not interact with each other at all. At this time, Stokes' Law can be used to describe the motion of bubbles.

However, for more concentrated bubbly liquids, if the separation of bubbles is not so large, the flow caused by one bubble will affect the motion of other bubbles, and vice versa, resulting in effective hydrodynamic interaction between the bubbles. Within a fixed volume, the liquid moves downwards on average to compensate for the rise of the bubbles. This fluid backflow hinders the rising of the bubbles and causes the average rise velocity to be less than that of an isolated bubble. As the gas fraction increases, the hindering effect becomes more obvious. In order to include this hindering effect, Richardson and Zaki (1954) proposed an empirical correlation [105]:

$$v_{RZ} = v_s\left(1-\varphi_{gas}\right)^n \quad (1\text{-}12)$$

where φ_{gas} is the gas fraction of the bubbly liquid and n is an experimentally determined constant varying with the Reynolds number. For low Re it is usually between 4.65 and 6.55 [106]. The *Richardson-Zaki law* has been proved to be a good agreement with experimental data of various gas fractions [107]. However, when the gas approach to the jamming transition 0.60, the bubbles will interact with each other and the rise velocity starts to deviate from this correlation [108].

1.5.5 Bubbles rise in non-Newtonian fluid

The current research on the rise of multiple bubbles is mainly focused on the interaction between bubbles in certain non-Newtonian fluids, such as Boger fluids and shear-thinning inelastic fluids.

For shear-thinning inelastic fluids (Fig. 1.22 (b)), the bubbles tend to form vertical doublets and large aggregations. Clustering is assumed to be triggered by the shear-thinning wake behind each bubble: the bubbles rising in the low-viscosity wake are unlikely to disperse from the side

to the high-viscosity area [109]. Once formed, this vertical doublet and triplet rises faster than a single bubble and traps more bubbles. As the cluster grows, its rising speed and inertia also increase. Eventually, the cluster became a large aggregate of bubbles, showing an elliptical shape and almost horizontal orientation. However, excessive inertia combined with the ability of small bubbles to deform (that is, under conditions of large *Re* and low *Eo*) tends to hinder bubble aggregation and promote dispersion.)

Boger fluids are a kind of viscoelastic fluid with constant (or nearly constant) viscosity [110]. Vélez investigated the the properties of bubbly flows in Boger fluids [111]. In their research, they did not change the gas volume fraction of a given bubble size, but experimented with two different bubble sizes at a fixed volume fraction. Interestingly, they found that small bubbles tend to aggregate and form vertical bubble chains as shown in Fig. 1.22 (c), while larger bubbles rise in a dispersed manner as shown in Fig. 1.22 (d). This change in behavior is consistent with bubble velocity discontinuity: in the specific fluid used in this study, these two dimensions cross the critical value of bubble velocity discontinuity.

Research on bubble rise in non-Newtonian fluids is mainly focused on low gas fractions below 1%. For higher gas fraction, the interaction between bubbles is more complex. The viscosity of viscoelastic shear-thinning fluids will decrease with the velocity of bubble rise; however, the detailed mechanisms are still unknown.

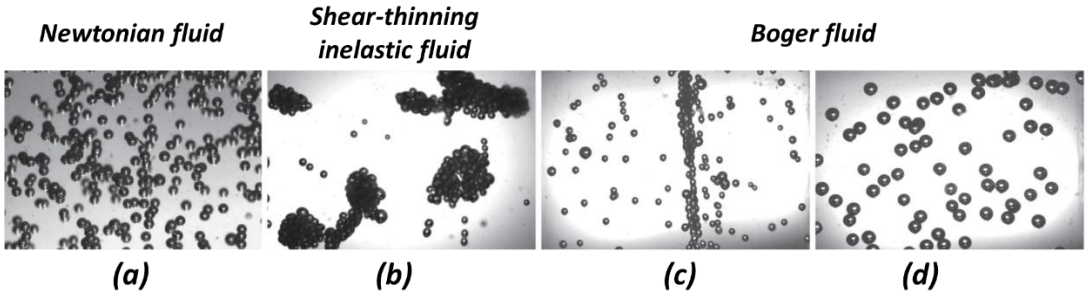

Fig. 1.22 Bubbles rise in Newtonian fluid (a), shear-thinning inelastic fluid (b) and Boger fluid (c), (d) [112]

1.6 Molecular dynamics simulation

Experimental methods, computer simulations and theoretical calculations have become three most important methods in modern chemical and physical research. In recent years, with the crossover and communication between research fields and the development of computer performance, computer simulation and theoretical calculation have been increasingly applied to various branches of the chemical and physical field. MD simulation is the most widely used method for computing materials, biological and other complex systems. MD simulation samples and detects the phase space composed of the coordinates and velocities of all particles in the system by integrating the Newtonian equation of motion, and calculates the position and

velocity of next time step based on the current position and velocity of the particle. Various properties of the system can be inferred by the statistical analysis results of the movement of each particle, such as the conformation and dynamic properties of the molecule, the thermodynamic properties of the system, and various equilibrium/non-equilibrium properties, etc. The advantage of MD simulation is that the trajectory of particles in the system has a precise physical basis. The dynamic change information and thermodynamic statistical information of the system can also be obtained at the same time. Therefore, it is widely used in the research of various microscopic systems.

1.6.1 Basic principles of molecular dynamics simulation

According to the Born-Oppenheimer approximation, MD simulation uses classical mechanics to describe the movement of atoms over time. The various properties of the system can be calculated through the following basic processes:

1. Input the initial configuration of the system, the potential energy function $V(\mathbf{r}_i)$ as a function of atom position, the position $\mathbf{r}_i$ and initial velocity $\mathbf{v}_{0i}$ of all atoms in the system. The initial velocity distribution satisfies the Maxwell-Boltzmann velocity distribution at the set temperature.

2. Calculate the force of each atom.

3. Update the configuration and simulate the motion of atoms by numerically solving Newton's equation of motion.

4. Repeat steps 2 and 3 according to the number of steps to be calculated to obtain the trajectory of the system evolution.

In the above process, the trajectory of a system containing N interacting atoms with time t is obtained by solving the Newtonian equation of motion of N atoms as

$$m_i \frac{\partial^2 \mathbf{r}_i}{\partial t^2} = \mathbf{F}_i, i = 1,...N \tag{1-13}$$

where m_i is the mass of the atom i, and the force $\mathbf{F}i$ experienced by the atom is the negative value of the derivative of the potential energy function $V(\mathbf{r}_i)$:

$$\mathbf{F}_i = -\frac{\partial}{\partial \mathbf{r}_i} V(\mathbf{r}_i) \tag{1-14}$$

Commonly used integration methods for solving Newtonian equations of motion in MD simulation include Verlet algorithm [113], Velocity-Verlet algorithm [114] and Leap-frog algorithm [115]. Among them, the Leap-frog algorithm is simple, efficient and stable. Therefore, the Leap-frog algorithm has become the most mainstream integration method at present. The

Leap-frog algorithm uses the position **r** at time *t* and the speed **v** at time $t-\frac{1}{2}\Delta t$ to calculate the force **F**(*t*), and update the speed and position using the following method:

$$\mathbf{v}(t+\frac{1}{2}\Delta t)=\mathbf{v}(t-\frac{1}{2}\Delta t)+\frac{\Delta t}{m}\mathbf{F}(t) \tag{1-15}$$

$$\mathbf{r}(t+\Delta t)=\mathbf{r}(t)+\Delta t\mathbf{v}(t+\frac{1}{2}\Delta t) \tag{1-16}$$

The speed at time t can be calculated by the following formula,

$$\mathbf{v}(t)=\frac{1}{2}[\mathbf{v}(t-\frac{1}{2}\Delta t)+\mathbf{v}(t+\frac{1}{2}\Delta t)] \tag{1-17}$$

The information of each frame in the trajectory of the system can be obtained by completing the integral solution of the above equation. According to the ergodicity assumption in statistical mechanics, the average value of various physical quantities *Q* of the system can be obtained by statistics:

$$Q=\lim_{M\to\infty}\frac{1}{M}\sum_{t_m}Q(r_i,v_i)_{t_m},(m=1,2,...,M) \tag{1-18}$$

1.6.2 Molecular forcefields

MD simulation uses a molecular forcefield to describe the potential energy function $V(\mathbf{r}_i)$ between atoms, and can further calculate the forces experienced by the atoms at various moments. The forcefield information is composed of the equations and the parameters of the equations that can generate the potential energy and its derivatives. It mainly describes the non-bonding interaction composed of electrostatic interaction and van der Waals interaction and the bonding interaction composed of information such as bond length and bond angle:

$$\begin{aligned} U &= U_{\text{elec}} + U_{\text{vdw}} && \text{(non-bonding interaction)} \\ &+U_{\text{bond}} + U_{\text{angle}} + U_{\text{outp}} + U_{\text{torsion}} && \text{(bonding interaction)} \end{aligned} \tag{1-19}$$

The electrostatic interaction U_{elec} in non-bonding interaction is expressed as:

$$U_{\text{elec}}(r_{ij})=f\frac{q_iq_j}{\varepsilon_r r_{ij}} \tag{1-20}$$

Among them, $f=\frac{1}{4\pi\varepsilon_0}$, ε is the dielectric constant. q_i and q_j are the charges of atom *i* and atom *j*, and r_{ij} is the distance between atom *i* and atom *j*.

Van der Waals interaction U_{vdw} is usually described by Lennard-Jones (LJ) 12-6 potential energy function, as shown in Equation 1-21:

$$U_{\text{vdw}}(r_{ij})=4\varepsilon_{ij}\left[\left(\frac{\sigma_{ij}}{r_{ij}}\right)^{12}-\left(\frac{\sigma_{ij}}{r_{ij}}\right)^{6}\right] \tag{1-21}$$

ε_{ij} and σ_{ij} are usually calculated using the Lorentz-Berthelot hybrid rule:

$$\begin{cases} \varepsilon_{ij} = \sqrt{\varepsilon_i \varepsilon_j} \\ \sigma_{ij} = \dfrac{\sigma_i + \sigma_j}{2} \end{cases} \tag{1-22}$$

ε_i and σ_i are the depth and diameter of the potential well of atom *i*, respectively.

The bonding effect of most forcefields is composed of the bond expansion term U_{bond}, the bond angle bending term U_{angle}, the off-plane potential energy U_{outp}, and the dihedral torsion term $U_{torsion}$. The form most commonly used to describe U_{bond}, U_{angle}, and U_{outp}, is the resonance potential,

$$U_{\text{bond}}(r_{ij}) = \frac{1}{2} k_{ij}^{b} (r_{ij} - b_{ij})^2 \tag{1-23}$$

U_{bond} describes the potential energy curve of bond length stretching vibration, where b_{ij} is the balance bond length between atoms *i* and *j*, and k_{ij}^{b} is the resonance potential energy parameter.

$$U_{\text{angle}}(\theta_{ijk}) = \frac{1}{2} k_{ijk}^{a} (\theta_{ijk} - \theta_0)^2 \tag{1-24}$$

U_{angle} describes the potential energy curve of the flexural vibration of the bond angle, where θ_{ijk} is the bond angle between atoms *i*, *j*, and *k*, θ_0 is the equilibrium angle of the bond angle, and k_{ijk}^{b} is the resonance potential energy parameter.

$$U_{\text{outp}}(\chi) = k_{\chi} (\chi - \chi_0)^2 \tag{1-25}$$

U_{outp} is used to describe the potential energy curve of the atom deviating from the plane formed by the other three adjacent atoms, where χ is the angle away from the plane, χ_0 is the equilibrium angle, and k_{χ} is the resonance potential energy parameter.

The dihedral angle formed by three adjacent bonds in the same molecule relates to the spatial configuration of the molecule. The torsional potential energy curve of the dihedral angle is periodic, which is usually described by multiple sets of cosine functions:

$$U_{\text{torsion}}(\varphi) = \sum_{i=1}^{N} \frac{V_i}{2} [1 + \cos(n_i \varphi - \varphi_{0,i})] \tag{1-26}$$

Where φ is the dihedral angle; *n* corresponds to the nth minimum point of the potential energy curve in the angle range of 0~360°, $\varphi_{0,i}$ is used to adjust the phase, and V_i is the barrier height corresponding to each extreme value. For more complex dihedral torsion potential energy curves, multiple items are often needed to fit properly.

According to the degree of fineness when modeling molecules, molecular forcefields are usually divided into all-atom forcefield (AA), united atom forcefield (UA), and coarse-gained

forcefield (CG). The all-atom forcefield clearly defines each atom as a particle, which has high accuracy and relatively expensive calculation cost. It is usually used for nano-scale simulations. After years of development, there are many kinds of all-atom forcefields available, and the parameterization methods of different forcefields are slightly different, and the applicable molecular types are also different. The most commonly used all-atom forcefields to describe small organic molecules and protein molecules are AMBER forcefield [116-118], CHARMM forcefield [119-121], OPLS-AA forcefield [122-124], etc. The united atom forcefield considers part of the hydrocarbyl group as a single particle located at the center of mass of the group, and the mass and charge of the joint atom are the sum of all atoms in the group. The united atom forcefield reduces the amount of calculation to a certain extent, but the description of the molecular structure is not complete. The more commonly used united atom forcefield includes the OPLS-UA forcefield [125] and the GROMOS forcefield [126-127].

The coarse-grained forcefield treats 3-4 heavy atoms and their connected hydrogen atoms as a bead, and describes the MD simulation process by calculating the interaction between the beads. It further reduces the degree of freedom of the system, greatly reduces the computational cost, and can simulate large-scale proteins, DNA molecules and biofilm systems on a mesoscopic scale. The coarse-grained forcefield retains the most basic molecular information. The most commonly used coarse-grained forcefields at this stage are the Martini forcefield [128-129] and the PLUM forcefield [130].

1.6.3 Temperature coupling

Temperature is one of the most critical properties in the simulation process. The temperature of the system needs to be adjusted in different statistical ensembles such as NVT and NPT. The temperature T in the MD simulation is defined by the particle velocity v_i:

$$\left\langle \frac{1}{2} m_i v_i^2 \right\rangle = \frac{1}{2} k_{\mathrm{B}} T \tag{1-27}$$

In the formula, k_B is Boltzmann's constant and $\langle\ \rangle$ means the average of ensemble.

The temperature coupling ensures that the temperature of the simulation system is maintained near the expected value by continuously correcting the velocity of the particles. Commonly used temperature coupling methods include Berendsen coupling algorithm [131], Nose-Hoover coupling algorithm [132-133] and Velocity-rescaling coupling algorithm [134].

The Berendsen algorithm realizes the connection to an external thermal bath with a given reference temperature T_0, and has a weak coupling with first-order kinetic characteristics. The deviation of the system temperature to T_0 is slowly corrected by the following formula:

$$\frac{\mathrm{d}T}{\mathrm{d}t} = \frac{T_0 - T}{\tau_T} \tag{1-28}$$

τ_T is the time constant. The smaller the value, the more accurate the temperature control. However, the Berendsen coupling will cause the particle velocity in the system to deviate from the Maxwell-Boltzmann velocity distribution, failing to produce a correct canonical ensemble.

The Nose-Hoover coupling algorithm directly adds a thermal bath to the equation of motion, and assigns virtual parameters to it to obtain a new equation of motion as the system evolves:

$$\frac{\mathrm{d}^2\mathbf{r}_i}{\mathrm{d}t^2} = \frac{\mathbf{F}_i}{m_i} - \frac{p_\xi}{Q}\frac{\mathrm{d}\mathbf{r}_i}{\mathrm{d}t} \tag{1-29}$$

$$Q = \frac{\tau_T^2 T_{ref}}{4\pi^2} \tag{1-30}$$

Q is the virtual mass of the hot bath and p_ξ is the momentum of the hot bath, which is calculated by the following equation of motion:

$$\frac{\mathrm{d}p_\xi}{\mathrm{d}t} = (T_0 - T) \tag{1-31}$$

The Nose-Hoover thermal bath produces particle velocities that satisfy the Maxwell-Boltzmann distribution, but exhibits oscillating characteristics during the relaxation process to the reference temperature, which is usually used in the pre-equilibration process.

The Velocity-rescaling coupling algorithm adds a random term to the Berendsen coupling algorithm to ensure that the correct velocity distribution of the particles in the system can be given. The kinetic energy is corrected according to the following formula:

$$\mathrm{d}K = (K_0 - K)\frac{\mathrm{d}t}{\tau_T} + 2\sqrt{\frac{KK_0}{N_f}}\frac{\mathrm{d}W}{\sqrt{\tau_T}} \tag{1-32}$$

In the formula, K is the kinetic energy of the system. N_f is the degree of freedom, and dW represents the Brownian motion process. The velocity-rescaling algorithm has first-order dynamics characteristics with no relaxation oscillations. Velocity-rescaling algorithm is currently a better temperature coupling algorithm.

1.6.4 Pressure coupling

Except temperature, many simulation processes also need to control the pressure of the system. In MD, the pressure of the system is closely related to the coordinates of the particles. The pressure coupling algorithm can be used to scale the coordinates of the particles to make the average pressure of the system constant at the desired value. Currently commonly used

pressure coupling algorithms are Berendsen pressure coupling algorithm [131] and Parrinello-Rahman pressure coupling algorithm [135].

Similar to the Berendsen temperature coupling algorithm, the Berendsen pressure coupling algorithm also conforms to the first-order dynamics characteristics. The coupling parameter τ_p controls the speed of the system pressure changing to the reference pressure $\mathbf{P}_0$:

$$\frac{\mathrm{d}\mathbf{P}}{\mathrm{d}t} = \frac{\mathbf{P}_0 - \mathbf{P}}{\tau_p} \tag{1-33}$$

Similarly, the Berendsen pressure coupling algorithm is a weak coupling algorithm, and it is impossible to define an accurate ensemble.

The Parrinello-Rahman pressure coupling algorithm uses an algorithm similar to the Nose-Hoover temperature coupling, which realizes the true NPT ensemble by changing the motion equation of the particles, and finally causes the motion equation to be updated to:

$$\frac{\mathrm{d}\mathbf{r}_i^2}{\mathrm{d}t^2} = \frac{\mathbf{F}_i}{m_i} - \mathbf{M}\frac{\mathrm{d}\mathbf{r}_i}{\mathrm{d}t} \tag{1-34}$$

M is the virtual mass matrix of the pressure bath, which is adjusted by setting the compressibility and coupling parameter τ_p. The Parrinello-Rahman pressure coupling algorithm is usually used in conjunction with the Nose-Hoover temperature coupling algorithm or the Velocity-rescaling temperature coupling algorithm to jointly control the pressure and temperature of the system during the simulation of the finished product.

1.7 Quantum chemistry calculations

1.7.1 Overview of quantum chemistry calculations

As a branch of theoretical chemistry and an interdisciplinary subject of chemistry and physics, quantum chemistry is a basic science that applies the basic principles and methods of quantum mechanics to study chemical problems. The structure and chemical properties of a molecule are closely related to the atomic composition of the molecule and its electronic arrangement or state of motion. Quantum chemistry starts from the basic laws of electronic motion to describe the relative spatial positions of all electrons and atoms in the system, so as to achieve to study the reactivity and structure of the system. Quantum chemistry calculations are very powerful and can be applied in many different systems, such as studying the structure and performance of stable and unstable molecules, the relationship between structure and performance, the interactions between molecules; the mutual collision and mutual reaction between molecules, which provides important theoretical tools for current chemical research.

The calculation methods of quantum chemistry mainly include: ab initio calculation method, semi-empirical method and density functional theory (DFT).

The ab initio calculation method is based on the Schrodinger equation. In the process of solving Schrodinger's equation, only a few basic physical constants are used, including the speed of light, Planck's constant, and the mass of electrons and nucleus. In the process of solving Schrödinger's equation, a series of mathematical approximations are used. Different approximations lead to different methods. The most classic mehod is the Hartree-Fock (HF) equation. The electronic structure and properties of the system can be obtained using self-consistent field method to solve this equation. The HF method can obtain good results for the stable molecules and some transition metals. It is a good basic theoretical method and the basis of other ab initio calculation methods. However, the HF method does not consider electron in theory, so it is insufficient in the application of some special systems.

The ab initio calculation method has a huge amount of calculation. The main difficulty is the calculation of the repulsive integrals between electrons in the HF equation. The number of these repulsive integrals is large and the calculation is cumbersome. Therefore, there are some schemes for simplifying the calculation of repulsive integrals, which are called approximate calculation methods. The approximate HF equation generally yields poor results. Taking some empirical parameters instead of some integrals in the approximate HF equation, while ignoring some integrals, satisfactory results can be obtained. This method is called the semi-empirical approximate calculation method. Common semi-empirical methods include AM1, MINDO/3, PM3, etc.

1.7.2 Density functional theory

In the Thomas-Fermi model developed independently by Thomas and Fermi in 1927, they used electron density instead of wave function to describe the multi-electron system. Although this model was not very successful in describing the entire molecule, this idea laid the foundation for the later well-known density functional theory (DFT).

The classical methods of electronic structure theory, especially the Hatree-Fock method and the self-consistent field method, are based on complex multi-electron wave functions. Density functional theory further considers exchange-correlation energy on the basis of Hatree-Fock approximation, which can describe the multi-electron system more accurately. Unlike the Hartree-Fock method, density functional theory uses electron density instead of wave function as the basic quantity for research, which makes the calculation easier, because the n electron wave function is a function of 3n variables, and the electron density is only a function of 3 variables. Therefore, density functional theory guarantees the accuracy of calculation when dealing with polyatomic systems or even macromolecular systems, and saves computational

costs more than the self-consistent field method. It is currently one of the most commonly used methods in computational chemistry.

Although the concept of density functional theory originated from the Thomas-Fermi model in 1927, it did not have a theoretical basis until the Hohenberg-Kohn theorem was proposed in 1964 [136]. Hobenberg-Kohn first theorem states that for a given nucleus coordinate, the energy and properties of the ground state of the system are only determined by the electron density. Hobenberg-Kohn second theorem shows that the ground state energy is obtained after the system energy is minimized with the ground state density as a variable. Designing an accurate functional is the key to the DFT method.

The total energy in the DFT method can be expressed as a function of ρ:

$$E(\rho) = E^{T}(\rho) + E^{V}(\rho) + E^{J}(\rho) + E^{XC}(\rho) \quad (1\text{-}35)$$

Among them, E^{T} is electron kinetic energy; E^{V} is the attraction potential energy of electron and atomic nucleus; E^{J} is the Coulomb repulsion energy between electrons; E^{XC} is the exchange-correlation energy. Among them, E^{V} and E^{J} are direct because they represent the classical Coulomb action, while E^{J} and E^{XC} are not direct. Finding high-precision exchange-correlation approximations is the main problem of density functional theory.

In 1965, Kohn and Sham [137] proposed the Kohn-Sham equation, which made it possible to accurately calculate the electron density of the system and the total energy of the system, thus opening the way for density functional theory to be used in practical calculations. In the framework of Kohn-Sham DFT, the most difficult many-body problem (due to the interaction of electrons in an external electrostatic potential) is simplified to the problem of the sports of an electron with no interaction in the effective potential field. This effective potential field includes the effects of external potential fields and coulomb interactions between electrons, such as exchange and correlation effects. Dealing with exchange and correlation effects is the difficulty in Kohn-Sham DFT. At present, there is no accurate method to solve the exchange-correlation energy E^{XC}. The simplest approximate solution method is Local Density Approximation (LDA). LDA approximately uses homogeneous electron gas to calculate the exchange energy of the system (the exchange energy of homogeneous electron gas can be accurately solved), and the correlation energy part uses the free electron gas fitting method to process.

Since the definition of the exchange-correlation energy functional includes a part of the contribution of kinetic energy, many researchers consider that the kinetic energy density should be included as a variable in the exchange-correlation functionals [138]. This is the meta-GGA functional. In order to improve the accuracy of the calculation results of various approximate functionals, in1988, Becke [139] proposed the idea of adding part of the exchange energy

calculated according to the Hartree-Fock method to the energy density functional, thereby constructing a series of hybrids exchange-correlation functionals. The mixed exchange-correlation energy expression form has achieved great success in the calculation of density functional theory. The commonly used exchange-correlation energy functional is to mix the Hartee-Fock exchange energy with the approximate exchange-correlation energy density functional in a fixed proportion. For example, "half to half" functional, its expression can be written as:

$$E_{XC}^{HH} = \frac{1}{2}E_{XC}^{HH} + \frac{1}{2}E_{XC}^{HH} \tag{1-36}$$

Because the theoretical basis of this type of hybrid density functional method is the adiabatic correlation formula, it is called the adiabatic correlation method. The methods including B3P, B3LYP, B1B95, PBEO, B97, B98, etc. Among them, the famous B3LYP functional which is the hybrid density functional composed of the Becke three-parameter hybrid exchange functional and Lee-Yang-Parr related functionals can be expressed as:

$$E_{\mathrm{XC}}^{\mathrm{B3LYP}} = aE_{\mathrm{X}}^{\mathrm{LDA}} + (1\text{-}a)E_{\mathrm{X}}^{\mathrm{HF}} + bE_{\mathrm{X}}^{\mathrm{Becke}} + cE_{\mathrm{C}}^{\mathrm{LYP}} + (1\text{-}c)E_{\mathrm{C}}^{\mathrm{VWN}} \tag{1-37}$$

In the formula, *a*, *b*, and *c* are parameters.

Due to the relatively small amount of calculation of density functional theory, it can be applied to larger molecular structures [140]. To a certain extent, the electronic correlation effect is considered, and satisfactory results can be obtained in predicting molecular structure and energy. Therefore, it is currently the most popular quantitative calculation method.

1.8 Proposal for the thesis

The photo-responsive wormlike micelle constructed by Gemini surfactants and cinnamic acid photo-responsive molecules has excellent photorheological properties and potential value in petrochemical, skin care, photosensitive devices, drug release and other fields. However, due to the limited experimental conditions and material resources, the photo-responsive mechanism and the influence of the molecular structure of cinnamate derivatives on its photo-sensitive ability have not been fully investigated. Wormlike micelles exhibit complex viscoelasticity. The rising behavior of bubbles has great industrial application value, and the current research on the rising behavior of bubbles in viscoelastic fluids is also very scarce. Based on this:

(1) We chose Gemini surfactant N, N'-bis(dodecyldimethyl)-1,2-ethane diammonium dibromide (12-2-12·2Br$^-$) and photo-sensitive small molecule *trans*-o-methoxycinnamic acid (*trans*-OMCA) to construct a photo-responsive self-assembly system. The photo-responsive behavior of the system and the microscopic mechanism of self-assembly morphology

transformation were studied through the combination of rheology, MD and quantitative calculation.

(2) Based on our understanding of the transformation mechanism of photo-responsive wormlike micelle, we selected three ortho-substituent cinnamates, *trans*-o-methoxy cinnamate (*trans*-OMCA), *trans*-o-hydroxy cinnamate (*trans*-OHCA), and *trans*-cinnamate (*trans*-CA), to construct photo-responsive wormlike micelle systems with Gemini surfactant trimethylene-1,3-bis (dodecyldimethylammonium bromide) (12-2-12·2Br^-). We investigated the photo-responsive behavior and photoisomerization reaction kinetics of wormlike micelle, combined with MD simulation and quantitative calculations to study the effects of different ortho-substituents in cinnamates on the photo-isomerization reaction rate and the photo-responsive behavior of wormlike micelles.

(3) Based on the previous two parts of the research, we further studied the photo-responsive wormlike micelle system composed of Gemini surfactant 12-3-12·2Br^- abd cinnamates with ortho-, meta- and para-methoxy (*trans*-o-methoxy cinnamate (*trans*-OMCA), *trans*-m-methoxy cinnamate (*trans*-MMCA) and *trans*-p-methoxy cinnamate (*trans*-PMCA)). MD simulation and quantitative calculation were used to study the influence of different substituent positions on photo-responsive behavior of wormlike micelle. In addition, we also calculated the structural properties of dozens of cinnamates, which provided theoretical guidance for experimentally constructing a wormlike micelle system with stronger photo-responsiveness.

(4) We chose a classic viscoelastic shear-thinning fluid (CTAB/NaSal wormlike micelle system) as bubbly liquid to study the rising of bubbles at relatively high gas fractions (5%-30%). Our experimental results deepen and enrich the research of bubble rising in non-Newtonian fluids, and also provide theoretical guidance for its industrial applications such as froth flotation.

Chapter 2 Molecular Dynamics Simulations and Quantitative Calculations on Unraveling Photo-responsive Behavior of Wormlike Micelles Constructed by 12-2-12·2Br$^-$ and *trans*-o-Methoxy-cinnamate

The results of this chapter have been published in *Langmuir* (*Langmuir* 2020 36 (32), 9499-9509).

2.1 Introduction

A great scientific challenge over the past years on soft matter field has been transferred to design adaptable materials in response to the triggers aroused by environmental changes, which can significantly alter their configuration and functionality [3]. Those smart self-assembly materials can dynamically respond to external environmental changes including electrical- [141], photo- [142], thermal- [143], pH- [144], magnetic- [145], CO_2-stimulus even multiple stimuli [146-148]. Among those stimuli, light stands out owing to its outstanding characteristics including responding non-invasively, operating simply, accessing easily and aiming at a precise spatial location [149-150]. The photo-responsive viscoelastic fluids composed of wormlike micelles are of particular interest because these viscoelastic fluids with tunable aggregate morphologies and rheological properties have played an increasingly important role in many fields such as microfluidics, drug delivery, sensors, drag reduction agent and so on [151-152]. As is well known, owing to special amphiphilic properties, surfactants can form different kinds of self-assembly aggregates such as spherical micelles [153], wormlike micelles [154], vesicles or gels [155-156], and liquid crystals (LCs) [157]. Without a doubt, smart self-assembly materials constructed by surfactants have become one of the hotspots that researchers pay much attention to recent years.

Adding certain photosensitive molecules directly to a surfactant solution is the most effective and simplest method to obtain a photo-responsive wormlike system [79]. For example, Raghavan proposed a simple photo-rheological fluid system based on the cationic surfactant cetyltrimethylammonium bromide (CTAB) and the photo-responsive organic derivative *trans*-ortho-methoxycinnamic acid (*trans*-OMCA) in aqueous solution [76]. The mixture of *trans*-OMCA and CTAB generated elongated and entangled wormlike micelles. After irradiation of UV-light, *trans*-OMCA transformed into *cis*-OMCA isomer. The alteration in molecular structure of OMCA aroused the long wormlike micelles to transform to short rod-like micelles with the solution viscosity degrading over 4 orders of magnitude. Following this paper, several studies were carried out revealing analogous effects in different surfactant solution containing

OMCA and its derivatives [158-159]. It is generally known that Gemini surfactants are a type of surfactant consisting of two amphiphilic chains linked by a spacer at or near the hydrophilic head groups. Unlike conventional surfactants, Gemini surfactants possess not only richer aggregation morphologies but also excellent physicochemical properties such as lower critical micelle concentration and stronger self-assembly ability. Based on Gemini surfactants and photo-sensitive molecules, a photo-responsive system with multiple photo-responsive behaviors can be constructed by employing photo-isomerization of *trans*-OMCA isomers into Gemini surfactant solution [160-161]. Therefore, extensive investigations on the photo-responsive wormlike micelle systems containing Gemini surfactants have a great value in soft matter fields.

However, a great challenge about explaining the different properties between *trans*/*cis*-OMCA and microscopic mechanisms of micelle transformation after UV irradiation still exists. Atomistic MD simulations and quantitative calculations provide us with a new solution to obtain specific self-assembly process of micelles, the details of packing patterns of certain molecule on the micelle surface, and energy changes on atom and molecular scale respectively [162-163]. In the past few years, the self-assembly process of surfactant has been well investigated using simulation method [164-167]. For example, Heerdt employed time-dependent DFT calculations and atomistic MD simulation to study photo-isomerization of *trans*/*cis*-OMCA isomers and the self-assembly of CTAB micelles with *trans/cis*-OMCA in water solution [168]. In order to save the simulation time, pre-assembled rod-like micelles in water solution were chosen as initial configuration in his simulation. The results showed that under low OMCA concentration, CTAB micelles and *cis*-OMCA formed several spherical micelles while *trans*-OMCA and CTAB micelles fused into long rod-like micelles, which agreed well with experiments. However, this study did not involve the infinite wormlike micelles and Gemini surfactant which has richer morphologies with different states and scales.

In this section, N, N'-bis(dodecyldimethyl)-1,2-ethane diammonium dibromide (12-2-12·2Br$^-$) was selected to construct the photo-responsive wormlike micelles because of the rich self-assembly morphologies and strong self-assembly capacity of 12-2-12·2Br$^-$. We utilized rheology and transmission electron microscopy (TEM) to study the micelle morphologies before and after UV illumination. Atomistic MD simulations with united-atom forcefield were employed to investigate the morphology transformation process of micelles after UV illumination at constant 12-2-12·2Br$^-$concentration and various *trans*/*cis*-OMCA concentrations. Owing to the large size of micelles, most of studies tend to use coarse-grained molecular dynamics (CG-MD) or united-atom forcefield with initial pre-assembled cylindrical micelles to simulate the self-assembly behavior [167-169]. However, in order to simulate the spontaneous self-assembly process of Gemini surfactants in solution, we employed a random

distribution of 12-2-12·2Br$^-$ surfactants in water solution as initial configuration. Density functional theory (DFT) calculations with B3LYP and M052X functionals were conducted to investigate the distinctions of energy and hydrophobicity properties between *trans*/*cis*-OMCA isomers. The present experimental and simulations studies on the photo-responsive behavior of surfactant micelles allow us to strengthen the comprehension towards the mechanism of photo-responsive behavior and to extend for further applications of photo-responsive systems.

2.2 Materials and Methods

2.2.1 Sample Preparation and UV-Light Irradiation

N, N-Bis(dodecyldimethyl)-1,2-ethane diammonium dibromide (12-2-12·2Br$^-$) was prepared according to our previous study [170]. Trans--methoxycinnamic acid (99%) was purchased from TCI Chemical Industry Development Co., Ltd without further purification. Furthermore, *trans*-ortho-methoxy cinnamate (*trans*-OMCA) used in this thesis was prepared by mixing *trans*-ortho-methoxy cinnamate with a slight excess of sodium hydroxide (NaOH) in solution. The mixed solution (17 mM 12-2-12·2Br$^-$/7 mM *trans*-OMCA) was prepared by quantitatively adding *trans*-OMCA to the 12-2-12·2Br$^-$ solutions, followed by standing in an incubator (25 ± 0.1°C) for 48 h to ensure equilibrium.

An ultra-high pressure short arc mercury lamp (CHF-XM35-500W) with a 365 nm optical filter was used to illuminate OMCA from *trans* to *cis*. Samples were put in a 10 ml quartz crucible and stirred constantly at 25°C ± 0.1 in a jacketed beaker connected to a low-temperature thermostat bath. The distance between the samples and the light source was fixed at 8 cm.

2.2.2 Rheology Measurements

Rheological properties were investigated using the double gap measurement system (C-DG26.7/T200, 23.831 mm ID, 27.597 mm diameter) of the Physical MCR 302 rheometer produced by Austrian Anton Paar Co., Ltd. A sample of about 8 ml was poured into the double gap and kept stable for at least 5 min before measurements. Steady shear rheology was measured by the shear rates changing from 0.01 s^{-1} to 1000 s^{-1}. The dynamic shear rheology was examined in the range of 0.05-100 Hz, with a fixed strain value (γ = 1%). The experimental temperature was controlled at 25.0 ± 0.1°C.

2.2.3 Transmission Electron Microscopy

The microstructures of aggregates were observed via transmission electron microscope (Jeol JEM-1400, Japan). Firstly, an appropriate amount of solution was slowly dropped on the

margin of the copper mesh containing the carbon support film; subsequently the sample was adsorbed on the copper mesh after a couple of minutes. Then the excess solution was removed by filter paper. After that, the samples were dyed with phosphotungstate for 10-20s, and finally the excess solution was cleaned with filter paper for observation as well.

2.2.4 Force-field parameters

Gaussian 09 quantum chemistry packages were used to optimize *trans*/*cis*-OMCA molecule structures as initial structures of atomistic MD simulations [171]. Solvation free energy and molar volume of OMCA isomers were also calculated by Gaussian 09 at the M052X/6-31G* level [172]. The interaction energies of typical 12-2-12^{2+}/OMCA packing patterns were obtained using 6-311g** basis set with B3LYP functional in SMD solvationmodel.

GROMOS96 45a3 forcefield was employed for all our simulations because of its good agreement with simulation research and experimental data [173-174]. The initial coordinates of 12-2-12^{2+} (Scheme 2.1 (a)) and *trans*/*cis*-OMCA^{-} (Scheme 2.1 (b)) molecules were generated using Gaussian 09. We utilized the ATB server to generate the forcefield parameters for the 12-2-12^{2+} [175]. The charge distribution and forcefield parameters on *trans*/*cis*-OMCA were obtained from the data of DFT calculations of Heerdt [168]. The charges assignments for 12-2-12^{2+} are showed in Table 2.1.

Table 2.1 The charge assignments for 12-2-12^{2+} used in the MD simulations.

12-2-12^{2+}					
Atom	charge (e)	Atom	charge (e)	Atom	charge (e)
C_1, C_{28}	0.231	C_7, C_{19}	0.029	C_{13}, C_{25}	0.104
C_2, C_{27}	0.231	C_8, C_{20}	-0.006	C_{14}, C_{26}	-0.065
C_3, C_{15}	0.143	C_9, C_{21}	0.009	C_{29}, C_{30}	0.069
C_4, C_{16}	0.082	C_{10}, C_{22}	0.029	N_1, N_2	0.139
C_5, C_{17}	0.009	C_{11}, C_{23}	-0.021		
C_6, C_{18}	0.029	C_{12}, C_{24}	-0.012		
Counter-ions					
atom	charge (e)	atom	charge (e)		
Br^-	-1.000	Na^+	1.000		

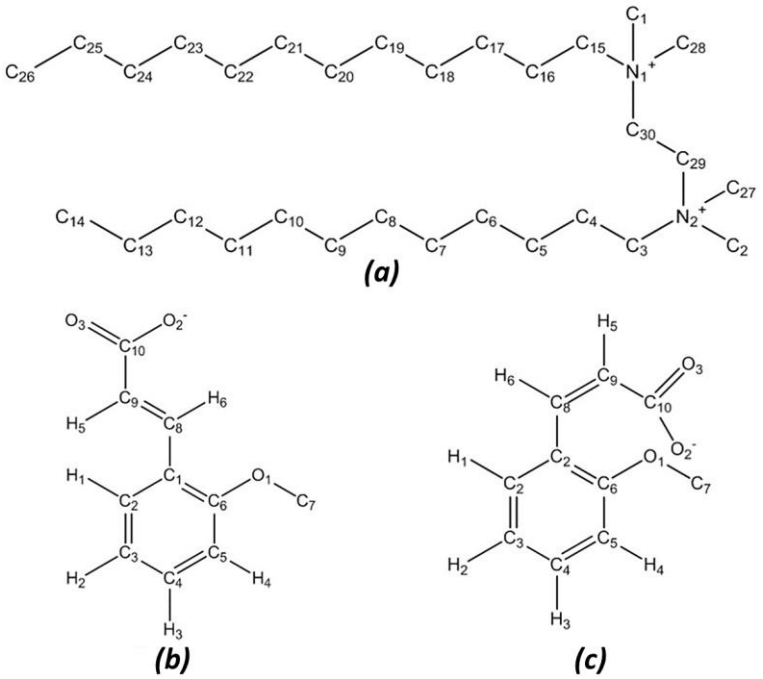

Scheme 2.1 Model structures and numberings of: (a) N, N'-bis(dodecyldimethyl)-1, 2-ethane diammonium ion (12-2-12^{2+}); (b) *trans*-ortho-methoxycinnamic acid ion (*trans*-OMCA^{-}); (c) *cis*-ortho-methoxycinnamic ion (*cis*-OMCA^{-}).

2.2.5 Simulation Details

2.2.5.1 Micelle simulation

A rectangle box of 6×6×12 nm^3 was constructed with 90 pure 12-2-12·2Br^{-} molecules. Then constant 12-2-12·2Br^{-} surfactant molecules (216) in a random arrangement and OMCA molecules of *trans/cis* with various number of 0, 54, 108, 162, 216, 270, 324 were dissolved randomly in approximately 37000 water molecules in a box of 7.5×7.5×24 nm^3 using Packmol [176]. For convenience, we define r_n as the ratio of the number of OMCA molecules to the number of 12-2-12·2Br^{-} molecules when the number of 12-2-12·2Br^{-} is constant at 216 in our simulations.

$$r_n = \frac{N_{OMCA}}{N_{Surfactant}} \tag{2-1}$$

Periodic boundary conditions were employed in all three dimensions to obtain the effectively infinite part of wormlike micelle. Corresponding number of counter ions Na+ were distributed in the box randomly as well. The 12-2-12·2Br^{-} concentrations were approximately 0.35 mol/L in small box and 0.25 mol/L in big box, which were far above the CMC (8.09 mmol/L) of 12-2-12·2Br^{-} in water solution [177]. The OMCA concentrations range from 0.07 to 0.33 mol/L. The details of box are shown in Table 2.

All the simulations were carried out by GROMACS 2018 packages [178]. Berendsen bath coupling scheme was used to maintain a constant temperature of 300 K and a constant pressure of 1 bar [131]. Semi-isotropic pressure coupling was applied owing to the convenience of simulating rod-like and wormlike micelles [168-169]. The simulation box was rescaled independently in z-direction but isotopically in x- and y- directions. The SPC water model was employed in all simulations [179]. The trajectories were saved every 2ps with a time-step of 2 fs. Interactions were subjected to a cutoff distance of 1 nm, and the long-range electrostatic interactions were handled with a grid size of 0.12 nm using the Particle Mesh Ewald technique [180]. Bonds containing hydrogen atoms were constrained using the Linear Constraint Solver (LINCS) [181]. The trajectories and configurations were visualized using VMD 1.9.2 [182].

2.2.5.1 Potential of mean force calculation

Two separate pre-assembly spherical micelles were constructed by Packmol software, then dissolved in water with the SPC water model in the box with size of 6nm × 6nm × 12nm, respectively. The solutions contained approximately 13000 water molecules, 32 *cis* or *trans* OMCA and corresponding counter ions. The steepest descent of energy minimization was employed. These two systems were carried out in NPT ensemble at 300 K and 1 atm for 50 ns with the time step of 2 fs. Periodic boundary conditions were applied in three dimensions. The temperature and pressure were controlled by the Berendsen bath coupling scheme [131]. Interactions were subjected to a cutoff distance of 1 nm where the long-range electrostatic interactions were set to 0.12 nm using the Particle Mesh Ewald technique. In the pulling process, the motion of micelles was restricted to maintain their initial configuration. A harmonic umbrella potential with a force constant of 1000 Kcal· mol^{-1}·nm^{-2} was applied between the COM of the micelle and a 12-2-12^{2+} ion or an $OMCA^{-}$ ion using pull code. Umbrella sampling simulations were carried out in 25 different windows ranging from 1.5nm to 6.5nm with a sequential stepwise reduction by 0.2 nm. The MD simulation time for each window was 10 ns. The potential of mean force was calculated from the sample windows using the Weighted Histogram Analysis Method which are implemented by g_wham command in GROMACS.

2.2.5.1 Interface simulation

The double layers of 12-2-12·$2Br^{-}$ were constructed by Packmol with the surface area 5×5 nm^2. Each layer contained 26 12-2-12·$2Br^{-}$ and 52 cis or trans OMCA isomers were distributed in the 12-2-12^{2+} layer randomly. The surfactant layers were position in a box 5×5×15 nm^3 at two sides of water. The water volume is 5×5×5 nm^3 with about 3800 water molecules with the SPC water model. The steepest descent of energy minimization was performed. After 5 ns NVT equilibrium, NPT ensemble was carried out at 298 K using the Nose-Hoover thermostat for 30 ns with the time step of 2 fs.

Table 2.2 Number of 12-2-12^{2+}, Br^{-}, OMCA^{-}, Na^{+} ions and water molecules in simulation box.

System	12-2-12^{2+}	Br^{-}	OMCA^{-}([mol/L])	Na^{+}	H_2O
12-2-12^{2+}					
1	90	180	-	-	11960
12-2-12^{2+} + *trans*-OMCA					
2	216	432	324 (0.40)	324	36626
3	216	432	270 (0.33)	270	36993
4	216	432	252 (0.31)	252	37218
5	216	432	216 (0.27)	216	37463
6	216	432	162 (0.20)	162	38057
7	216	432	108 (0.13)	108	38546
8	216	432	54 (0.07)	54	39037
12-2-12^{2+} + *cis*-OMCA					
9	216	432	324 (0.40)	324	36630
10	216	432	270 (0.33)	270	37066
11	216	432	252 (0.31)	252	37203
12	216	432	216 (0.27)	216	37510
13	216	432	162 (0.20)	162	38070
14	216	432	108 (0.13)	108	38663
15	216	432	54 (0.07)	54	38972

2.3 Results and Discussion

2.3.1 Photo-responsive behaviors of the wormlike micelle system

2.3.1.1 Microstructure.

The wormlike micelles formed in 17mM 12-2-12·2Br^{-}/7mM *trans*-OMCA aqueous solution were singled out to study the responsive behavior after UV irradiation. The microstructures of the aggregates after different UV irradiation times are obtained by TEM combined with a negative staining technique. As can be seen from Fig. 2.1, the system initially performed an entangled and dense network structure, indicating the generation of wormlike micelles. The network structure started to branch into rod-like micelle after 40 min UV irradiation. Further prolonging the UV irradiation time, the micelles continued to split into spherical micelles subsequently, and the rod-like micelles were entirely transformed into spherical micelles when the UV irradiation time is 60 min. Obviously, the wormlike micelles formed by the Gemini surfactant 12-2-12·2Br^{-} and *trans*-OMCA have excellent photo-

responsiveness and the system changes from wormlike micelles to rod-like micelles and until spherical micelles after UV irradiation.

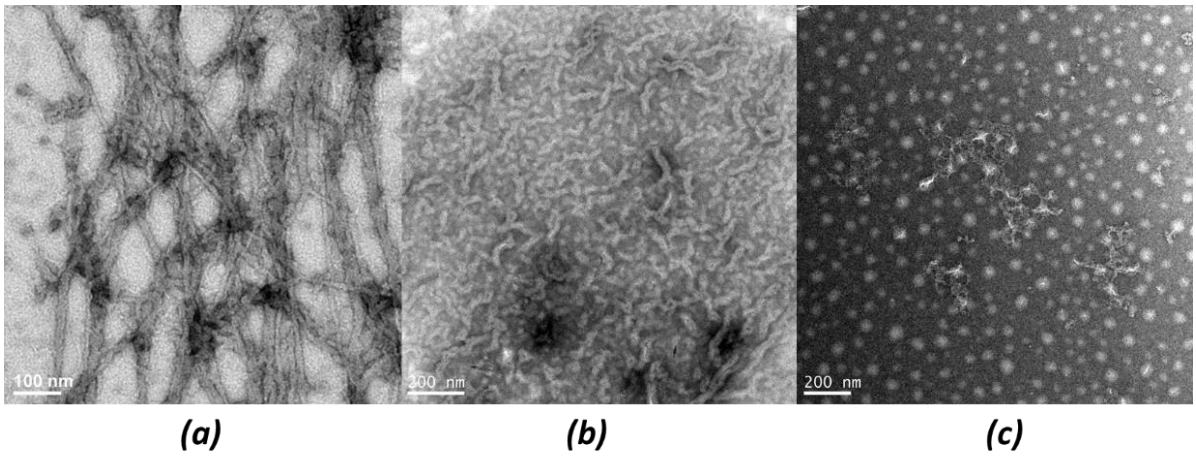

Fig. 2.1 TEM images for the sample of 17 mM 12-2-12·2Br$^-$/7 mM *trans*-OMCA system at 25°C with the prolongation of UV irradiation time [(a) 0 min; (b) 40 min; (c) 60 min].

2.3.1.2 Rheological properties.

Fig. 2.2 provides the rheological properties of 17 mM 12-2-12·2Br$^-$/7 mM *trans*-OMCA mixed solution under different UV irradiation time. It can be seen from Fig. 2.2 (a) that the high viscosity and the appearance of the shear-thinning phenomenon and zero-shear viscosity of 17 mM 12-2-12·2Br$^-$/7 mM trans-OMCA indicates the formation of wormlike micelles before UV irradiation. The wormlike micelles entangle with each other to form a network structure. The network structure is difficult to be destroyed when the shear rate is lower and therefore the platform appears (zero-shear viscosity, η_0). However, when the shear rate is relatively higher, the network structure will firstly disentangle, then be destroyed and transform into short rod-like micelles. Therefore, the shearing-thinning behavior occurs. With the prolongation of UV irradiation time, the shear-thinning behavior of the system gradually disappears accompanied by a decrease of the viscosity of the system. It reconfirms that the longer wormlike micelles can be destroyed after a period of UV irradiation and be transformed into smaller micelles; the results are coincided with the previous TEM observation. The zero-shear viscosity (Fig. 2.2 (b)) of the present system drops rapidly within 40 min and almost keeps constant over 60 min. The viscosity of the system decreases by about 3 orders of magnitude (from 2.7 ± 0.1Pa·s to 7.3± 0.1mPa·s) within 60 min. The viscoelasticity curves (Fig. 2.2 (c)) and the Cole–Cole plots (Fig. 2.2 (d)) of samples undergo different UV irradiation time once again prove the fact that the transformation from wormlike micelle to spherical micelles after UV irradiation.

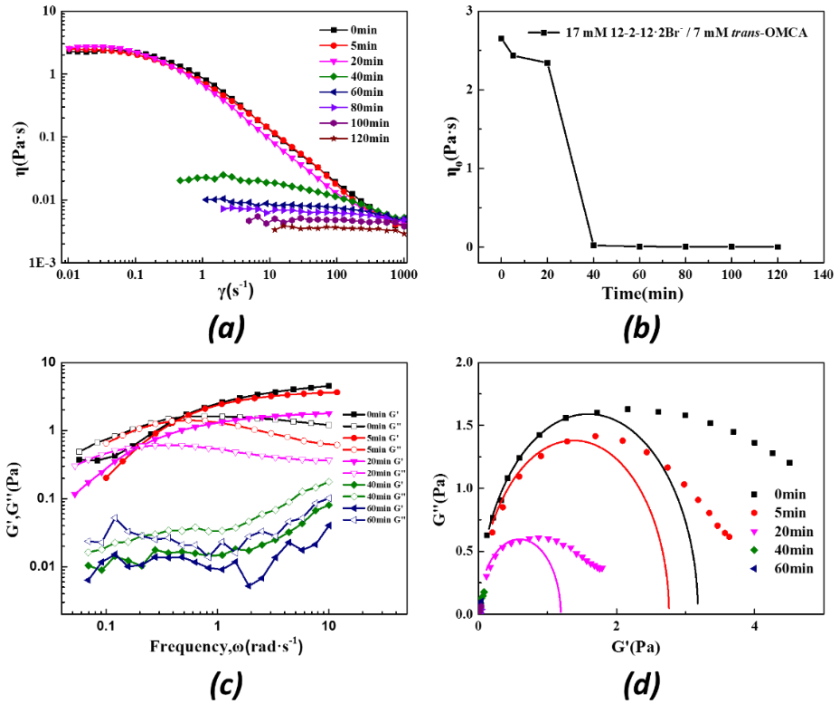

Fig. 2.2 Effect of UV irradiation time on rheological properties for the system of 17 mM 12-2-12·2Br⁻/7 mM *trans*-OMCA at 25°C (a) steady shear viscosity, (b) zero-shear viscosity, (c) dynamic frequency sweep, and (d) Cole–Cole plots.

2.3.2 Snapshots of micelles

In general, 12-2-12·2Br⁻ can form aggregates with different morphologies in aqueous solution depend on its concentration [183]. At very low concentration, 12-2-12·2Br⁻ molecules tend to aggregate into a multitude of spherical micelles. Fig. 2.3 provides the snapshot of the species formed in 12-2-12·2Br⁻ aqueous solution after 100ns MD simulation. Obviously, the spherical micelles are formed. The average aggregation number of the formed micelles is 22.5, which is very close to the experimental aggregation number of 21.2 [184]. The simulation result is in good agreement with that obtained by experiments.

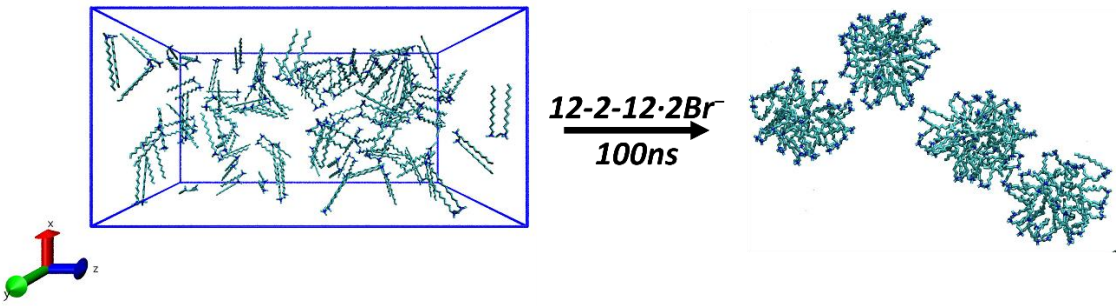

Fig. 2.3 Snapshots for the initial simulation box and final micelle morphology of pure 90 12-2-12·2Br⁻ surfactants. (The cyan molecules are 12-2-12^{2+}; for clarity, water, and Br⁻ ions are not shown.)

In order to obtain the detailed aggregation information after introducing OMCA and the influence of isomerization of OMCA, simulations of 12-2-12·2Br⁻ with *trans*-OMCA and *cis*-OMCA were carried out respectively. Fig. 2.4 presents the snapshots of simulation results. With the addition of *trans*-OMCA, a rod-like micelle appears firstly (r_n = 0.75). After that, a rod-like micelle similar with r_n = 0.75 was formed with denser bulk density when more *trans*-OMCA molecules were introduced to the 12-2-12·2Br⁻ system (r_n = 1). When r_n reaches 1.25, rod-like micelles further merged into a long wormlike micelle with several ellipsoidal micelles. Finally, at the highest OMCA concentration (r_n = 1.5), the micelle with *trans*-OMCA molecules grew into the elongated and intertwined network structure. The main reason for morphologies changes is that OMCA molecule is amphiphilic. After being added to 12-2-12·2Br⁻ system, OMCA will participate in the micelle formation with 12-2-12·2Br⁻. Meanwhile, owing to the strong electrostatic interaction between the head groups of cationic 12-2-12·2Br⁻ and anionic OMCA as well as π-cation interaction between the benzene ring of OMCA and the charged head group of 12-2-12·2Br⁻, the bulk density of micelles increases, inducing the formation of rod-like micelles even wormlike micelles [185-186].

After being irradiated under UV light, *trans*-OMCA isomerizes into *cis*-configuration. Rod-like micelles formed by *trans*-OMCA split into small, spherical micelles when r_n = 0.75. After that, surfactant micelles started to split to an ellipsoidal micelle and a rod-like micelle (r_n = 1). Subsequently, with the increase of *cis*-OMCA molecules to r_n = 1.25, a whole rod-like micelle appeared. Finally, at the highest *cis*-OMCA concentration (r_n = 1.5), the network micelles ruptured into a long wormlike micelle. Morphology changes because of the increase of the steric hindrance of OMCA after the photoisomerization, which disturbs the internal structure of the micelles. This steric effect and the electrostatic interaction as well as π-cation interaction will compete and finally affect the micellar morphology together. When the *cis*-OMCA concentration is lower, the steric hindrance effect is dominant, so that long micelles are split into smaller micelles. When the *cis*-OMCA concentration is higher, the electrostatic interaction as well as π-cation interaction start to be stronger than steric hindrance effect. At this time, the micelles begin to lengthen, while they are still smaller than that formed in *trans*-OMCA system.

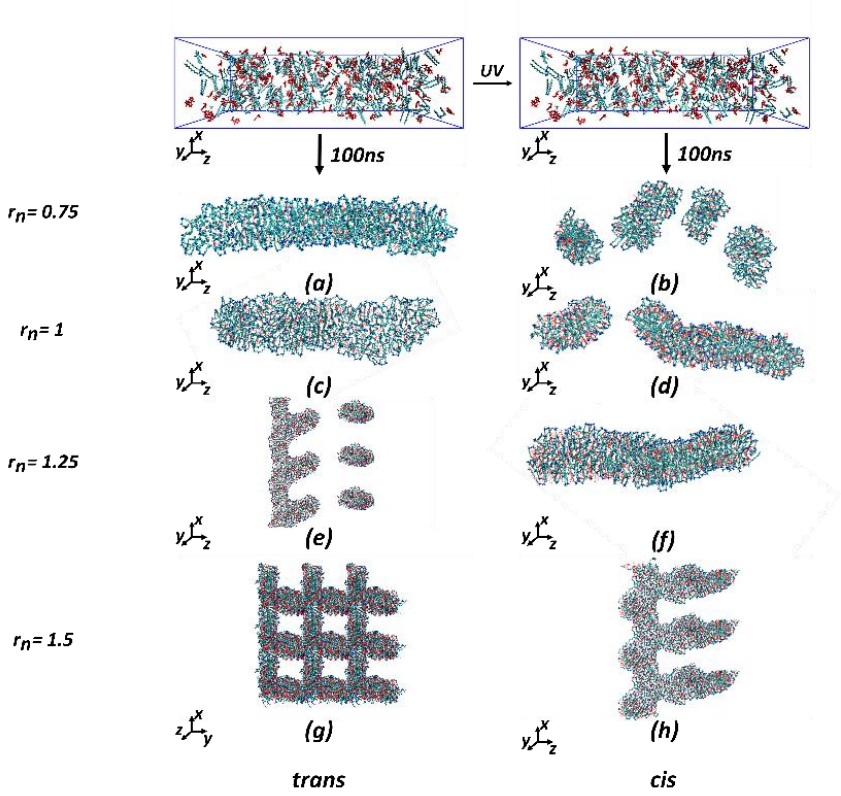

Fig. 2.4 Snapshots for the initial simulation box and final micelle morphologies of r_n = 0.75 [(a) and (b)]; r_n = 1 [(c) and (d)]; r_n = 1.25 [(e) and (f)]; r_n = 1.5 [(g) and (h)]. The left is aggregates containing 12-2-12·2Br$^-$ and *trans*-OMCA. The right is aggregates containing 12-2-12·2Br$^-$ and *cis*-OMCA. (a), (b), (c), (d), (f) have one period. (The cyan molecules are 12-2-12^{2+}; the red molecules are OMCA; for clarity, water and ions are not shown. Specially, to show the long wormlike and network morphologies, (e), (h) have three periods and (g) have nine periods.)

To testify the formation of micelles with special morphologies, the specific density information of ions in these systems are calculated and provided in Fig. 2.5. As shown in Fig. 2.5, 12-2-12^{2+} molecules mixed with *cis*-OMCA at r_n = 0.75 integrate into four spherical micelles, therefore four peaks are found in (b) along z axis. The long and finite rod-like micelle has a corona-shape peak such as (a), (c), (f), (g1). (d) and (e1) represent that spherical micelle and rod-like micelle coexist. When the long and infinite wormlike micelles appear, the density curve along x axis is infinite and successive like (e2), (g2) and (h2). The network micelles have infinite and successive curve in both x and y axis but they are not successive in z axis, as shown in (g1), (g2) and (g3).

From the result above, the 12-2-12·2Br$^-$ and *trans*-OMCA micelle perform obvious photo-responsive behavior, which is corresponding to the phenomenon that the long wormlike micelles gradually break into shorter units after UV light in our TEM results. The specific morphologies during micelle transformation in Fig. 2.1 are all captured in our simulation in Fig.

2.4. Nevertheless, to understand how the *cis/trans*-OMCA isomers impact differently on the surfactant micelle morphology, the deeper discussion of mechanisms of micelle transformation is of great value.

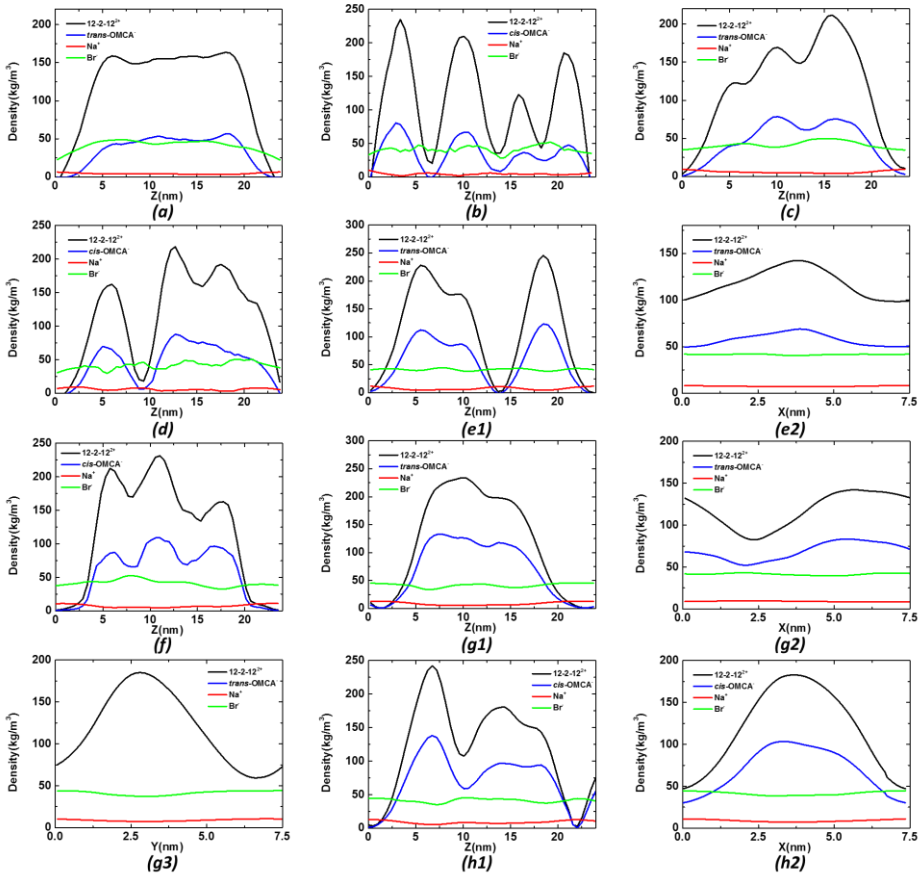

Fig. 2.5 The average density distributions of 12-2-12 (black line), OMCA (blue line), Na^+ (red line), Br^- (green line) along x (e2, g2, h2), y (g3), z (a, b, c, d, e1, f, g1, h1) at last 100 frames. The graph numbers are corresponding to the numbers of morphologies in Fig. 2.4.

2.3.3 Packing of 12-2-12·2Br⁻/OMCA

The packing patterns between OMCA and 12-2-12·2Br^- impact the morphology of micelles directly. Therefore, the radial distribution functions (RDF) between the N_1 atoms of hydrophilic head group in 12-2-12·2Br^- for micelles formed by pure 12-2-12·2Br^- and 12-2-12·2Br^- with 162 OMCA isomers were calculated firstly. The $g(r)$ between particle A and B can be defining as:

$$g_{AB}(r) = \frac{\langle \rho_B(r) \rangle}{\langle \rho_B \rangle_{local}} = \frac{1}{\langle \rho_B \rangle_{local}} \frac{1}{N_A} \sum_{i \in A}^{N_A} \sum_{j \in B}^{N_B} \frac{\delta(r_{ij}-r)}{4\pi r^2} \quad (2\text{-}2)$$

where $\langle \rho_B(r) \rangle$ is the density of particle *B* at a distance *r* around *A* particles, and $\langle \rho_B \rangle_{local}$ is the average density of particle *B* at a radius of r_{max} over all spheres around *A* particles. Usually, the value of r_{max} is half length of the box. The averaging is also carried out in time.

As is shown in the Fig. 2.6 (a), the $g(r)$ curve between N_1-N_1 atoms in 12-2-12·2Br^- system has two peaks located on 0.91 and 1.2nm. With the addition of *trans*-OMCA molecules, the two peaks shift left. The first peak of *trans*-OMCA moves to 0.64nm and the peak height has a considerable increase. The second peak moves to 0.86 nm. After isomerization, the first peak does not move while the second peak locates at 0.81 nm. The left shifting and height increase of the peaks suggest that the addition of OMCA promotes a closer packing between head groups of 12-2-12·2Br^-. This is because that the strong electrostatic association between OMCA and 12-2-12^{2+} ions decreases the surface charges of micelles, thereby reducing the effective area of charged head groups. And it is noticeable that the height of first peak for system containing *trans*-OMCA is significantly higher than that of the system containing *cis*-OMCA, suggesting that 12-2-12·2Br^- surfactants in *trans*-OMCA system have a closer and more ordering packing than in *cis*-OMCA system.

C_3 in benzene ring, C_7 in methoxy, and C_{10} in carboxyl of OMCA are the key atoms to calibrate the main position of OMCA. The $g(r)$ between them and the N_1 atoms in 12-2-12·2Br^- was also calculated. As can be seen in Fig. 2.6 (b), the two isomers pack in very different patterns. The $g_{N_1\text{-}C_3}(r)$ function curves have a peak at 0.85 nm for system containing *trans*-OMCA and a peak at 0.48 nm for system containing *cis*-OMCA. The $g_{N_1\text{-}C_7}(r)$ witnesses a similar distribution with a peak at 0.52 nm for systems containing both *cis*- and *trans*-OMCA. A sharp N_1-C_{10} peak was observed at 0.43 nm for *trans*-OMCA system in $g_{N_1\text{-}C_{10}}(r)$ curve and at 0.46 nm for *cis*-OMCA system. The proximity of C_3 to N_1 of *cis*-OMCA system implies that its emergence on the micelle surface while the C_3 of *trans*-OMCA is embedded into the micelle. For both isomers, C_7 is inserted inside the micelle (but not as deep as C_3 for *trans*-OMCA) and C_{10} is distributed on the surface of micelle. The sharp N_1-C_{10} peak reveals a highly orderly arrangement between these two atoms. The approaching of C_{10} to N_1 for *trans*-OMCA system discloses a stronger electrostatic interaction between the charge centers of *trans*-OMCA and 12-2-12·2Br^-.

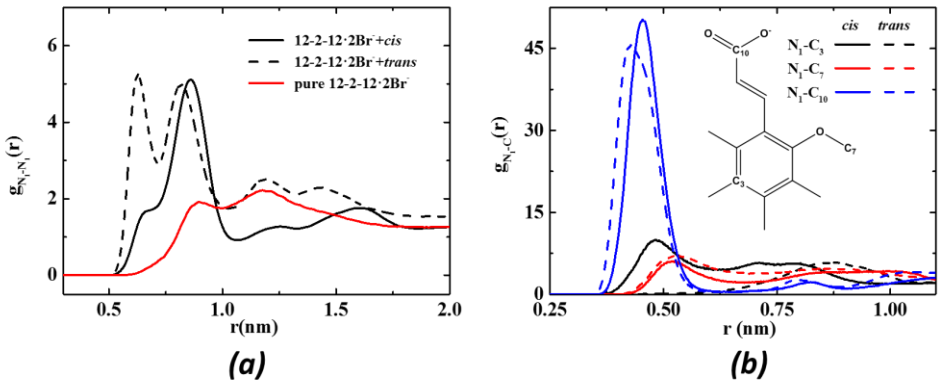

Fig. 2.6 Radial distribution functions (a) between nitrogen atoms $g_{N_1\text{-}N_1}(r)$ and (b) between nitrogen N_1 atoms from 12-2-12·2Br⁻ and specific carbon atoms from OMCA isomers, $g_{N_1\text{-}C}(r)$ at r_n = 0.75.

Fig. 2.7 shows the representative packing intercepted from micelles at r_n = 0.75. Combining the results of $g(r)$ with Fig. 2.6, we can easily capture the difference in packing patterns of *cis/trans*-OMCA: the aromatic ring of *cis*-OMCA is situated on the surface of micelles while that of *trans*-OMCA is inserted into the hydrophobic alkyl chain of 12-2-12·2Br⁻; the carboxyl groups of both *cis/trans*-OMCA are oriented on the surface of micelles and the methoxy groups of them are embedded into the micelles. Meanwhile, on the micelle surface, it is noticeable that there are more red parts (oxygen atoms in OMCA) on 12-2-12·2Br⁻/*trans*-OMCA micelle surface than in 12-2-12·2Br⁻/*cis*-OMCA micelle surface. And we can hardly observe the white parts (hydrogen atoms in OMCA) on 12-2-12·2Br⁻/*trans*-OMCA micelle surface. These atoms distribution confirms that the aromatic ring of *trans*-OMCA is embedded entirely into the 12-2-12·2Br⁻ micelle and that of *cis*-OMCA lies on the surface of micelles.

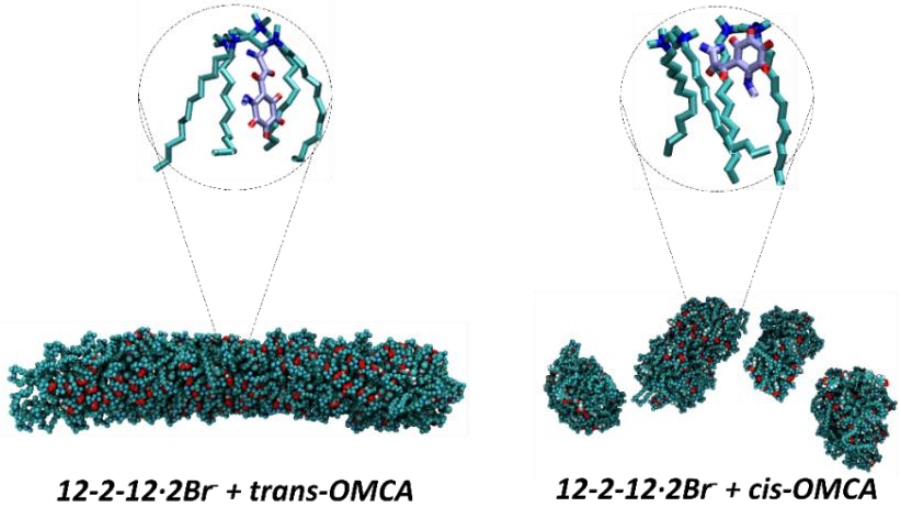

Fig. 2.7 The arrangements of 12-2-12·2Br⁻ and OMCA molecules on micelles at r_n = 0.75. (The cyan parts are 12-2-12^{2+}; the red parts are OMCA⁻; the red beads and white beads are oxygen atoms and hydrogen atoms in OMCA.)

The distinctions of *cis/trans*-isomer on the micelle surface can also be characterized by the solvent accessible surface area (SASA) between micelles and water. The SASA means the surface area of the micelle that is accessible to the solvent. In Gromacs, a 1.4Å spherical solvent probe is used to scan the surface of the micelle by default. The part with a charge between -0.2 and 0.2 is regarded as hydrophobic area, and the other part is the hydrophilic area. The SASA of surfactant micelles under different concentrations are displayed in Fig. 2.8. With the increase of the OMCA concentration, the total area, the hydrophilic area, and the hydrophobic area decrease. This indicates that the micelle become denser and the contact area with solution decreases because of the stronger electrostatic interaction.

Table 2.3 presents some geometrical properties for the micelles at $\boldsymbol{r_n}$ = 0.75 in our simulation. From Table 2.3, we can find that there is a larger hydrophobic area for 12-2-12·2Br$^-$/*cis*-OMCA mixed micelles while the hydrophilic area of 12-2-12·2Br$^-$/*trans*-OMCA micelles witnesses a contrary result. Obviously, the *trans*-OMCA molecules expose their carboxyl group to the water whereas *cis*-OMCA molecules expose their benzene ring to the water. The difference in SASA reconfirms the different packing patterns of *cis*- and *trans*-isomers on micelle surface.

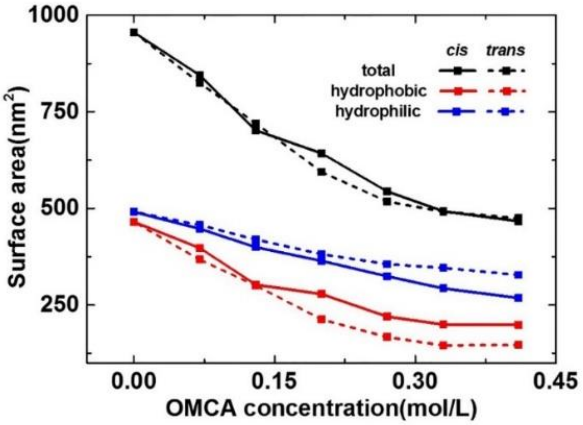

Fig. 2.8 The hydrophobic(a_{pho}), hydrophilic(a_{phi}) and total(a_{tot}) surface areas of 12-2-12·2Br$^-$/OMCA micelles with the OMCA concentration change.

Table 2.3 Geometric parameters of micelles of $\boldsymbol{r_n}$ = 0.75 at the end of the MD simulations: micelle volume(V); hydrophobic(a_{pho}), hydrophilic(a_{phi}) and total(a_{tot}) surface areas; the length of alkyl chain (l); the critical packing parameter (*P*).

System ($\boldsymbol{r}$ = 0.75)	V (nm^3)	a_{pho} (nm^2)	a_{phi} (nm^2)	a_{tot} (nm^2)	L (nm)	*P*
cis-OMCA	84.2	278.4	364.2	642.6	1.25	0.19
trans-OMCA	153.1	212.7	381.7	594.4	1.26	0.33

The different $g(r)$, atom distribution and SASA between *cis/trans*-OMCA and 12-2-12·2Br$^-$ at concentration r_n = 0.75 can interpret the different packing patterns of *cis/trans*-OMCA on micelles. The trend of spherical or rod-like micelles formation can also be explained by another important parameter, the critical packing parameter [24]. In our simulation, l is calculated by the distance between C_{15} and C_{26}. As is shown in Table 2.3, the P values for micelles with *cis/trans*-OMCA are 0.19 and 0.33, respectively. These values suggest that the most stable and favorable morphologies for *cis/trans*-OMCA at r_n = 0.75 are spherical shape and rod-like shape. In other words, when the *trans*-isomers photo-isomerize into *cis*-isomers after UV irradiation, the originally stable rod-like micelle will become unstable. To reacquire a stable structure, rod-like micelles will gradually break up and transform into several spherical micelles.

2.3.4 Micelle transition

From above, we can see that the packing patterns of OMCA and 12-2-12·2Br$^-$ affect the morphology of micelles. In order to further explore the mechanism of micelle transition after the UV irradiation, the quantitative calculations and other MD methods are adopted to further analyze the detailed information including geometric structure of OMCA, hydrophilicity of OMCA and the interaction energy between OMCA and 12-2-12·2Br$^-$ at the molecular scale.

2.3.4.1 Geometry

Firstly, the optimized structures of OMCA molecules are shown in the Fig. 2.9. The value is the angle between the plane of benzene ring and carboxyl in OMCA. We can find that almost all atoms of a *trans*-OMCA molecule are oriented at a same plane with an angle 180° while the angle (140°) and shorter distance (6.46 Å) between C_{10} and H_3 of *cis*-OMCA molecule show its three-dimensional configuration and higher bending degree. Moreover, as can be seen in Table 2.4, *trans*-OMCA molecule has a smaller molar volume. Therefore, when inserted into the 12-2-12·2Br$^-$ layers, *trans*-OMCA molecule is easier to embedded into hydrophobic interior of 12-2-12·2Br$^-$ and shows a more ordering arrangement. After UV irradiation, owing to higher bending degree and larger volume, *cis*-OMCA molecules occupy more space and has a farther distance to the charged head group of 12-2-12·2Br$^-$, which has been testified via $g(r)$ of N_1-C_{10} in Fig. 2.6. Therefore, the arrangement between OMCA and 12-2-12·2Br$^-$ becomes looser and the interactions between OMCA and 12-2-12·2Br$^-$ become weaker, giving rise to the break of micelles.

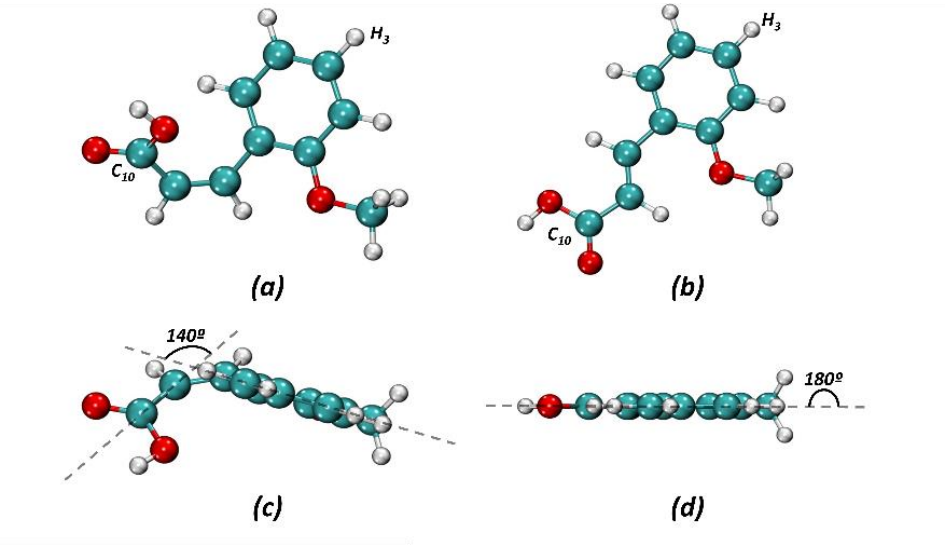

Fig. 2.9 The structures of OMCA molecules after being optimized at the M052X/6-31G* level. (a), (c) *cis*-OMCA top and front view; (b), (d) *trans*-OMCA top and front view.

Table 2.4 Solvation Free Energy of *cis/trans*-OMCA, distance between H_3 and C_{10} and molar volume calculated by Gaussian 09 at M052X/6-31G* level in SMD solvation model.

	Solvation free energy (kJ/mol)	C_{10}-H_3 Distance (Å)	Molecular volume (cm^3/mol)
cis-OMCA	-40.56	6.46	125.16
trans-OMCA	-37.68	9.02	122.23

2.3.4.2 Hydrophilicity

Subsequently, we explore the hydrophobicity of *cis*/*trans*-OMCA by calculating the solvation free energy using Gaussian 09 at M052X/6-31G* level in SMD solvation model. Solvation free energy represents the intensity of hydrophilic capacity of a molecule. The free energy of solvation refers to the change in free energy that moves a solute molecule in a gas phase state of 1 atm into a solvent to become a solvation state of 1 mol. As is shown in Table 2.4, the solvation free energies of *cis*-OMCA and *trans*-OMCA are -40.56 kJ/mol and -37.68 kJ/mol. Obviously, *cis*-OMCA is more hydrophilic, and it should have a stronger trend to move to the water rather than stay in the micelle than *trans*-OMCA. In order to verify this inference, we constructed an air/water interface with well-arranged surfactant layers consisting of 26 12-2-12·2Br^- (CMC concentration) and 52 OMCA are oriented randomly between the 12-2-12·2Br^-.[47] Excessive OMCA molecules ensure that OMCA molecules are able to escape from surfactant layers. Fig. 2.10 provides the snapshots of 12-2-12·2Br^- on air-water interface before and after MD simulations with 12-2-12·2Br^-/OMCA proportion of 26/52. According to Fig. 2.10, after 30ns MD simulation, several OMCA molecules are observed to escape from the

surfactant layer and move toward the water solution. Obviously, the number of escaping *cis*-OMCA molecule is much more than that of *trans*-OMCA. The stronger hydrophilicity of *cis*-OMCA drives it to run from the hydrophobic interior of 12-2-12·2Br$^-$ to the water. Once the *cis*-OMCA escape from its position, the original wormlike micelles break into rod-like micelles even spherical micelles correspondingly.

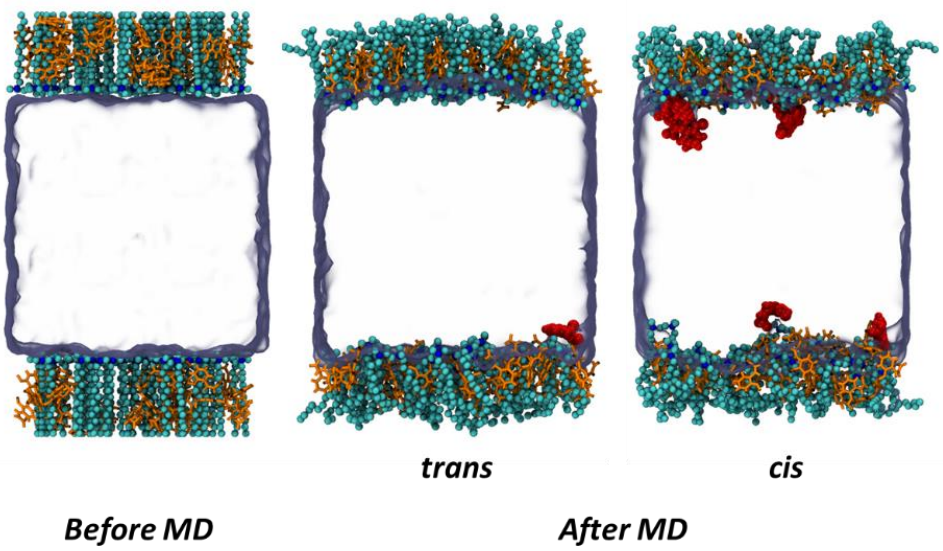

Fig. 2.10 Snapshots of 12-2-12·2Br$^-$ on air-water interface before and after MD simulations with 12-2-12·2Br$^-$/OMCA proportion of 26/52. (Red parts are OMCA molecules escaping from micelles; yellow parts are OMCA molecules embedded into micelles; cyan parts are 12-2-12·2Br$^-$ layers. The middle transparent part is water.)

2.3.4.3 Energy

The relative interaction energy between surfactant and *cis/trans*-OMCA of different packing patterns is explored. Two representative packing patterns of *cis*-OMCA (Fig. 2.11 (a), (b)) and *trans*-OMCA (Fig. 2.11 (c), (d)) from the micelle at the last snapshot in our MD simulations were singled out. One was the benzene ring oriented into the 12-2-12·2Br$^-$ alkyl chain and another was the benzene located on the micelle surface. The basis set 6-311g** with B3LYP functional in SMD solvation model was employed to calculate the interaction energies. The relative interaction energies of these four packing ways are 35.5, 3.1, 8.5 and 0 kJ/mol. For *cis*-OMCA, the structure (b) that the benzene rings appear on the micelle surface is more stable and for trans-OMCA, the structure (d) that the benzene rings are embedded on the micelle interior is more stable. This means that when *trans*-OMCA (d) becomes *cis*-OMCA (a) after photo-isomerization, to obtain a stable packing configuration OMCA molecule will change its previously stable packing (a) to the packing (b). This transformation results in the loosing of the micelle structure and finally induces the fission of micelle.

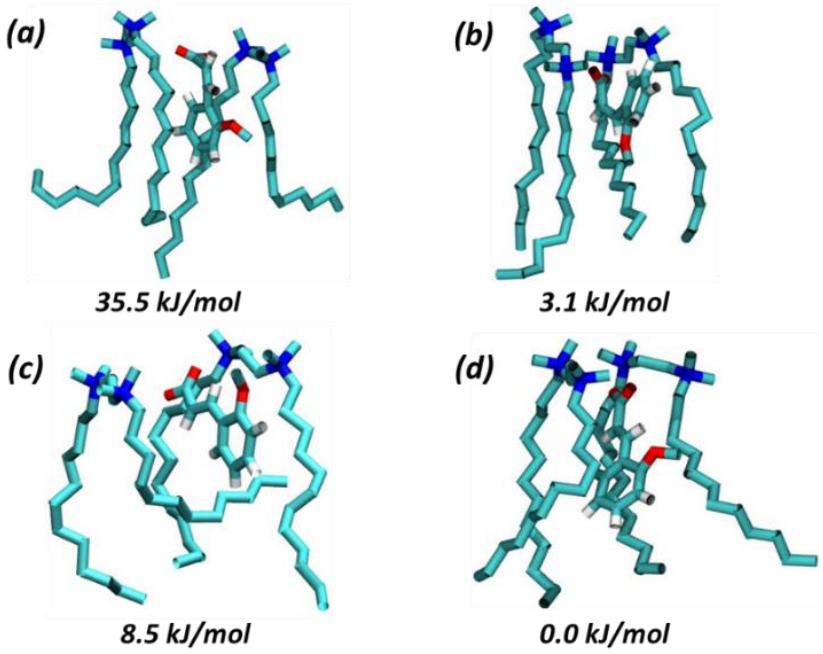

Fig. 2.11 Relative interaction energies (kJ/mol) of specific packing patterns between 12-2-12^{2+} and OMCA^{-} on micelles. The benzene rings of (a) and (d) are embedded into the micelles and the benzene rings of (b) and (c) appear on the micelle surface. (a) and (b) are *cis*-OMCA. (c) and (d) are *trans*-OMCA. (For clarity, hydrogen atoms are not shown.)

Fig. 2.12 shows LJ interaction energy, Coulombic interaction energy, and total interaction energy between OMCA and 12-2-12^{2+} at r_n = 0.75. We find that these three interactions between *trans*-OMCA and 12-2-12·2Br^{-} are stronger than those between *cis*-OMCA and 12-2-12·2Br^{-}. This means that 12-2-12^{2+} and *trans*-OMCA have a stronger counter-ion binding capacity. Therefore, the stronger shielding effect of *trans*-OMCA on the electrostatic repulsion between the head groups of 12-2-12·2Br^{-} induce a denser packing of 12-2-12·2Br^{-} than in 12-2-12·2Br^{-}/*cis*-OMCA system. The stronger electrostatic interaction between *trans*-OMCA and 12-2-12·2Br^{-} is consistent with the results obtained by $g(r)$ calculations between N_1-C_{10}. The specific values of interaction energy are summarized in Table 2.5.

Table 2.5 Interaction energies between OMCA^{-} and 12-2-12^{2+} ions at r_n = 0.75 after equilibrium in MD simulations:

System	Coulombic (kJ / mol)	LJ (kJ / mol)	Total Interaction (kJ / mol)
cis-OMCA	-16807.90	-13316.07	-30123.97
trans-OMCA	-17402.15	-14632.52	-32034.68

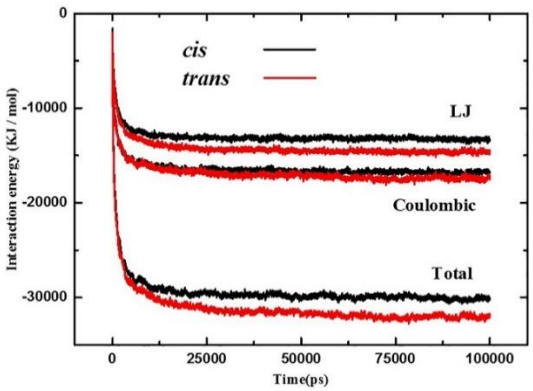

Fig. 2.12 Interaction energies (kJ/mol) between 12-2-12^{2+} and OMCA$^-$ during MD simulations at r_n = 0.75.

Furthermore, we calculated the PMF by sampling method. The potential of mean force is the potential energy obtained by integrating the average force of the configuration ensemble, which can be calculated by:

$$\mathrm{PMF}(r) = -k_B T \ln g(r) \qquad (2\text{-}3)$$

where k_B is the Boltzmann constant and $g(r)$ is the radial distribution function.

The PMF in Fig. 2.13 represents the change of potential under a given pull force which pulls out a molecule from a pre-assembled spherical micelle to different distances. From Fig. 2.13 (a), we can see that it is much easier to pull out a *cis*-OMCA$^-$ ion from the stable spherical micelle than pull out a *trans*-OMCA$^-$ ion. The results once again approved that *cis*-OMCA molecules are more likely to escape from micelles to the solution. In Fig. 2.13 (b), the PMF of pulling out a *trans*-OMCA$^-$ is much larger than pulling out a *cis*-OMCA$^-$ from spherical micelle formed by OMCA and 12-2-12·2Br$^-$. This indicates that the spherical micelle containing *trans*-OMCA have a more stable configuration than that containing *cis*-OMCA.

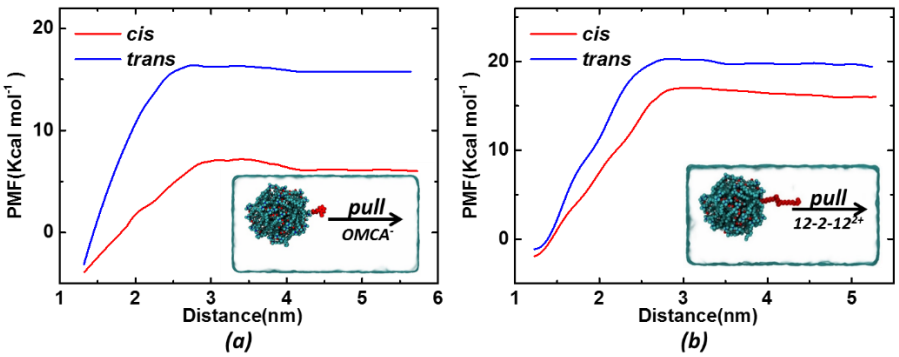

Fig. 2.13 Potentials of mean force (PMF) of pulling out an OMCA or 12-2-12^{2+} ion from a spherical micelle formed by 32 12-2-12·2Br$^-$ and 32 OMCA to different distances.

2.3.5 The mechanism of photo-responsive behavior.

Based on the above analysis, the mechanism of photo-responsive behavior for 12-2-12·2Br⁻/*trans*-OMCA micelle is proposed (Fig. 2.14). Obviously, the packing pattern between 12-2-12·2Br⁻ and OMCA determines the existing morphology of micelle directly and the three primary factors affect the packing pattern between 12-2-12·2Br⁻ and OMCA: geometric structure of OMCA, hydrophilicity of OMCA and the interaction energy between OMCA and 12-2-12·2Br⁻. Firstly, it's noteworthy that the relatively planar structure of *trans*-OMCA and lower bending degree make *trans*-OMCA easier to insert into the interval of surfactants. It's demonstrated by $g(r)$ and SASA that the different molecular geometry of *trans/cis*-OMCA influences their packing ways: the aromatic ring of *trans*-OMCA is completely embedded into the hydrophobic alkyl chain of 12-2-12·2Br⁻ and that of *cis*-OMCA is exposed to the surface of micelle. Thereby, there is a closer arrangement between the charged center of *trans*-OMCA and 12-2-12·2Br⁻, bringing about a stronger electrostatic interaction and π-cation interaction. After UV irradiation, the steric hindrance of *cis*-OMCA molecule becomes larger and the electrostatic interaction and π-cation interaction become weaker leading to the disintegration of original micelle.

Secondly, a lower solubility in water has been proved to be related to a stronger association with micelles.[24] Through comparing the solvation free energy, it is demonstrated that *trans*-OMCA is more hydrophobic than *cis*-OMCA. The stronger hydrophobicity of *trans*-OMCA indicates that the *trans*-OMCA remains associated with micelles to a larger degree.[24] On the contrary, the stronger hydrophilicity of *cis*-OMCA endows it the chance to move towards the outer layer of micelles and even escape from the 12-2-12·2Br⁻ micelle layers, and finally induce the split of the micelle.

Finally, by calculating interaction energy, the micelles containing *cis*-OMCA are proved to be less stable. After the photoisomerization of *trans*-OMCA, to obtain a stable packing pattern with a lowest energy, *cis*-OMCA will change its packing pattern from embedding the aromatic ring into micelle to orienting that on the surface of micelle. Therefore, the long rod-like micelles will split into several spherical micelles.

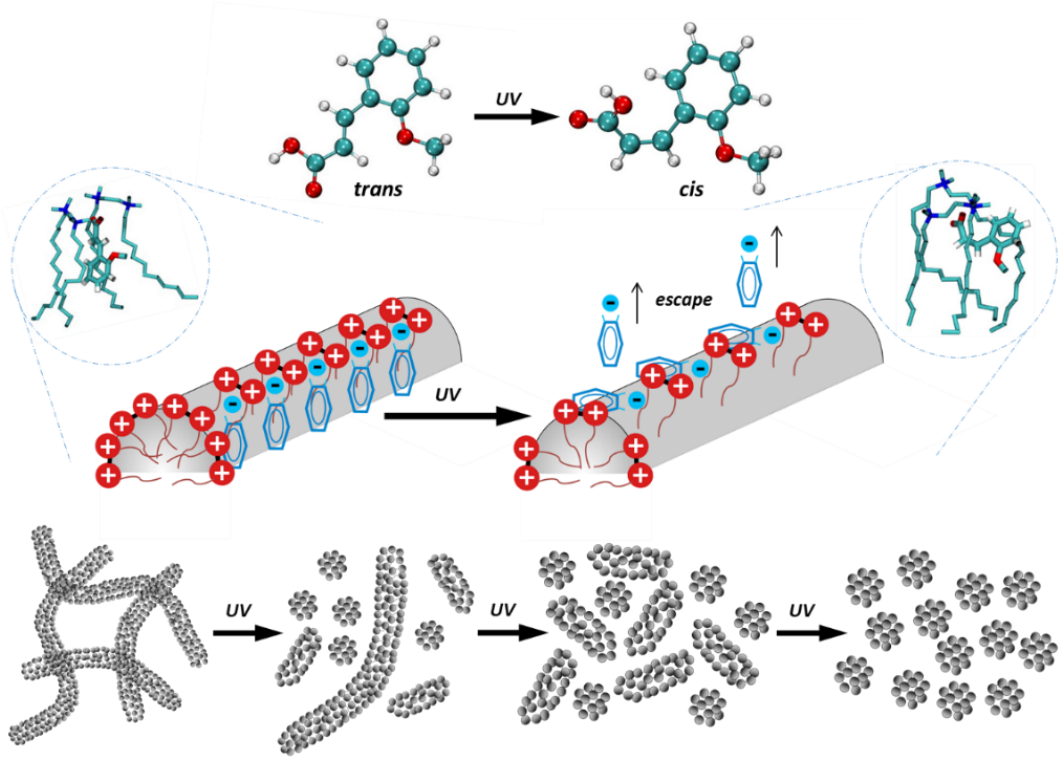

Fig. 2.14 The mechanism of photo-responsive 12-2-12·2Br⁻/*trans*-OMCA micelle morphology transition.

2.4 Conclusions

In this chapter, we investigated photo-responsive behavior of Gemini surfactant 12-2-12·2Br⁻ and *trans/cis*-OMCA using rheology, TEM experiments, atomistic MD simulations, and DFT calculations. Firstly, *trans*-OMCA associates strongly with 12-2-12·2Br⁻, leading to the formation of wormlike micelles. Upon irradiation of UV light, *trans*-OMCA photoisomerizes into *cis*-OMCA. The wormlike micelles crack to rod-like micelle and finally to spherical micelles. Three primary factors (geometry, hydrophilicity and energy) affecting those micelle transitions are unraveled systematically. The larger steric hindrance of *cis*-OMCA weakens π-cation interaction and electrostatic interaction. The stronger hydrophilicity of *cis*-OMCA leads to the moving of *cis*-OMCA from the interval of micelles to the solution. Moreover, the *cis*-OMCA has a weaker interaction with the 12-2-12·2Br⁻ than *trans*-OMCA. All these factors induce the breakage and repacking of wormlike micelles.

Regarding the experimental research on photo-responsive wormlike micelles systems, 12-2-12·2Br⁻ and OMCA in water solution emerged as a photo-responsive system with different morphologies. At high concentration, 12-2-12·2Br⁻ surfactant will form vesicles even liquid crystals with large aggregation number. After UV light, the vesicle firstly transforms into long and elongated wormlike micelles and with the UV irrational time prolonged, the wormlike micelles will continue to break up and finally split into spherical micelles. Because of the

multiple transformation process from vesicle to wormlike micelle and finally to spherical micelle, multiple control of the viscosity of the system can be achieved via UV light. We have studied several morphologies such as spherical, ellipsoidal, rod-like, wormlike and network micelles. However, owing to the scale limitation of simulation box, we cannot simulate the vesicles with micron size through united atom forcefield. From experiments after the *trans/cis*-OMCA photoisomerization, the complete transformation process from wormlike micelles to spherical micelles costs 60 minutes whereas the initial alteration in morphology takes place at the first few seconds. Moreover, several papers which depict the self-assembly aggregates of surfactant confirm that the micelle breakage and coalescing processes happen at the millisecond to second timescale under standard conditions [187-189]. However, the timescale of atomistic MD simulations is within microsecond. These scales could not entirely satisfy the time in micellar transformation and size of vesicle. Coarse-Grained (CG) model has an extended timescale which might accomplish the simulation of vesicle, but the subtle alterations of packing patterns between OMCA and 12-2-12·2Br^- will be hard to capture. To the best of our knowledge, rare articles report different aggregate self-assembly process and those aggregate transition process using atomistic MD simulation for 100ns from a random arrangement of surfactant solution. We achieve this simulation successfully. Various micelle morphologies and specific packing patterns during micellar transformation were displayed. The causes of those different packing were elucidated comprehensively and systematically. Our simulation morphologies are in good agreement with our TEM results and others' experimental as well as calculation results. The present molecular-level details of the micellar repacking process and mechanism of aggregate transformation can be utilized to design novel photo-rheological systems with tunable rheological properties. Such photo-responsive system will widen the application prospect in microscale engineering fields such as drug delivery, soft materials, smart fluids and purification and separation.

Chapter 3 Molecular Dynamics Simulations and Quantitative Calculation of Photo-responsive Behavior of Wormlike Micelles Constructed by Gemini Surfactant 12-3-12·2Br⁻ and Cinnamate Derivatives with different ortho-substituents

3.1 Introduction

In last chapter, we studied the photo-responsive behavior of wormlike micelles constructed by Gemini surfactant 12-2-12·2Br⁻ and photo-sensitive molecule *trans*-OMCA. To further promote the photo-responsive ability of photo-responsive wormlike micelles, it is important to study the wormlike micelles constructed with different photo-sensitive cinnamate molecules. As we know, the subtle difference in the substituents at the phenyl ring of cinnamates has a significant impact on the velocity of photo-isomerization reaction of cinnamate derivatives and the interaction between cinnamate derivatives and surfactant, which further influence the photo-responsive behavior of the photo-responsive wormlike micelles. Promkatkaew's group [190] used B3LYP geometric optimization and SAC/SAC-CI calculations to study the effects of hydroxyl, nitro, and fluorine substitutions at ortho-, meta-, and para- position of cinnamate derivatives on the velocity photo-isomerization reaction. The results indicated that ortho- and meta-substituted derivatives have longer emission lifetimes than those at the para derivatives. Although the quantitative calculation method can accurately capture the differences between molecules, the microscopic changes in the morphology of micelles cannot be observed. MD simulations provide a way to visualize these interesting photo-responsive phenomena, to capture how substituents on the phenyl ring affect the packing pattern between photo-sensitive molecule and surfactant and to elucidate the mechanism of morphology transition of surfactant self-assembly. However, most studies on the surfactant self-assembly use coarse-grained (CG) forcefield in order to save simulation time. As a result, the subtle changes of molecular structure before and after UV irradiation have not been well observed and understood. For example, Zheng's group [191] used a coarse-grained model to investigate the photo-responsive self-assembly and disassembly process of cis-, trans-AzoC10/alpha-CD mixture at a timescale of ten microseconds. Their results indicate that there is a significant correlation between the size and shape of aggregates and the molecular structure and concentrations of *trans*-AzoC10. As for the slight change in structure of AzoC10 and the effects of it before and after UV irradiation were not fully investigated.

The influence of the substituents at the benzene ring on the kinetic of photo-isomerization reaction is quite complicated. In addition, the insufficient investigation of micellar transition mechanism and the variation of viscoelastic properties of photo-responsive wormlike micelle of Gemini surfactants and cinnamates mixed system under UV irradiation have severely hindered their industrial application. Therefore, the study of the effects of different substituents at aromatic ring of cinnamates on photo-responsive behavior of wormlike micelles constructed by Gemini surfactants and cinnamates exhibits an important research value.

In this chapter, three aromatic cinnamates *trans*-o-methoxy cinnamate (*trans*-OMCA), *trans*-o-hydroxy cinnamate (*trans*-OHCA), and *trans*-cinnamate (*trans*-CA) were selected as photo-sensitive molecules to adjust the morphology of surfactant assemblies in the photo-responsive system. The Gemini surfactant timethylene-1, 3-bis (dodecyldimethylammonium bromide) (12-3-12·2Br^-) was specified as the elementary entity of surfactant assemblies. The photo responsive wormlike micelles were then constructed by aromatic cinnamates and 12-3-12·2Br^-. The corresponding morphologies during the photo-responsive process of the studied wormlike micelles were observed by transmission electron microscopy (TEM) and the kinetics of photo-isomerization of three *trans*-isomers were studied by UV-Vis absorption spectrum and high performance liquid chromatography (HPLC). MD simulations and quantitative calculations were employed to simulate the morphological transformation of micelles under UV irradiation and to investigate the differences of structure and properties between cinnamates with various ortho-substituent groups. Especially, we constructed simulation systems using different numbers of *trans/cis*-isomers to simulate the UV irradiation time. Our simulations and calculations display the detailed information about how photo-sensitive molecules participate in the construction and fission of wormlike micelles composed of cinnamates and 12-3-12·2Br^- before and after UV irradiation and elucidate the impacts of different ortho-substituents on the photo-behavior of these photo-responsive systems. This study allows us to optimize the photo-responsive self-assembly system containing Gemini surfactants and cinnamates, which is of great importance for the design of smart responsive systems and expansion of their applications in soft material and other fields.

3.2 Materials and methods

3.2.1 Materials

In this chapter, timethylene-1,3-bis (dodecyldimethylammonium bromide); 12-3-12·2Br⁻) was synthesized according to our previous work [192]. Three cinnamate derivatives, *trans-o*-methoxy cinnamic acid (99%), *trans-o*-hydroxycinnamic acid (99%), and *trans*-cinnamic acid (99%) were purchased from TCI Chemical Industry Development Co., Ltd. And we prepared *trans-o*-methoxy cinnamate (*trans*-OMCA), *trans-o*-hydroxyl cinnamate (*trans*-OHCA), and *trans*-cinnamate (*trans*-CA) solutions by mixing *trans*-cinnamic acid with sodium hydroxide (NaOH) at a concentration of 1.1 times that of cinnamic acid into solution. All samples were prepared by ultrapure water from Millipore system. The structures of Gemini surfactant 12-3-12·2Br⁻ and three cinnamate ions *trans/cis*-CA, *trans/cis*-OHCA and *cis*/ *trans*-OMCA are shown in Scheme. 3.1.

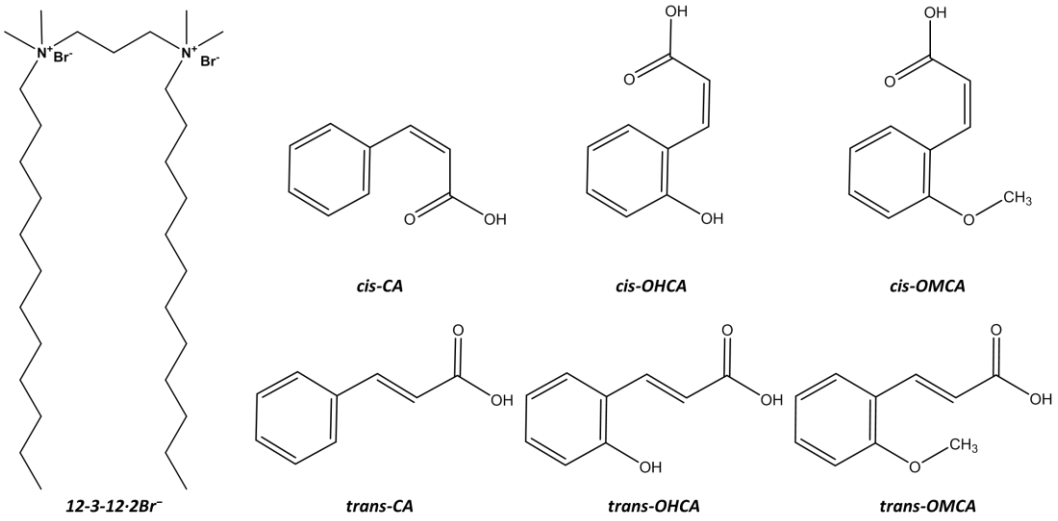

Scheme. 3.1 Structures of Gemini surfactant 12-3-12·2Br⁻ and cinnamate derivatives (*trans/cis*-CA, *trans/cis*-OHCA and *trans/cis*-OMCA)

3.2.2 Preparation of the wormlike micelle solution

Three different wormlike micelles were prepared by mixing 12-3-12·2Br⁻ solution and cinnamate derivative solution to keep the concentration of the Gemini surfactant at 40 mM and the concentration of cinnamates at 24 mM. The prepared solutions were stored at 25°C ± 0.1 for three days.

3.2.3 UV irradiation

The ultra-high pressure short-arc mercury lamp (CHF-XM35-500W) with a 365 nm

optical filter was applied to illuminate the solution to make cinnamate derivatives to photo-isomerize from *trans*-form to *cis*-form. About 3.0g Samples were placed in a 10 ml quartz crucible and stirred continuously at 25 ± 0.1°C in a jacketed beaker connected to a low-temperature thermostat bath. The distance between the samples and the light source was fixed at 20 cm.

3.2.4 High performance liquid chromatography details

High performance liquid chromatography (HPLC) was used to obtain the conversion fraction of the system under UV irradiation. The chromatographic separation was carried out by using ultra performance liquid chromatograph with an C_{18} column (250 × 4.6 mm, 5 μm, Agilent Germany). The temperature of the column was maintained at 25 ± 0.1°C during the analyzing process. 20 μl sample was injected and eluted with the mobile phase 0.1% phosphoric acid solution /acetonitrile = 60/40 in 15 min. The conversion fraction is defined as *f*, which can be calculated by

$$f = \frac{c_i - c_e}{c_i} \tag{3-1}$$

where c_i is the initial concentration of *trans*-isomer and c_e is the equilibrium concentration of *trans*-isomer.

3.2.5 Rheological property measurement

Anton Paar MCR 302 rheometer (Anton Paar, Graz, Austria) was used to measure the steady and dynamic rheological properties of the studied WLM solutions with a cone plate system (CP50-1) with a radius of 50 mm and a taper angle of 1°. Flow curves were measured at a range of shear rate from 0.01 s^{-1} to 1000 s^{-1} and the dynamic frequency sweep was measured with a fixed strain value (γ = 1%) and a frequency of 0.1-100 Hz at 25.0 ± 0.1°C.

3.2.6 Microstructure observation of the micelles by TEM

The microstructure of surfactant aggregates was observed by TEM (Jeol JEM-1400, Japan). Firstly, about 10μL sample was dripped onto the margin of the copper and adsorbed on the copper mesh after a few minutes; the excessive solution was eliminated with filter paper. Subsequently, the sample was negatively stained with phosphotungstate for 5-10s, and the excessive solution was absorbed by filter paper.

3.2.7 Quantitative calculations and force-field parameters

The structures of six *trans/cis*-cinnamate derivatives ions were optimized by Gaussian 09 quantum chemistry packages through a hybrid functional B3LYP at the 6-311+g (d, p) level. The optimized structures will be used as initial structures of MD simulations and to calculate

the molar volume of six *trans/cis*-cinnamate molecules. The electrostatic potential distribution of cinnamate ions were calculated using Multiwfn software packages [193]. The solvation free energy of cinnamate ions were calculated Gaussian 09 at the M052X/6-31G* level. The interaction energies of the packing pattern between 12-3-12^{2+} and *trans/cis*-cinnamates were obtained using 6-311g+** basis set with B3LYP functional in SMD solvation model.

Since the force field GROMOS96 45a3 [173] has been proved to be in good agreement with the experimental data in many surfactant micellar systems [194], we adopted GROMOS96 45a3 forcefield in all our molecular simulations. We optimized the initial structure and generated the coordinates of 12-3-12^{2+} (Fig. 2.1(a)) and *trans/cis*-cinnamate ions using Gaussian 09. The force field parameters for 12-3-12^{2+}, *trans/cis*-CA, *trans/cis*-OHCA were generated by the ATB server. The dihedral angle information of *trans/cis*-cinnamate ions were obtained from Heerdt's literature [168] which had been well estimated by DFT calculations. As to *trans/cis*-OMCA, the corresponding parameters can be found in our previous work [194].

3.2.8 Simulation details

The box size of the pure 12-3-12·2Br$^-$ surfactant molecule was set to 7.5×7.5×12 nm^3. For the cinnamates and 12-3-12·2Br$^-$ surfactant system, the cuboid box size in MD simulations was set to 7.5×7.5×24 nm^3 in order to fully show the wormlike micelle. Periodic boundary conditions were set in all three dimensions. In all our simulation systems, the concentration of 12-3-12·2Br$^-$ was approximately 0.23 mol/L, which is far above the CMC (0.91 mM) of 12-3-12·2Br$^-$ in aqueous solution [195]. For the pure 12-3-12·2Br$^-$ system, 90 12-3-12·2Br$^-$ surfactant molecules were dissolved in 19834 water molecules. For the cinnamates and 12-3-12·2Br$^-$ surfactant mixed system, the number of 12-3-12·2Br$^-$ molecules was fixed at 180 and the number of *trans/cis*-cinnamate ions was defined according to their conversion fractions that obtained by experiment (HPLC). All the surfactants and cinnamates were arranged randomly with approximately 37000 water molecules using Packmol. Corresponding number of counter ions of Br$^-$ and Na$^+$ were added in the box in a random assignment as well to maintain the charge equilibrium of the system. The simulation details of our systems are displayed in Table 3.1.

Table 3.1 Number of 12-3-12^{2+}, Br^-, cinnamate derivatives, Na^+ ions and water molecules in simulation box.

System	12-3-12^{2+}	Br^-	*cis/trans*-isomers	Na^+	H_2O
12-3-12^{2+}					
1	90	180	0/0	0	19834
12-3-12^{2+} + OMCA					
2	180	360	0/135	135	38233
3	180	360	32/103	135	38295
4	180	360	88/47	135	38230
5	180	360	118/17	135	38227
12-3-12^{2+} + OHCA					
6	180	360	0/135	135	38253
7	180	360	32/103	135	38290
8	180	360	88/47	135	38330
12-3-12^{2+} + CA					
9	180	360	0/135	135	38397
10	180	360	32/103	135	38327

The MD simulations were preformed using GROMACS 2018 software packages. The constant temperature of 298.15 K and the constant pressure of 1 bar were kept by Berendsen bath coupling scheme. Semi-isotropic pressure coupling was conducted in order to simulate rod-like and wormlike micelles. The simulation box was independently scaled in z- direction but was isotopically scaled in x- and y- directions. The time step was 2 fs in all simulations. The SPC water model was employed. The trajectories were saved every 2ps. For all the system, the simulation time is 100ns. The short-range electrostatic cutoff and short-range Van der Waals cutoff were set to 1.0 nm, and the long-range electrostatic interactions were set to 0.12 nm by PME (Particle Mesh Ewald) method. Bonds were constrained using LINCS (Linear Constraint Solver) algorithm. VMD 1.9.2 was employed to visualize and display the trajectories and configurations of simulated system.

3.2.9 PMF calculation details

Six pre-assembly spherical micelles containing 32 12-3-12·2Br^- and 32 cinnamates at initial and equilibrium states (32 *trans*-CA for f = 0, 24 *trans*-CA and 8 *cis*-CA for f = 0.24, 32 *trans*-OHCA for f = 0, 11 *trans*-OHCA and 21 *cis*-OHCA for f = 0.65, 32 *trans*-OMCA for f = 0, 4 *trans*-OMCA and 28 *cis*-OMCA for f = 0.88, respectively) were constructed by Packmol software and put in the box with the size of 6nm × 6nm × 12nm. Approximately 13000 water

molecules by the SPC water model were added into boxes. The steepest descent of energy minimization was used. Then the MD simulation were carried out in NPT ensemble at 298.15 K and 1 atm for 50 ns with the time step of 2 fs for six systems. Periodic boundary conditions were applied in three dimensions. The temperature and pressure were controlled by the Berendsen bath coupling scheme. Interactions were subjected to a cutoff distance of 1 nm where the long-range electrostatic interactions were set to 0.12 nm using the Particle Mesh Ewald technique. In the pulling process, the motion of micelles was restricted to maintain their initial configuration. A harmonic umbrella potential with a force constant of 1000 Kcal· mol^{-1}·nm^{-2} was applied between the COM of the spherical micelle and a 12-3-12^{2+} ion using pull code. Umbrella sampling simulations were carried out in 25 different windows ranging from 1.5nm to 6.5nm with a sequential stepwise reduction by 0.2nm. The MD simulation time for each window was 10 ns. The PMF was calculated from the sample windows using the Weighted Histogram Analysis Method which are implemented by g_wham command in GROMACS.

3.3 Results and Discussions

3.3.1 Photo-responsive behavior of the 12-3-12·2Br^-/cinnamates mixed systems

In order to investigate the effect of the ortho substituents of the photosensitive molecules on the photo-responsive behavior of the photo-responsive fluids, three different wormlike micelles were constructed (40 mM 12-3-12·2Br^-/24 mM cinnamates), and the photo-responsiveness of the studied wormlike micelles were investigated by observing the structure transition induced by UV irradiation. The microstructures of the aggregates that undergone different UV irradiation time were obtained through TEM. As shown in Fig. 3.1, the system containing 40 mM 12-3-12·2Br^-/24 mM *trans*-CA initially performs an entangled and dense network structure of wormlike micelles. After 160 min UV irradiation, the structure of micelles does not change significantly. As for the system of 40 mM 12-3-12·2Br^-/24 mM *trans*-OHCA, the wormlike micelles entangle with each other and form a denser and flexible network structure before UV irradiation. However, the intertwined network structures begin to unravel and become loose after 160 min UV irradiation. For 40 mM 12-3-12·2Br^-/24 mM *trans*-OMCA, the surfactant molecules firstly form long and entangled wormlike micelles, while after the 160 min UV irradiation, the wormlike micelles transform into the short rod-like micelles and even spherical micelles.

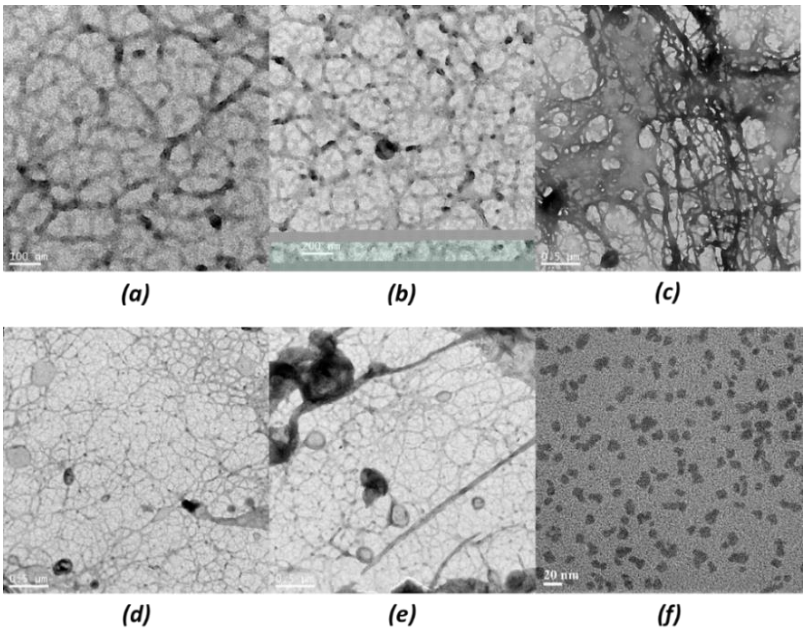

Fig. 3.1 TEM images of the sample of 40 mM 12-2-12·2Br⁻/24 mM *trans*-cinnamates at 25°C under different UV irradiation time [(a) *trans*-CA, 0 min; (b) *trans*-CA, 160 min; (c) *trans*-OHCA, 0 min; (d) *trans*-OHCA, 160 min; (e) *trans*-OMCA, 0 min; (f) *trans*-OMCA, 160 min].

The rheological property variation is the most significant reflection of the morphology and structure transition of surfactant aggregates. In order to explore the morphological changes of the wormlike micelles after UV irradiation, the steady shear viscosity and dynamic viscoelastic behavior of 40 mM 12-2-12·2Br⁻/24 mM cinnamates were studied in detail. All systems composed of 40 mM 12-2-12·2Br⁻/24 mM cinnamates reached equilibrium after 160 min UV irradiation. Fig. 3.2 shows the steady shear curves and dynamic viscoelastic modulus of 40 mM 12-3-12·2Br⁻/24 mM *trans*-cinnamates undergoing different UV irradiation time. Generally, it can be seen from Fig. 3.2 (a), (b), and (c) that the viscosity of the studied photo-responsive fluids shows a plateau at lower shear rates while exhibits a shear-thinning phenomenon in the higher shear rate region before UV illumination, which prove that the studied system is composed by typical wormlike micelles [196]. As for the dynamic frequency sweep measurement, the viscoelastic modulus of these wormlike micellar solutions exhibits a typical Maxwell behavior [197], which can be depicted by following equations.

$$G'(\omega) = G_0 \frac{\omega^2 \tau_R^2}{1+\omega^2 \tau_R^2} \tag{3-2}$$

$$G''(\omega) = G_0 \frac{\omega \tau_R}{1+\omega^2 \tau_R^2} \tag{3-3}$$

$$G_0 = 2G^* \tag{3-4}$$

Here G' is the elastic modulus, G'' is the viscous modulus. ω is the angular frequency. The relaxation time τ_R is calculated by $1/\omega_c$, where ω_c is the angular frequency at the intersection of

G' and G''. G_0 is the elastic plateau modulus value at higher ω. If G' does not reach an apparent plateau value at higher frequency, the estimation of G_0 can be calculated from equation (3-4), where G^* is the G' at ω_c.

For the 12-3-12·2Br⁻/*trans*-CA system, the zero-shear viscosity (η_0, the viscosity at plateau) decreases from 1.1 Pa·s to 0.74 Pa·s after 160 minutes UV irradiation. In addition, the elastic modulus (G') and viscous modulus (G'') curves of 12-3-12·2Br⁻/*trans*-CA (Fig. 3.2(d)) show an inconspicuous change before and after 160 min UV irradiation, suggesting the imperceptible changes of the viscoelasticity and further the morphology of the wormlike micelles after UV irradiation. These rheological results suggest that the photo-responsiveness of wormlike micelles formed in 12-3-12·2Br⁻/*trans*-CA system is almost negligible. However, for the system containing *trans*-OHCA, the phenomenon of shear-thinning still exists while the η_0 is significantly reduced from 19.7 Pa·s to 2.63 Pa·s after undergoing 160 min UV irradiation. Regarding the dynamic viscoelastic behavior, it can be seen that the frequency at intersection of curves for the variation of G' and G'' with frequency increase gradually with the prolonging of UV irradiation time. Obviously, the relaxation time of the wormlike micelles decrease, indicating the weakening of the network structure [198]. In terms of the wormlike micelles containing *trans*-OMCA, the shearing-thinning phenomenon becomes more and more subtle and tends to disappear with UV irradiation and the intersection of G' and G''disappears gradually (at 80 minutes). This may be due to the transition of wormlike micelles to shorter rod-like micelles and even spherical micelles after UV irradiation.

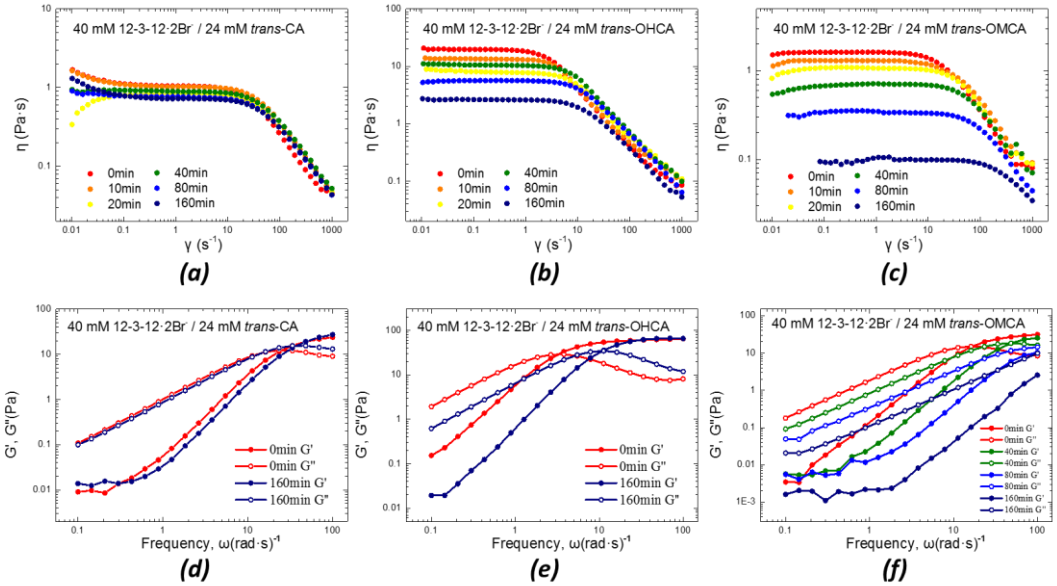

Fig. 3.2 Steady shear viscosity curves (*trans*-CA (a), *trans*-OHCA (b), *trans*-OMCA (c)) and the dynamic viscoelastic modulus (*trans*-CA (d), *trans*-OHCA (e), *trans*-OMCA (f)) of the systems of 40 mM 12-3-12·2Br⁻/24 mM cinnamates with different UV irradiation time at 25°C

For providing the more intuitive changes of wormlike micelles, some structural parameters of wormlike micelles were calculated according to the following equations [199].

$$\frac{G_0}{G''_{\min}} = \frac{L}{L_e} \tag{3-5}$$

$$L_e = \frac{\xi_M^{5/3}}{L_P^{2/3}} \tag{3-6}$$

$$\xi = \left(\frac{k_B T}{G_0'}\right)^{1/3} \tag{3-7}$$

L is the average extension length. L_e is the entanglement length between two entanglements. G''_{min} represents the minimum value of G'' at higher frequency; ξ refers to hydraulic correlation length (representing the mesh size of micelle network); L_p is the persistence length of micelles, $L_p \approx$ 15-20 nm [200]; k_B is Boltzmann constant ($k_B = 1.3806 \times 10^{-23}$ J/K); T is Kelvin temperature. According to these equations, the L and L_e values of wormlike micelles with different UV irradiation time were obtained and showed in Table 3.2. Obviously, after 160 min of UV irradiation, the length of the wormlike micelles containing *trans*-CA was slightly reduced from 289-350 nm to 213-258 nm, while the wormlike micelles containing *trans*-OHCA witness a sharp drop in length from 548-663 nm to 347-420 nm after 160 min UV illumination. The reduction in length of wormlike micelles containing *trans*-OMCA is the most significant (from 355-430 nm to 167-202 nm). the wormlike micelles almost fission within 40 min UV irradiation, which is confirmed by the disappearance of the intersection of G' and G''. Obviously, the sensitivity of the wormlike micelles to UV irradiation is *trans*-OMCA > *trans*-OHCA > *trans*-CA. The rheological results are in good agreement with the TEM images.

Table 3.2 Variation of rheological parameters of the wormlike micelle constructed by 40 mM 12-3-12·2Br$^-$/24 mM *trans*-cinnamates with the prolongation of UV irradiation time at 25 °C.

	UV time (min)	G^* (Pa)	G_0' (Pa)	G''_{min} (Pa)	ω_c (rad/s)	τ (s)	ξ	L_e(nm)	L(nm)
CA	0	12.2	23.8	9.1	25.1	0.040	5.6×10^{-8}	110-133	289-350
	160	38.1	27.4	13.1	15.5	0.064	5.4×10^{-8}	102-124	213-258
OHCA	0	28.9	64.7	7.5	3.3	0.31	4.0×10^{-8}	63-77	548-663
	160	33.8	65.6	11.9	10.6	0.094	4.0×10^{-8}	63-76	347-420
OMCA	0	15.2	31.4	8.4	17.5	0.057	5.1×10^{-8}	95-115	355-430
	40	18.0	25.5	16.2	48.4	0.021	5.5×10^{-8}	106-129	167-202

3.3.2 The photo-isomerization kinetics of the cinnamates

In order to explore the intrinsic reason for the difference of the photo-responsive behaviors of the studied three cinnamates, the photo-isomerization reaction kinetics of these cinnamates were studied firstly. To ensure that the *trans*-isomers are converted to *cis*-isomers as much as possible, the solution for constructing worm like micelles originally was diluted 1000 times (40 μM 12-3-12·2Br$^-$/24 μM *trans*-isomer) The UV-Vis absorption spectrum and high performance liquid chromatography (HPLC) were applied to obtain the conversion fraction. The HPLC results are shown in Fig. 3.3. From the ratio of peak height before and after UV irradiation, we can obtain the equilibrium conversion fractions *f* of *trans*-CA, *trans*-OHCA and *trans*-OMCA are 0.24, 0.65 and 0.88.

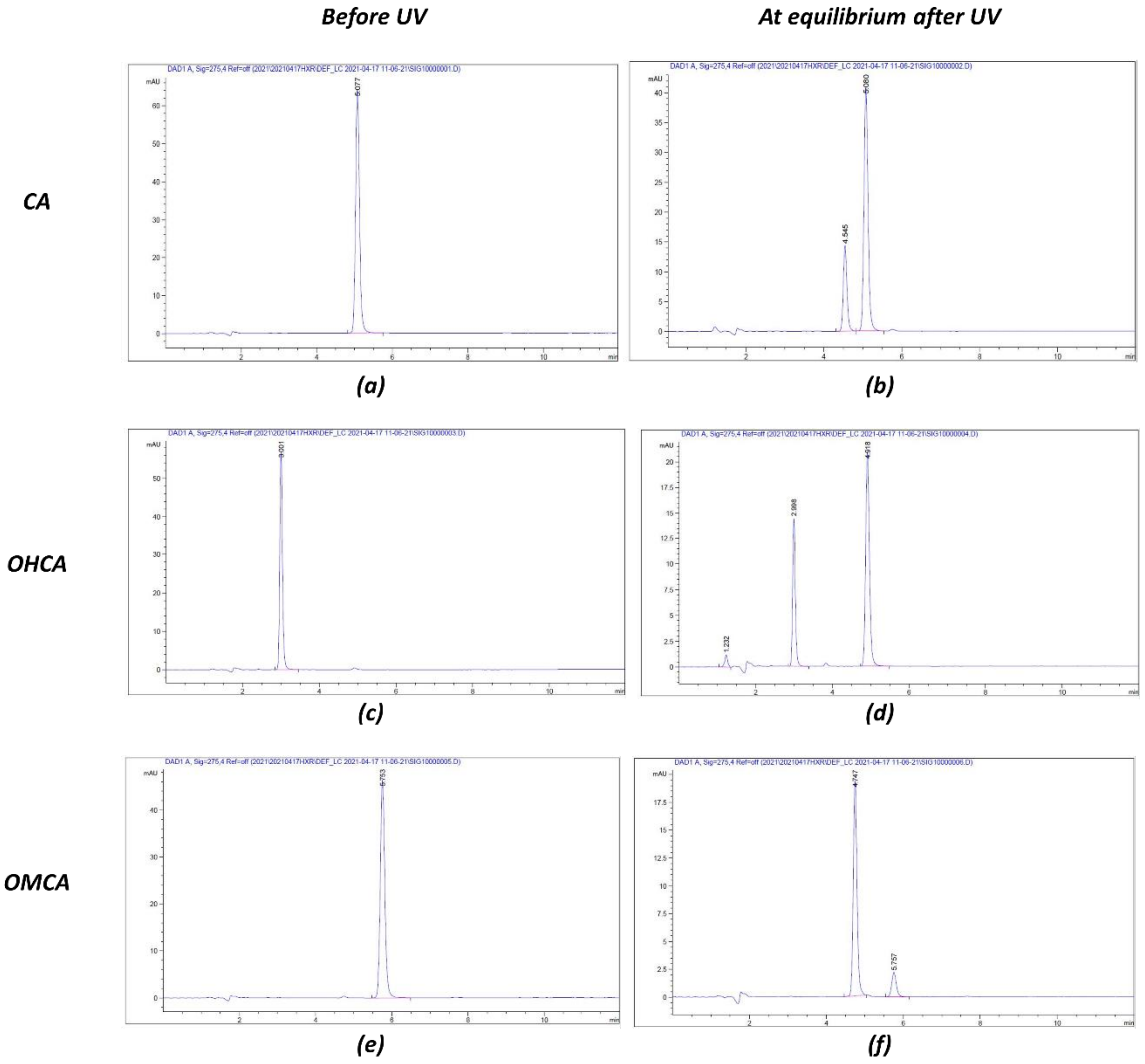

Fig. 3.3 High performance liquid chromatography spectra of three cinnamate derivatives before UV-irradiation and in equilibrium state after UV irradiation.

After we know the equilibrium conversion fraction of the cinnamates, the variation of conversion fraction with time can be plotted. Fig. 3.4 provides the variation of conversion

fraction for different cinnamates with UV irradiation time and the corresponding kinetic curves. From our previous work [211], the photo-isomerization reaction of cinnamates usually follows the law of the first order opposite reaction. Therefore, we plotted the variation of $ln\frac{c_i-c_e}{c_i-c_e-c}$ with time and found that these points are perfectly comply with the law of the first order opposite reaction. Then a linear fit was used to fit these kinetic curves to obtain the slopes (k_1+k_{-1}) so that the reaction equilibrium constant (K_c), forward rate constant (k_1) and reverse rate constant (k_{-1}) can be calculated by the following equations.

$$K_c = \frac{c_e}{c_i - c_e} \tag{3-8}$$

$$K_c = \frac{k_1}{k_{-1}} \tag{3-9}$$

These kinetic parameters are provided in Table 3.3. As shown in Table 3.3 and Fig. 3.4, it can be seen that the order of f and K_c is *trans*-OMCA (f = 0.88, K_c = 7.33) > *trans*-OHCA (f = 0.65, K_c = 1.88) > *trans*-CA (f = 0.24, K_c = 0.31). This confirms our experimental results that *trans*-OMCA experience a dramatic morphology transition from wormlike micelle to rod-like micelle even spherical micelle whereas the micelle length of *trans*-OHCA and *trans*-CA is just shortened under long enough UV irradiation.

For the kinetics of the three photo-isomerization reactions, the order of k_1 is *trans*-OMCA (1.09) > *trans*-OHCA (0.12) > *trans*-CA (0.006), indicating that at same concentration of *trans*-cinnamate, the forward photo-isomerization reaction rate of *trans*-OMCA is the fastest. This is consistent with the experiment results of the highest morphological transition rate and micellar shortening rate of *trans*-OMCA.

It is reported that among the many factors of affecting the kinetic of photo-isomerization reaction of the cinnamates, the existence of the lone-pair electrons should have a positive effect in lowering the energy barrier of the double bond rotation, thereby accelerating the photo-isomerization reaction rate [211]. That is why the conversion velocity of the *trans*-OMCA and *trans*-OHCA with lone-pair electrons on the oxygen atom of the methoxy group and hydroxyl group next to the aromatic ring are higher. Besides, the methoxy group in benzene ring may benefit to lower the energy barrier of the rotation potential of the double bond more than hydroxyl group. Obviously, the photo-responsive behavior of the system not only related to the photochemical reaction rate directly but also depends on the change of the molecular geometry before and after UV irradiation. To further explain the mechanism of the photo-responsive behavior of the micelles at a microscopic level, the MD simulations and quantitative calculations are needed.

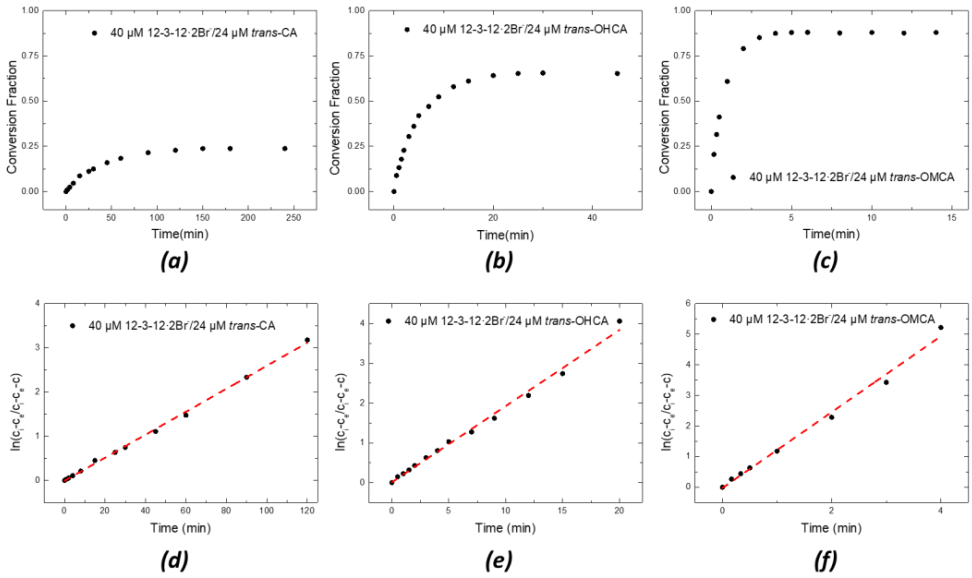

Fig. 3.4 Conversion fraction curves with UV irradiation time ((a), (b), (c)) and kinetic curves ((d), (e), (f)) of 40 μM 12-3-12·2Br⁻/24 μM *trans*-cinnamates ((a), (d) *trans*-CA, (b), (e) *trans*-OHCA, (c), (f) *trans*-OMCA)) at 25°C.

Table 3.3 The conversion fraction *f*, the slope (k_1+k_{-1}) of the kinetic curve, reaction equilibrium constant (*Kc*), forward rate constant (k_1) and reverse rate constant (k_{-1}) of the photo-isomerization reaction of *trans*-CA, *trans*-OHCA and *trans*-OMCA at 25°C.

	CA	**OHCA**	**OMCA**
f	0.24	0.65	0.88
k_1+k_{-1}	0.026	0.19	1.24
K_c	0.31	1.88	7.33
k_1	0.006	0.12	1.09
k_{-1}	0.020	0.07	0.15

3.3.3 Micelles of pure 12-3-12·2Br⁻ in water

To better understanding the complex photo-responsive behaviors of the assemblies containing 12-3-12·2Br⁻ and different cinnamates, it is necessary to study the self-assembly behavior of single 12-3-12·2Br⁻ in water. It is well known that different concentrations of 12-3-12·2Br⁻ surfactant will form aggregates with different morphologies [207]. As the concentration of 12-3-12·2Br⁻ increases, morphologies with larger scale and much more aggregation number can be found. Fig. 3.5 shows the snapshots of the initial and final configuration of single 12-3-12·2Br⁻ simulation box. From Fig. 3.5, it can be found that the randomly assignment 90 12-3-12·2Br⁻ molecules finally form three spherical micelles after 100 ns MD simulation. The average aggregate number is 30, which is in good agreement with the

experimental value 32 [201]. This confirmed that GROMOS96 45a3 forcefield and our simulation parameters are feasible.

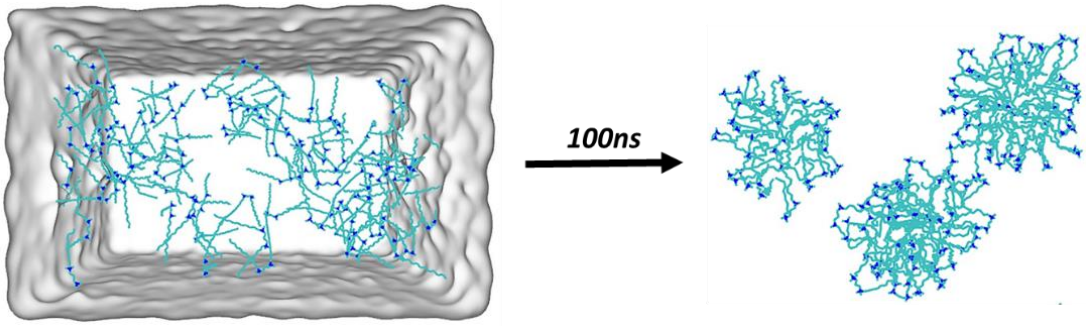

Fig. 3.5 Snapshots of the initial and final configuration of pure 12-3-12·2Br$^-$ surfactants. (The cyan molecules are 12-3-12^{2+}; the transparent parts are water; for clarity, Br$^-$ ions are not shown.)

3.3.4 Self-assembly behavior of 12-3-12·2Br$^-$ and cinnamates in water

Due to the electrostatic interaction between polar head of surfactants and counter ions in solution, 12-3-12·2Br$^-$ micelles will display a more complex morphology in the presence of counter ions with hydrophobic structure [196-197]. Fig. 3.6 displays snapshots of the initial simulation box and final micelle morphologies (12-3-12^{2+} / cinnamate derivatives = 180:135) at different conversion fraction after 100ns simulation at 298.15K. It can be seen from Fig. 3.6, after 100 ns MD simulation, the 12-3-12^{2+} ions with *trans*-cinnamates all form a wormlike morphology from a random arrangement. After enough UV light, the photo-isomerization of *trans*-CA reaches equilibrium at f = 0.24 (equilibrium conversion of *trans*-CA). The micelle containing *trans*-CA hardly changes and maintains the wormlike shape after 100 ns simulation. This result means the mixed micelles containing *trans*-CA will still maintain the morphology of worm micelles and will never be transformed into rod-like or spherical micelles after being exposed to infinite ultraviolet light. For system containing *trans*-OHCA, when f = 0.24, the wormlike micelle starts to rupture and finally appears the coexistence of short rod-like and spherical micelle at f = 0.65 (equilibrium conversion of *trans*-OHCA). This phenomenon suggests that the long and twined wormlike micelles constructed by 12-3-12·2Br$^-$ and *trans*-OHCA have the potency to transform into rod-like and spherical micelles after being exposed to enough ultraviolet light. For *trans*-OMCA system, the shape of wormlike micelle remains when f = 0.24. The wormlike micelle splits into rod-like micelles once f reaches to 0.65. After long enough UV irradiation (equilibrium conversion of *trans*-OMCA f = 0.88), the micelles will eventually transform into spherical micelles.

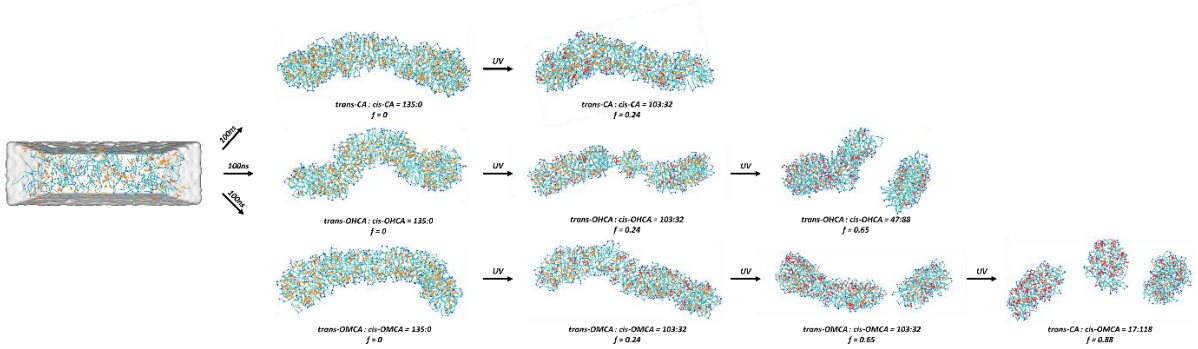

Fig. 3.6 Snapshots Snapshots of the initial simulation box and corresponding micelle morphologies of 12-3-12^{2+} / cinnamate derivatives = 180:135 at different conversion fraction after 100 ns simulation at 298.15 K. (The cyan parts are 12-3-12^{2+}; the orange parts are *trans*-isomers; the red parts are *cis*-isomers. For clarity, water, Br^- and Na^+ are not shown.)

In order to confirm these special morphologies, the density profiles along z axis of these micelles were calculated and shown in Fig. 3.7. Obviously, before UV irradiation the wormlike micelle is formed represented by the corona-shape curves of 12-3-12^{2+}. After UV irradiation, the variation of density distributions of 12-3-12^{2+} in three systems are the same as the micelle transition tend. The density distribution curve of CA system maintains the corona-shape at f = 0.24. The corona-shape of density distribution curve for OHCA fission into a small corona-shape peak and a sharp peak at f = 0.65. The sharp peak and the small corona-shape peak of 12-3-12^{2+} in curves reconfirms the morphology of short rod-like micelle and spherical micelle. Three sharp peaks appear at f = 0.88 for OMCA, implying the formation of three spherical micelles. Obviously, the photo-responsive behavior of three *trans*-cinnamate is successfully simulated. These special morphologies in our simulation are in good agreement with our TEM experiments that wormlike micelles containing *trans*-OMCA and *trans*-OHCA will gradually break into smaller aggregates, while wormlike micelles containing *trans*-CA can still maintain initial shape at equilibrium even undergoing long enough UV irradiation.

Based on all the above experimental results, it can be preliminarily concluded that the photo-responsiveness of the system containing cinnamates is derived from the photo-isomerization rate and the equilibrium conversion fraction of *trans*-CA. In order to study the photo-responsive behavior more systematically, further simulation and calculation such as critical packing parameter, packing patterns, potentials of mean force, potential distribution and so forth were performed and discussed in the following sections

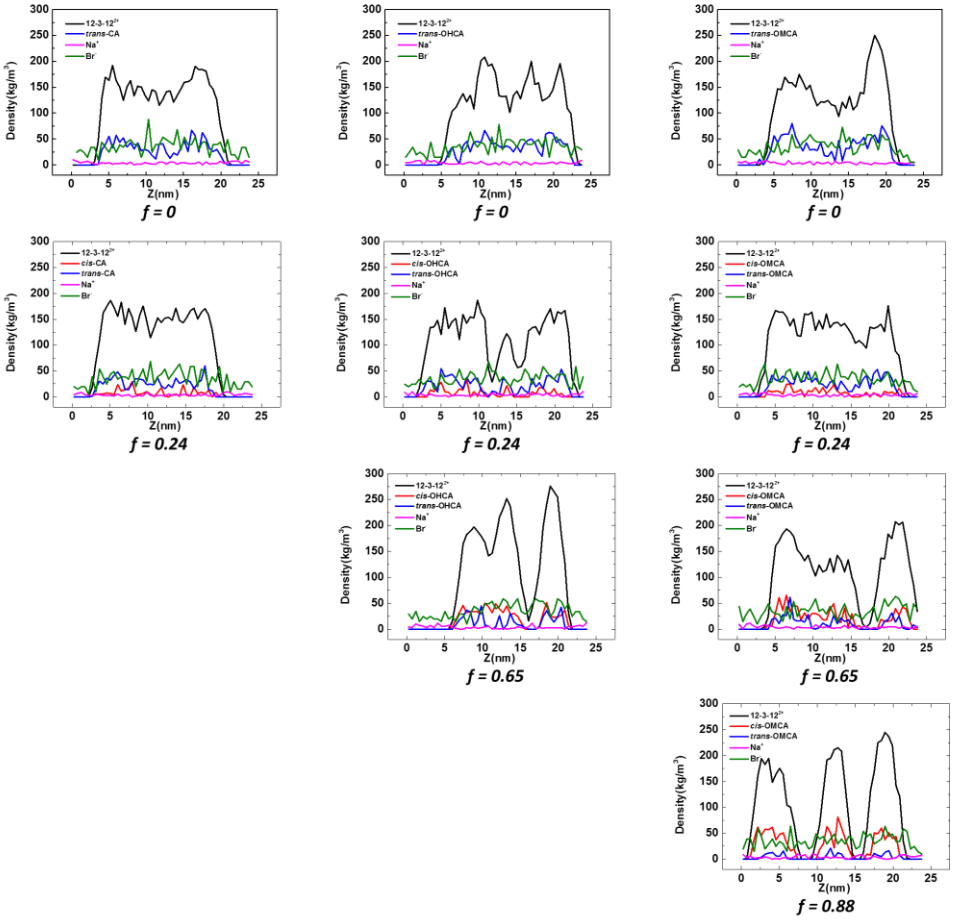

Fig. 3.7 The density distributions of 12-3-12^{2+}, cinnamate derivatives, Na^+, Br^- along z axis in systems at different *f*.

3.3.5 Critical packing parameter of the micelles

The systems undergo different UV irradiation time present different morphologies. To explore the difference of micelles containing *trans/cis*-cinnamates, some important parameters of the micelles were calculated and shown in Table 3.4. The critical packing parameter [2] is a significant parameter of determining the micelle morphology. As shown in Table 3.4, the *P* values of the micelles containing CA at $f = 0$ and 0.24 (0.48 and 0.40) imply that the wormlike micelles are the relatively stable and favorable morphology at $f = 0$ and 0.24. For the micelles containing *trans*-OHCA, with the increase of *f*, the *P* values decrease though still locate in the region of 0.33~0.5. This maybe the reason for the length of wormlike micelles containing *trans*-OHCA are shorten under the UV irradiation. The wormlike micelles containing *trans*-OMCA witness the same tendency as wormlike micelles containing *trans*-OHCA, while at $f = 0.88$, the *P* is reduced to 0.29 ($P \leq 0.33$), correspondingly that the wormlike micelles transformed into spherical micelles. In our simulation, the *P* values are very consistent with TEM images in Fig. 3.1.

Table 3.4 Geometric information of micelles and interaction energy between 12-3-12^{2+} and *cis/trans*-isomers after system equilibrium in MD simulations: V, volume (nm^3) of the last frame; a_{pho}, hydrophobic (nm^2), a_{phi}, hydrophilic (nm^2) and a_{tot}, total (nm^2) surface areas of the last frame; l, the length of alkyl chain (nm); *P*; E_{coul}, coulomb interaction energy (kJ/mol); E_{LJ} Lennard-Jones interaction energy (kJ/mol); E_{tol}, total interaction energy.

System	*f*	V	a_{pho}	a_{phi}	a_{tot}	l	*P*	E_{coul}	E_{LJ}	E_{tol}
trans-CA	0	182.1	167.7	319.5	487.2	1.2	0.47	-11571.4	-10810.4	-22381.8
	0.24	154.4	178.4	322.2	500.6	1.2	0.40	-11523	-10659.7	-22182.7
trans-OHCA	0	170	178	327.2	505.2	1.2	0.43	-10729	-10899.1	-21628.1
	0.24	159.3	199.5	333.9	533.4	1.2	0.40	-10539.3	-10780.2	-21319.5
	0.65	130.1	205.2	318.7	523.9	1.2	0.34	-10230.2	-10648.9	-21879.1
trans-OMCA	0	183.1	154.2	335.5	489.7	1.2	0.45	-11827.1	-12739.6	-24566.7
	0.24	166.1	172.4	323.2	495.7	1.2	0.43	-11709.6	-12536.4	-24246
	0.65	139.6	187	330.8	517.8	1.2	0.35	-11361.9	-12190.6	-23552.5
	0.88	101.6	208.8	317.3	526.1	1.2	0.27	-11211.3	-12063.6	-23274.9

3.3.6 The energy difference in micelles transition

The relative energy and its variation can estimate the stability of the micelles and illustrate the mechanism of the micelle transformation. The interaction energies among 12-3-12^{2+} and cinnamate derivatives in system at different *f* are calculated by g_energy in Gromacs. The curves of the interaction energy with simulation time are displayed in Fig. 3.8. It can be seen from Table 3.4 that the absolute values of the coulomb interaction energy, Lennard-Jones interaction energy as well as total interaction energy all decrease with the increases of *f*, indicating that the electrostatic interaction energy and van der Waals interaction between 12-3-12^{2+} and cinnamate derivatives become weaker after UV irradiation, which cause the fission of the micelles.

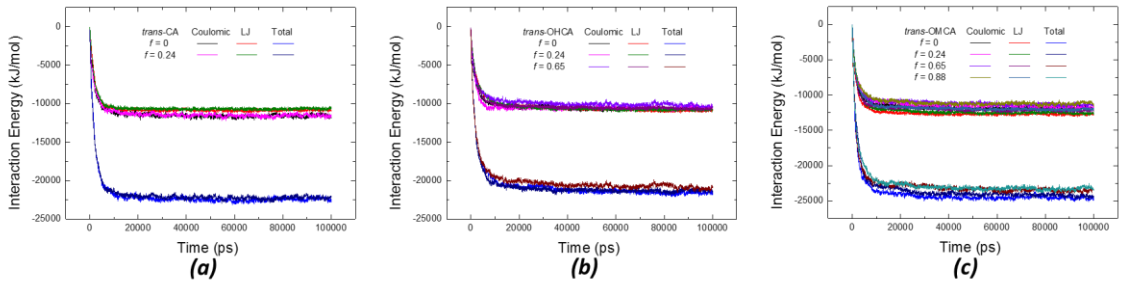

Fig. 3.8 The interaction energy (Coulombic, LJ and total interaction energy) between 12-3-12^{2+} and cinnamate (*cis*-isomers and *trans*-isomers) in the system calculated by g_energy at different *f* with simulation time (a) *trans*-CA; (b) *trans*-OHCA; (c) *trans*-OMCA.

Subsequently, we used umbrella sampling method to calculate potentials of mean force (PMF) versus pulling distance during the process of pulling out a 12-3-12^{2+} ion from a pre-assembled spherical micelle composed of 32 12-3-12^{2+} ions and corresponding number of three cinnamates at initial and equilibrium *f*. ΔPMF represents the energy of pulling a 12-3-12^{2+} ion from the initial position to the infinity. Fig. 3.9 displays the variation of PMF for pulling out a 12-3-12^{2+} ion from a pre-assembled spherical micelle at initial state ($f = 0$) and equilibrium state. As shown in Fig. 3.9, the ΔPMFs decrease for all the cinnamates when the systems are at equilibrium conversion fraction under UV irradiation, implying that it is easier to pull out a 12-3-12^{2+} from the spherical micelle after UV irradiation. This can be attributed to the weaker association between 12-3-12^{2+} ions in micelle with the photo-isomerization of *trans*-isomer.

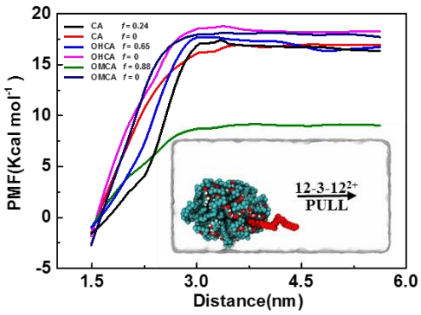

Fig. 3.9 Potentials of mean force (PMF) of pulling out a 12-3-12^{2+} ion from a pre-assembled spherical micelle at conversion fraction $f = 0$, 0.24 for *trans*-CA; $f = 0$, 0.65 for *trans*-OHCA; $f = 0$, 0.88 for *trans*-OMCA.

3.3.7 Packing patterns between cinnamate derivatives and 12-3-12^{2+}

The photo-responsive behavior and the corresponding difference of three wormlike micelle systems has been revealed to a certain extent during our simulation process. However, to fully understand how these *trans/cis*-isomers affect the stability and the morphology of micelle, the radial distribution functions between the N_1 atoms of different 12-3-12^{2+} in system ($g_{N_1\text{-}N_1}(r)$ in Fig. 3.10) as well as that between the N_1 atom of 12-3-12^{2+} and the C_3 atom of the cinnamates ($g_{N_1\text{-}C_3}(r)$ in Fig. 3.11) were calculated to explore the packing pattern of species in micelles. As shown in Fig. 3.10, the $g_{N_1\text{-}N_1}(r)$ function curves of containing three cinnamate derivative systems all show three peaks at approximately 0.62, 0.82 and 1.4 nm, indicating the formation of a hexagonal crystalline-like structure [178]. With the increase of *f*, the height of the first peaks ($g_{N_1\text{-}N_1}(r)$) for the systems decreases gradually, indicating the interaction between surfactants become weaker and weaker and leading to a less orderly arrangement of surfactants after the photo-isomerization of cinnamate. Reasonably, the micelles will rupture when the interaction is weak enough.

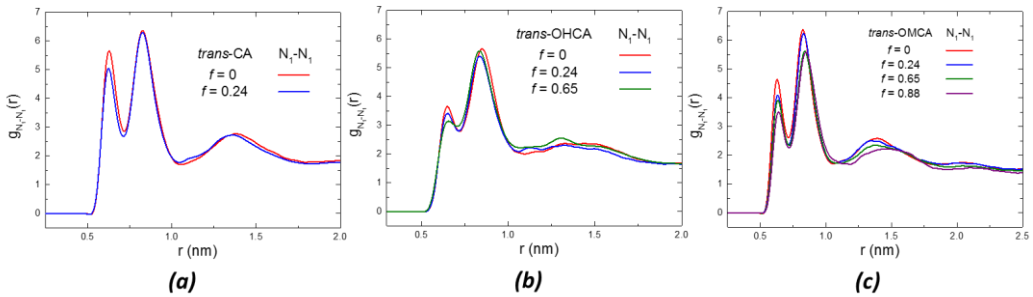

Fig. 3.10 Radial distribution functions $g_{N1\text{-}N1}(r)$ of N_1-N_1 atoms ((a) *trans*-CA (b) *trans*-OHCA (c) *trans*-OMCA) for the system 12-3-12^{2+}/*trans*-cinnamates = 180:135 at different conversion fraction.

For the $g_{N1\text{-}C3}(r)$ curve in Fig. 3.11, the systems containing cinnamate derivatives show the same trend as well. Before UV irradiation, the $g_{N1\text{-}C3}(r)$ has one peak at 0.85 nm, however, a new peak appears at 0.48 nm once *trans*-cinnamates start to photo-isomerization into *cis*-isomers and the height of the new peak gradually increase with the increase of *f*, suggesting that the arrangement between N_1 and C_3 becomes more orderly on micellar surface, which should be attributed to the variation of packing pattern of the species in micelles. The aromatic ring of *trans*-cinnamates is located in the interior of the micelle, far away from the head group of 12-3-12·2Br^- while the aromatic ring of *cis*-isomers is distributed on the surface of micelles, close to the head group of 12-3-12^{2+}, which have been confirmed by subsequent simulation (Fig. 3.12).

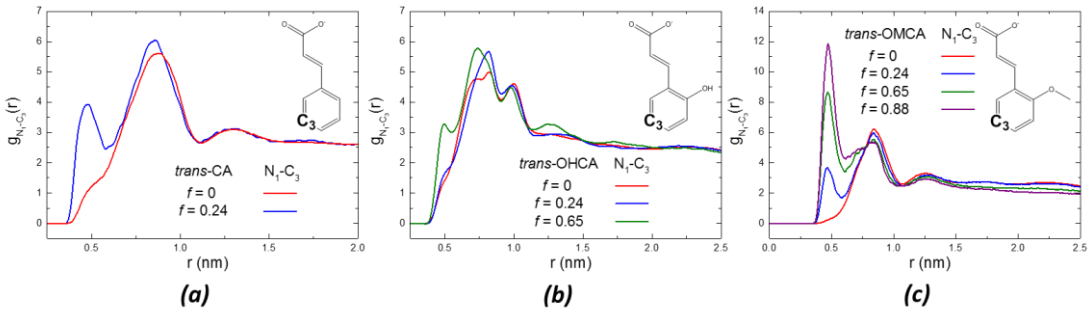

Fig. 3.11 Radial distribution functions $g_{N1\text{-}C3}(r)$ of N_1-C_3 ((a) *trans*-CA (b) *trans*-OHCA (c) *trans*-OMCA) for the system 12-3-12^{2+}/*trans*-cinnamates = 180:135 at different conversion fraction.

Fig. 3.12 displays the representative packing patterns between the cinnamate and 12-3-12^{2+} ions intercepted from micelle. It is obvious that the *cis*-isomer is orient on the surface of the micelles horizontally and its aromatic ring and carboxyl are located close with the head group of 12-3-12^{2+}. The hydroxyl of *cis*-OHCA and the methoxy of *cis*-OMCA insert into the interior of the micelles. While the *trans*-isomer is plugged into the micelle vertically. The aromatic ring of *trans*-cinnamates is embedded into the hydrophobic region formed by surfactant alkyl chains. The carboxyl of *trans*-cinnamates is close to center of the head group

of 12-3-12^{2+}. The existing positions of hydroxyl for OHCA and the methoxy for *trans*-OMCA have unobvious changes in micelles before and after UV irradiation. It is clear that the aromatic rings will flee away from the interior of micelles and orient on the surface of the micelles when the *trans*-cinnamates are photo-isomerized to *cis*-cinnamates. Correspondingly, the packing between *cis*-cinnamates and 12-3-12^{2+} become looser and looser and the long wormlike micelles tend to rupture into rod-like and even spherical micelles.

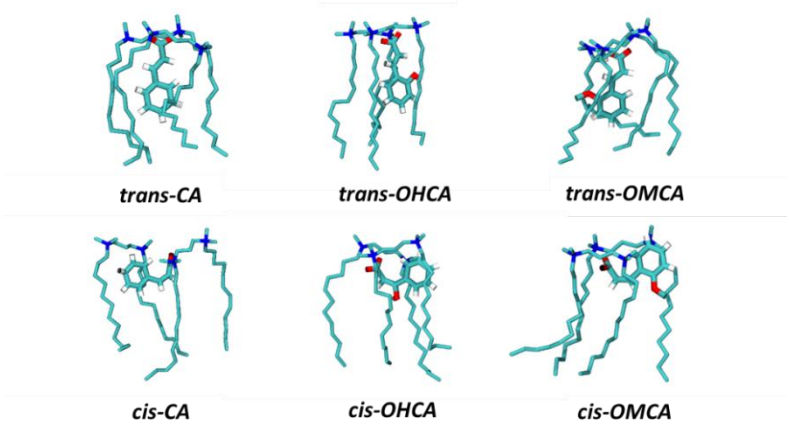

Fig. 3.12 The representative packing patterns between 12-3-12^{2+} and *trans/cis*-cinnamates intercepted from micelles of last frame in MD simulations.

Furthermore, the packing pattern can also be deduced from the solvent-accessible surface area of micelles. Table 3.4 and Fig. 3.13 provide the information of hydrophobic, hydrophilic and total surface areas of aggregates with the variation of *f*. The hydrophobic area increases with *f*, which reconfirmed the hydrophobic aromatic ring of *trans*-isomer is oriented inside the micelles while that of *cis*-isomers is exposed on the surface of micelle.

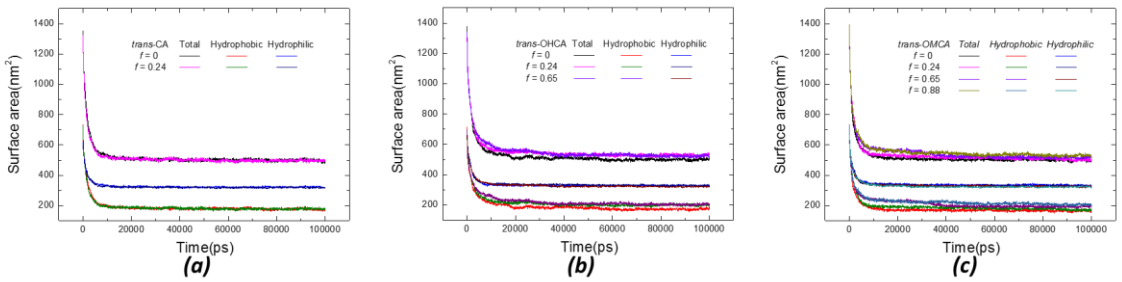

Fig. 3.13 The hydrophobic (a_{pho}), hydrophilic (a_{phi}) and total (a_{tot}) surface areas of aggregates containing 12-3-12^{2+} and cinnamate derivatives at different *f* with simulation time. (a) *trans*-CA; (b) *trans*-OHCA; (c) *trans*-OMCA.

So far, the different numbers of *trans/cis*-cinnamates have been used to represent the different conversion fractions to simulate the system after UV irradiation. The morphological transition process of micelles containing three different cinnamates under UV irradiation was

successfully simulated. *P* and density distributions demonstrate these special micelle morphologies, the interaction energy and the PMFs prove that the micelles containing more *trans*-isomers has higher stability. The aromatic ring of *trans*-cinnamate tends to insert into the hydrophobic region of micelle while that of *cis*-cinnamate apt to orient on the micelle surface. The calculated $g(r)$ and solvent-accessible surface area further provide the packing pattern information of different micelles. However, a more in-depth understanding of these difference quantitatively at atom level is still needed.

3.3.8 The difference in geometry structure of cinnamate derivative molecules

The photo-responsiveness difference of the wormlike micelle containing the cinnamates with different substituents should be attributed to the difference of the molecular properties such as molecule volume, solvation free energy, bond angle, and electrostatic potential distributions before and after UV irradiation. To further explore the distinction between theses cinnamates and how the ortho-substituents affect the photo-isomerization ability, the Gaussian 09 quantum chemistry packages are used on different basis set. Firstly, the structures of *trans/cis*-cinnamates are optimized at b3lyp/6-311+g (d, p) level and shown in Fig. 3.14. From Fig. 3.14, it can be seen that *trans*-cinnamates have a planar structure while the *cis*-cinnamates have a three-dimensional structure. This means that the *trans*-cinnamate is easier to insert into the micelle and the carboxyl of the *trans*-cinnamate is closer to the head group of 12-3-12·2Br^-, thereby forming a denser morphology compared with that of system containing *cis*-cinnamates. The angle α (defined as the dihedral angle between the aromatic ring plane and carbonyl plane) was calculated further. The α values of *trans*-isomers are all 180°, indicating a planar structure. For the *cis*-isomers, the α values are 57.8° (*cis*-CA), 66.1° (*cis*-OHCA) and 66.1° (*cis*-OMCA) respectively. Obviously, the α of *cis*-CA is smaller, implying that the cinnamates ion is more like a plane while the *cis*-OHCA and *cis*-OMCA ions show a significant curvature, indicating that *cis*-OHCA and *cis*-OMCA occupy more space in micelles than *cis*-CA. This can also be proved by the calculated molar volumes**.** Table 3.5 summarizes the corresponding parameters calculated by Gaussian 09. The smallest molar volume of *trans*-OHCA means the smallest steric hindrance, which can explain the tightest arrangement of *trans*-OHCA ions in micelle. The molar volumes of *trans*-isomer for OMCA and OHCA are smaller than that of the *cis*-isomer. This suggests that the space steric of OMCA and OHCA is strengthen after UV irradiation, causing the micelles to become looser and looser until break. All these geometric parameters indicate that after UV irradiation, the arrangement of surfactant in micelle become loose and some *cis*-OHCA and *cis*-OMCA ions can escape from 12-3-12^{2+} layers owing to the increase of steric hindrance after UV irradiation, which maybe the main reason for the higher sensitivity to UV of micelles containing *trans*-OHCA and *trans*-OMCA. The lower sensitivity of system

containing CA ions should be attributed to the decrease of its steric hindrance after UV irradiation and the *cis*-CA ions remain embedded in the 12-3-12^{2+} layers. Obviously, the existence of ortho-substituents enhances the difference of the molecular steric hindrance before and after UV irradiation and strengthen the photo-responsive ability correspondingly. The cinnamate with ortho-methoxy group has better photo-responsive ability than that with ortho-hydroxyl.

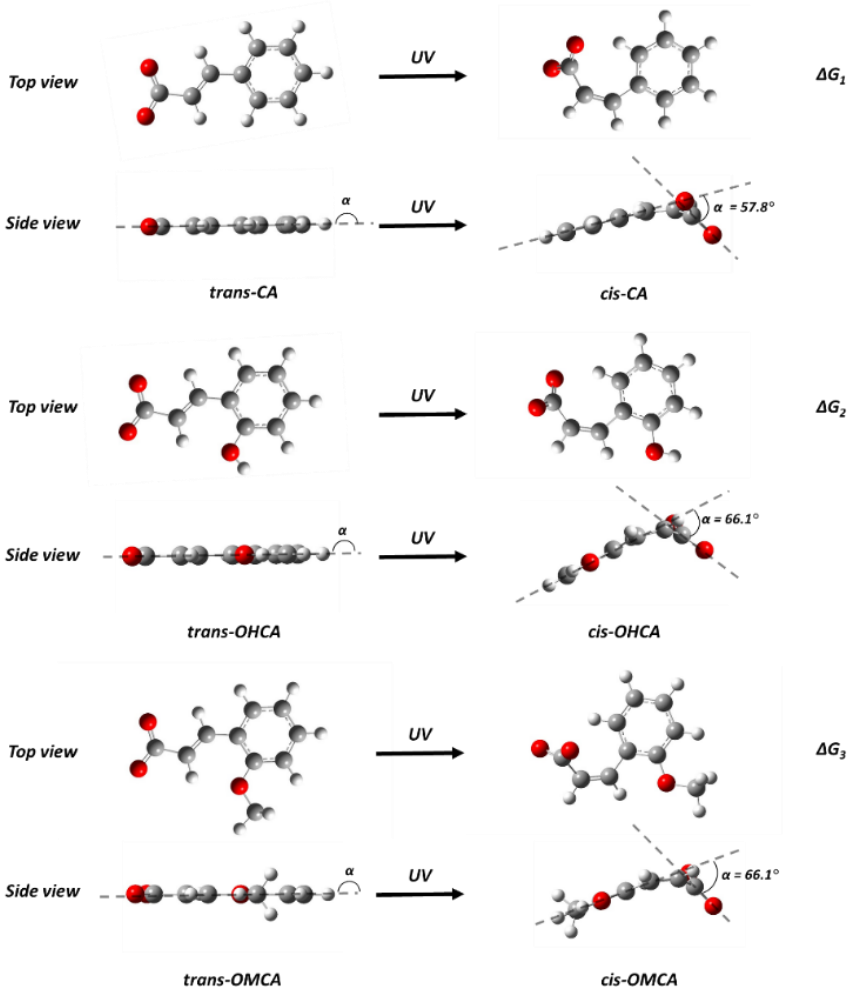

Fig. 3.14 The top view and side view of optimized structures of *trans/cis*-cinnamate ions after being optimized at the b3lyp/6-311+g (d, p) level.

3.3.9 Electrostatic potential distribution of *trans/cis*-cinnamates

The electrostatic potential distributions of these three cinnamate ions have been calculated and shown in Fig. 3.15. It can be seen that the maximum of negative charge is concentrated on the carboxyl group and the minimum of negative charge is concentrated on the aromatic ring. The order of the maximum value of the electrostatic potential is *trans*-OMCA (-7.37 eV) > *trans*-OHCA (-7.36 eV) > *trans*-CA (-7.19 eV), while the electrostatic potential distributions in

trans-OHCA is most uneven owing to the presence of hydroxyl. This indicates that *trans*-OHCA has the strongest electrostatic association with 12-3-12^{2+} which can explain why the wormlike micelles containing *trans*-OHCA have the denser arrangement and the solution has higher viscosity. For *cis*-isomers, the maximum of the electrostatic potential of *cis*-isomers is lower (*cis*-CA (-6.94 eV) < *cis*-OHCA (-7.02 eV) < *cis*-OMCA (-7.04 eV)) and more evenly distributed than *trans*-isomers. Therefore, the weaker electrostatic potential leads to the weaker electrostatic interaction with surfactant and finally causes the formation of loosen micelles. Then the evener electrostatic distribution allows the aromatic ring to stay on the micelle surface other than insert into the surfactant layer. The significant decrease of the electrostatic potential maximum for OHCA and OMCA after UV irradiation endows the system with a better photo-responsive ability. The introduction of hydroxyl and methoxy groups in the adjacent position of cinnamate enlarge the differences of both electrostatic potential of carboxyl group and the uneven distribution of electrostatic potential before and after the UV irradiation, resulting in the higher sensitivity of the system to UV irradiation.

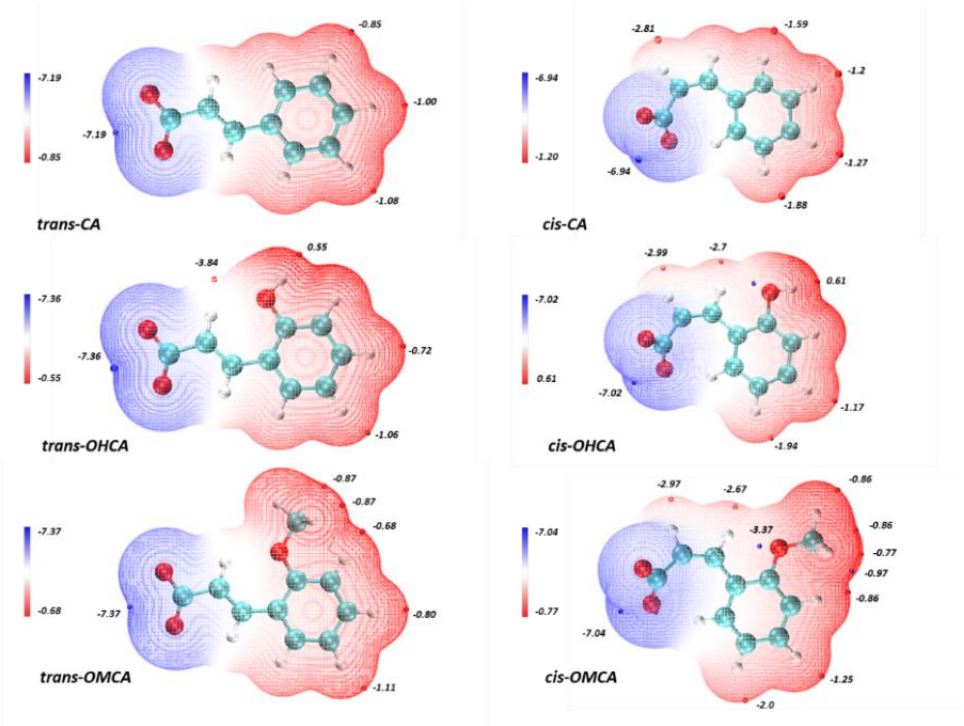

Fig. 3.15 The electrostatic potential distributions (eV) of *trans/cis*-cinnamate derivative ions after being optimized at the b3lyp/6-311+g (d, p) level. The blue points represent the minimum of potential distributions in near area. The red points represent the maximum of potential distributions in near area.

3.3.10 Hydrophilicity of *trans/cis*-cinnamates

Subsequently, we explored the solvation free energies of these cinnamate molecules at the M052X/6-31G* level in SMD solvation model and the results are showed in Table 3.5. The

solvation free energy represents the hydrophilicity of the molecule. The solvation free energies of *cis*-isomers are all higher than *trans*-isomers, revealing that the *cis*-isomers are easier to escape from the micelles and linger in the solution owing to higher hydrophilicity. ΔE is the difference of solvation free energy between *trans* / *cis*-isomers. As can be seen, the order of ΔE is ΔE (OMCA) >ΔE (OHCA) > ΔE (CA). This implies that the *cis*-OMCA ions are more likely to flee away from the micelles than OHCA and CA ions after photo-isomerization. In addition, compare with CA, the existence of hydrophilic ortho-substituents (hydroxyl and methoxy) enhances not only the hydrophilicity of the molecule but also the hydrophilic difference of cinnamate before and after UV irradiation. Reasonably, the system composed by cinnamate with different ortho-substituents show different photo-responsive behaviors.

3.3.11 Interaction energy of representative packing patterns

To further study the photo-responsive mechanism at an atom level in detail, two typical packing patterns of *trans/cis*-isomers in micelle in MD simulations were intercepted for calculating the interaction energy between *trans/cis*-isomers and 12-3-12^{2+} at special packing patterns by using Gaussian at 6-311+g** basis set with B3LYP functional in SMD solvation model. One packing pattern is the aromatic ring embedded into the 12-3-12^{2+} alkyl chain layer ((a), (d), (e), (h), (i), (l)) and the other is the aromatic ring oriented near the head group of 12-3-12·2Br$^-$ ((b), (c), (f), (g), (j), (k)). For convenience, the relative lower interaction energies for packing pattern (d) (h) (l) are set as 0 kJ/mol. The calculation results are shown in Fig. 3.16. The interaction energy among *cis*-cinnamate and surfactants is lower when aromatic ring oriented near the head group of 12-3-12·2Br$^-$. While for *trans*-cinnamate packing patterns, the energy of the *trans* packing with aromatic rings embedded into micelle is relatively lower. Obviously, the lower interaction energy keeps the micelle more stable. For CA, although the *cis* packing (a) and *trans* packing (d) have similar packing patterns (aromatic rings embedded into micelle), the interaction energy of *cis* packing is higher than that of *trans* packing. This means that when the stable *trans* packing (d) transforms into *cis* packing (a) after UV irradiation, to obtain a new stable state, the *cis*-CA will change its previously packing pattern from embedding into micelle (a) to orienting on the surface of micelle (b). It is the same for OHCA and OMCA. Furthermore, the differences of interaction energy between two *cis* packing patterns for CA, OHCA and OMCA are calculated. They are 15.84, 22.81 and 31.68 kJ/mol for CA, OHCA and OMCA, respectively. These energy differences also provide some information about the ability of micelle transformation after UV irradiation in some degree (OMCA > OHCA > CA), which is very consistent with the experiment results. Simultaneously, this energy difference implies that the introduction of ortho-subsistent can promote the transformation of micelle morphology by UV irradiation.

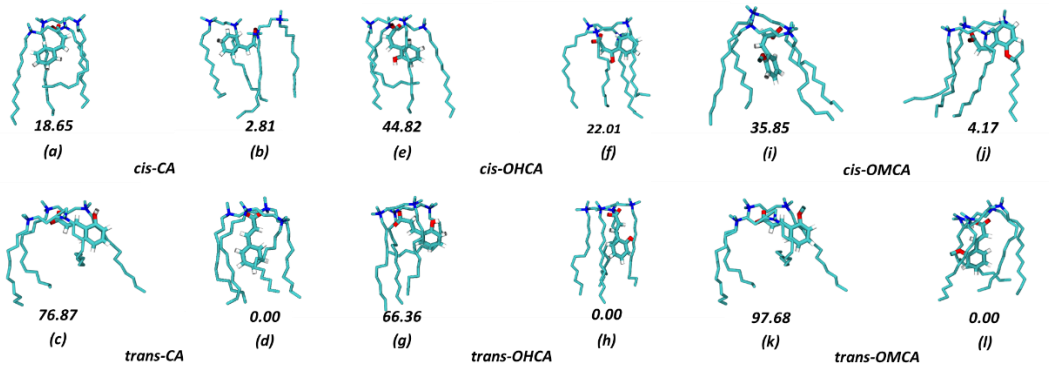

Fig. 3.16 The different packing patterns and corresponding relative interaction energies (kJ/mol) of 12-3-12·2Br$^-$ and *trans/cis*-cinnamate derivatives on micelles. (In (a), (d), (e), (h), (i), (l), aromatic rings are embedded into micelle. In (b), (c), (f), (g), (j), (k), aromatic rings are oriented on the surface of micelle. For clarity and convenience, hydrogen atoms on 12-3-12^{2+} are not shown and the relative lower interaction energies for packing pattern (d) (h) (l) are set as 0 kJ/mol.)

3.3.12 Reaction equilibrium constant

The reaction equilibrium constant is an important parameter to determine the conversion fraction of the photo-isomerization reaction of cinnamates. We calculated the Gibbs free energy by Gaussian at b3lyp/6-311+g (d, p) level and then obtained the reaction equilibrium constant (K) at 25°C by:

$$K = exp\left(-\frac{\Delta G}{RT}\right) \tag{3-10}$$

where R is the molar gas constant (R = 8.3145 J/(mol·K)) and T is the Kelvin temperature. The calculation results are shown in Table 3.5. The subscript g denotes the value which is calculated by Gaussian 09. The subscript s represents the singlet state, and t represents the triplet state. As shown in Table 3.5, in the ground state, $\Delta G_{g\text{-}s}$ values of the three photo-isomerization reactions are 19.33 (*trans*-CA), 16.21(*trans*-OHCA) and 14.36 (*trans*-OMCA) kJ/mol, respectively. The positive values of $\Delta G_{g\text{-}s}$ indicate that these photo-isomerization reactions cannot proceed spontaneously without UV irradiation. And the corresponding $K_{g\text{-}s}$ values are 4.10×10^{-4} (*trans*-CA), 1.45×10^{-3} (*trans*-OHCA) and 3.05×10^{-3} (*trans*-OMCA). The *trans*-OMCA has the largest $K_{g\text{-}s}$, indicating the highest conversion fraction. Under the UV irradiation, the cinnamate molecules are excited to the triplet state, the $\Delta G_{g\text{-}t}$ values of three photo-isomerization reactions become negative, implying that the reactions occur. The order of the corresponding $K_{g\text{-}t}$ value is 2.06×10^{4} (*trans*-CA) < 2.92×10^{4} (*trans*-OHCA) < 6.72×10^{4} (*trans*-OMCA), indicating that *trans*-OMCA has the highest conversion fraction. The result is consistent with that obtained by experiment.

Table 3.5 The solvation free energy and the difference of them between *trans/cis*-cinnamate molecules, molar volume of cinnamate ions, Gibbs free energy ($\Delta G_{g\text{-}s}$ and $\Delta G_{g\text{-}t}$) and reaction equilibrium constant ($K_{g\text{-}s}$ and $K_{g\text{-}t}$) at singlet and triplet at 25°C calculating by Gaussian 09.

System	*trans*-CA	*cis*-CA	*trans*-OHCA	*cis*-OHCA	*trans*-OMCA	*cis*-OMCA
Solvation free energy (kJ/mol)	-35.28	-37.16	-53.97	-56.39	-37.68	-40.56
Molar volume (cm^3/mol)	116.16	104.50	107.35	110.60	122.23	125.16
ΔE (kJ/mol)	-1.88		-2.42		-2.88	
$\Delta G_{g\text{-}s}$ (kJ/mol)	19.33		16.21		14.36	
$\Delta G_{g\text{-}t}$ (kJ/mol)	-24.63		-31.20		-33.26	
$K_{g\text{-}s}$	4.10×10^{-4}		1.45×10^{-3}		3.05×10^{-3}	
$K_{g\text{-}t}$	2.06×10^{4}		2.92×10^{4}		6.72×10^{4}	

3.3.13 Mechanism of photo-responsive transition of wormlike micelles

Considering all the above experimental, simulation and calculation results comprehensively and systematically, the underlying mechanisms of the photo-responsive transition of wormlike micelles containing *trans*-CA, *trans*-OHCA and *trans*-OMCA were speculated and shown in Fig. 3.17. The planar structure and lower steric hindrance and hydrophilicity of *trans*-cinnamates as well as the higher electrostatic potential in carboxyl endow them with a denser packing pattern (*trans*-cinnamates vertically insert into the surfactant hydrophobic layers.) with surfactants, thereby forming wormlike micelles. After UV irradiation, the *trans*-cinnamates photo-isomerize into *cis*-cinnamates. The higher steric hindrance and hydrophilicity as well as the lower electrostatic potential in carboxyl and evener electrostatic distribution of *cis*-cinnamates lead to a loose packing pattern (*cis*-cinnamates orient at the micelle surface.) which weakens the interaction between surfactants and finally causes the fission of micelles.

Among three cinnamate, the presence of ortho-substituents in cinnamate enlarges the difference between the steric hindrance, electrostatic distribution and hydrophilicity of *trans/cis*-cinnamates. These larger differences before and after UV irradiation allows the *cis*-OMCA and *cis*-OHCA to escape away from the micelle and linger in solution more easily than *cis*-CA and lead to the micelle transformation. Besides, the conversion fraction of the photo-isomerization reaction is the most important factor determining the degree of morphological transition of wormlike micelle. The existence of the ortho-substituents increases the equilibrium constant of the photo-isomerization reaction (OMCA increases most.). Therefore, *trans*-OMCA

is endowed with the best photo-responsive capability.

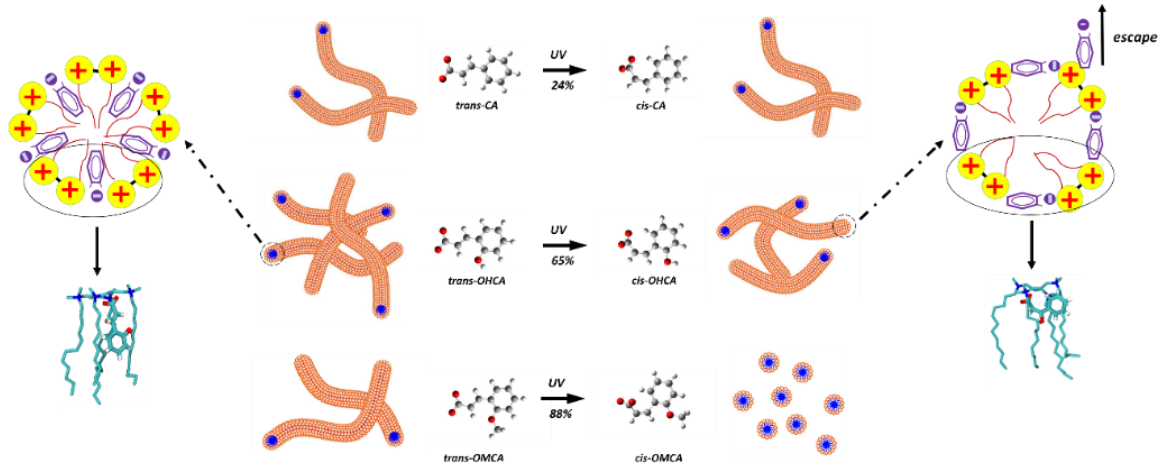

Fig. 3.17 Mechanism of 12-3-12·2Br⁻ and cinnimate derivatives micelle morphology transition under UV irradiation.

3.4 Conclusions

In this chapter, we used experimental methods such as rheology, TEM, UV-Vis absorption spectroscopy and HPLC, combined with MD simulation and quantitative calculations to study the photo-responsive behavior of wormlike micelles constructed by Gemini surfactant 12-3-12·2Br⁻ and three cinnamates. In experiment, the three systems show varying degrees of photo-response capabilities. The wormlike micelle system containing *trans*-OMCA has the strongest photo-responsive ability, with a morphology transition from wormlike to spherical after long enough UV irradiation. The wormlike length of *trans*-OHCA system is shortened while for *trans*-CA, the wormlike micelle maintains its shape. The kinetics results show that *trans*-OMCA has the highest equilibrium conversion fraction and the fastest reaction rate, followed by *trans*-OHCA and *trans*-CA.

In simulation, different numbers of *trans/cis*-isomers represents the conversion fraction. The micellar morphologies corresponding to our experimental results were successfully captured and verified by the density distribution and the *P*s. The different packing patterns between 12-3-12·2Br⁻ and *trans/cis*-isomers (*trans*-isomers are embedded into the hydrophobic layers of surfactants and *cis*-isomers orient at the micelle surface.) were visualized and characterized by $g(r)$ and SASA. ΔPMFs and the interaction energy of certain packing patterns confirm that the micelle containing *trans*-isomers is more stable.

In quantitative calculations, the higher steric hindrance and hydrophilicity as well as the lower electrostatic potential of *cis*-isomers allow *cis*-isomer to flee away from the micelles and stay at solution, thereby causing the breakage of the micelles. In addition, the presence of ortho-

substituent in cinnamate promotes the difference of the steric hindrance, electrostatic distribution and hydrophilicity of *trans/cis*-isomers and further influences the packing pattern of them with 12-3-12^{2+} in micelles. The higher difference in electrostatic potential distributions and the highest difference in solvation free energy, molecule volume as well as the highest reaction equilibrium constant indicates the best photo-responsive ability of trans-OMCA. However, the limit of the time scale and box scale of MD simulation prevent us from simulating longer, more entangled wormlike micelles at a longer timescale. And the transition state and the mechanism of the kinetic of these photo-isomerization reaction will be the focus of our further research.

Our systematical study of the photo-responsive wormlike micelles constructed by Gemini surfactant and cinnamates will expand its application prospects in microscale engineering fields such as the drug delivery, optoelectronic materials, smart fluids and purification and separation.

Chapter 4 Molecular Dynamics Simulations and Quantitative Calculation of Photo-responsive Behavior of Wormlike Micelles Constructed by Gemini Surfactant 12-3-12·2Br$^-$ and Cinnamte Derivatives with Different Methoxy Position

4.1 Introduction

In the previous chapter, we discussed the influence of different ortho-substituents of cinnamates on the photo-responsive behavior of 12-3-12·2Br$^-$ wormlike micelles. The results show that the existence of orth-substituents affects the molar volume, hydrophilicity, electrostatic potential distributions, reaction equilibrium constant of the *cis/trans*-cinnamates and further affects the photo-responsive behavior of the wormlike micelles. In this chapter, we will further study the effects of the methoxy position (ortho-, meta, para-) in cinnamates on photo-responsive behavior of the wormlike micelle composed of Gemini surfactant 12-3-12·2Br$^-$ and *trans*-methoxycinnamic acid (*trans*-MCA). MD simulations are used to reproduce the micelle transition after UV irradiation and to characterize the micelle properties. Quantitative calculations are also used to optimize the molecular structure and obtain the hydrophilicity, molar volume and electrostatic potential distributions of *trans/cis*-cinnamates. Furthermore, we select 24 cinnamates with different substituents in ortho-, meta, para-position and compare the photo-sensitive of them.

4.2 Materials and methods

4.2.1 Quantitative calculation details and force-field parameters

We optimized the structures of 24 kinds of *trans/cis*-cinnamates by Gaussian 09 quantum chemistry packages through a hybrid functional B3LYP at the 6-311+g (d, p) level. Among them, the optimized structures of *trans/cis*-ortho-methoxycinnamic acid (*trans/cis*-OMCA), *trans/cis*-meta-methoxycinnamic acid (*trans/cis*-MMCA) and *trans/cis*-para-methoxycinnamic acid (*trans/cis*-PMCA) were used as initial structures in MD simulations. The molar volume, the Gibbs free energy of *trans/cis*-cinnamate ions, photo-isomerization reaction equilibrium constants and the interaction energies of the representative packing pattern of 12-3-12^{2+}/cinnamate were calculated at B3LYP/6-311+g (d, p) level with SMD solvation model. The electrostatic potential distribution of cinnamate derivatives ions were calculated by Multiwfn

software packages. The solvation free energy of *trans/cis*-cinnamate derivatives were calculated at the M052X/6-31G* level in SMD solvation model.

The force field GROMOS96 45a3 is used in our MD simulations owing to its good consistency with the experimental data which has been confirmed in our previous studies. We optimized the initial structure and generated and the coordinates of 12-3-12^{2+} and *trans/cis*-OMCA, *trans/cis*-MMCA and *trans/cis*-PMCA using Gaussian 09. The structures of Gemini surfactant 12-3-12·2Br^{-} and *trans/cis*-OMCA, *trans/cis*-MMCA and *trans/cis*-PMCA are shown in Fig. 4.1. The force field parameters for *trans/cis*-MMCA and *trans/cis*-PMCA were generated by the ATB server and the force field parameters for *trans/cis*-OMCA and12-3-12·2Br^{-} can be obtain from last chapter.

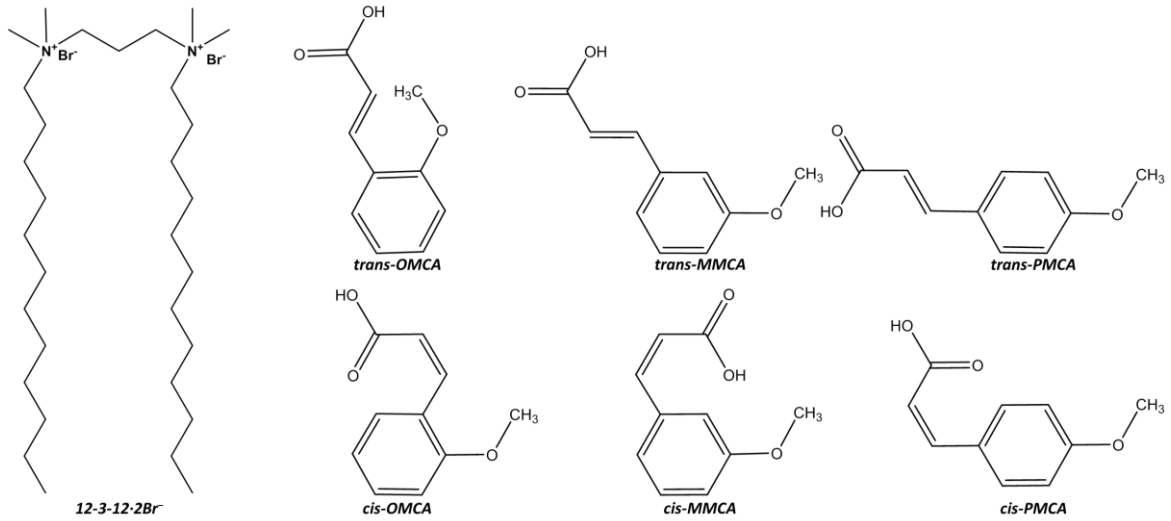

Fig. 4.1 Structures of Gemini surfactant 12-3-12·2Br^{-} and *trans/cis*-OMCA, *trans/cis*-MMCA and *trans/cis*-PMCA.

4.2.2 Simulation Details

The cuboid box size in MD simulations was scaled to 7.5 × 7.5 × 24 nm^3. Periodic boundary conditions were set in all three dimensions. In our simulation system, the number of 12-3-12·2Br^{-} molecules was fixed at 180. Correspondingly, the concentration of 12-3-12·2Br^{-} was approximately 0.23 mol/L, which is far above the CMC (0.91 mM) of 12-3-12·2Br^{-} in aqueous solution. The number of *trans/cis*-cinnamates in simulation system depends on the experimental conversion fraction which has been published (0.88 for *tran*-OMCA, 0.91 for *trans*-MMCA and 0.82 for *trans*-PMCA) [211]. Here, we define *f* as the conversion fraction. The surfactant and cinnamate ions as well as corresponding number of counter ions of Br^{-} and Na^{+} were distributed randomly in approximately 37000 water molecules using Packmol. The system details are exhibited in Table 4.1.

Table 4.1 Number of 12-3-12^{2+}, Br^-, cinnamate derivatives, Na^+ ions and water molecules in simulation box.

System	12-3-12^{2+}	Br^-	*cis/trans*-isomers	Na^+	H_2O
			12-3-12^{2+} + OMCA		
1	180	360	0/135	135	38233
2	180	360	118/17	135	38227
			12-3-12^{2+} + MMCA		
3	180	360	0/135	135	38235
4	180	360	123/12	135	38260
			12-3-12^{2+} + PMCA		
5	180	360	0/135	135	38223
6	180	360	111/24	135	38327

MD simulations were carried out by GROMACS 2018 software packages. Berendsen bath coupling scheme was used to maintain a constant temperature at 298.15 K and pressure at 1 bar. The simulation box was independently scaled in z- direction but was isotopically scaled in x- and y- directions by semi-isotropic pressure coupling in order to simulate rod-like and wormlike micelles. Simulation time was set to 100 ns with a 2 fs time step and the trajectories were saved every 2ps. The SPC water model was employed. The short-range electrostatic cutoff and short-range Van der Waals cutoff were set to 1.0 nm, and the long-range electrostatic interactions were set to 0.12 nm by PME (Particle Mesh Ewald) method. LINCS (Linear Constraint Solver) algorithm were used to constrain bonds. VMD 1.9.2 was employed to visualize and display the trajectories and configurations.

4.3 Results and Discussions

4.3.1 Self-assembly behavior of 12-3-12·2Br⁻ and *trans*-cinnamates in water

We have proved in previous chapter that the pure 12-3-12·2Br⁻ can self-assemble into several spherical micelles with the aggregation number 30, which confirm the feasibility of GROMOS96 45a3 forcefield. Subsequently, we simulated the system containing 180 12-3-12·2Br⁻ and 135 cinnamates with different *cis/trans* ratio to represent the initial and equilibrium conversion fraction from an entirely random arrangement state. The snapshots of the simulation box and initial as well as the final micelle morphologies after 100 ns simulation at 298.15K are shown in Fig. 4.2. Obviouly, without UV irradiation, 12-3-12·2Br⁻/ *trans*-cinnamates system self-assemble into a wormlike micelle after 100 ns MD simulation owing to the strong electrostatic attraction between polar head of surfactants and counter ions in solution. After enough UV irradiation, the wormlike micelle containing *trans*-OMCA transforms into spherical micelles. At equilibrium conversion fraction, wormlike micelles containing *trans*-MMCA and *trans*-PMCA fission into short rod-like micelles. The simulation results are in good agreement with the experiment [211].

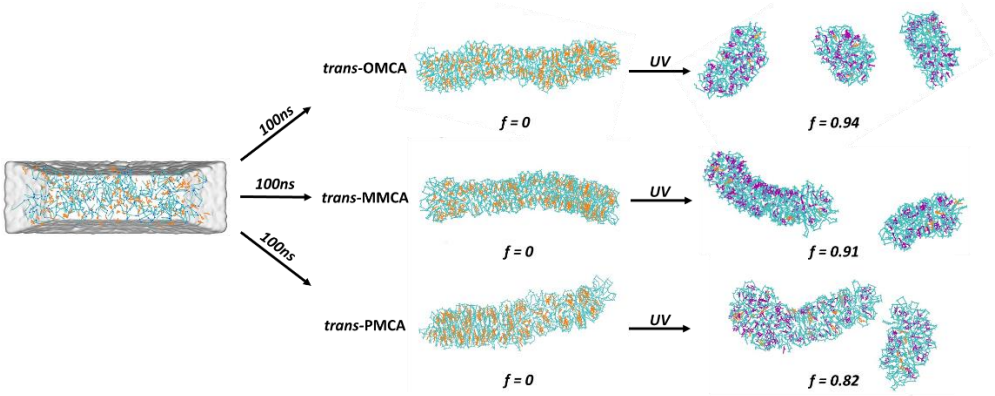

Fig. 4.2 Snapshots of the initial simulation box and corresponding micelle morphologies of 12-3-12^{2+} / *trans*-cinnamates = 180:135 at equilibrium conversion fraction after 100ns simulation at 298.15K. (The cyan parts are 12-3-12^{2+}; the orange parts are *trans*-isomers; the purple parts are *cis*-isomers. For clarity, water, Br^- and Na^+ are not shown.)

Fig. 4.3 shows the calculated density distributions of the ions with the z direction of the box. The formation of micelles with different morphologies can be testified through density distribution. It can be seen from Fig. 4.3 (a) (b) (c) that the density curve of 12-3-12^{2+} at $f = 0$ shows a continuous corona-shape peak, indicating the formation of a long wormlike micelle. The wormlike micelle containing *trans*-OMCA fissions into three spherical micelles with the density curve (d) exhibiting three sharp peaks. The peak of density curve of *trans*-MMCA (e)

and *trans*-PMCA (f) ruptures into two corona-shape peaks, suggesting the formation of two short rod-like micelles. For (f), the trough between two peaks do not reach zero, which is attribute the overlapping of micelles in z direction.

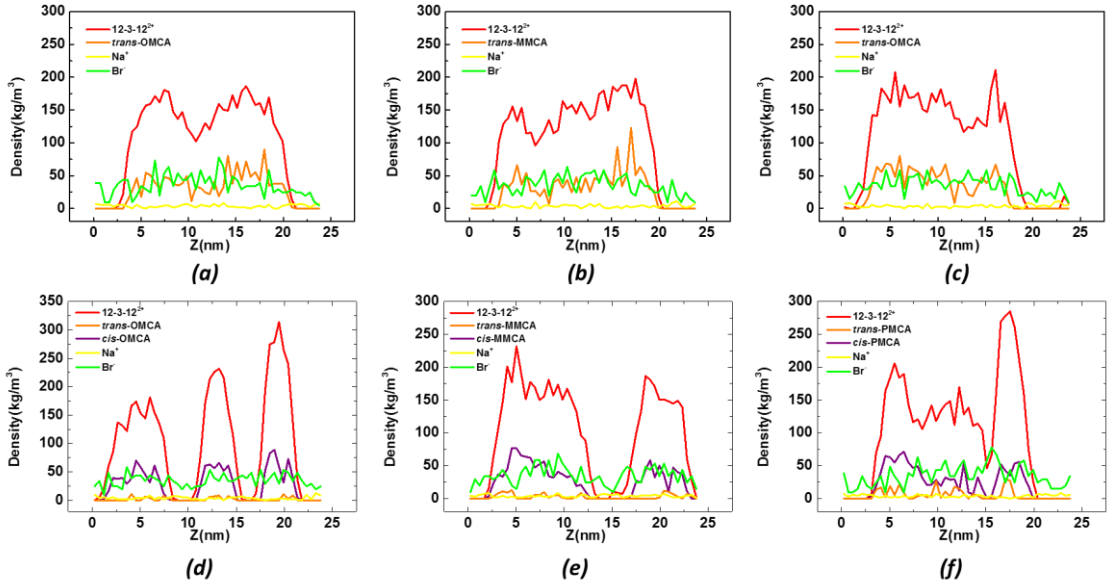

Fig. 4.3 The density distributions of 12-3-12^{2+}, *trans/cis*-cinnamate ions, Na^+, Br^- along z axis at different *f*.((a) *trans*-OMCA *f* = 0; (b) *trans*-MMCA *f* = 0; (c) *trans*-MMCA *f* = 0; (d) *trans*-OMCA *f* = 0.88; (e) *trans*-OMCA *f* = 0.91; (f) *trans*-PMCA *f* = 0.82)

The wormlike micelles with different position of substituent group exhibits different photo-responsive ability under the UV irradiation. The critical packing parameter is a significant parameter which can be used to explain the micelle morphology. The *P*s of these systems and corresponding parameters were calculated and shown in Table 4.2. As shown in Table 4.2, although the *P* value of micelles containing *trans*-OMCA remains in the wormlike micelle region ($0.33 < P < 0.5$), they still decrease from 0.44 to 0.35 (at $f = 0$ and 0.94), which implies that the length of wormlike micelle is shortened and tend to transform into spherical micelle. For the micelles containing *trans*-MMCA, the *P* values are 0.46 and 0.42 (at $f = 0$ and 0.91). This may explain that the wormlike micelle containing *trans*-MMCA is transformed to two short rod-like micelle after UV irradiation. For *trans*-PMCA system, the same trend as *trans*-MMCA can be found. When at $f = 0.82$, the *P* is reduced to 0.38 from 0.53 ($f = 0.82$), indicating that the wormlike micelle tends to shorten. The *P* values are very consistent with the micelle morphology in Fig. 4.2 and in experiments [211], which can give a good prediction on the micelle morphologies and a good explanation of micelle transition.

4.3.2 The energy difference in micelles transition

The interaction energy and its variation can estimate the stability of the micelles and

illustrate the mechanism of the micelle transformation. The variation of interaction energy (Coulombic, LJ and total interaction energy) with time between 12-3-12^{2+} and cinnamates (including *cis* and *trans*) ions is shown in Fig. 4.4 and the equilibrium interaction energies of systems are calculated and shown in the Table 4.2. It can be seen from Fig. 4.4 that the six systems reach to the equilibrium at approximately 10 ns. The Coulombic, LJ and total interaction energy all decrease after UV irradiation, causing the wormlike micelle to become unstable and eventually fission. This indicates the interaction between 12-3-12^{2+} and *cis*-isomers is weaker than that of *trans*-isomers. Based on the interaction energy and the *P*s result, we can draw a conclusion that wormlike micelle composed by 12-3-12·2Br^{-} and *trans*-cinnamates is relatively more stable than that of *cis*-cinnamates. After the UV irradiation, *trans*-cinnamates start to photo-isomerize into their *cis*-form, and the difference in interaction energies of sysyem is tha main drive force that causes the wormlike micelle to fission.

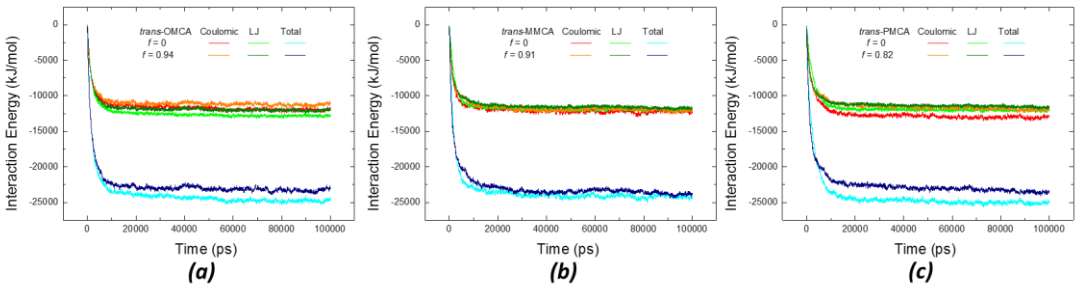

Fig. 4.4 The interaction energy (Coulombic, LJ and total interaction energy) between 12-3-12^{2+} and MCA (*cis*-isomers and *trans*-isomers) at different *f* with simulation time (a) *trans*-OMCA; (b) *trans*-MMCA; (c) *trans*-PMCA.

4.3.3 Packing patterns between MCAs and 12-3-12^{2+}

From above, we have studied the difference of the photo-responsive behavior of the systems containing *trans*-cinnamates with different methoxy-substituent position. In order to further understand the mechanism of micelle transformation, it is very important to understand how *trans/cis*-cinnamates arrange in micelles. Firstly, we calculated $g(r)$ of certain atoms to characterize the packing pattern between 12-3-12^{2+} ions and cinnamates. Fig. 4.5 displays the radial distribution functions ($g_{N_1\text{-}N_1}(r)$) between the N_1 atoms of different 12-3-12^{2+} in system. It can be seen from Fig. 4.5 that before and after UV irradiation, all curves show three continuous peaks, indicating that an orderly repeating hexagonal crystal structure 12-3-12^{2+} is formed. The first peak positions of $g_{N_1\text{-}N_1}(r)$ of the system containing *trans*-OMCA and *trans*-PMCA appears at 0.64 nm, and the height of the peaks decreases, indicating a less orderly arrangement of 12-3-12^{2+} after UV irradiation. While for *trans*-MMCA, after the UV irradiation, the increase of the first peak height indicates the formation of a more orderly arrangement

between 12-3-12^{2+} ions, representing a weaker photo-responsive ability of wormlike micelle containing *trans*-MMCA.

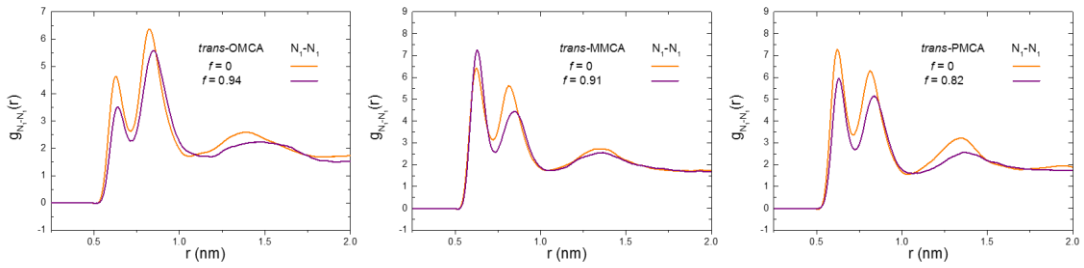

Fig. 4.5 Radial distribution functions $g_{N1\text{-}N1}(r)$ of different 12-3-12^{2+} for cinnamate systems at initial and equilibrium conversion fraction.

To further obtain the packing pattern between 12-3-12^{2+} and cinnamates in micelle, the radial distribution functions $g_{N1\text{-}C}(r)$ between N_1 atom of 12-3-12^{2+} and specific C atoms (C_3, C_7, C_{10}) in cinnamates at initial and equilibrium conversion fraction were calculated and shown in Fig. 4.6. It can be seen from Fig. 4.6, before the UV irradiation, the first peak of $g_{N1\text{-}C3}(r)$ curves for *trans*-cinnamates located at 0.84 nm. After the UV irradiation, a new first peak appears at 0.48 nm, indicating a closer packing between the benzene ring in *cis*-cinnamates and the head group of 12-3-12^{2+} than in *trans*-cinnamates. Specially, for *trans*-MMCA, another new peak appears at 0.74 nm in (h) after the UV light. Three peaks in $g_{N1\text{-}C3}(r)$ indicate the formation of a periodic hexagonal crystalline-like structure, implying that the wormlike micelle containing *cis*-MMCA has a more orderly configuretion.

The C_7 in the methoxy is the most representative atom characterizing the difference of the packing pattern between three MCA and 12-3-12^{2+}. From Fig. 4.6 (b) (e) (h), the $g_{N1\text{-}C7}(r)$ curves of three systems are quite different. For *trans*-OMCA, the $g_{N1\text{-}C7}(r)$ curve exhibits a high peak at 0.51 nm before and after the UV irradiation. The lower height of the peak suggests that the C_7 in *cis*-OMCA have a less orderly arrangement with the head group of 12-3-12^{2+} after UV irradiation. For *trans*-MMCA, the peaks of the $g_{N1\text{-}C7}(r)$ appear at 0.51 nm and 1.1 nm and the peak at 1.1 nm is higher than that at 0.51 nm, indicating that more C_7 atoms are arranged at 1.1 nm away from N_1. After UV irradiation, the height of the first peak of the $g_{N1\text{-}C7}(r)$ at 0.51 increases sharply, implying that more C_7 atoms were transferred to the position 1.1 nm away from N_1 in a more orderly arrangement. For *trans*-PMCA, before the UV irradiation, the first peak is located at a quite far position (1.12 nm) owing to the presence of para-methoxy. After UV irradiation, the peak shifts to left (0.68 nm), indicating a rearrangement of the C_7 close to the head group of surfactants.

The $g_{N1\text{-}C10}(r)$ of the MCA reflects the strength of the electrostatic interaction because N_1 and C_{10} are the charge center of surfactant and cinnamates, respectively. It can be seen from

Fig. 4.6 (c) (f) (i), all the $g_{N1\text{-}C10}(r)$ exhibits the same distribution with a sharp peak near 0.44nm, which indicates that a strong electrostatic interaction between cinnamates and surfactants. For OMCA, the peak moved slightly from 0.43 nm to 0.45 nm after UV irradiation with no change in the peak height, indicating that electrostatic interaction between 12-3-12·2Br$^-$ and OMCA becomes weaker. For MMCA, the peak position and height of $g_{N1\text{-}C10}(r)$ are nearly unchanged. Furthermore, the peak height of PMCA decreases after the UV, indicating the weaker electrostatic interaction after UV irradiation. It is worth noting that the Coulombic interaction energies of *trans*-OMCA and *trans*-PMCA at f = 0 are much higher than the Coulombic interaction energies at equilibrium, while *trans*-MMCA is almost the same. This is consistent with $g(r)$ results.

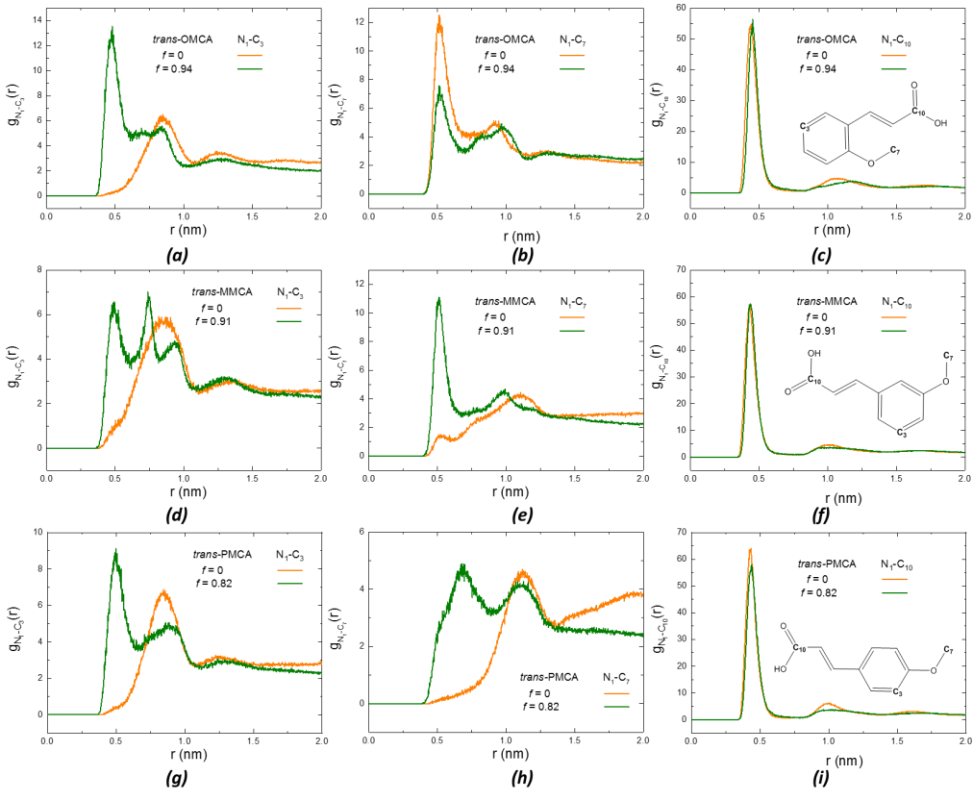

Fig. 4.6 Radial distribution functions $g_{N1\text{-}C}(r)$ between N_1 atom of 12-3-12^{2+} and C_3, C_7, C_{10} atoms of cinnamates at initial and equilibrium conversion fraction. ((a) (d) (g) N_1-C_3; (b) (e) (h)N_1-C_7; (c) (f) (i) N_1-C_{10}; (a) (b) (c) *trans*-OMCA; (d) (e) (f) *trans*-MMCA; (g) (h) (i) *trans*-PMCA)

Fig. 4.7 exhibits the representative packing patterns between the *trans/cis*-cinnamates and 12-3-12^{2+} ions intercepted from the micelle of the last frame in MD simulations. As can be seen from Fig. 4.7, the *trans*-cinnamates insert into the micelle vertically. Their methoxy group and aromatic ring are completely inserted into the hydrophobic layer of surfactant more and more deeply, in the order of ortho-, meta- and para-. The carboxyls of *trans*-cinnamates are close to

center of the head group of 12-3-12^{2+} owing to the strong electrostatic interaction. On the contrary, *cis*-cinnamates are located horizontally on micelle surface. Their aromatic ring and carboxyl groups are close to the head group of 12-3-12^{2+}, and the methoxy of them inserted into the interior of the micelles except for the *cis*-PMCA whose methoxy are oriented on the micellar surface. Thus, when *trans*-cinnamates photo-isomerize into *cis* form after UV irradiation, the aromatic rings will detach from the interior of micelles and rearrange on the surface of the micelles. This rearrangement loosens the packing pattern and weakens the interaction between cinnamates and 12-3-12^{2+}, leading to wormlike micelles to fission into short rod-like even spherical micelles.

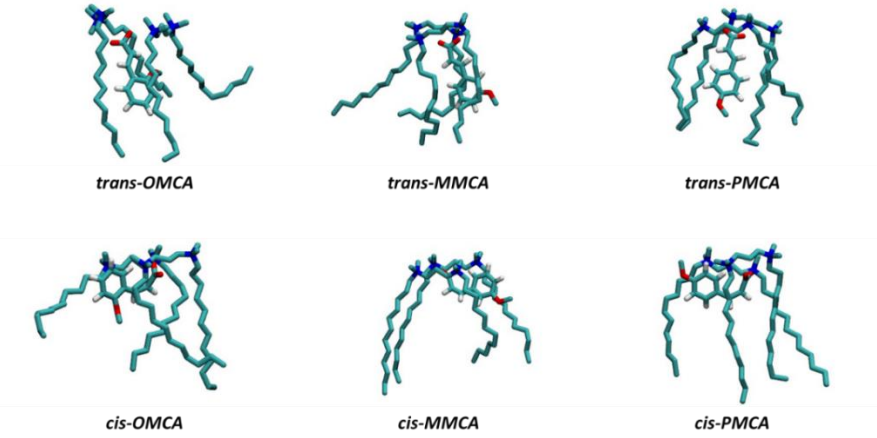

Fig. 4.7 The representative packing patterns between 12-3-12^{2+} and *trans/cis*-cinnamates with different methoxy-substituent positions intercepted from micelles of last frame in MD simulations.

The packing pattern can also be deduced from the solvent-accessible surface area of micelles. To further study the difference in packing pattern of cinnamates and surfactant in micelle The solvent accessible surface including hydrophobic (a_{pho}), hydrophilic (a_{phi}) and total surface area of the micelle containg three cinnamates at iniatial and equilibrium are calculated and shown in Fig. 4.8 and Table 4.2. It can be seen from Fig. 4.8 that the surface areas of three systems all decrease before 10 ns and keep stable after 10 ns, implying the surfactant molecules self-assemble into a certain morphology and maintain this morphology till the end of simulation. The hydrophobic surface area all incrase after UV irradiation, which reconfirm that the beneze ring of *trans*-cinnamate is inserted into the micelle layer while that of *cis*-cinnamate is oriented on the micelle surface. In addition, the hydrophilic surface areas of micelles containg *trans*-OMCA and *trans*-MMCA decrease after UV irradiation while that of *trans*-PMCA increases, proving that the methoxy of *cis*-OMCA and *cis*-MMCA are embedded into micelle while that of *cis*-PMCA is oriented on micelle surfacr after UV irradiation.

Table 4.2 Geometric information of micelles and interaction energy between 12-3-12^{2+} and *cis/trans*-MCAs after system equilibrium in MD simulations: V, volume (nm^3) of the last frame; a_{pho}, hydrophobic (nm^2), a_{phi}, hydrophilic (nm^2) and a_{tot}, total (nm^2) surface areas of the last frame; l, the length of alkyl chain (nm); *P*; E_{coul}, coulomb interaction energy (kJ/mol); E_{LJ} Lennard-Jones interaction energy (kJ/mol); E_{tol}, total interaction energy; the average hydrogen bond number.

System	*f*	V	a_{pho}	a_{phi}	a_{tot}	l	*P*	E_{coul}	E_{LJ}	E_{tol}	H bond
trans-OMCA	0	177.2	165.5	336.7	502.2	1.2	0.44	-11988.5	-12807.5	-24796	294.4
	0.94	140.7	215.8	327.6	543.4	1.2	0.35	-11266.8	-12048.1	-23314.9	279.3
trans-MMCA	0	178.1	182.4	323	505.5	1.2	0.46	-12211.9	-11974.3	-24186.2	280.4
	0.91	158.7	189.4	317.6	507	1.2	0.42	-12044	-11733.2	-23777.1	226.8
trans-PMCA	0	201.3	176.2	315	491.2	1.2	0.53	-13015.1	-12039.3	-25054.4	241.9
	0.82	147	188.6	325.7	514.3	1.2	0.38	-11924.1	-11577.3	-23481.3	248.2

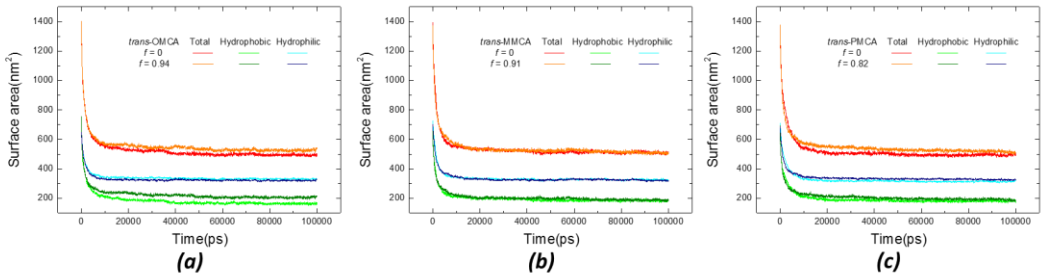

Fig. 4.8 The hydrophobic (a_{pho}), hydrophilic (a_{phi}) and total (a_{tot}) surface areas of aggregates containing 12-3-12^{2+} and methoxy sodium cinnamates at different *f* with simulation time. (a) *trans*-OMCA; (b) *trans*-MMCA; (c) *trans*-PMCA.

In addition, the packing pattern can also be reflected from the hydrogen bond. The number of the hydrogen bond between the cinnamate ions and the water were calculated and shown it in Fig. 4.9. With the methoxy shifting from the ortho to meta and para position, the methoxy of *trans*-cinnamate is inserted more and more deeply into the interior of micelles. Thereby the number of the hydrogen bond between *trans*-cinnamate and the water decreases. After the UV irradiation, because the methoxy of *cis*-OMCA and *cis*-MMCA (more inner) is plugged into the interior of the micelle, the number of the hydrogen bond of the systems containing OMCA and MMCA decreases while for *trans*-MMCA, the number of hydrogen bond drop more sharply. On the contrary, because the packing pattern for *cis*-PMCA and surfactant has been changed into the methoxy group lying on the micelle surface instead of being inserted into the micelle like *trans*-PMCA after UV irradiation, there is a converse trend that the number of hydrogen bond between *trans*-PMCA and the water increases.

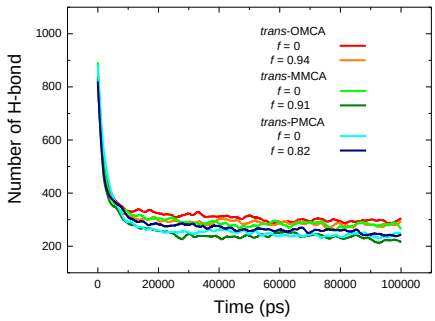

Fig. 4.9 The hydrogen bond numbers between cinnamate ions and water in simulation system before and after UV irradiation

4.3.4 Quantitative calculations

4.3.4.1 Geometry structure of three cinnamates

In order to further explore the geometrical differences between OMCA, MMCA and PMCA and how the position of methoxy substituent affects the photo-response behavior of wormlike micelles, the Gaussian 09 quantum chemistry packages were used. Firstly, the structures of *trans/cis*-cinnamates were optimized using b3lyp/6-311+g (d, p) basis set and shown in Fig. 4.10. It can be seen from Figure 4.10 that *trans*-cinnamates have a planar structure, while *cis*-cinnamates has a three-dimensional structure. This indicates that when 12-3-12^{2+} and cinnamates form micelles in the solution, *trans*-MCA is more likely to insert vertically into the micelles, thus forming a dense morphology. For the *trans*-cinnamates ions, α values (the dihedral angle between the aromatic ring plane and carbonyl plane) are 180°, which confirms their planar structure. For the *cis*-cinnamates ions, α values are 66.1° (*cis*-OMCA), 60.9° (*cis*-MMCA), and 46.9° (*cis*-PMCA). It indicates that when the methoxy group moves from the ortho position to the meta position and the para position, the structure of *cis*-cinnamates is closer and closer to a plane structure.

The molar volume directly reflects the steric hindrance of the molecule. Table 4.4 lists the calculated molar volumes of cinnamates ions. Obviously, before UV irradiation, the molar volume of *trans*-cinnamates ions increases as the methoxy group moves from the ortho position to the meta position to the para position. After UV irradiation, except for the sharp increase in the molar volume of *cis*-OMCA ion, the molar volume of *cis*-MMCA and *cis*-PMCA ions decreased significantly. The increase in the degree of bending and molar volume of OMCA ions after UV irradiation promotes its steric hindrance, which leads to the loosening and rupture of micelles. For MMCA and PMCA ions, the molar volume decreases after UV illumination, which is not conducive to the transformation of wormlike micelles. This confirms our experimental results that *trans*-OMCA wormlike micelles break up into spherical and rod-like

micelles after UV illumination, while *trans*-MMCA and *trans*-PMCA are converted into shorter wormlike micelles. We can also conclude that the presence of meta- and para-methoxy groups will reverse the difference in the molar volume of cinnamate derivatives before and after UV irradiation, leading to a decrease in photo-responsive ability of wormlike micelle.

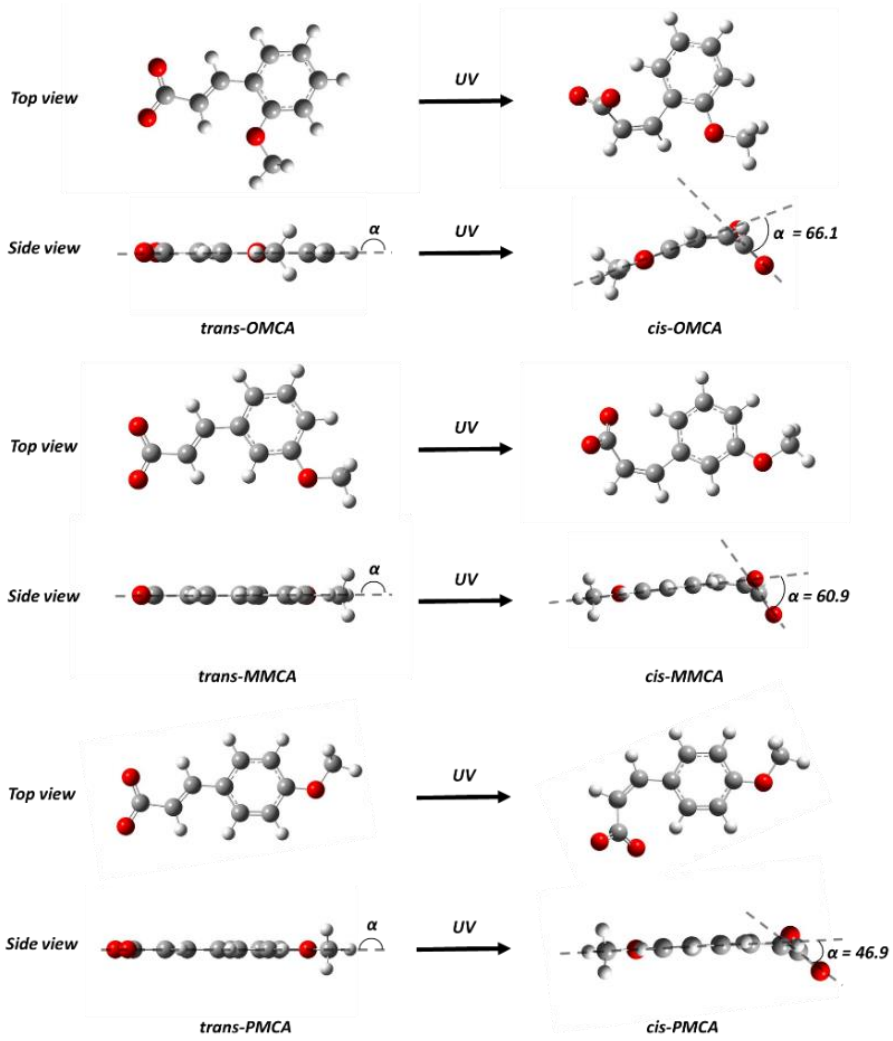

Fig. 4.10 The top view and side view of optimized structures of *trans/cis*-MCAs ions after being optimized at the b3lyp/6-311+g (d, p) level.

4.3.4.2 Electrostatic potential distributions of three cinnamates

To obtain more microscopic and precise molecular information, the electrostatic potential distributions (eV) were calculated and shown in Fig. 4.11. It can be seen from Fig. 4.11, the negative electrostatic potential of *trans/cis*-cinnamate ions are mainly concentrated on the carboxy group. The maximums of negative electrostatic potential of *trans*-cinnamates are larger than those of *cis*-cinnamates and the electrostatic potential distributions of *cis*-cinnamates are evener. These evidences indicate that *trans*-cinnamates have a stronger electrostatic interaction with surfactants when forming micelle. After UV irradiation, the electrostatic potential

distribution in carboxyl group decreases, and more potential is transferred to the benzene ring. The weaker electrostatic interaction between *cis*-cinnamates and surfactants lead to the rupture of micelle. Among the three types of *cis*-cinnamates, the electrostatic potential distribution in carboxyl group of *cis*-OMCA decreases the most (0.33), indicating the strongest photo-response ability of wormlike micelle containing *trans*-OMCA. Owing to the presence of methoxy at meta and para position, the difference in maximum of electrostatic potential in carboxyl group decreases, leading to a drop in photo-responsive ability of wormlike micelle.

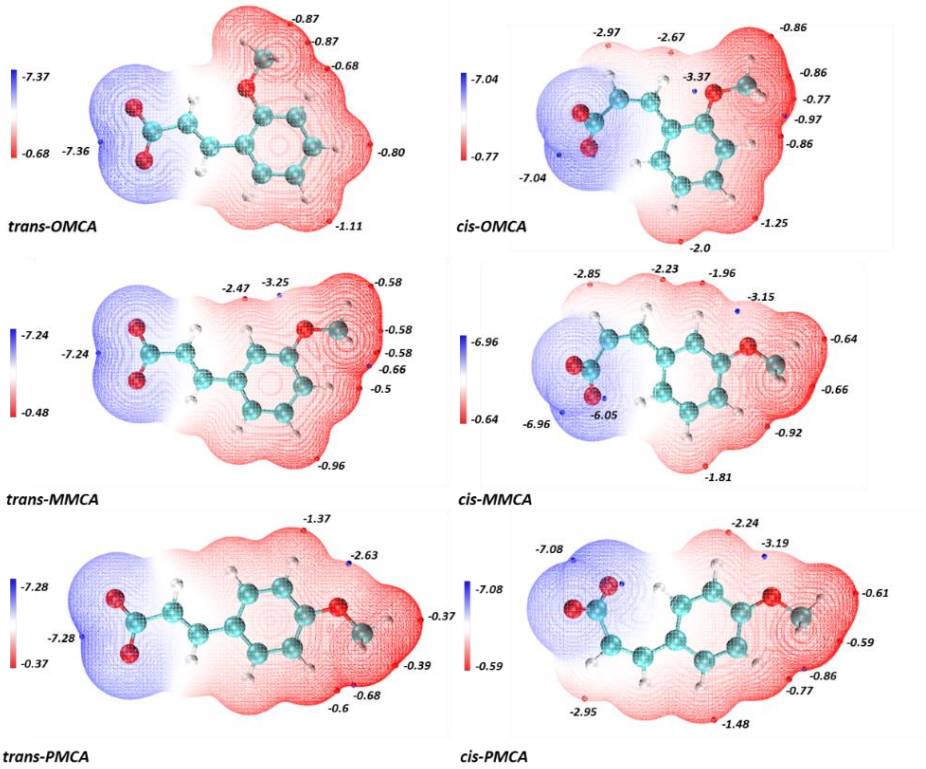

Fig. 4.11 The electrostatic potential distributions (eV) of *trans/cis*-cinnamate ions after being optimized at the b3lyp/6-311+g (d, p) level. The blue dots represent the minimum of potential in near area. The red dots represent the maximum of potential in near area.

4.3.4.3 Hydrophilicity

The molecular structure also has an important impact on the hydrophilicity of the molecules. To explore the difference of hydrophilicity for these *trans/cis*-cinnamate molecules, we calculated the solvation free energies of them at the M052X/6-31G* level in SMD solvation model and summarized the results in Table 4.3. The solvation free energy represents the strength of the hydrophilicity of the molecule. The higher the absolute value of solvation free energies, the stronger the hydrophilicity of the molecule. As shown in Table 4.3, before the UV irradiation, the order of the solvation free energy is *trans*-PMCA > *trans*-MMCA > *trans*-OMCA. This order indicates that the *trans*-OMCA has the strongest hydrophobicity, which may be the reason for the strongest binding with the 12-3-12^{2+}. After UV irradiation, the solvation free energy of

cis-OMCA increases, indicating that *cis*-OMCA is more likely to escape from micelles and linger in the solution due to its higher hydrophilicity. On the contrary, the MMCA and PMCA witness a slight and sharp drop in the solvation free energy. The decrease of the hydrophilicity tends to drive the *cis*-MMCA and *cis*-PMCA to stay in the micellar layer instead of heading to the solution, thereby reducing the photo-responsive ability of corresponding wormlike micelle. The farther distance between the methoxy group and the double bond for *trans*-MMCA and *trans*-PMCA reverses the difference in molar volume and hydrophilicity of them before and after the UV irradiation, thereby reducing micellar transition velocity and degree of wormlike micelle.

Table 4.3 The solvation free energy and the molecule volume of *trans/cis*-cinnamate ions calculating by Gaussian 09.

System	*trans*-OMCA	*cis*-OMCA	*trans*-MMCA	*cis*-MMCA	*trans*-PMCA	*cis*-PMCA
Solvation free energy (kJ/mol)	-37.68	-40.56	-29.66	-27.72	-30.44	-27.44
Molar volume (cm^3/mol)	113.7	146.5	129	99.3	152.3	136.4

4.3.4.4 Interaction energy of representative packing patterns

Furthermore, to obtain the energy information more accurately, we intercepted two typical packing patterns between *trans/cis*-cinnamates and 12-3-12^{2+} in micelles from MD simulation to calculate their interaction energies and show the results in Fig. 4.12. One is that the benzene ring is embedded in the surfactant hydrophobic layer ((b), (c), (f), (g), (j), (k)), and the another one is that the benzene ring is oriented near the head group of 12-3-12·2Br$^-$ ((a), (d), (e), (h), (i), (l)). For convenience, the relative lower interaction energies for packing pattern (b) (f) (j) are set to 0 kJ/mol. As shown in Fig. 4.12, for the *trans*-isomers, the packing pattern that the benzene ring is embedded in the micelle has relatively low energy, imply that the micelle with this packing pattern is more stable. While for the *cis*-isomer, the packing pattern of the benzene ring on the surface of the micelle is relatively stable. This means that when the stable *trans* packing pattern is converted to the *cis* packing pattern after UV irradiation, in order to reobtain a stable packing pattern, the *cis*-isomer will change its packing pattern (the benzene ring are moved from the micelle interior to the micelle surface). This change of the packing pattern will cause the loosening and rupture of the micelles. In addition, the difference in the interaction energy between the two *cis* packing patterns of OMCA, MMCA and PMCA is 96.8, 1.0 and 17.2 kJ/mol, respectively. These differences reflect the ability to change their packing pattern after UV irradiation is OMCA > PMCA > MMCA. This sequence is very consistent with our experimental results.

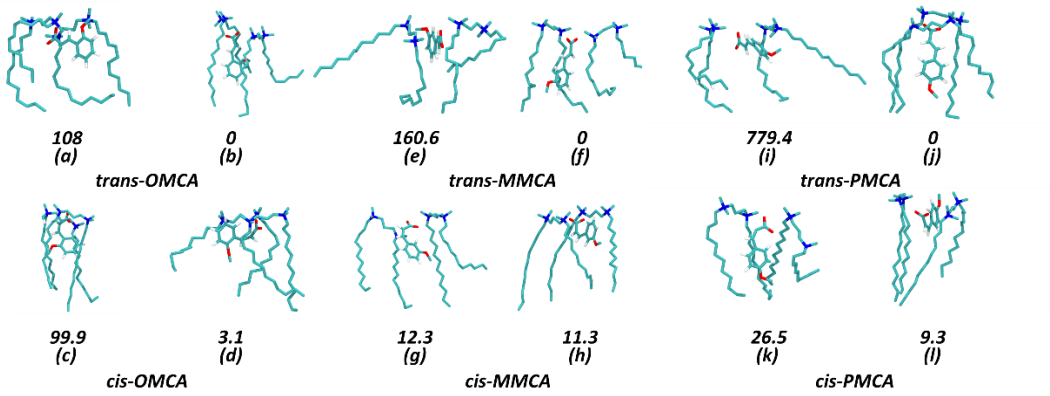

Fig. 4.12 The different packing patterns and corresponding relative interaction energies (kJ/mol) of 12-3-12^{2+} and OMCA, MMCA, PMCA. (In (a), (d), (e), (h), (i), (l), the aromatic rings are oriented on the surface of micelle. In (b), (c), (f), (g), (j), (k), the aromatic rings are embedded into the alkyl chain of the 12-3-12^{2+}. For clarity, hydrogen atoms on 12-3-12^{2+} and methoxy group are not shown. For convenience, the interaction energy of packing pattern which the aromatic ring is embedded into micelle for *trans*-isomer is set to 0 kJ/mol.)

4.3.5 The prediction of photo-sensitivity for different cinnamic acid

In addition, to screen out the cinnamic acid with the best photosensitive ability, we selected several cinnamic acids with different electron donating substituents at ortho-, meta- and para-positions and calculated a series of parameters including molar volume and solvation free energy and their difference (ΔV ΔE), and photo-isomerization reaction equilibrium at singlet state ($K_{g\text{-}s}$) and triplet state ($K_{g\text{-}t}$), the maximum of negative electrostatic potensial (*cis*-max, *trans*-max), and their difference (Δmax) of *trans/cis*- cinnamic acid under UV irraidaition. The calcaulted results are shown in Fig. 4.14. Those cinnamic acid are meta-hydroxylcinnamic acid (MHCA), para-hydroxylcinnamic acid (PHCA), ortho-sulfhydrylcinnamic acid (OSCA), meta-sulfhydrylcinnamic acid(MSCA), para-sulfhydrylcinnamic acid (PSCA), ortho-methylthiocinnamic acid (OMTCA), meta-methylthiocinnamic acid (MMTCA), para-methylthiocinnamic acid (PMTCA), ortho-aminocinnamic acid (OACA), meta-aminocinnamic acid (MACA), para-aminocinnamic acid (PACA), ortho-methylaminocinnamic acid (OMACA), meta-methylaminocinnamic acid (MMACA), para-methylaminocinnamic acid (PMACA), ortho-dimethylaminocinnamic acid (ODACA), meta-dimethylaminocinnamic acid (MDACA), para-dimethylaminocinnamic acid (PDACA), ortho-nitrocinnamic acid (ONCA), meta-nitrocinnamic acid (ONCA), para-nitrocinnamic acid (ONCA), respectively. And their chemical structures are shown in Fig. 4.13.

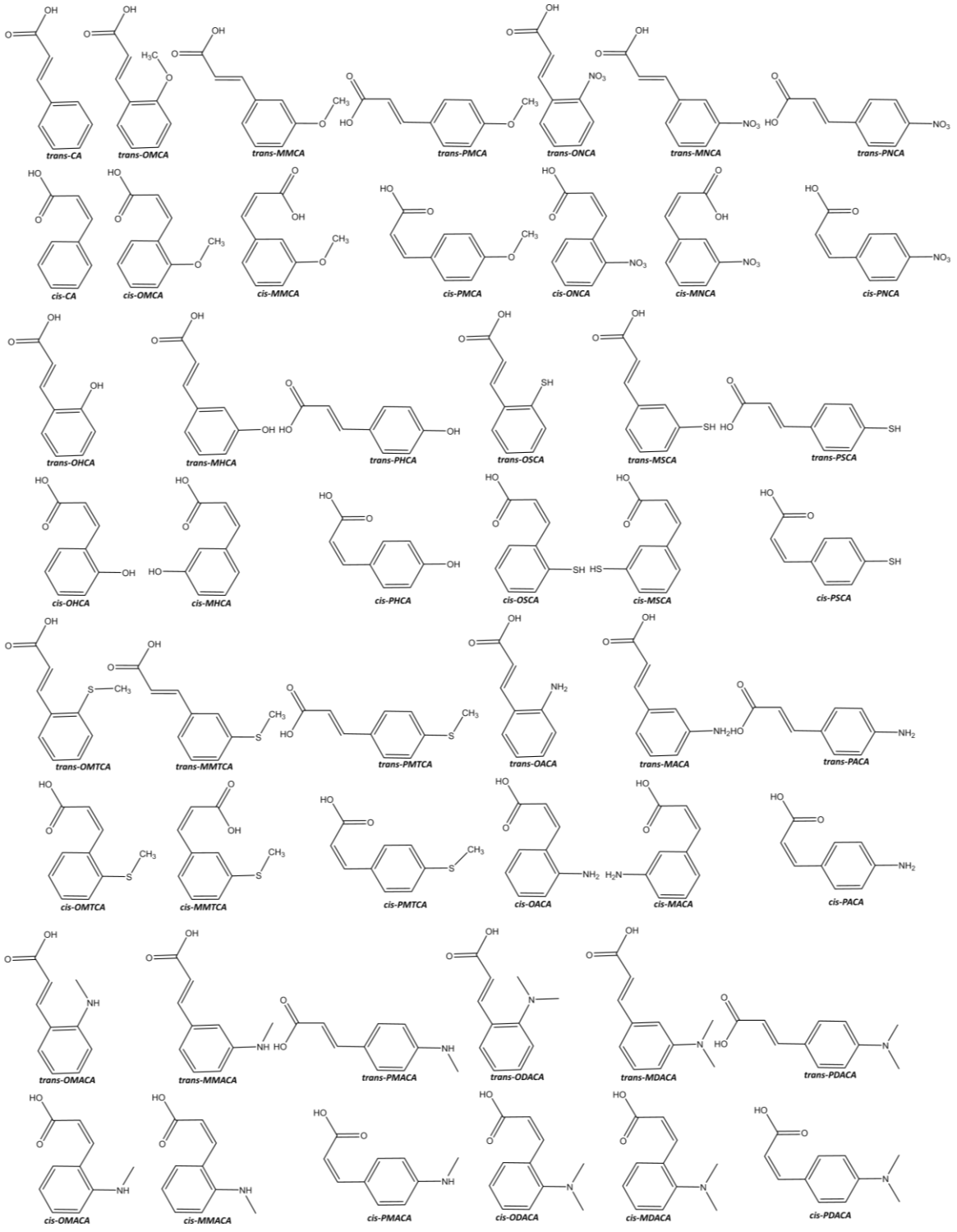

Fig. 4.13 The structures of cinnamic acids for calculations to screen out the photosensitive molecule with the best photosensitive ability

Fig. 4.14 shows the difference in ionic molar volume (ΔV the black column) of *trans/cis*-cinnamic acid ions and in solvation free energy (ΔE the red column) before and after UV irraidaition, photo-isomerization reaction equilibrium constants at singlet state $K_{g\text{-}s}$ and triplet

state $K_{g\text{-}t}$, the maximum of negative electrostatic potensial *cis*-maximun, *trans*-maximun, and their difference Δmax of *trans/cis*-cinnamic acid ions. According to our previous work, positive ΔV and negative ΔE values help to promote the photo-responsive ability of corresponding wormlike micelle. We can see from Fig. 4.14 that there are only OMCA, ODACA, PHCA and PNCA that meet this condition. In addition, it can be seen from Table 4.4 that at triplet state, the $K_{g\text{-}t}$ values of several cinnamates are greater than 1000, including OMCA, OHCA, OMACA, MMCA, PMCA and PMTCA, which represents a good conversion fraction after long enough UV irradiation. As for the Δmax, the values of OMCA, OHCA, OMTCA, OSCA, ONCA, MNCA, MSCA and PNCA are larger than 0.3, indicating that the electrostatic interaction with surfactant of these corresponding cinnamates decrease more significantly after UV irradiation. Based on the above results, among all cinnamates, the largest ΔV and ΔE as well as the larger Δmax under UV irradiation, and the higher equilibrium constant endow OMCA with a best photo-sensitivity.

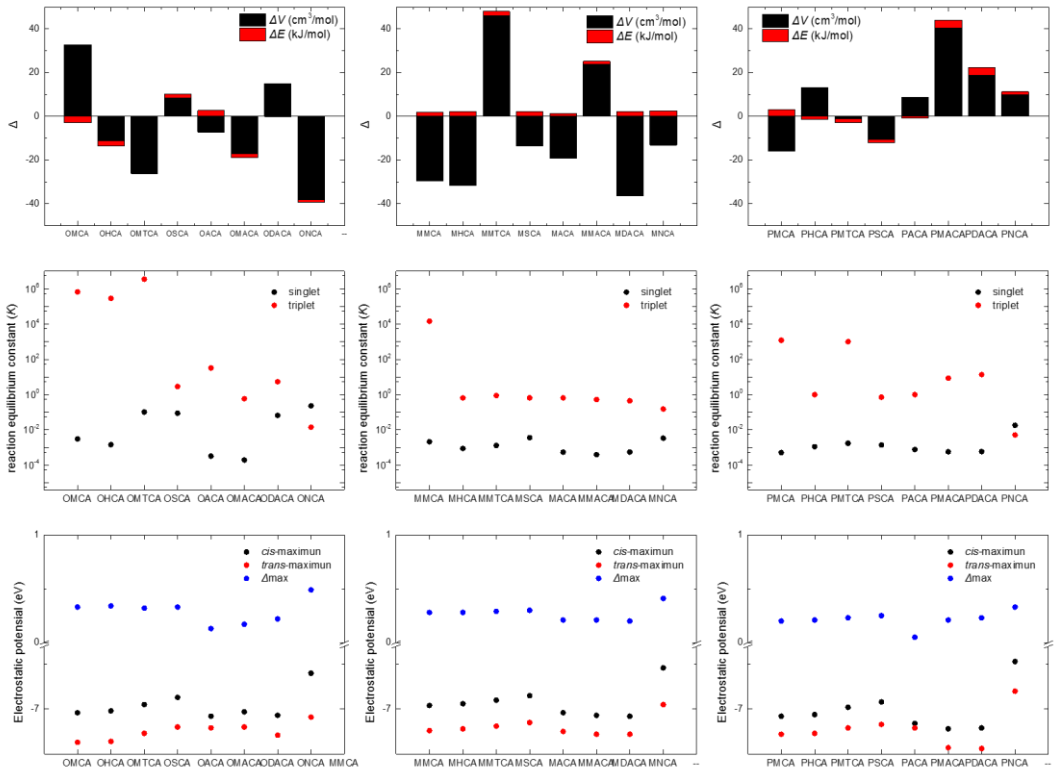

Fig. 4.14 The calculated difference of ionic molar volume (ΔV (cm^3/mol) the black column) and solvation free energy (ΔE (kJ/mol) the red column), and photo-isomerization reaction equilibrium constants at singlet state $K_{g\text{-}s}$ and triplet state $K_{g\text{-}t}$, the maximum of negative electrostatic potensial (eV) *cis*-maximun, *trans*-maximun, and their difference Δmax of *trans/cis*-cinnamic acids after UV irraidaition.

4.4 Conclusion

In this chapter, we have combined MD simulations with quantitative calculations to study the photo-responsive behavior of the wormlike micelle systems containing Gemini surfactant 12-3-12·2Br$^-$ and three *trans*-methoxy-cinnimates with methoxy group in ortho-, meta- and para- position. In MD simulations, we have simulated the wormlike micelles, rod-like and spherical micelles corresponding to the experimens and the transition between them successfully before and after UV irradiation. These micelle morphologies were recomfirmed by the density distribution and the *P*s. The different packing patterns between 12-3-12·2Br$^-$ and *trans*/*cis*-isomers were visualized and then confirmed by $g(r)$ and SASA. The interaction energy between 12-3-12·2Br$^-$ and *trans/cis*-isomers illustrates that the micelle containing *trans*-isomers is more stable.

Quantitative calculations including the electrostatic potential distributions, solvation free energy, molecule volume, angle α and interaction energy of typical packing patterns help us to explore the difference in structure and property between *trans*/*cis*-isomers. These results indicate that the presence of ortho-substituent in cinnamate has a more significant impact on strengthening the difference of the steric hindrance, electrostatic distribution and hydrophilicity of the *trans*/*cis*-cinnamates before and after UV irradiation and further promotes the photo-responsive ability of corresponding wormlike micelle.

We further used the quantitative calculations to predict the photo-sensitivity of several cinnamic acids. Considering the molar volume, hydrophilicity, electrostatic distribution, reaction equilibrium constant comprehensively, the photo-sensitivity of OMCA is the best.

Chapter 5 The rise of bubbles in shear thinning fluid

5.1 Introduction

Bubbly liquids have many practical applications, for instance in flotation of minerals, water purification, two-phase reactors, and fizzy drinks. The role of the bubbles can be active to fix impurities or passive to change the fluid texture. However, due to the large density difference between the liquid and the gas, the bubbles will rise in most of the cases. In flotation or purification this allows to concentrate the material to be separated from the solution in the foam at the top. In many applications, the fluids are non-Newtonian which brings changes the bubble dynamics in ways that are not fully understood yet [202].

The motion of single bubbles in Newtonian liquids under the action of gravity has been extensively investigated [203]. The problem is more complex than for solid particles because bubbles usually deform and may even shrink under the action of capillary pressure. Bubbles can deform if viscous or inertial forces are able to overcome the capillary forces. The degree to which bubbles are deformed can be predicted using the capillary and Weber numbers [204]. Their motion also depends on the surface boundary condition: the surface is usually immobile due to residual contaminants but may become mobile in the presence of surfactants [205]. Bubbles may also shrink or grow due to capillary pressure differences (Ostwald ripening) and coalesce.

Bubble rise is non-Newtonian fluids has been recently reviewed by Zenit and Feng [202]. When bubbles rise in a non-Newtonian fluid new feature can be observed: instead of flattening, the bubbles can take the form of a tear drop with a sharp tip. In shear-thinning fluids, increased velocity of the bubble leads to increased shear, which results in a decreased drag. The combination of shape change and decreased drag has been shown to result in a velocity jump, where the rise velocity of single bubbles increases sharply above a critical radius.

Once several bubbles are rising together, they interact. While the pair-wise interaction in non-Newtonian fluids is still not fully understood [202], it is known that the interaction depends on the rheology of the suspending fluid, and in shear thinning fluids (of interest in the current thesis), the bubbles tend to approach each other. This is because the leading bubble will leave the fluid in its wake in a state of lower viscosity, thus allowing the following bubbles to rise faster and to catch up. Indeed, bubbles organising in columns or into clusters are frequently observed. Clustered bubbles rise faster than those that remain separated.

In Newtonian fluids an increase of bubble volume fraction leads to a decrease in the rise velocity [203]. However, in shear thinning fluids a maximum has been observed as a function of bubble volume fraction [206], the studies have explored volume fractions of bubbles up to 10 %.

The increase can occur, both because of higher shear rates around the concentrated bubbles, which leads to lower viscosities, and because of clustering.

In order to explore the influence of the fluid rheology of bubble rise, we chosed a model shear thinning fluid composed of wormlike micelles of CTAB (cetytrimethyl ammonium bromide) NaSal (sodium salicylate). Moderate concentrations of NaSal result in Newtonian solutions of increasing viscosity before becoming shear thinning and viscoelastic at higher concentrations. This system has been widely used in many studies involving flow of shear thinning fluids [207]. Recently Kostrezwa [208] explored single particle sedimentation in CTAB/NaSal mixtures (4 mm stainless steel sphere), where they found a decrease of the sedimentation velocity with decreasing micellar length in agreement with lower viscosities.

In this thesis, we will address the case of small bubbles in solutions of micelles of varying viscosity. We measured the bubble rise velocity at different gas volume fractions in the different solutions. We are interested in bubble rise in concentrated dispersions of bubbles, volume fractions up to 30 %, as these high volume fractions are encountered in applications such as flotation. The difference between bubble rise in Newtonian and shear thinning fluids were systemically studied. We show that bubble rise in the shear thinning fluids is faster than predicted from the viscosity of the solutions if the shear is sufficient for the bubbles to experience the shear thinning of the fluids. If the bubble rise is sufficiently slow and the bubbles experience a constant viscosity, the bubbles rise as in Newtonian fluids. We also discuss the implications of the particular dependence on bubble volume fraction to flotation design.

5.2 Materials and Methods

5.2.1 Materials

The surfactant cetyltrimethylammonium bromide (CTAB) was purchased from Sigma-Aldrich with 99 % purity. Sodium salicylate (NaSal) was purchased from VWR with 100 % purity. They were used without further purification. Ultrapure water with a resistivity of 18.2 MΩ.cm produced using a Veolia water purification system was used to prepare all samples.

5.2.2 Sample preparation

Series of solutions were prepared with 20 mM of CTAB and increasing concentrations of NaSal (0-13 mM) by adding ultrapure water into the weighed compounds. The solutions were sonicated in a Branson 3510 Ultrasonic Cleaner for 1 h to homogenise the solution. The solutions were stored at room temperature (22 ℃) for at least 24 h to ensure equilibration.

5.2.3 Rheology

The viscosity of the samples was measured using an MCR302 rheometer (Anton Paar, Graz, Austria). A cone plate system (CP50-2) with a radius of 50 mm and a taper angle of 2 ° was used. The temperature is controlled with a Peltier plate and set to 22 °C. The samples were inserted in the rheometer about 5 min before the measurement. Flow curves were measured at increasing shear rates from 0.01 s^{-1} to 1000 s^{-1}. The shear moduli were measured with a constant strain of $\gamma = 1$ %.

5.2.4 Generation of bubbly liquids

Bubbly liquids were prepared using the double syringe method, which has been characterised by Gaillard [209] Two 10 mL syringes from Fisher scientific were used with a tube connector with an inner radius of 2 mm. The CTAB/NaSal mixed solutions were poured into the syringe directly. The gas fraction of air was measured using the syringe indicators, and is known to ± 2 %. The syringe pistons were pushed back and forth 30 times for each sample to obtain bubbles of well-defined radius (typically between 15 and 40 μm). The gas fraction φ_{gas} was varied between 5 % and 30 % in the samples.

5.2.5 Bubble size

A Malvern Mastersizer laser granulometer (Malvern Instruments, France) was employed to measure the surface weighted mean radius of the bubbles (R_{32}, Sauter radius). The sample dispersion unit was filled with 10 mM CTAB solution, this concentration was sufficient to ensure that the bubbles were stable during measurement but less wasteful of CTAB as each measurement requires two litres of solution. After generation of the bubbles, the samples were transferred into the sample dispersion unit of Mastersizer with the stirring speed 1000 r/min. The bubble size was measured 10 times with a 3 s measurement time and an average taken.

5.2.6 Bubble rise velocity

After preparation, the bubbly liquids were immediately transferred into glass vials. A Ueye camera was used to observe the bubble rise. The time interval between images was 30 seconds for most experiments, but for the samples with very fast bubble rise the interval was decreased to 5 seconds.

The Image J software was used to analyse the photographs, monitoring the grey scale I of pixels. In order to locate the front accurately, we determined the front position corresponding to different grey values. The details on how to obtain the average grey value of a certain area and the corresponding front position can be found in Figure 5.6.

5.2.7 Surface tension

The surface tension experiments were performed with a Tracker instrument (Teclis, France) at 20°C in the rising bubble configuration A bubble was created and the surface tension was measured during 10 minutes at which point it had reached its equilibrium value for all of the samples and no longer changed. These values are shown in Table 5.1.

Table 5.1 Surface tension of mixed CTAB/NaSal solutions. CTAB concentration: 20 mM

NaSal concentration (mM)	0	4	10	13
Surface tension (mN/m)	35.1	31.5	27.4	27.0

The surface tension decreases when the NaSal concentration increases, a common effect for salts (they screen the electrostatic repulsion between surfactant polar heads, the surface layer becoming more compact).

5.3 Results and Discussion

5.3.1 Rheology of micellar solutions

In order to interpret the rise of bubbles in micellar solutions, we need to determine the viscoelastic properties of the solutions, which depend on the concentration of NaSal. The increase in the concentration of NaSal causes the micelles to gradually change from small elliptical ones to long tangled worm-like micelles, and the solutions become viscoelastic [210].

We have measured the flow curves of mixed solutions for 20 mM CTAB and different NaSal concentrations, as shown in Fig. 5.1. These solutions exhibit two types of behaviour, at low shear rates viscosity is independent of shear rate, however above a critical shear rate they become shear thickening (empty symbols) or shear thinning (filled symbols).

For pure CTAB solution and CTAB solutions with low NaSal concentrations (0, 2, 4, 8, 9 mM empty symbols) at low shear rates the viscosity is independent of shear rate, and they behave as Newtonian fluids. As the concentration of NaSal increases to 8 and 9 mM, the viscosity of the solution increases to several times that of pure CTAB solution. At high shear rates (30-100 s^{-1}) a shear thickening is observed. As will be seen later, the shear rates experienced by the bubbles are smaller and we will call these solutions “Newtonian” in the following.

In the solutions at higher concentrations (NaSal concentration = 10, 11, 11.5, 12, 12.5, 13 mM, filled symbols) a viscosity plateau at low shear rates is observed, which is followed by a shear thinning behaviour. Shear thinning starts at lower shear rates as the concentration of NaSal

increases. These samples will be referred to as “shear thinning”.

The response of the solutions to shear can be explained by the structure of the micelles. In pure CTAB solution and at low low NaSal concentrations, the surfactants self-assemble into small cylindrical micelles [210-211]. As the concentration of NaSal increases to 8 and 9 mM, the viscosity of the solution increases, as the length of the micelles increases. This is because as the concentration of NaSal increases, the Sal^- ions incorporate into the surfactant layer. The observed shear-thickening phenomenon is induced by the formation of shear-induced structures, the origin of which is not yet fully understood [212].

When the concentration of NaSal reaches 10 mM, the length of the wormlike micelles is large, they begin to entangle. As the shear rate increases, above a critical value the solutions become shear thinning and the viscosity starts to decay as $\dot{\gamma}^{-1}$ This behaviour has been attributed to shear banding [212-213].

The frequency dependence of the shear moduli G' and G'' are shown in Fig. 5.2. The storage modulus G' remains smaller than the loss modulus G'' up to 10 mM NaSal, meaning that the solutions are predominantly viscous. At larger salt concentration, G' become slightly larger than G'' above frequencies of the order of 1 Hz. Even for the largest salt concentration, the storage modulus is very small (G' less than about 1 Pa).

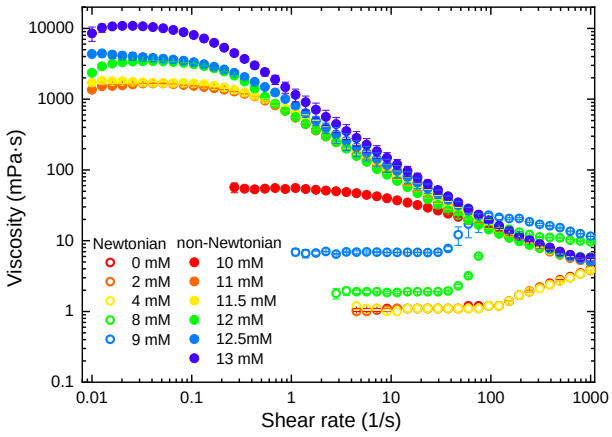

Fig. 5.1 Flow curves of solutions containing CTAB (20 mM) and NaSal (0-13mM) at 22°C. The Newtonian solutions have empty symbols and the shear thinning filled symbols, the NaSal concentrations are indicated in the legend.

Fig. 5.2 shows the variation of the shear moduli G' and G'' with the frequency for the mixed system of 20 mM CTAB and (0-13 mM NaSal) at 22°C. The storage modulus G' remains smaller than the loss modulus G'' for Newtonian solutions, meaning that the solutions are predominantly viscous. When the solution becomes non-Newtonian (NaSal concentration above 10 mM), G' is smaller than the G'' at low shear rates, but G' surpasses G'' above

frequencies of the order of 1 Hz. Even for the largest salt concentration, the storage modulus is very small (*G'* less than about 1 Pa).

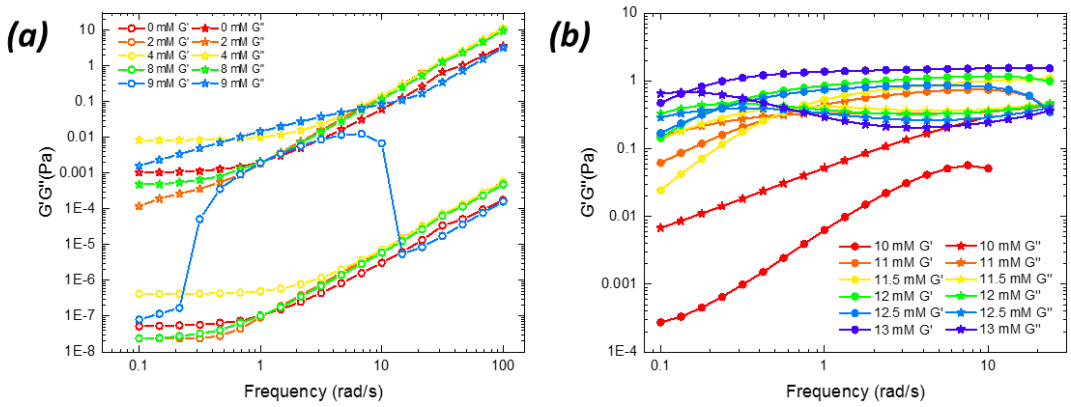

Fig. 5.2 The The storage modulus G' and loss modulus G'' with frequency for the 20mM CTAB and NaSal (0-13mM) samples at 22°C. (a) Newtonian solution; (b) shear-thinning solutions.

5.3.2 Bubble size

The generation of bubbles in viscous fluids is not easy. We made the bubbles using the double syringe method with bubble volume fractions ranging from 5 to 30 %. In this gas fraction range, all the gas is incorporated into the solution. We did not use higher gas volume fractions as all the gas can no longer be incorporated into the most viscous samples. Once the bubbles are formed, we measure their size using a Mastersizer 3000. The Sauter radius R_{32} is shown in Fig. 5.3 for all the samples studied. The error bars denote the standard deviation between ten subsequent measurements. The bubbles made in the Newtonian solutions are shown with empty symbols and the bubbles in the shear thinning solutions with filled symbols.

The bubble size is the smallest for the samples with the lowest concentrations of NaSal and remains almost constant until 8 and 9 mM NaSal when a transition to larger bubbles is observed. These two samples are still Newtonian but have higher viscosities than the other samples.

For small NaSal concentrations, the average bubble radii are between 12 and 22 μm (still larger with 8 and 9 mM NaSal). The bubble size increases weakly, but systematically, with gas volume fraction φ_{gas}. The bubble size distributions are shown in Fig. 5.4. As φ_{gas} increases, the bubble size distributions become wider. In the shear thinning solutions, the bubble sizes are larger, between 25 to 35 μm. There is no dependence of the bubble size on the gas fraction, but as with the Newtonian solutions, the bubble sizes have wider distributions at higher gas fractions.

The bubble size is in principle affected by surface tension: the lower the tension, the easier

it should be to make bubbles and hence the smaller the radius. Table 5.1 shows that surface tension decreases with NaSal concentration. This should lead to a smaller bubble size, but this is not what we observe. This suggests that other factors control bubble size. In the two syringe method Gaillard *et al*. found that bubble size increases with φ_{gas} and decreases with viscosity [209]. The trend observed with φ_{gas} with the Newtonian solutions in Fig. 5.3 is consistent with this work, but here the more viscous samples have larger bubbles. In the work of Gaillard *et al* the solutions used were Newtonian, whereas our solutions are shear-thinning or shear-thickening at high shear rates. In the two-syringe method, as the bubbly liquid passes through the constriction, it experiences very high shear rates. We estimated the shear rate from the piston velocity ≈ 10 cm/s and the constriction radius of 2 mm as around 50 s^{-1}. This is close to the shear-thinning transition, which makes prediction of the viscosity. In any case, a full understanding of the bubble generation in shear thinning fluids is beyond the scope of this thesis.

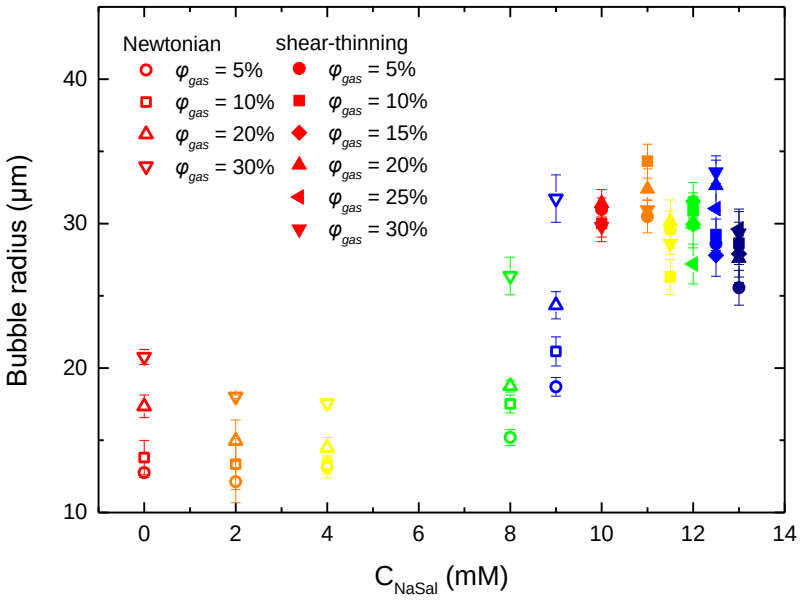

Fig. 5.3 Sauter radius of bubbles produced in solutions with CTAB (20 mM) and NaSal (0-13mM) at 22 °C. The corresponding bubble size distributions can be found in Fig. 5.4.

Fig. 5.4 shows the size distributions of bubbles made with the two-syringe technique using solutions containing 20mM CTAB and various amounts of NaSal (0-13mM) at 22°C. In Newtonian fluids, the bubble size distributions become wider with increase of φ_{gas}, and the peak position moves to higher values. In the non-Newtonian solutions, no obvious dependence of bubble size on gas fraction can be found.

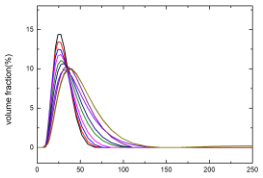

20mM CTAB φ_{gas}= 5%

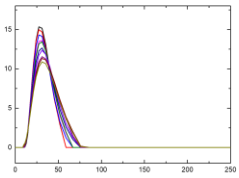

20mM CTAB φ_{gas}= 10%

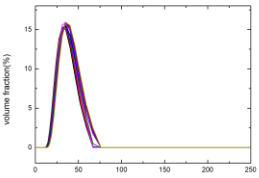

20mM CTAB φ_{gas}= 20%

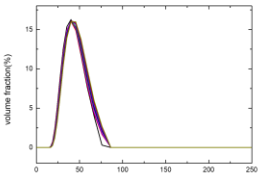

20mM CTAB φ_{gas}= 30%

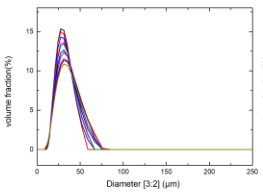

20mM CTAB+2mM NaSal φ_{gas}= 5%

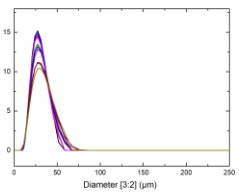

20mM CTAB+2mM NaSal φ_{gas}= 10%

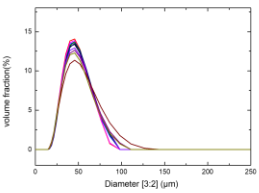

20mM CTAB+2mM NaSal φ_{gas}= 20%

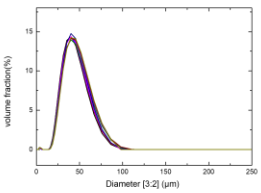

20mM CTAB+2mM NaSal φ_{gas}= 30%

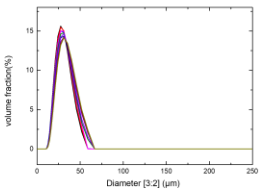

20mM CTAB+4mM NaSal φ_{gas}= 5%

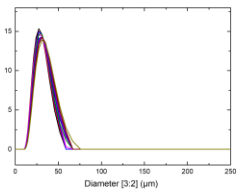

20mM CTAB+4mM NaSal φ_{gas}= 10%

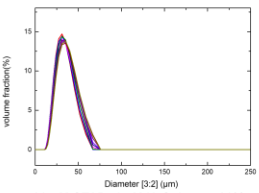

20mM CTAB+4mM NaSal φ_{gas}= 20%

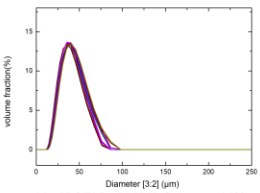

20mM CTAB+4mM NaSal φ_{gas}= 30%

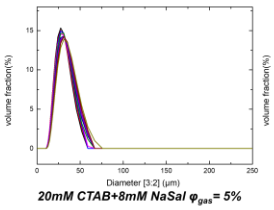

20mM CTAB+8mM NaSal φ_{gas}= 5%

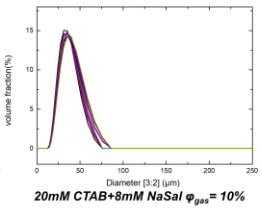

20mM CTAB+8mM NaSal φ_{gas}= 10%

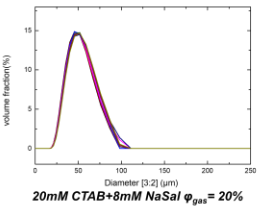

20mM CTAB+8mM NaSal φ_{gas}= 20%

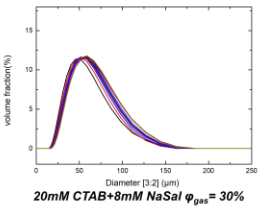

20mM CTAB+8mM NaSal φ_{gas}= 30%

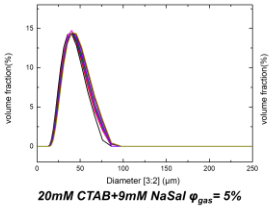

20mM CTAB+9mM NaSal φ_{gas}= 5%

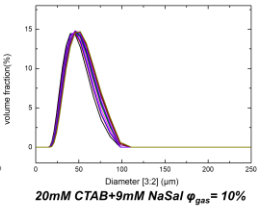

20mM CTAB+9mM NaSal φ_{gas}= 10%

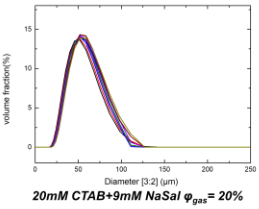

20mM CTAB+9mM NaSal φ_{gas}= 20%

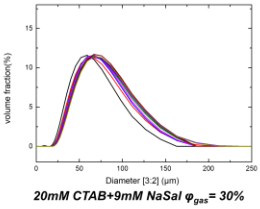

20mM CTAB+9mM NaSal φ_{gas}= 30%

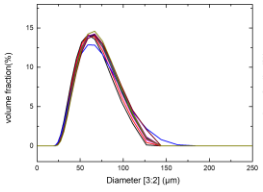

20mM CTAB+10mM NaSal φ_{gas}= 5%

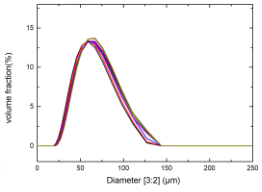

20mM CTAB+10mM NaSal φ_{gas}= 10%

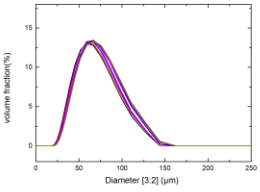

20mM CTAB+10mM NaSal φ_{gas}= 20%

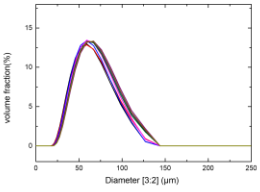

20mM CTAB+10mM NaSal φ_{gas}= 30%

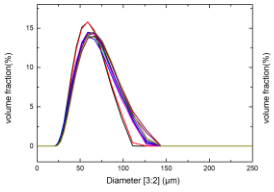

20mM CTAB+11mM NaSal φ_{gas}= 5%

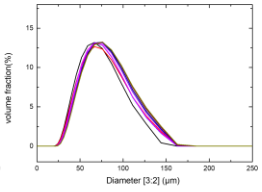

20mM CTAB+11mM NaSal φ_{gas}= 10%

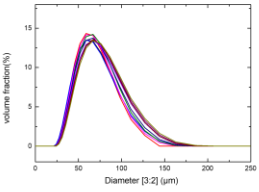

20mM CTAB+11mM NaSal φ_{gas}= 20%

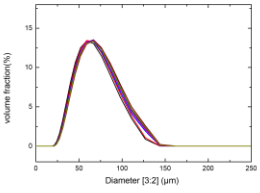

20mM CTAB+11mM NaSal φ_{gas}= 30%

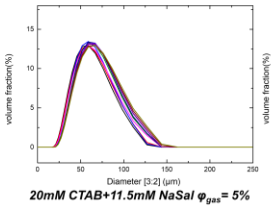

20mM CTAB+11.5mM NaSal φ_{gas}= 5%

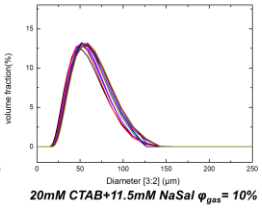

20mM CTAB+11.5mM NaSal φ_{gas}= 10%

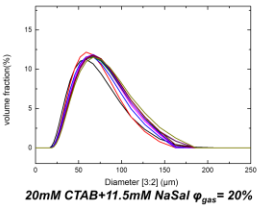

20mM CTAB+11.5mM NaSal φ_{gas}= 20%

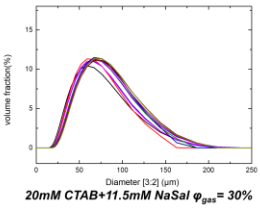

20mM CTAB+11.5mM NaSal φ_{gas}= 30%

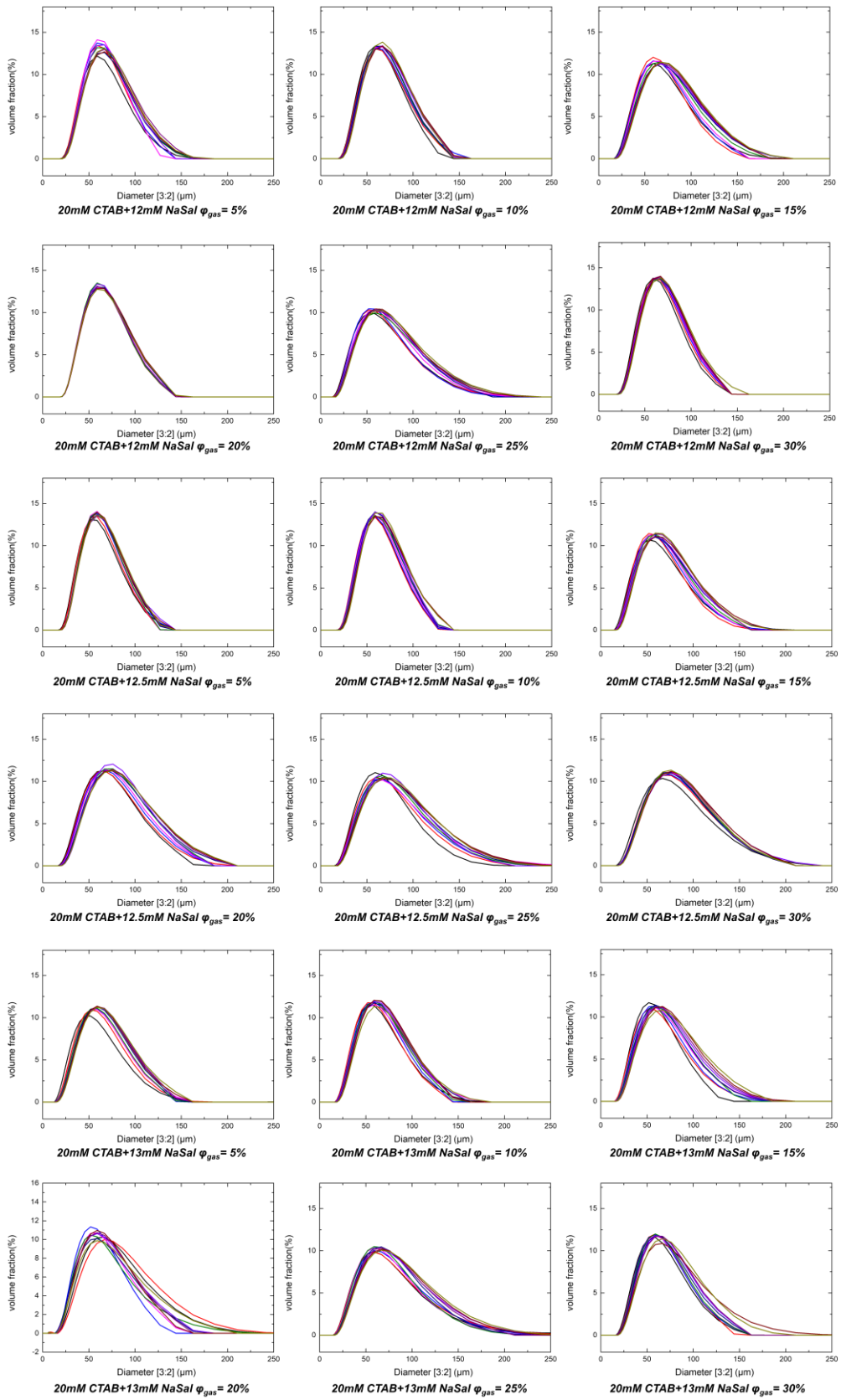

Fig. 5.4 Bubble size distribution of 20 mM CTAB and various amounts of NaSal (0-13 mM) for bubbles made with the two-syringe method at 22 °C. The volume fraction represents the gas fraction.

Fig. 5.5 shows the width of the bubble size distribution at half height and the width normalized by the bubble size. The width exhibits the same trends as the bubble size with the increase of the viscosity and gas fraction,

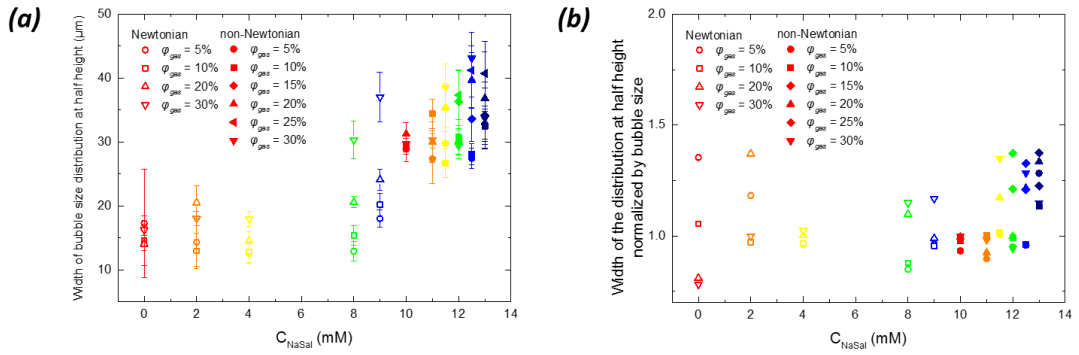

Fig. 5.5 Width of the size distribution at half height for bubbles (a) and width of the distribution at half height normalized by bubble size (b) in solutions of 20 mM CTAB and NaSal (0-13 mM) at 22 °C

5.3.3 Measure of the bubble rise velocity

In order to investigate how bubbles rise in the CTAB/NaSal solutions, we took photographs of bottles filled with bubbly liquids in transmission to track the rise of the bubble front. Fig. 5.6 (a) shows photographs of the bottles during bubble rise in solutions containing 20 mM CTAB/4 mM NaSal and φ_{gas} = 5%. The bubbly liquid appears black, as the bubbles scatter light strongly. In time, bubbles rise and a front between the bubbly liquid and a clear liquid (devoid of bubbles) becomes visible. We define I as grey value of the pixel and define the top of the bubble liquid as Height = 0. The front moves upwards in time and from the evolution of its position, we measure the bubble rise velocity using the Image J software and draw the variation of corresponding gray value with the front height of bubbly liquid at different time, as shown in Fig. 5.6 (b).

The intensity in our images varies between 0 and 160. We chose three grey values I = 40, 80 and 120 (smaller I means darker regions) and measured the corresponding front position versus time. The results are shown in Fig. 5.6 (c). The front position varies linearly with time, but the rise velocities for each grey value are different at 0.31 mm/s (I = 40), 0.23 mm/s (I = 80), 0.18 mm/s (I = 120). The differences are due to the broadening of the rise front, which in turn is caused by the polydispersity in bubble size. As the smallest bubbles rise more slowly, the lowest intensity will be sensitive to the smallest bubbles. In the following we will use the measurements with I = 80, which is the average intensity in the images to define the position of the bubble rise front.

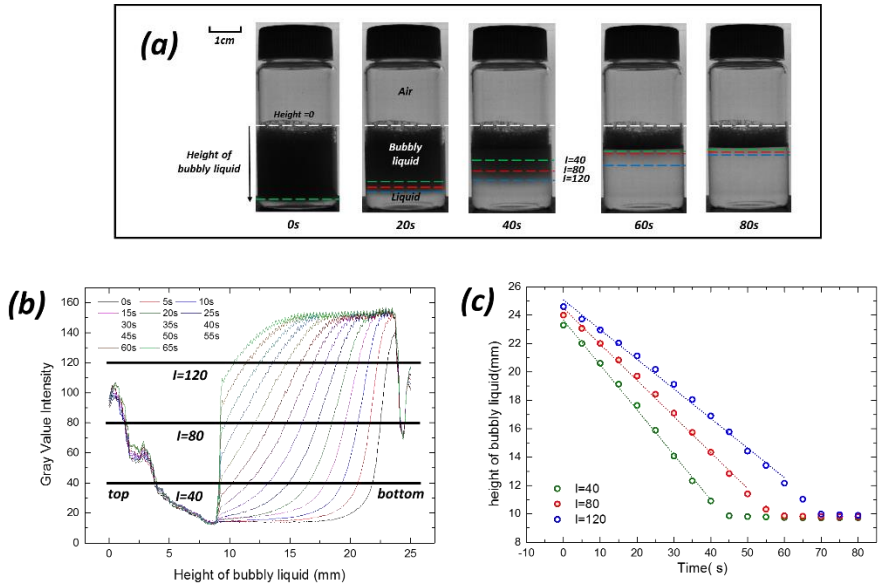

Fig. 5.6 (a) Images of the bottles containing bubbly liquids at different times, showing the front evolution. The three horizontal lines (green, red and blue) indicate the position of the front for the three different grey levels I = 40, 80 and 120 respectively. (b) Grey value curves at different times (The overlapped curves at heights below 8 mm are the top black part, which represents the foams.) (c) Height of bubbly liquid versus time for different grey levels. Solution with 20 mM CTAB and 4 mM NaSal and φ_{gas}= 5%

Fig. 5.7 shows the variation of the gray value with the height of the front during bubble rise process (a) and the bubble rise velocity curve (b) of the 20 mM CTAB and 11.5 mM NaSal at φ_{gas}= 5%. For non-Newtonian fluids at low NaSal concentration, like the Newtonian fluids, the velocity of bubble rise is constant and the gray value curve is smooth.

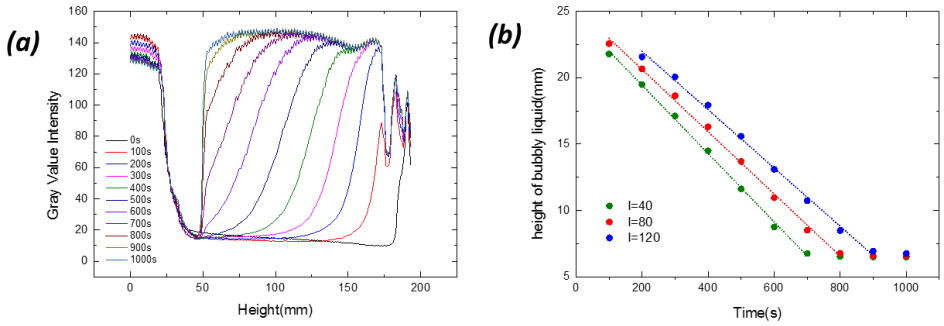

Fig. 5.7 (a) The gray value curve and (b) The bubble rise curve area of 20mM CTAB and 11.5 mM NaSal at φ_{gas}= 5%.

The front velocities are constant in time for all samples (different NaSal concentrations and gas fractions), except for the largest NaSal concentration (13 mM). In this sample the velocity changes with time, as shown in Fig. 5.8. In Fig. 5.8 (a), photographs of the bottles are shown at different stages of the bubble rise process. Fig. 5.8 (b) shows the gray value curve

versus the front height while the front height (for I = 40, 80 and 120) are shown in Fig. 5.8 (c). There is a lot of noise for the gray value curve at long time, indicating the high polydispersity of the bubble size for non-Newtonian fluids. We can observe an initial "fast" rise of the bubbles during a few 100 seconds (as seen in the inset of Fig. 5.8 (c). After this the bubbles slow down dramatically and the creaming process takes more than 15 hours. The final photograph of Fig. 5.8 (a) is taken after 63 000 s so 17.5 hours after the start, and still some small bubbles remain in solution. We will now discuss the expected bubble rise regimes, before comparing the bubble rise velocities to the predictions.

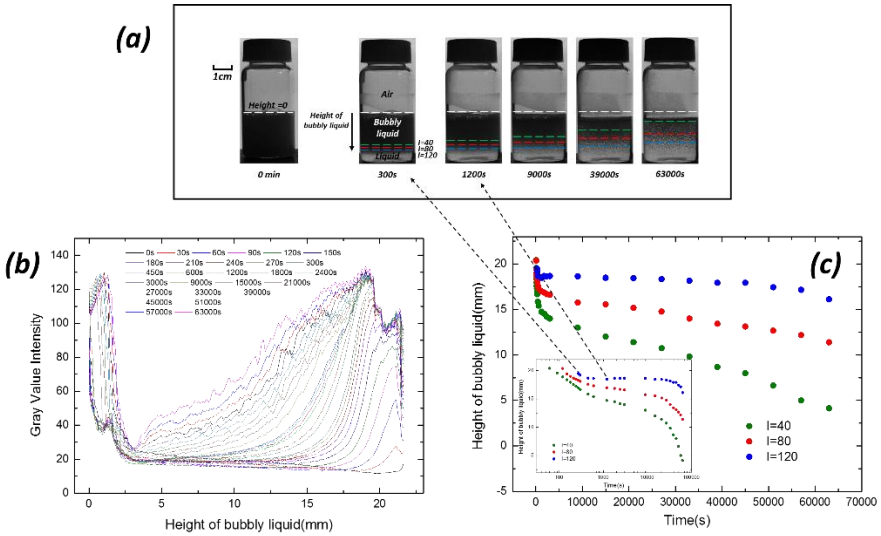

Fig. 5.8 (a) Images of the bottles containing bubbly liquids at different times, showing the front evolution at the different intensity levels I = 40 (green), 80 (red) and 120 (blue). The white line indicates the level of the bubbly liquid at the beginning of the experiment. (b) The gray value with the height of the front (c) Height of bubbly liquid versus time for different grey levels. The inset is a semi-logarithmic plot. The system shown in the image is a solution with 20mM CTAB and 13 mM NaSal at φ_{gas}= 5%.

5.3.4 Bubble rise regime

Bubble rise is known to depend on several factors: Reynolds number; bubble surface boundary condition and; whether the bubbles can deform or not. We studied relatively small bubbles (R < 35μm), for which the Reynolds number Re is small

$$Re = \frac{2\rho v R}{\eta} \tag{5-1}$$

where ρ and η are respectively the fluid density and viscosity, v the velocity, and R the bubble radius. For pure CTAB solutions, using $\rho = 10^3$ Kg/m^3, η = 1 mPa/s, v = 0.3 mm/s, R = 20 μm, we find Re ~10^{-2}. For the shear thinning solutions, v decreases and η increases and Re decreases. Therefore, the experiments are all carried out in a region of small Re.

Bubbles remain spherical if both the inertial and viscous forces are small compared to

surface tension forces [217]. This happens when the Weber number *We* and the capillary number *Ca* are small:

$$We = \frac{\rho v^2 R}{\gamma} \tag{5-2}$$

$$Ca = \frac{\eta v}{\gamma} \tag{5-3}$$

Here, with γ = 35 mN/m, $We \sim 10^{-7}$ and $Ca \sim 10^{-5}$ are both very small for pure CTAB solutions. For the solutions with NaSal, the viscosity increases but the velocity decreases, so both numbers remain small, and we can safely assume that our bubbles are not deformed during the rise process.

A further question concerns the boundary condition at the bubble surface, which would change the bubble rise velocity. In dilute surfactant solutions and small Reynolds numbers, the surfaces of rising bubbles are immobilized by surface tension gradients and Marangoni forces created by the liquid flow: surfactant is depleted from the bubbles' apex and it accumulates at their rear. The bubbles behave as solid particles [203]. When surfactant concentration is higher, the depleted surfaces can be replenished by surfactant adsorbing from the bulk. The problem was discussed in detail by Maldarelli and co-workers [205] who predicted that the Marangoni force is larger for smaller bubbles. Above the critical micellar concentration, the adsorption kinetics is also controlled by the micelle lifetime, which is very long (minutes) in the presence of salt. It is therefore likely that in our experiments, the bubble surfaces can be considered as immobile.

In this case the bubble rise velocity for a single bubble in a Newtonian fluid would be given by the Stokes expression:

$$v_s = \frac{2\Delta\rho g R^2}{9\eta} \tag{5-4}$$

$\Delta\rho$ is the difference between the gas and the fluid densities.

The Stokes expression is valid for a single particle and corrections have been proposed to account for the influence of particle concentration. When the particles behave as hard spheres, the phenomenological expression of Richardson and Zaki [214] is accurate up to large volume fractions:

$$v = v_s(1-\varphi_{gas})^n \tag{5-5}$$

Here φ_{gas} is the particle volume fraction. The exponent n varies with the Reynolds number *Re*. In the current flow regimes, we expect the n = 4.5 [215], very close to what describes data with solid particles at the *Re* encountered here [216-217].

5.3.5 Bubble rise in Newtonian solutions

In the following we will use the measurements with $I = 80$, which is the average grey value in the rising front. Fig. 5.9 shows the variation of the bubble rise velocity normalised by the Stokes velocity, v/v_s as a function of gas fraction for the Newtonian solutions measured with $I = 80$. The different velocities collapse onto a single mastercurve, as expected for Newtonian fluids. We calculate v_s using equation 3 with the experimentally measured viscosities and Sauter radii. We use the radii measured just after generation, as we do not expect the bubble size to change during their rise. This is because Ostwald ripening is too slow to change it during the rise process and we do not observe any coalescence. We can estimate the rate of Oswald ripening which does not change much with bubble volume fraction [218] and is given for small φ_{gas} by

$$\Omega = \frac{dR^3}{dt} = \frac{8}{9} \frac{\gamma D_m He^*}{P} \tag{5-6}$$

where D_m is the gas diffusion coefficient in water, He^* the Henry constant expressed as the volume fraction of gas in water and P the atmospheric pressure. For bubbles with R = 20 μm in water, $D_m = 2.6\times10^{-9}$ m^2/s, $He^* = 0.013$, which results in $\Omega \sim 10^{-17}$ m^3/s, and increase in radius of about 2 μm in 100s.

We cannot follow the individual bubbles as they rise to see if they coalesce or not. However, once all the bubbles have reached the top of the solution and form a froth, its height remains constant, suggesting the absence of coalescence. Therefore, we do not expect to have any coalescence during the bubble rise process either, as the volume fraction of bubbles is much smaller.

Small bubbles rise sufficiently slowly and the shear rate is small enough, so that the solution viscosity remains Newtonian throughout the process. For the sample at 20mM CTAB/4 mM NaSal at $\varphi_{gas} = 5\%$ the velocity is the highest at $v \sim 0.25$ mm/s. At this velocity we have the maximum shear on the bubbles, which we can estimate as $\dot{\gamma} = v/R \sim 20$ s^{-1}. This shear rate is lower than the shear rate at the onset of shear-thickening and the liquids remain Newtonian during the front motion.

The Richardson and Zaki prediction calculated using Equation (5-5) is shown in Fig. 5.10 with a black line. We can see that within error bars, the data is in good agreement with the model. The extrapolation to $\varphi_{gas} = 0$ coincides with the Stokes velocity calculated with the average Sauter radius, confirming that the bubbles behave as solid particles, as the velocity would have been higher if the bubble surfaces were mobile. Note that the Richardson and Zaki prediction does not work when larger bubbles are used [219].

In Fig. 5.10 (a) and Fig. 5.9 (b), the data for $I = 40$ and $I = 120$ are also shown. The former is slightly above the R-Z curve, while the latter is below the Richardson-Zaki curve curve. This is because the bubbly liquids are polydisperse, and at $I = 40$ we follow the largest bubbles, while

at $I = 120$ the smallest ones.

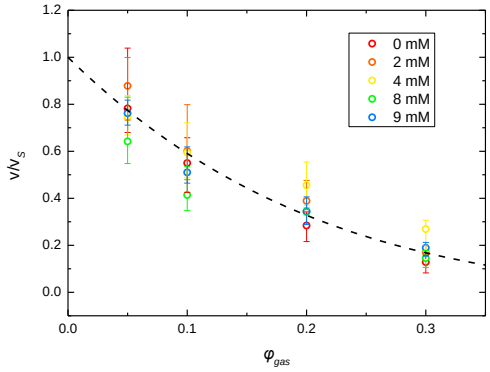

Fig. 5.9 The bubble rise velocity v normalised using the Stokes velocity v_s, as a function of gas fraction for the Newtonian solutions. The velocity is measured using the intensity $I = 80$. The solid line is the Richardson and Zaki prediction of equation (5-5) with $n = 4.5$.

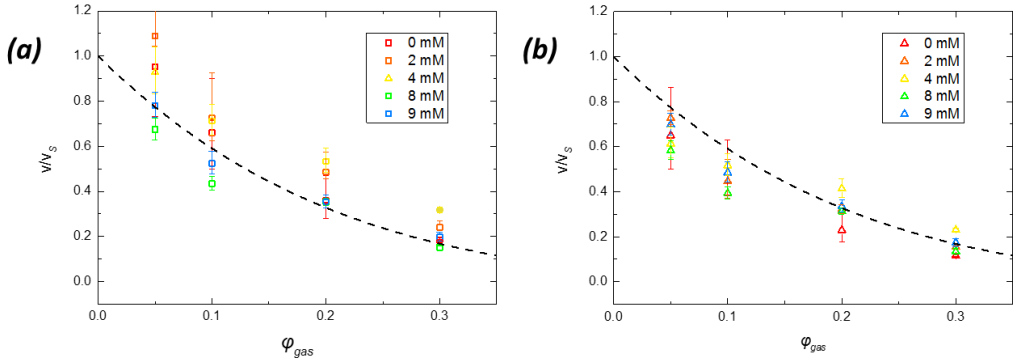

Fig. 5.10 Normalized rise velocity v/v_s as a function of gas fraction measured using the intensity $I = 40$ (a) and $I = 120$ (b) for Newtonian solutions. The solid line is the Richardson and Zaki prediction of equation (5-5) with $n = 4.5$.

5.3.6 Bubble rise velocity in non-Newtonian solutions

For the shear thinning solutions, the initial front velocities are shown in Fig. 5.11(a) as a function of gas volume fraction. As in the Newtonian solutions, the velocity decreases with increasing NaSal concentration, so with increasing viscosity of the samples. In order to better compare the allure of the φ_{gas} dependencies we normalised the velocities with the velocity at $\varphi_{gas} = 0.05$. The results are shown in Fig. 5.11 (b), with the predicted evolution by Richardson and Zaki shown as the dashed line.

The decrease of the rise velocity with gas fraction is much weaker than predicted by Equation (5-5) and almost vanishes at large NaSal concentration (see Fig. 5.11 (b)). Therefore, the Richardson and Zaki prediction does not seem to apply here. For the most viscous samples,

the velocity can even be higher at higher φ_{gas} as seen with the samples with 12.5 and 13 mM of NaSal, we will come back to this a little later.

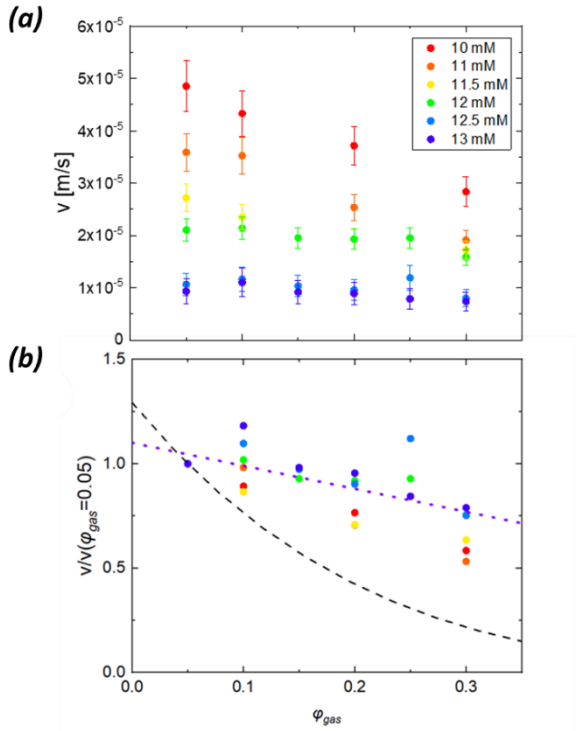

Fig. 5.11 (a) Front rise velocity, v as a function of φ_{gas} for the non-Newtonian solutions, i.e., CTAB 20 mM with NaSal 10-13 mM indicated in the legend. The velocities are measured using $I = 80$. (b) Front velocity normalised by the velocity at $\varphi_{gas} = 0.05$, the dashed line shows the prediction of Richardson and Zaki equation. The weak variation of the velocity as a function of φ can be described using $\frac{v}{v(\varphi_{gas}=0.05)} = 1.1(1-\varphi_{gas})$ the dotted (colour) line.

The evolution of the rise velocity with φ_{gas} is different than with Newtonian solutions, however this might be because the viscosity experienced by the bubbles depends on their velocity. We can compare the bubble rise velocities to those found in Newtonian solutions if we can estimate the viscosity experienced by the bubbles as they rise (as done for single particles sedimenting in viscoelastic solutions by Gheissary et al for example [220]). We use the velocity at $\varphi_{gas} = 0.05$ and and the average bubble radius $\langle R \rangle$ of 30 µm to estimate the shear rate as $\dot{\gamma} \sim \frac{v(\varphi_{gas} = 0.05)}{R}$. We can then calculate $v_s(\eta)$ using equation (5-4) with $\eta(\dot{\gamma})$ and $\langle R \rangle$. The front velocities normalised by $v_s(\eta)$ are shown in Fig. 5.12.

For the sample at NaSal = 10 mM (black points) the normalised velocities with the estimated $v_s(\eta)$ are close to 1 (between 0.7 and 1.2). This can be explained by the low shear rate experienced by the bubbles at 1.6 s^{-1}, which lies on the Newtonian plateau. However, for all of the other samples the situation is very different, and the measured velocities are around

10 times higher (for NaSal = 13 mM they are almost 20 times higher). Either our estimation of the shear rate and hence the velocity is poor, or then we are in a different bubble rise regime.

Vélez-Cordero and Zenit showed that at small *Re* and large *Bo* bubbles cluster while they rise [221]. The prediction for the free bubble to clustering could be predicted from studies on pairs of bubbles and is due to attractive hydrodynamic interactions acting via the bubbles wake. The studies were done with lower φ_{gas} and larger monodisperse bubbles. Comparing to their predictions, the bubbles in our systems could be expected to be in the clustering regime, however due to the high volume fractions and small bubble sizes we do not observe clustering in the videos. Clustering could therefore explain the faster than expected bubble rise of Fig. 5.12. It could also explain the weak (or non-monotonous) rise velocities of Fig. 5.11 (b), as it has been shown to cause both higher rise velocities and a non-monotonous velocity dependence on φ_{gas} [202].

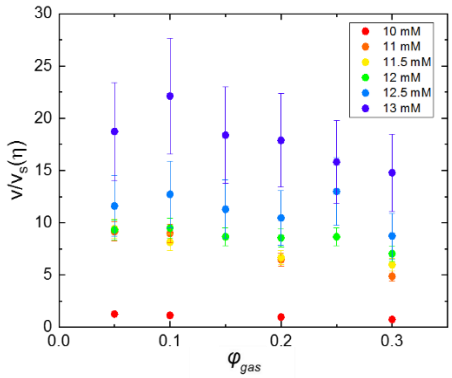

Fig. 5.12 Bubble front rise velocity *v* of the non-Newtonian samples normalised by the Stokes velocity calculated using η estimated at the shear rate around the bubbles v/R.

Another peculiarity of bubbles' motion observed for the most viscous liquid (13 mM Na Sal) is the fact that it slows down considerably after some tens of minutes, as seen in Fig. 5.7. The second bubble rise velocity is also quite constant in time; it is shown with the initial velocity in Fig. 5.13. The second velocity is around 10^{-7} m/s, which is 100 times slower than the initial velocity.

If we look at the photographs in Fig. 5.7 (a) corresponding to the slow rise regime, we can see that the volume fraction of bubbles left is relatively small, with most of the bubbles having risen during the first stage. The samples are polydisperse and we know that the smallest bubbles lag behind. If we use the bubble rise velocity to again estimate the shear rate, we find $\dot{\gamma} \approx 10^{-2}$, which is on the Newtonian plateau with $\eta\,(\dot{\gamma} = 10^{-2}) = 10.7$ Pa·s. We have seen that on the Newtonian plateau, the Stokes velocity compares well with the rise velocity, therefore we can estimate the size of bubbles rising at such slow velocities. We find $R = 22$ µm, which is in the

tail of the bubble size distribution (around 10% of the bubbles). This suggests that how the bubbles rise could be different depending on their size within the polydisperse samples. The larger bubbles rise fast enough to experience shear rates within the shear thinning regime, while the smaller bubbles rise so slowly that they experience shear rates on the Newtonian plateau and hence maximal fluid viscosity. It might also be that the smaller bubbles cluster less than the larger ones, which would lead to a significant decrease in the rise velocity.

We do not see such a slow rising population of bubbles at the lower concentrations of NaSal. This is because even for the next sample with 12.5 mM NaSal the plateau viscosity is 3.9 Pa·s, which means that only bubbles with $R <$ 13 μm would reach the second creaming regime. The tail of the bubble size distribution is very close to this value and there are hardly any bubbles of this size in the samples, and explains why we do not observe the slower bubble rise in the other samples.

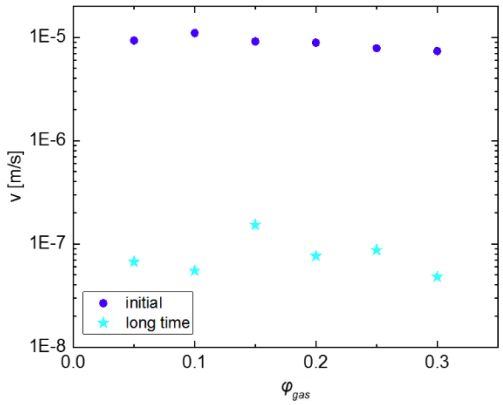

Fig. 5.13 The front rise velocity v of the initial bubble rise, and the velocity at long times, once it has considerably slowed down. Both were measured using I = 80. Solution with 20mM CTAB and 13 mM NaSal at φ_{gas}= 5%.

5.3.7 Flotation in a shear thinning fluid

Foam flotation is used to purify and separate materials from fluids: the material attaches onto the bubble surfaces, which rise up for separation. An important parameter to quantify foam flotation is the bubble surface area flux $\dot{S}$, which tells how much surface area is swept up per second and is directly linked to how efficiently the process works [222-223]. In a bubble column $\dot{S}$ is given by product of the average bubble rise velocity $v(\varphi_{gas})$ and the number density of bubbles:

$$N \propto \frac{\varphi_{gas}}{R} \tag{5-7}$$

$$\dot{S} = v(\varphi_{gas}) \frac{\varphi_{gas}}{R} \tag{5-8}$$

As v varies very differently in the Newtonian and the non-Newtonian fluids, we can expect $\dot{S}$ to also change.

In Newtonian fluids the Richardson Zaki expression works well, as given by equation (5-5). For the non-Newtonian fluids, we saw that the velocity depends weaklier on φ_{gas} (for example in Fig. 5.11 (a)). The velocity varies with volume fraction as

$$v_{Non\text{-}Newt} \propto (1-\varphi_{gas})^{1} \tag{5-9}$$

which has been shown by the dotted line in Fig. 5.11 (b). We can therefore use the two expressions for velocity to estimate $\dot{S}$ in Newtonian and shear thinning fluids. This results in very distinctive bubble surface area variations with φ_{gas}, as shown in Fig. 5.14. Indeed, if maximisation of the bubble surface area flux is an objective, in Newtonian fluids the optimum is at $\varphi_{gas} = 0.16$, while in non-Newtonian fluids higher φ_{gas} would improve the area flux. Our experiments are limited to gas fractions less than 0.3, and we cannot speculate about what happens at higher φ_{gas}. However, our results suggest that the parameters for optimum flotation when non-Newtonian fluids are present can be very different from those with Newtonian fluids.

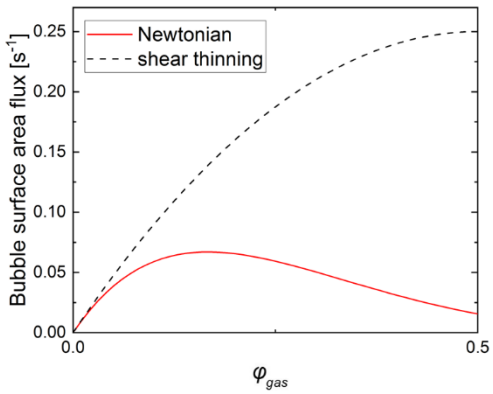

Fig. 5.14 Bubble surface area flux as a function of bubble volume fraction for Newtonian and non-Newtonian fluids. The dependence is very different, and the maximum in non-Newtonian fluids occurs at a much higher φ_{gas}.

5.4 Conclusion

We have explored bubble rise in micellar solutions of varying viscosity, with both Newtonian and shear thinning properties. We made the bubbles using two connected syringes, and observe two plateaus of bubble size: smaller bubbles at the lowest concentrations of NaSal where the bubbles are Newtonian until a viscosity jump at high shear rates, and larger bubbles in the shear thinning fluids.

The rise of the concentrated suspensions of bubbles in the Newtonian fluids is well described using the Richardson and Zaki description. However, in the shear thinning fluids

different phenomena can be observed depending on the shear rate around the bubbles, which in turn changes with bubble size and rise velocity. If the bubbles rise sufficiently slowly (smaller bubbles) such that the shear rate is on the Newtonian plateau, the bubble rise velocity is close to that expected from the Stokes velocity. However, once the shear rate around the bubbles is high enough to reach the shear thinning regime, the bubbles will rise faster and prediction using local shear rates lead to an underestimation of the bubble rise velocity, probably because of the onset of bubble clustering.

The variation of the bubble rise velocity as a function of volume fraction of bubbles is much weaker than in Newtonian fluids. Indeed, an exponent of $n = 1$ instead of around 4.5 in the Richardson and Zaki expression describes the data reasonably well. This can have important implications to the flotation process in shear thinning fluids, as we show that the maximum area flux occurs at higher gas volume fractions than found in Newtonian fluids.

Our results give insight into bubble rise of concentrations solutions of bubbles in shear thinning fluids, which have been little studied so far, despite their importance in applications. The interaction through the shear thinning fluid leads to changes in the bubble rise velocity, the exact origin of which requires further experimental and theoretical works.

Chapter 6 Conclusions

This thesis is focused on the photo-responsive behavior of a series of wormlike micelles constructed by Gemini surfactant and different cinnamates and on the applications (bubble rise) of wormlike micelles.

(1) The photo-responsive behavior of wormlike micelles constructed by 12-2-12·2Br$^-$ and *trans*-OMCA and the mechanism of its photo-responsiveness are investigated. Owing to the electrostatic interaction, *trans*-OMCA associates strongly with 12-2-12·2Br$^-$, leading to the formation of wormlike micelles. After UV irradiation, *trans*-OMCA photoisomerizes into *cis*-OMCA and then wormlike micelles break to rod-like micelles and finally to spherical micelles. Three primary factors (geometry, hydrophilicity and energy) affecting the micelle transition are unraveled systematically. The larger steric hindrance of *cis*-OMCA weakens π-cation interaction and electrostatic interaction after UV irradiation. The stronger hydrophilicity of *cis*-OMCA leads to the moving of *cis*-OMCA from micelle interior to solution. Moreover, *cis*-OMCA has a weaker interaction with the 12-2-12·2Br$^-$ than *trans*-OMCA after UV irradiation. All these factors induce the breakage and repacking of wormlike micelles.

(2) To further investigate the effects of cinnamate structures on the photo-responsive behavior of corresponding wormlike micelles, we combined experimental methods such as rheology, TEM, UV-Vis absorption spectroscopy and HPLC with calculation methods such as MD simulations and quantitative calculations to study the photo-responsive behavior of three wormlike micelle systems constructed by Gemini surfactant 12-3-12·2Br$^-$ and cinnamates (*trans*-CA, *trans*-OHCA and *trans*-OMCA, respectively).

Our experimental results show that three wormlike micelles have different photo-responsive behavior. Due to the most rapide photoisomerization velocity of *trans*-OMCA under UV and the highest *trans*-to-*cis* conversion fraction, the wormlike micelle system containing *trans*-OMCA has the most sensitive photo-responsive behavior (wormlike micelles are transformed into spherical micelle). On the contrary, the slowest photo-isomerization reaction rate and lowest conversion fraction of *trans*-CA under UV irradiation cause the wormlike micelles containing *trans*-CA to be insensitive to light; for *trans*-OHCA, the conversion fraction and the reaction rate are at an intermediate level, causing the shortening of the wormlike micelles.

In our simulation, the micelle transition corresponding to the experiment under UV is captured. The different packing patterns between cinnamates and surfactant (*trans*-isomers are embedded into the hydrophobic layers of surfactants while *cis*-isomers orient at the micelle surface) lead to the fission of wormlike micelles under UV irradiation. The quantitative

calculation results show that the presence of ortho-methoxy and ortho-hydroxyl in cinnamate has a significant impact on increasing the equilibrium constant of photo-isomeriaztion reaction and enhancing the difference of the steric hindrance, electrostatic distribution and hydrophilicity of the *trans/cis*-cinnamates, thereby improving the photo-responsive ability of wormlike micelle. And ortho-methoxy has better effects.

(3) Based on the previous research, to comprehensively study the effects of cinnamate structure on the photo-responsive behavior of corresponding wormlike micelles, MD simulations and quantitative calculations were used to investigate the influence of ortho-, meta- and para-methoxy on the photo-responsive behavior of the wormlike micelle systems containing Gemini surfactant 12-3-12·2Br^- and three *trans*-methoxy-cinnimates *trans*-OMCA, *trans*-MMCA and *trans*-PMCA.

In MD simulations, the micelle morphologies corresponding to the experimental results initially and at equilibrium were successfully captured and reconfirmed by density distributions and *P*s. Three systems show different packing patterns. With the increasing distance between methoxy and carbon-carbon double bond, the methoxy inserts more and more deeply into the micelle. In addition, the benzene rings of *trans*-isomers are embedded into the hydrophobic layers of surfactants while those of *cis*-isomers orient at the micelle surface. After UV irradiation, the motion of benzene ring in cinnamates cause the rupture of wormlike micelle.

Quantitative calculations reveal that when the methoxy is oriented in meta-, and para-position, the molar volume and hydrophilicity of cinnamates decrease after UV irradiation, which hinders the escape of *cis*-isomers, thereby weakening the photo-responsive ability of wormlike micelles. For OMCA, the ortho-methoxy is closest to the carbon-carbon double bond so that they have the largest difference in steric hindrance, electrostatic distribution and hydrophilicity before and after UV irradiation. Furthermore, the photo-sensitivity of 24 cinnamic acid ions are predicted according to their molar volume, hydrophilicity, electrostatic distribution, reaction equilibrium constant. Base on the information comprehensively, among 24 cinnamates, the photo-sensitivity of OMCA is the best.

In summary, the micellar transition mechanism of the wormlike micelles constructed by Gemini surfactant and cinnamate has been well studied. We also screened out the cinnamic acid with the best photo-responsiveness (*trans*-OMCA) among the 24 cinnamic acids. However, we still haven't found a cinnamic acid with photosensitivity that exceeds *trans*-OMCA. We will try to search more cinnamic acids and the transition state and kinetic mechanism of these cinnamic acids photoisomerization reactions will be the focus of our further research. The limitation of the time scale of the united-atom force field and the size of the box prevents us from simulating larger-sized and more complex self-assemblies, such as vesicles and gels. We will focus on the

coarse-grained force field to simulate large-scale self-assemblies. In addition, the irreversible transformation of wormlike micelles containing cinnamates hinders their industrial application. We will try to use some reversible photosensitive molecules to build a photo-responsive system in further research.

(4) We investigate the bubble rise behavior in shear thinning solutions made of cetyltrimethylammonium bromide (CTAB) and sodium salicylate (NaSal) (a common wormlike system). The results show when the NaSal concentration is low, the solutions are Newtonian fluids and the rise of the concentrated suspensions of bubbles in these fluids is well described using the Richardson and Zaki description. For the shear thinning solutions, the Richardson-Zaki relation no longer applies. Bubble clustering leads to faster rise velocities and a weaker dependence on the bubble volume fraction. At the largest concentrations two rise regimes are observed, the smaller bubbles have lower shear rates around them and they experience higher viscosities. If they rise sufficiently slowly, the shear rate reaches the plateau region, and their rise is comparable to the Stokes expectations. However, when the shear rates are in the shear thinning regimes, the bubble rise is faster than expected.

Our results also show that maximum area flux in the shear thinning solutions occurs at higher gas volume fractions than found in Newtonian fluids, and this peculiar dependence of the rise velocity with volume fraction of bubbles in the shear thinning solutions can have important implications in flotation. And in the future, we will probe more finely the different rise regimes of the bubbles in higher viscosity solutions, and study the variation of fluid structure around the bubble. In addition, it would be interesting to control the rise velocity of bubbles with external stimuli such as light or electricity.

References

[1] Nakama Y. Surfactants. Cosmetic Science and Technology: Theoretical Principles and Applications. Elsevier. 2017: 231-244.

[2] Israelachvili N. Intermolecular and surface forces. ACADEMIC PR. 2011, 20: 535-576.

[3] Chu Z, Dreiss A, Feng Y. Smart wormlike micelles. Chem. Soc. Rev. 2013, 42(17): 7174-7203.

[4] Sharma V D, Ilies M A. Heterocyclic cationic gemini surfactants: a comparative overview of their synthesis, self-assembling, physicochemical, and biological properties. Med Res Rev. 2014, 34(1): 1-44.

[5] Chu Z, Feng Y, Su X, et al. Wormlike micelles and solution properties of a C_{22}-tailed amidosulfobetaine surfactant. Langmuir. 2010, 26(11): 7783-7791.

[6] Jiang Y, Li F, Luan Y, et al. Formation of drug/surfactant catanionic vesicles and their application in sustained drug release. Int J Pharm. 2012, 436(1-2): 806-814.

[7] Loos M, Feringa B L, van Esch J H. Design and Application of Self-Assembled Low Molecular Weight Hydrogels. Eur. J. Org. Chem. 2005(17): 3615-3631.

[8] Cheng N, Hu Q, Bi Y, et al. Gels and lyotropic liquid crystals: using an imidazolium-based catanionic surfactant in binary solvents. Langmuir. 2014, 30(30): 9076-9084.

[9] Xu W, Yin Q, Gao Y, et al. Solvent and Substituent Effects on the Aggregation Behavior of Surface-Active Ionic Liquids with Aromatic Counterions and the Dispersion of Carbon Nanotubes in their Hexagonal Liquid Crystalline Phase. Langmuir. 2015, 31(46): 12644-12652.

[10] Shang Y, Liu H, Hu Y, et al. Aqueous Two-Phase System (ATPS) Containing Gemini (12-3-12·2Br^-) and SDS: Phase Diagram and Properties of ATPS. J. Dispersion Sci. Technol. 2006, 27(3): 335-339.

[11] Liang Y, Xu S, Shang Y, et al. Aqueous four-phase system of SDS/DTAB/PEG/NaBr/H2O. Colloids Surf., A. 2014, 4(54): 152-158.

[12] Shang Y, Liu H, Hu Y, et al. Phase behavior and microstructures of the Gemini (12-3-12·2Br^-)/SDS/H_2O ternary. Colloids Surf., A. 2007, 294(13): 203-211.

[13] Shang Y, Liu H, Hu Y, et al. Effect of salts on the aqueous two-phase system in mixed solutions of Gemini (12-3-12·2Br^-) and sodium dodecyl sulfate. Colloids Surf., A. 2007, 302(13): 58-66.

[14] Hartmann V, Cressely R. Simple salts effects on the characteristics of the shear thickening exhibited by an aqueous micellar solution of CTAB/NaSal. EPL. 2007, 40(6):691.

[15] Cates M, Candau S. Statics and dynamics of wormlikesurfactant micelles. J. Phys.: Condens. Matter. 1990, 2(33): 6869.

[16] Ballesta P, Lettinga M P, Manneville S. Superposition rheology of shear-banding wormlike micelles. J. Rheol. 2008, 51(5):1047-1072.
[17] Montalvo G, Khan A. Rheological properties of a surfactant-induced gel for the lysozyme–sodium dodecyl sulfate-water system. Colloid Polym. Sci. 2005, 283(4):402-412.
[18] Cates E. Reptation of living polymers: dynamics of entangled polymers in the presence of reversible chain-scission reactions. Macromolecules. 1987, 20(9): 2289-2296.
[19] Rogers A, Calabrese A, Wagner J. Rheology of branched wormlike micelles. Curr. Opin. Colloid Interface Sci. 2014, 19(6): 530-535.
[20] Dreiss A. Wormlike micelles: where do we stand? Recent developments, linear rheology and scattering techniques. Soft Matter. 2007, 3(8): 956.
[21] Wang D, Dong R, Long P, et al. Photo-induced phase transition from multilamellar vesicles to wormlike micelles. Soft Matter. 2011, 7(22): 10713-10719.
[22] He K, Xu L, Gao Y, et al. Evaluation of surfactant performance in fracturing fluids for enhanced well productivity in unconventional reservoirs using Rock-on-a-Chip approach. J. Pet. Sci. Eng. 2015, 135:531-541.
[23] Tu Y, Gao M, Ten H, Shang Y, Fang B, Liu H. A gemini surfactant-containing system with abundant self-assembly morphology and rheological behaviors tunable by photoinduction. RSC Adv. 2018, 8:16004-16012.
[24] Dong R, Zhong Z, Hao J. Self-assembly of onion-like vesicles induced by charge and rheological properties in anionic–nonionic surfactant solutions. Soft Matter. 2012, 8(30):7812-7826.
[25] Menger F M, Littau C A. Gemini-surfactants: synthesis and properties. J. Am. Chem. Soc. 1991, 113(4): 1451-1452.
[26] Menger F M,Keiper J S. Gemini surfacants. Angew. Chem., Int. Ed. 2000, 39(2000): 1906-1920.
[27] Shukla D, Tyagi V K. Cationic gemini surfactants: a review. J. Oleo Sci. 2006, 55(8): 381-390.
[28] Kumar N, Tyagi R. Industrial Applications of Dimeric Surfactants: A Review. J. Dispersion Sci. Technol. 2014, 35(2): 205-214.
[29] Xu Q, Wang L, Xing F. Synthesis and properties of dissymmetric gemini surfactants. Journal of surfactants and detergents. 2011, 14(1): 85-90.
[30] Oda R, Candau S J, Huc I. Gemini surfactants, the effect of hydrophobic chain length and dissymmetry. Chem. Commun. 1997, 21(3): 2105-2106.
[31] Oda R, Huc I, Danino D, et al. Aggregation Properties and Mixing Behavior of Hydrocarbon, Fluorocarbon, and Hybrid Hydrocarbon-Fluorocarbon Cationic Dimeric

Surfactants. Langmuir. 2000, 16(25): 9759-9769.
[32] Huc I, Oda R. Gemini surfactants: studying micellisation by ^{1}H and ^{19}F NMR spectroscopy. Chem. Commun. 1999, 26(20): 2025-2026.
[33] Lu T, Huang J, Li Z, et al. Effect of Hydrotropic Salt on the Assembly Transitions and Rheological Responses of Cationic Gemini Surfactant Solutions. J. Phys. Chem. B. 2008, 112(10): 2909-2914.
[34] Zana R. Dimeric and oligomeric surfactants. Behavior at interfaces and in aqueous solution: a review. Adv. Colloid Interface Sci. 2002, 97(1): 205-253.
[35] Zana R, Xia J. Gemini surfactants: synthesis, interfacial and solution-phase behavior, and applications. CRC Press. 2003, 117-127.
[36] Ao M, Xu G, Pang J, et al. Comparison of aggregation behaviors between ionic liquid-type imidazolium gemini surfactant [C_{12}-4-C_{12}im]Br_2 and its monomer [C_{12}mim]Br on silicon wafer. Langmuir. 2009, 25(17): 9721-9727.
[37] Tian M, Fan Y, Ji G, et al. Spontaneous aggregate transition in mixtures of a cationic gemini surfactant with a double-chain cationic surfactant. Langmuir. 2012, 28(33): 12005-12014.
[38] Bernheim A, Zana R, Talmon Y. Microstructures in Aqueous Solutions of Mixed Dimeric Surfactants: Vesicle Transformation into Networks of Thread-Like Micelles. J. Phys. Chem. B. 2000, 104(51): 12192-12201.
[39] Chen H, Ye Z, Han L, et al. Temperature-induced micelle transition of gemini surfactant in aqueous solution. Surf. Sci. 2007, 601(10): 2147-2151.
[40] Zana R, Talmon Y. Dependence of aggregate morphology on structure of dimeric surfactants. Nature. 1993, 362(6417): 228-230.
[41] Hait K, Moulik P. Gemini surfactants: a distinct class of self-assembling molecules. Current Science. 2002, 82(9): 1101-1111.
[42] Drummond J, Fong C. Surfactant self-assembly objects as novel drug delivery vehicles. Curr. Opin. Colloid Interface Sci. 1999, 4(6): 449-456.
[43] Liu C, Ny A, Schmidt J, et al. Photo-Assisted Gene Delivery Using Light-Responsive Catanionic Vesicles. Langmuir. 2009, 25(10):5713-5724.
[44] Brown P, Butts P, Eastoe J. Stimuli-responsive surfactants. Soft Matter. 2013, 9(8): 2365
[45] Li W, Yang Y, Liu L, et al. Dual stimuli-responsive self-assembly transition in zwitterionic/anionic surfactant systems. Soft Matter. 2015, 11(21): 4283-4289.
[46] Pileni P. The role of soft colloidal templates in controlling the size and shape of inorganic nanocrystals. Nat. Mater. 2003, 2(3): 145-149.
[47] Theato P, Sumerlin S, O'Reilly K, et al. Stimuli responsive materials. Chem. Soc. Rev. 2013, 42(17): 7055-7064.

[48] Dai S, Ravi P, Tam C. Thermo- and photo-responsive polymeric systems. Soft Matter. 2009, (4)5:2513-2533.
[49] Stuart C, Huck S, Genzer J, et al. Emerging applications of stimuli-responsive polymer materials. Nat. Mater. 2010, 9(2): 101-113.
[50] Fameau L, Arnould A, Saint-Jalmes A. Responsive self-assemblies based on fatty acids. Curr. Opin. Colloid Interface Sci. 2014, 19(5): 471-479.
[51] Xue X, Zhu J, Zhang Z, et al. Soluble Main-Chain Azobenzene Polymers via Thermal 1,3-Dipolar Cycloaddition: Preparation and Photoresponsive Behavior. Macromolecules. 2010, 43(6): 2704-2712.
[52] Peng S, Guo Q, Hartley P G, et al. Azobenzene moiety variation directing self-assembly and photoresponsive behavior of azo-surfactants. J. Mater. Chem. C. 2014, 2(39): 8303-8312.
[53] Zhao G, Wu X, Luan R, et al. CO_2-controllable smart nanostructured fluids in a pseudo-Gemini surfactant system. J. Mol. Liq. 2019, 27(4): 133-139.
[54] Lu H, Shi Q, Wang B, et al. Spherical-to-wormlike micelle transition in a pseudogemini surfactant system with two types of effective pH-responsive groups. Colloids Surf., A. 2016, 49(4): 74-80.
[55] Lin Y, Qiao Y, Cheng X, et al. Hydrotropic salt promotes anionic surfactant self-assembly into vesicles and ultralong fibers. J Colloid Interface Sci. 2012, 369(1): 238-244.
[56] Lin Y, Han X, Huang J, et al. A facile route to design pH-responsive viscoelastic wormlike micelles: Smart use of hydrotropes. J Colloid Interface Sci. 2009, 330(2): 449-455.
[57] Chu Z, Feng Y. pH-switchable wormlike micelles. Chem Commun. 2010, 46(47): 9028-9030.
[58] Jessop P G, Mercer S M, Heldebrant D J. CO_2-triggered switchable solvents, surfactants, and other materials. Energy Environ. Sci. 2012, 5(6): 7240.
[59] Zhang Y, Feng Y, Wang Y, et al. CO_2-switchable viscoelastic fluids based on a pseudogemini surfactant. Langmuir. 2013, 29(13): 4187-4192.
[60] Tsuchiya K, Orihara Y, Kondo Y, et al. Control of viscoelasticity using redox reaction. J. Am. Chem. Soc. 2004, 126(39): 12282-12283.
[61] Kern F, Zana R, Candau S J. Rheological properties of semidilute and concentrated aqueous solutions of cetyltrimethylammonium chloride in the presence of sodium salicylate and sodium chloride. Langmuir. 1991, 7(7): 1344-1351.
[62] Kalur C, Frounfelker D, Cipriano H, et al. Viscosity increases with temperature in cationic surfactant solutions due to the growth of wormlike micelles. Langmuir. 2005, 21(24): 10998-11004.
[63] Tanner S. Davies, Aimee M. Ketner, Raghavan* S R. Self-Assembly of Surfactant Vesicles

that Transform into Viscoelastic Wormlike Micelles upon Heating. J. Am. Chem. Soc. 2006, 128(20): 6669-6675.
[64] Eastoe J, Vesperinas A. Self-assembly of light-sensitive surfactants. Soft Matter. 2005, 1(5): 338.
[65] Fameau A, Arnould A, Lehmann M, et al. Photoresponsive self-assemblies based on fatty acids. Chem Commun. 2015, 51(14): 2907-2910.
[66] Chu Z, Dreiss A, Feng Y. Smart wormlike micelles. Chem. Soc. Rev. 2013, 42(17): 7174-7203.
[67] Wang Y, Ma N, Wang Z, et al. Photocontrolled Reversible Supramolecular Assemblies of an Azobenzene-Containing Surfactant with α-Cyclodextrin. Angew. Chem., Int. Ed. 2007, 119(16): 2881-2884.
[68] Oh H, Ketner M, Heymann R, et al. A simple route to fluids with photo-switchable viscosities based on a reversible transition between vesicles and wormlike micelles. Soft Matter. 2013, 9(20): 5025-5033.
[69] Lin Y, Cheng X, Qiao Y, et al. Creation of photo-modulated multi-state and multi-scale molecular assemblies via binary-state molecular switch. Soft Matter. 2010, 6(5): 902-908.
[70] Minkin I. Photo-, Thermo-, Solvato-, and Electrochromic Spiroheterocyclic Compounds. Chem. Rev. 2004, 104(5): 2751-2776.
[71] Khairutdinov F, Hurst K. Photocontrol of Ion Permeation through Bilayer Membranes Using an Amphiphilic Spiropyran. Langmuir. 2001, 17(22): 6881-6886.
[72] Lee Y, Diehn K, Sun K, et al. Reversible photorheological fluids based on spiropyran-doped reverse micelles. J. Am. Chem. Soc. 2011, 133(22): 8461-8463.
[73] Sakai K, Imaizumi Y, Oguchi T, et al. Adsorption Characteristics of Spiropyran-Modified Cationic Surfactants at the Silica/Aqueous Solution Interface. Langmuir. 2010, 26(12): 9283-9288.
[74] Tangso J, Fong K, Darwish T, et al. Novel Spiropyran Amphiphiles and Their Application as Light-Responsive Liquid Crystalline Components. J. Phys. Chem. B. 2013, 117(35): 10203-10210.
[75] Ketner M, Kumar R, Davies S, et al. A simple class of photorheological fluids: surfactant solutions with viscosity tunable by light. J. Am. Chem. Soc. 2007, 129(6): 1553-1559.
[76] Kumar R, Raghavan R. Photogelling fluids based on light-activated growth of zwitterionic wormlike micelles. Soft Matter. 2009, 5(4): 797-803.
[77] Kumar R, Ketner A M, Raghavan R. Nonaqueous photorheological fluids based on light-responsive reverse wormlike micelles. Langmuir. 2010, 26(8): 5405-5411.
[78] Du M, Dai C, Chen A, et al. Investigation on the aggregation behavior of photo-responsive

system composed of 1-hexadecyl-3-methylimidazolium bromide and 2-methoxycinnamic acid. RSC Adv. 2015, 5(84): 68369-68377.
[79] Zhao M, Gao M, Dai C, et al. Investigation of Novel Triple-Responsive Wormlike Micelles. Langmuir. 2017, 33(17): 4319-4327.
[80] Jia K, Hu J, Dong J, et al. Light-responsive multillamellar vesicles in coumaric acid/alkyldimethylamine oxide binary systems: Effects of surfactant and hydrotrope structures. J. Colloid Interface Sci. 2016, 477: 156-165.
[81] Bi Y, Zhao L, Hu Q, et al. Aggregation Behavior of Imidazolium-Based Surface-Active Ionic Liquids with Photoresponsive Cinnamate Counterions in the Aqueous Solution. Langmuir. 2015, 31(46): 12597-12608.
[82] Long J, Li L, Jin Y, et al. Synergistic solubilization of polycyclic aromatic hydrocarbons by mixed micelles composed of a photoresponsive surfactant and a conventional non-ionic surfactant. Sep. Purif. Technol. 2016, 16(9): 11-17.
[83] Shi H f, Wang Y, Fang B, et al. Light-responsive threadlike micelles as drag reducing fluids with enhanced heat-transfer capabilities. Langmuir. 2011, 27(10): 5806-5813.
[84] Zhao Q, Wang Y, Yan Y, et al. Smart nanocarrier: self-assembly of bacteria-like vesicles with photoswitchable cilia. ACS nano. 2014, 8(11): 11341-11349.
[85] Tomatsu I, Peng K, Kros A. Photoresponsive hydrogels for biomedical applications. Adv Drug Deliv Rev. 2011, 63(15): 1257-1266.
[86] Aleandri S, Speziale C, Mezzenga R, et al. Design of Light-Triggered Lyotropic Liquid Crystal Mesophases and Their Application as Molecular Switches in "On Demand" Release. Langmuir. 2015, 31(25): 6981-6987.
[87] Howard, Barnes. Bubbles, drops and particles in non-Newtonian fluids. J. Non-Newtonian Fluid Mech. CRC Press. 1995.
[88] Clift R, Grace R, Weber E. Bubbles, Drops and Particles. Academic Press, New York, 1978.
[89] Bhaga D, Weber E. Bubbles in viscous liquids: shapes, wakes and velocities. J. Fluid Mech. 1981, 105: 61-85.
[90] Grace R, Wairegi T, Nguyen H. Shapes and velocities of single drops and bubbles moving freely through immiscible liquids. Trans. Inst. Chem. Eng. 1976, 54(15): 169-173.
[91] Grace R. Hydrodynamics of Liquid Drops in Immiscible Liquids. Handbook of Fluids in Motion. 1983, 38:14-17.
[92] Clift R, Grace R, Weber E. Bubbles, Drops and Particles. Academic Press, New York, 1978.
[93] Chen L, Garimella V, Reizes A, Leonardi, E. The development of a bubble rising in a viscous liquid. J. Fluid Mech. 1999, 387: 61-96.
[94] Hadamard S. Mouvement permanent lent d'une sphere liquide et visqueuse dans un liquide

visqueux. C.R. Acad. Sci. 1911,152:1735-1738.
[95] Rybczynski W, Ueber die fortschreitende bewegung einer fluessigen kugel in einem zachen medium. Bulletin Acad. Sci. Cracovie, 1911:40-46.
[96] Calderbank H. Gas absorption from bubbles. Chem. Eng. 1967, 45: 209-233.
[97] Miyahara T, Yamanaka S. Mechanics of motion and deformation of a single bubble rising through quiescent highly viscous Newtonian and non-Newtonian Media. J. Chem. Eng. Jpn. 1993, 26(3): 297-302.
[98] De Kee D, Chhabra P. A photographic study of shapes of bubbles and coalescence in non-Newtonian polymer solutions. Rheological Acta. 1988, 27: 656-660.
[99] De Kee D, Carreau J, Mordarski J. Bubble velocity and coalescence in viscoelastic liquids. Chem. Eng. Sci. 1986, 41(9): 2273-2283.
[100] Astarita G, Apuzzo G. Motion of gas bubbles in non-Newtonian liquids. AIChE J. 1965, 11(5): 815-820.
[101] Calderbank P, Johnson D, Loudon J. Mechanics and mass transfer of single bubbles in free rise through some Newtonian and non-Newtonian liquids. Chem. Eng. Sci. 1970, 25(2): 235-256.
[102] Rodrigue D. A simple correlation for gas bubbles rising in power-law fluids. Can. J. Chem. Eng. 2002, 80(2): 289-292.
[103] Herrera-Velarde J, Zenit R, Chehata D. The flow of non-Newtonian fluids around bubbles and its connection to the jump discontinuity. J. Non-Newtonian Fluid Mech. 2003, 111(2): 199-209.
[104] Dewsbury H, Tzounakos A, Karamanev G. Wall Effects for the Free Rise of Solid Spheres in Moderately Viscous Liquids. Can. J. Chem. Eng. 2002, 80(5): 974-978.
[105] Richardson F, Zaki N. The sedimentation of a suspension of uniform spheres under conditions of viscous ow. Chem. Eng. Sci. 1954, 3(2):65-73.
[106] THE EXPERIMENTAL VERIFICATION OF RICHARDSON-ZAKI LAW ON EXAMPLE OF SELECTED BEDS USED IN WATER TREATMENT. Electron. J. Pol. Agric. Univ., 2007, 10(2).
[107] Drenckhan W, Hutzler S. Structure and energy of liquid foams. Adv. Colloid Interface Sci. 2015, 224:1-16.
[108] Weaire D, Phelan R. A counter-example to kelvin's conjecture on minimal surfaces. Philos. Mag. Lett. 1994, 69(2):107-110.
[109] Vélez-Cordero R, Sámano D, P Yue, et al. Hydrodynamic interaction between a pair of bubbles ascending in shear-thinning inelastic fluids. J. Non-Newtonian Fluid Mech. 2011, 166(1-2):118-132.

[110] James D. Boger fluids. Annu. Rev. Fluid Mech. 2009, 41:129-42.
[111] Velez-Cordero JR, S´amano D, Zenit R. Study of the properties of bubbly flows in Boger-type fluids. J. Non-Newtonian Fluid Mech. 2012, 175(76):1-9.
[112] Zenit R, Feng JJ. Hydrodynamic Interactions Among Bubbles, Drops, and Particles in Non-Newtonian Liquids. Annu. Rev. Fluid Mech. 2018, 50:505-534.
[113] Verlet L. Computer "Experiments" on classical fluids. I. thermodynamical properties of Lennard-Jones molecules. Phys. Rev. 1967, 159(1): 98-103.
[114] Swope C, Andersen C, Berens H, Wilson R. A computer simulation method for the calculation of equilibrium constants for the formation of physical clusters of molecules: Application to small water clusters. J. Chem. Phys. 1982, 76(1): 637-649
[115] Hockney W, Goel P, Eastwood W. Quiet high-resolution computer models of a plasma. J. Comput. Phys. 1974, 14(2): 148-158.
[116] Cornell D., Cieplak P, Bayly I, Gould R, Merz M, Ferguson M, Spellmeyer C, Fox T, Caldwell W, Kollman A. A Second Generation Force Field for the Simulation of Proteins, Nucleic Acids, and Organic Molecules. J. Am. Chem. Soc. 1995, 117(19): 5179-5197.
[117] Wang M, Cieplak P, Kollman A. How well does a restrained electrostatic potential (RESP) model perform in calculating conformational energies of organic and biological molecules? J. Comput. Phys. 2000, 21(12): 1049-1074.
[118] Weiner J, Kollman A, Nguyen T, Case A. An all-atom force field for simulations of proteins and nucleic acids. J. Comput. Chem. 1986, 7(2): 230-252.
[119] Brooks R, Bruccoleri E, Olafson D, States J, Swaminathan S, Karplus M. CHARMM: A program for macromolecular energy, minimization, and dynamics calculations. J. Comput. Chem. 1983, 4(2): 187-217.
[120] Foloppe N, Mackerell D. All-atom empirical force field for nucleic acids: I. Parameter optimization based on small molecule and condensed phase macromolecular target data. J. Comput. Chem. 2000, 21(2): 86-104.
[121] Hart K, Foloppe N, Baker M, Denning J, Nilsson L, Mackerell D. Optimization of the CHARMM Additive Force Field for DNA: Improved Treatment of the BI/BII Conformational Equilibrium. J. Chem. Theory Comput. 2012, 8(1): 348-362.
[122] Damm W, Frontera A, Tirado-Rives J, Jorgensen L. OPLS all-atom force field for carbohydrates. J. Comput. Chem. 1997, 18(16): 1955-1970.
[123] Jorgensen L, Maxwell S, Tirado-Rives J. Development and Testing of the OPLS All-Atom Force Field on Conformational Energetics and Properties of Organic Liquids. J. Am. Chem. Soc. 1996, 118(45): 11225-11236.
[124] Robertson J, Tiradorives J, Jorgensen L. Improved Peptide and Protein Torsional

Energetics with the OPLS-AA Force Field. J. Chem. Theory Comput. 2015, 11(7): 3499-3509.
[125] Jorgensen L, Tirado-Rives J. The OPLS [optimized potentials for liquid simulations] potential functions for proteins, energy minimizations for crystals of cyclic peptides and crambin. J. Am. Chem. Soc. 1988, 110(6): 1657-1666.
[126] Daura X, Mark E, Van Gunsteren F. Parametrization of aliphatic CHn united atoms of GROMOS96 force field. J. Comput. Chem. 1998, 19(5): 535-547.
[127] Oostenbrink C, Villa A, Mark E, Van Gunsteren F. A biomolecular force field based on the free enthalpy of hydration and solvation: The GROMOS force-field parameter sets 53A5 and 53A6. J. Comput. Chem. 2004, 25(13): 1656-1676.
[128] Marrink J, De Vries H, Mark E. Coarse Grained Model for Semiquantitative Lipid Simulations. J. Phys. Chem. B. 2004, 108(2): 750-760.
[129] Marrink J, Risselada J, Yefimov S, Tieleman P, De Vries H. The MARTINI Force Field: Coarse Grained Model for Biomolecular Simulations. J. Phys. Chem. B. 2007, 111(27): 7812-7824.
[130] Dawson K, Maciejczyk M, Jankowska E, Bujnicki M. Coarse-grained modeling of RNA 3D structure. Methods. 2016, 103: 138-156.
[131] Berendsen C, Postma M, Van Gunsteren F, Dinola A, Haak R. Molecular dynamics with coupling to an external bath. J. Phys. Chem. B. 1984, 81(8): 3684-3690.
[132] Nosé S. A molecular dynamics method for simulations in the canonical ensemble. Mol. Phys. 1984, 52(2): 255-268.
[133] Hoover G. Canonical dynamics: Equilibrium phase-space distributions. Phys. Rev. A. 1985, 31(3): 1695-1697.
[134] Bussi G, Donadio D, Parrinello M. Canonical sampling through velocity rescaling. J. Chem. Phys. 2007, 126(1): 014101.
[135] Parrinello M, Rahman A. Polymorphic transitions in single crystals: A new molecular dynamics method. J. Appl. Phys. 1981, 52(12): 7182-7190.
[136] Hohenberg P, Kohn W. Inhomogeneous Electron Gas. Phys. Rev.1964(38): B864-B871.
[137] Kohn W, Sham J. Self-Consistent Equations Including Exchange and Correlation Effects. Phys. Rev. 1965, 140(4A): 11-33.
[138] Parr G. Density-functional theory of atoms and molecules. Oxford University Press. 1989.
[139] Becke P. Density-functional exchange-energy approximation with correct asymptotic behavior. Physical Review A. 1988, 38(6):3098-3100.
[140] Holthausen C. A chemist's guide to density functional theory. Wiley. 2001: 41-64.
[141] Dylla-Spears R, Wong L, Miller E, Feit D, Steele W, Suratwala T. Charged micelle halo mechanism for agglomeration reduction in metal oxide particle based polishing slurries.

Colloids Surf., A. 2014, 447, 32-43.
[142] Tu Y, Gao M, Ten H, Shang Y, Fang B, Liu H. A gemini surfactant-containing system with abundant self-assembly morphology and rheological behaviors tunable by photoinduction. RSC Adv. 2018, 8, 16004-16012.
[143] Yang H, Leow R, Chen X. Thermal-Responsive Polymers for Enhancing Safety of Electrochemical Storage Devices. Adv. Mater. 2018, 30(170): 43-47.
[144] Tu F, Lee D. Shape-Changing and Amphiphilicity-Reversing Janus Particles with pH-Responsive Surfactant Properties. J. Am. Chem. Soc. 2014, 136(6):9999-10006.
[145] Yang J, Yan H, Niu F, Zhang H. Probing of the magnetic responsive behavior of magnetorheological organogel under step field perturbation. Colloid Polym. Sci. 2018, 296(6): 309-317.
[146] Zhou D, Kuchel P, Dong S, Lucien P, Perrier S, Zetterlund B. Polymerization-Induced Self-Assembly under Compressed CO_2: Control of Morphology Using a CO_2-Responsive MacroRAFT Agent. Macromol. Rapid Commun. 2019, 40(2): 1800335.
[147] Lin C, Xu M, Zhang W, Yang L, Xiang Z, Liu Y. Highly ordered and multiple-responsive graphene oxide/azoimidazolium surfactant intercalation hybrids: a versatile control platform. Langmuir. 2017, 33: 3099-3111.
[148] Yang Z, Wei J, Sobolev I, Grzybowski A. Systems of mechanized and reactive droplets powered by multi-responsive surfactants. Nature. 2018, 553: 313-318.
[149] Sakai K, Yamazaki R, Imaizumi Y, Endo T, Sakai H, Abe M. Adsolubilization by a photo-responsive surfactant. Colloids Surf. A. 2012, 410(9): 119-124.
[150] Huang Y, Kim H. Light-controlled synthesis of gold nanoparticles using a rigid, photoresponsive surfactant. Nanoscale. 2012, 51(4): 6312-6317.
[151] Long J, Tian S, Niu Y, Li G, Ning P. Reversible solubilization of typical polycyclic aromatic hydrocarbons by a photoresponsive surfactant. Colloids Surf. A. 2014, 454(5): 172-179.
[152] Kim C, Kim E, Ha L, Lee G, Lee J, Jeong W. Highly stable and reduction responsive micelles from a novel polymeric surfactant with a repeating disulfide-based gemini structure for efficient drug delivery. Polymer. 2017, 133(9): 102-109.
[153] Jayaraman A, Mahanthappa K. Counterion-Dependent Access to Low-Symmetry Lyotropic Sphere Packings of Ionic Surfactant Micelles. Langmuir. 2018, 34(6): 2290-2301.
[154] Kwiatkowski L, Molchanov S, Sharma H, Kuklin I, Dormidontova E, Philippova, E. Growth of wormlike micelles of surfactant induced by embedded polymer: role of polymer chain length. Soft Matter. 2018, 14(5), 4792-4804.
[155] Mondal S, Pan A, Patra A, Mitra K, Ghosh S. Ionic liquid mediated micelle to vesicle

transition of a cationic gemini surfactant: a spectroscopic investigation. Soft Matter. 2018, 14(8): 4185-4193.
[156] Owoseni O, Zhang Y, Omarova, M, Li, X, Lal, J, McPherson, G. L, John, V. T. Microstructural characteristics of surfactant assembly into a gel-like mesophase for application as an oil spill dispersant. J. Colloid Interface Sci. 2018, 524(5): 279-288.
[157] Li Q, Wang J, Lei N, Yan M, Chen X, Yue X. Phase behaviours of a cationic surfactant in deep eutectic solvents: from micelles to lyotropic liquid crystals. Phys. Chem. Chem. Phys. 2018, 20(32): 12175-12181.
[158] Hyder Ali, A, Srinivasan, K. S. V. Photoresponsive Functionalized Vinyl Cinnamate Polymers: Synthesis and Characterization. Polym. Int. 2015, 43(1): 310-316.
[159] Baglioni, P, Braccalenti, E, Carretti, E, Germani, R, Goracci, L, Savelli, G, Tiecco, M. Surfactant-based photorheological fluids: effect of the surfactant structure. Langmuir. 2009, 25(7), 5467-5475.
[160] Tu Y, Ye Z, Lian C, Shang Y, Teng H, Liu H. UV-Responsive Behavior of Multistate and Multiscale Self-Assemblies Constructed by Gemini Surfactant 12-3-12·2Br$^-$ and trans-o-Methoxy-cinnamate. Langmuir, 2018, 34(6), 12990-12999.
[161] Tu Y, Chen, Q, Shang, Y, Teng, H, Liu, H. Photoresponsive Behavior of Wormlike Micelles Constructed by Gemini Surfactant 12-3-12·2Br– and Different Cinnamate Derivatives. Langmuir, 2019, 35(5): 4634-4645.
[162] Poorsargol M, Sohrabi B, Dehestani M. Study of the Gemini Surfactants Self-Assembly on Graphene Nanosheets: Insights from Molecular Dynamic Simulation. J. Phys. Chem. A. 2018, 122(13): 3873-3885.
[163] Tomasello G, Garavelli M, Orlandi G. Tracking the stilbene photoisomerization in the S(1) state using RASSCF. Phys. Chem. Chem. Phys. 2013, 15(6): 19763-19773.
[164] Tang J, Qu Z, Luo J, He L, Wang P, Zhang P, Huang Y. Molecular Dynamics Simulations of the Oil-Detachment from the Hydroxylated Silica Surface: Effects of Surfactants, Electrostatic Interactions, and Water Flows on the Water Molecular Channel Formation. J. Phys. Chem. B. 2018, 122(6): 1905-1918.
[165] Zhang J, Zhang Y, Li J, Wang P, Sun X, Yan Y. Effect of organic salt on the self-assembly of ammonium gemini surfactant: An experiment and simulation study. Colloids Surf., A. 2018, 548(15): 198-205.
[166] Sangwai, A. V, Sureshkumar, R. Coarse-grained molecular dynamics simulations of the sphere to rod transition in surfactant micelles. Langmuir, 2011, 27, 6628-6638.
[167] Wang Z, Larson G. Molecular dynamics simulations of threadlike cetyltrimethylammonium chloride micelles: effects of sodium chloride and sodium salicylate

salts. J. Phys. Chem. B. 2009, 113(18), 13697-13710.
[168] Heerdt G, Tranca I, Markvoort J, Szyja M, Morgon H, Hensen J. Photoisomerization induced scission of rod-like micelles unravelled with multiscale modeling. J. Colloid Interface Sci. 2018, 510(17): 357-367.
[169] Wang P, Pei S, Wang M, Yan Y, Sun X, Zhang J. Coarse-grained molecular dynamics study on the self-assembly of Gemini surfactants: the effect of spacer length. Phys. Chem. Chem. Phys. 2017, 19(7): 4462-4468.
[170] Yue L, Wang Y, He Z, Chen J, Shang Y, Liu H. Effect of ionic liquid C2mimBr on rheological behavior of Gemini surfactant 12-2-12 aqueous solution. Colloid Polym. Sci. 2015, 293(28), 2373-2383.
[171] Frisch J, Trucks W, Schlegel B, Scuseria E, Robb A, Cheeseman R, Scalmani G, Barone V, Mennucci B, Petersson A, Nakatsuji H, Caricato M, Li X, Hratchian P, Izmaylov F, Bloino J, Zheng G, Sonnenberg L, Hada M, Ehara M, Toyota K, Fukuda R, Hasegawa J, Ishida M, Nakajima T, Honda Y, Kitao O, Nakai H, Vreven T, Montgomery J, Peralta E, Ogliaro F, Bearpark M, Heyd J, Brothers E, Kudin N, Staroverov N, Kobayashi R, Normand J, Raghavachari K, Rendell P, Burant C, Iyengar S, Tomasi, J, Cossi M, Rega N, Millam M, Klene M, Knox E, Cross B, Bakken V, Adamo C, Jaramillo J, Gomperts R, Stratmann E, Yazyev O, Austin J, Cammi R, Pomelli S, Ochterski W, Martin L, Morokuma K, Zakrzewski G, Voth A, Salvador P, Dannenberg J, Dapprich S, Daniels D, Farkas B, Ortiz V, Cioslowski J, Fox J. Gaussian 09, Revision A.1; Gaussian, Inc.: Wallingford, CT. 2009.
[172] Ho J, Klamt A, Coote L. Comment on the correct use of continuum solvent models. J. Phys. Chem. B. 2010, 114(16): 13442-13444.
[173] Schuler D, Daura X, Gunsteren V. An improved GROMOS96 force field for aliphatic hydrocarbons in the condensed phase. J. Comput. Chem. 2001, 22(5): 1205-1218.
[174] Jia X, Chen J, Wang B, Liu W, Hao J. Molecular dynamics simulation of shape and structure evolution of preassembled cylindrical cetyltrimethylammonium bromide micelles induced by octanol. Colloids Surf. A. 2014, 457(8): 152-159.
[175] Malde K, Zuo L, Breeze M, Stroet M, Poger D, Nair C, Mark E. An automated force field topology builder (ATB) and repository: version 1.0. J. Chem. Theory Comput. 2011, 7(4): 4026-4037.
[176] Martínez L, Andrade R, Birgin G, Martínez M. PACKMOL: A package for building initial configurations for molecular dynamics simulations. J. Comput. Chem. 2010, 30(12): 2157-2164.
[177] Alimohammadi H, Javadian S, Gharibi H, Tehrani-Bagha A, Alavijeh R, Kakaei K. Aggregation behavior and intermicellar interactions of cationic Gemini surfactants: Effects of alkyl chain, spacer lengths and temperature. J. Chem. Thermodyn. 2012, 44(18): 107-115.

[178] Abraham J, Murtola T, Schulz R, Páll S, Smith C, Hess B, Lindahl E. GROMACS: High performance molecular simulations through multi-level parallelism from laptops to supercomputers. SoftwareX, 2015, 1(4):19-25.
[179] Berendsen J, Postma P, van Gunsteren F, Hermans J. Interaction Models for Water in Relation to Protein Hydration. Intermol. Forces. 1981 : 331-342.
[180] Essmann U, Perera L, Berkowitz L, et al. A smooth particle mesh Ewald method. J. Chem. Phys. 1995, 103(21): 8577-8593.
[181] Hess B, Bekker H, Berendsen et al. LINCS: a linear constraint solver for molecular simulations. J. Comput. Chem. 1997, 18(3): 1463-1472.
[182] Humphrey W, Dalke A, Schulten K. VMD: visual molecular dynamics. J. Mol. Graphics. 1996, 14(8): 33-38.
[183] Bernheim-Groswasser A, Zana R, Talmon Y. Sphere-to-cylinder transition in aqueous micellar solution of a dimeric (gemini) surfactant. J. Phys. Chem. B. 2000, 104(21), 4005-4009.
[184] Alargova G, Kochijashky I, Sierra L, Zana R. Micelle aggregation numbers of surfactants in aqueous solutions: a comparison between the results from steady-state and time-resolved fluorescence quenching. Langmuir, 1998, 14(19): 5412-5418.
[185] Drechsler M, Verbavatz M. Role of the surfactant headgroup on the counterion specificity in the micelle-to-vesicle transition through salt addition. J. Colloid Interface Sci. 2008, 319(15): 542-548.
[186] Janiak J, Tomšič M, Lundberg D, Olofsson G, Piculell L, Schillén K. Soluble aggregates in aqueous solutions of polyion-surfactant ion complex salts and a nonionic surfactant. J. Phys. Chem. B. 2014, 118(11): 9745-9756.
[187] Kubo W, Kambe S, Nakade S, et al. Photocurrent-determining processes in quasi-solid-state dye-sensitized solar cells using ionic gel electrolytes. J. Phys. Chem. B. 2003, 107(9): 4374-4381.
[188] Oelschlaeger C, Waton G, Candau J, Cates E. Structural, Kinetics, and Rheological Properties of Low Ionic Strength Dilute Solutions of a Dimeric (Gemini) Surfactant. Langmuir. 2002, 18(4): 7265-7271.
[189] Oda R, Huc I, Homo C, Heinrich B, Schmutz M, Candau S. Elongated aggregates formed by cationic gemini surfactants. Langmuir. 1999, 15(8): 2384-2389
[190] Promkatkaew M, Suramitr S, Karpkird T, et al. Photophysical properties and photochemistry of substituted cinnamates and cinnamic acids for UVB blocking: Effect of hydroxy, nitro, and fluoro substitutions at ortho, meta, and para positions. Photochem. Photobiol. Sci. 2014, 13(3):583-594.
[191] Chen Z, Huo J, Hao L, et al. Multiscale modeling and simulations of responsive polymers.

Curr. Opin. Chem. Eng. 2019, 23(7):21-33.
[192] Chen L, Shang Y, Liu H, et al. Effect of the spacer group of cationic gemini surfactant on microemulsion phase behavior. J. Colloid Interface Sci. 2006, 301(2):644-650.
[193] Tian L, Chen F. Multiwfn: A multifunctional wavefunction analyzer. J. Comput. Chem. 2012, 33(5):580-592.
[194] Chen Q, Liu W, Liu. H, Huang X, Shang Y, Liu H, Molecular Dynamics Simulations and Density Functional Theory on Unraveling Photoresponsive Behavior of Wormlike Micelles Constructed by 12-2-12·2Br⁻ and trans-ortho-Methoxy Cinnamate, Langmuir. 2020, 36(20): 9499–9509.
[195] Li R, Yan F, et al. The self-assembly properties of a series of polymerizable cationic gemini surfactants: Effect of the acryloxyl group. Colloids Surf., A. 2014, 444(4):276-282.
[196] Lin Z, Cai J, Scriven L, et al. Spherical-to-Wormlike Micelle Transition in CTAB Solutions. J.phys.chem. 1994, 98(23):5984-5993.
[197] Clausen M , Vinson K, Minter R, et al. Viscoelastic micellar solutions: microscopy and rheology. J. phys. Chem. 1992, 96(1):474-484.
[198] Acharya P, Kunieda H. Wormlike micelles in mixed surfactant solutions. Adv Colloid Interface, 2006, 123(0):401-413.
[199] Koehler D, Raghavan R, Kaler W. Microstructure and Dynamics of Wormlike Micellar Solutions Formed by Mixing Cationic and Anionic Surfactants. J. Phys. Chem. B. 2000, 104(47):114-129.
[200] Liu W, Ye Z, Chen Q, et al. Effect of the Substituent Position on the Phase Behavior and Photoresponsive Dynamic Behavior of Mixed Systems of a Gemini Surfactant and trans-Methoxy Sodium Cinnamates, Langmuir. 2021, 37 (9): 9518–9531.
[201] Danino D, Talmon Y, Zana R. Alkanediyl-alpha, omega-Bis(Dimethylalkylammonium Bromide) Surfactants (Dimeric Surfactants). 5. Aggregation and Microstructure in Aqueous Solutions. Langmuir. 1995, 11(5):1448-1456.
[202] Clift R, Grace R, Weber E. Bubbles, drops, and particles. Courier Corporation. 2005.
[203] Legendre D, Zenit R, Velez-Cordero JR. On the deformation of gas bubbles in liquids. Phys. Fluids. 2012, 24(4): 113.
[204] Palaparthi R, Papageorgiou T, Maldarelli C. Theory and experiments on the stagnant cap regime in the motion of spherical surfactant-laden bubbles. J. Fluid. Mech. 2006, 559:1.
[205] Vélez-Cordero R, Zenit R. Bubble cluster formation in shear-thinning inelastic bubbly columns. J. Nonnewton. Fluid. Mech. 2011, 166:32–41.
[206] Rothstein P, Mohammadigoushki H. Complex flows of viscoelastic wormlike micelle solutions. J. Nonnewton. Fluid. Mech. 2020, 285:104382.

[207] Kostrzewa M, Delgado A, Wierschem A. Particle settling in micellar solutions of varying concentration and salt content. Acta Mech. 2016, 227(3):677-692.
[208] Gaillard T, Roché M, Honorez C, Jumeau M, Balan A, Jedrzejczyk C, et al. Controlled foam generation using cyclic diphasic flows through a constriction. Int. J. Multiph. Flow. 2017, 96(6):173-187.
[209] Lam N, Do C, Wang Y, Huang R, Chen W. Structural properties of the evolution of CTAB/NaSal micelles investigated by SANS and rheometry. Phys. Chem. Chem. Phys. 2019, 21(13):18346-18351.
[210] Clausen M, Vinson K, Minter R, Davis T, Talmon Y, Miller G. Viscoelastic micellar solutions: Microscopy and rheology. J. Phys. Chem. 1992, 96(2):474-484.
[211] Cates ME, Fielding SM. Rheology of giant micelles. Adv Phys 2006; 55:799–879.
[212] Padding T, Briels J, Stukan R, Boek S. Review of multi-scale particulate simulation of the rheology of wormlike micellar fluids. Soft Matter. 2009, 5(14):4367-4375.
[213] Richardson F, Zaki N. The sedimentation of a suspension of uniform spheres under conditions of viscous flow. Chem. Eng. Sci. 1954, 3(14): 65-73.
[214] Sankaranarayanan K, Shan X, Kevrekidis IG, Sundaresan S. Analysis of drag and virtual mass forces in bubbly suspensions using an implicit formulation of the lattice Boltzmann method. J. Fluid. Mech. 2002, 452(14):61-96.
[215] Blazejewski R. Apparent viscosity and settling velocity of suspensions of rigid monosized spheres in Stokes flow. Int. J. Multiph. Flow. 2012; 39:179-185.
[216] Nicolai H, Herzhaft B, Hinch J, Oger L, Guazzelli E. Particle velocity fluctuations and hydrodynamic self-diffusion of sedimenting non-Brownian spheres. Phys. Fluids. 1995, 7(9):12-23.
[217] Taylor P. Ostwald ripening in emulsions. Adv. Colloid. Interface. Sci. 1998; 75(41):107-163.
[218] Loisy A, Naso A, Spelt PDM. Buoyancy-driven bubbly flows: Ordered and free rise at small and intermediate volume fraction. J. Fluid. Mech. 2017, 816(4):94-141.
[219] Gheissary G, Van Den Brule BHAA. Unexpected phenomena observed in particle settling in non-Newtonian media. J. Nonnewton. Fluid.Mech. 1996, 67(15):1-18.
[220] Prakash R, Majumder K, Singh A. Flotation technique: Its mechanisms and design parameters. Chem. Eng. Process. 2018, 127(5):249-270.
[221] Finch A, Xiao J, Hardie C, Gomez O. Gas dispersion properties: bubble surface area flux and gas holdup. Miner. Eng. 2000, 13(9):365-372.

Appendix Publication list

[1] **Chen Q**, Liu W, Liu. H, Huang X, Shang Y, Liu H. Molecular Dynamics Simulations and Density Functional Theory on Unraveling Photoresponsive Behavior of Wormlike Micelles Constructed by 12-2-12·2Br⁻ and trans-ortho-Methoxy Cinnamate. Langmuir, 2020, 36, 32, 9499–9509.

[2] **Chen Q**, Gao F, Shang Y, Liu H. Effects of Macromolecular Crowding on Structure of DNA. Biomed J Sci&Tech Res, 2018, 7,4.

[3] **Chen Q**, Liu W, Ye Z, Shang Y, Liu H. Molecular Dynamics Simulations and Density Functional Theory on Photo-responsive Behavior of Wormlike Micelles Constructed by Gemini Surfactant 12-3-12·2Br⁻ and Different Cinnamate Derivatives. Journal of Colloid & Interface Science. (Under review)

[4] **Chen Q**, Restagno F, Langevin D, Salonen A. The rise of bubbles in shear thinning fluid. Journal of Colloid & Interface Science. (Under review)

[5] Tu Y, **Chen Q**, Shang Y, Teng H, Liu H. Photo-responsive Behavior of Wormlike Micelles Constructed by Gemini Surfactant 12-3-12·2Br- and Different Cinnamate Derivatives. Langmuir, 2019, 35,13 4634-3645.

[6] Liu W, **Chen Q**, Shang Y, Teng H, Liu H. Semi-quantitative Analysis of the UV-responsive Behavior of Anisotropic Phase Constructed by Gemini Surfactant 12-3-12·2Br⁻ and trans-ortho-Methoxycinnamate. Colloids and Surfaces A, 2020, 605, 20, 125348

[7] Liu W, Ye Z, **Chen Q**, Huang X, Shang Y, Liu H, Meng H, He Y, Dong Y. Effect of the Substituent Position on the Phase Behavior and Photoresponsive Dynamic Behavior of Mixed Systems of a Gemini Surfactant and trans-Methoxy Sodium Cinnamates. Langmuir, 2021, 37, 31, 9518−9531

Acknowledgements

I will show my sincere thanks to Prof. Anniina Salonen, Prof. Dominique Langevin and Prof. Frédéric Restagno and Prof. Yazhuo Shang for their enduring support and patience throughout my thesis. This thesis was completed with their constructive suggestions and inspiring encouragement. Their deep understanding of interface physics and chemistry has greatly helped me design and conduct experiments scientifically. Their desire for scientific research and considerate care always encourages me to use appropriate methods to analyze problems and overcome difficulties.

Thank Prof. Yazhuo Shang for giving me the opportunity to study abroad. Thank Prof. Anniina Salonen for offering me the impressive experience of conducting the research in Laboratoire de Physique des Solides. Thanks for the financial support of China Scholarship Council.

I feel lucky that I am surrounded by intelligent and helpful member of MMOI group: Emmanuelle Rio, Liliane Léger, François Boulogne, Christophe Poulard, Sandrine Mariot, Anna Kharlamova, Laura Wallon, Chiara Guidolin, Marina Pasquet, Marie Corpart, Aymeric Duigou Majumdar, Julian Wailliez, Raphaelle Taub, Suzanne Lafon, Elina Gilbert, Manon Marchand, Jonas Miguet, Marion Grzelka and Ning Jiang. Thank you for your meticulous help and company in my daily life and in research when I was in Orsay.

Sincere gratitude should also go to my group mates in China: Yi Guo, Meng Li, Hengjiang Liu, Meng Zhou, Mengge Gao, Yan Tu, Ruijin Wang, Zhicheng Ye, Xiangrong Huang, Jie Shuai, Wenxiu Liu, Jiajie Hu, Xinrui Li, Hanglin Li, Zilong Li, Xinyue Sun, Zheng Wu, Xin Bai, Jingwen Wang, Xin Li, Hao Feng, Yawen Lv, Zhuoyao Ni, Yuchen Cong, Lin Ding, Ning Di, Zhicheng Liu, Shiqiang Cheng and Tianyi Gao. Thanks for your assistance and companionship during my five-year PhD study at ECUST.

I am extremely grateful to my friends Guanfei Shen, Zehua Song, Weishu and Guohui Gao and in France. Your basketball skills, cooking skills and game time made my life no longer monotonous in France. You are really talkative and funny guys, which made me so much joy in the journey. I can remember every scene as if it happened yesterday.

Especially this thesis owes a debt to my friends Bin Lei, Yapeng Niu, Xiaohui Gao, Tony Yang, Young Weng (Se Jiong), He Li, Mengqi Wu, Manyu Chen, Shiqun Wu. Your company and support are the most significant motivation for me to finish my PhD for five years.

Finally, I would like to give my heartfelt thanks to my parents, for their endless love and care for me. You always tell me that the world is a more beautiful place than you can suppose, and then you release me into future, the black row of cedars under the dawn in the distance.

Though the chilling winter wind shakes me with solitude and frustration, when you look at me with love, the color of snowy mountains and moonlight paint on me. I love you forever.

Resumé substantiel de la thèse

1 Introduction

Au cours des dernières décennies, les matériaux intelligents auto-assemblés capables de répondre de manière dynamique aux stimuli environnementaux externes (y compris l'électricité, la lumière, le magnétisme, la chaleur, le pH, le CO_2, etc.) ont été un point névralgique de la recherche pour les chercheurs. Parmi eux, l'auto-assemblage sensible à la lumière construit par des tensioactifs a attiré l'attention des scientifiques. Ce système d'auto-assemblage sensible au stimulus a non seulement des morphologies d'auto-assemblage abondantes et différentes échelles d'auto-assemblage, y compris des micelles sphériques, des micelles vermiformes, des vésicules, des gels, des cristaux liquides cristallins lyotropes (LC) et aqueux à deux phases (ATPS), etc., et son positionnement est propre, précis, sans interférence et facile à utiliser. Ces avantages le distinguent dans les domaines de la libération de médicaments, de l'industrie pétrochimique, de la catalyse commutable, de la modification de surface, de la bio-ingénierie, des matériaux photosensibles intelligents et des systèmes optiques, présentant une grande valeur d'application. Parmi ces auto-assemblages réactifs, les micelles de type ver sensibles à la lumière ont une variété de morphologies de micelles contrôlables et une large gamme de propriétés rhéologiques réglables, ce qui en fait des applications pratiques dans les fluides rhéologiques optiques, les dispositifs photosensibles, les réducteurs de traînée, etc. CUHK brille.

L'introduction de petites molécules photosensibles dans le système tensioactif est le moyen le plus simple d'obtenir un système micellaire ressemblant à un ver sensible à la lumière. La capacité de réponse à la lumière du système dépend de la capacité d'auto-assemblage du tensioactif d'une part. Par rapport aux tensioactifs monocaténaires traditionnels, la capacité d'auto-assemblage des tensioactifs Gemini à la même concentration est beaucoup plus forte que celle des tensioactifs conventionnels. L'excellente capacité d'auto-assemblage et le comportement d'agrégation riche des tensioactifs Gemini font que le système sensible à la lumière composé de petites molécules sensibles à la lumière joue un rôle plus important dans les applications industrielles.

La capacité de réponse à la lumière des micelles ressemblant à des vers sensibles à la lumière dépend non seulement de la capacité d'auto-assemblage des tensioactifs du système, mais aussi de la photosensibilité des petites molécules sensibles à la lumière dans le système. La double liaison carbone-carbone dans la structure moléculaire de l'acide cinnamique est tordue de trans à cis à une longueur d'onde ultraviolette de 365 nm. Cette réaction de photoisomérisation conduit à un changement dans l'agencement de l'auto-assemblage du

système, qui à son tour provoque des changements dans la configuration macroscopique des micelles et des changements dans les propriétés macrophysiques et chimiques, et parce que les molécules d'acide cinnamique elles-mêmes ont une certaine activité de surface, faible coût, excellente photosensibilité. Par conséquent, les micelles ressemblant à des vers sensibles à la lumière composées de petites molécules photosensibles à base d'acide cinnamique et de tensioactifs Gemini sont devenues un objet de recherche brûlant à l'heure actuelle. La structure moléculaire détermine la nature de la molécule.Les différents substituants sur les petites molécules photosensibles à base d'acide cinnamique et les différentes positions de ces substituants auront un grand impact sur la capacité de photoisomérisation de la petite molécule d'acide cinnamique et la capacité de photoréponse du grand impact. En raison de la limitation des conditions expérimentales, la recherche sur le mécanisme microscopique du comportement sensible à la lumière des micelles ressemblant à des vers sensibles à la lumière est insuffisante.En même temps, en raison de la complexité et de la difficulté de la synthèse et de la main-d'œuvre et du matériel limités. ressources, il nous est difficile de photosensibiliser une grande variété d'acides cinnamiques.De petites molécules mènent des expériences une à une pour vérifier et comparer leurs capacités de réponse à la lumière. Avec le développement de la chimie computationnelle, les méthodes de calcul par simulation informatique représentées par la simulation de dynamique moléculaire (MD) et le calcul quantitatif peuvent nous aider à résoudre ces problèmes.

Dans le processus industriel, le comportement de mélange de gaz-liquide à deux phases est très commun.Par rapport au système de film liquide où la phase gazeuse est la phase continue, la phase gazeuse se manifeste plus comme la phase dispersée sous forme de bulles dispersées en phase liquide. Dans de nombreuses applications industrielles, telles que la flottation par mousse, la bière et les boissons gazeuses, la purification des eaux usées, la séparation en deux phases, etc., le comportement de montée des bulles joue un rôle très important. Parce que la bulle est déformable, sa forme va changer avec la vitesse de montée et le comportement rhéologique de la phase continue.Au contraire, la forme de la bulle affecte la vitesse de montée et le comportement rhéologique de la phase continue. Cette interaction conduit à un comportement ascendant des bulles très compliqué.Par conséquent, les recherches actuelles sur le comportement ascendant des bulles se concentrent principalement sur les fluides newtoniens et certains fluides ayant un comportement rhéologique relativement simple, tels que les fluides de Boger et les fluides inélastiques amincissants par cisaillement. Les fluides diluants viscoélastiques par cisaillement sont des fluides très courants dans les applications industrielles, telles que les solutions polymères, les solutions polymères, les peintures, les revêtements, les huiles lourdes, etc. Il existe peu de recherches sur le comportement ascensionnel des bulles dans

les fluides fluidifiants viscoélastiques, de sorte que la recherche sur le comportement ascensionnel des bulles dans les fluides fluidifiants viscoélastiques a une grande valeur d'application théorique et pratique. La solution de micelles en forme de ver auto-assemblée par les tensioactifs est un fluide de fluidification par cisaillement viscoélastique très typique. Il est simple à préparer et peu coûteux. Avec le changement de concentration de tensioactif ou de sel de contre-ion, le système changera Présentant différentes propriétés rhéologiques, ce est très approprié pour étudier le comportement ascensionnel des bulles dans les fluides fluidifiants viscoélastiques.

2 Simulations de dynamique moléculaire et calculs quantitatifs sur le dénouement du comportement photo-réactif de micelles en forme de ver construites par 12-2-12·2Br$^-$ et *trans*-o-méthoxy-cinnamate

Nous avons choisi le tensioactif Gemini N, N'-bis(dodécyldiméthyl)-1,2-éthane diammonium dibromure (12-2-12·2Br$^-$) et la petite molécule photosensible d'acide trans-o-méthoxycinnamique (*trans*-OMCA) pour construire un système d'auto-assemblage photosensible. Le comportement photosensible du système et le mécanisme microscopique de transformation de la morphologie de l'auto-assemblage ont été étudiés en combinant rhéologie, dynamique moléculaire et calcul quantitatif.

Le mécanisme de comportement photosensible pour la micelle 12-2-12·2Br$^-$/*trans*-OMCA est proposé (Fig. 2.14). De toute évidence, le motif de tassement entre 12-2-12·2Br$^-$ et OMCA détermine directement la morphologie existante de la micelle et les trois principaux facteurs affectent le motif de tassement entre 12-2-12·2Br$^-$ et OMCA : structure géométrique de l'OMCA, hydrophilie de l'OMCA et de l'énergie d'interaction entre l'OMCA et le 12-2-12·2Br−. Tout d'abord, il convient de noter que la structure relativement plane du trans-OMCA et le degré de flexion inférieur rendent le trans-OMCA plus facile à insérer dans l'intervalle des tensioactifs. Il est démontré par $g(r)$ et SASA que la géométrie moléculaire différente du trans/cis-OMCA influence leurs modes de tassement : le cycle aromatique du *trans*-OMCA est complètement noyé dans la chaîne alkyle hydrophobe de 12-2-12·2Br$^-$ et celle de *cis*-OMCA est exposé à la surface de la micelle. De ce fait, il y a un arrangement plus étroit entre le centre chargé de trans-OMCA et 12-2-12.2Br$^-$, provoquant une interaction électrostatique et une interaction -cation plus fortes. Après irradiation UV, l'encombrement stérique de la molécule cis-OMCA devient plus grand et l'interaction électrostatique et l'interaction cation-cation s'affaiblissent, conduisant à la désintégration de la micelle d'origine.

Deuxièmement, il a été prouvé qu'une solubilité plus faible dans l'eau était liée à une

association plus forte avec les micelles.24 En comparant l'énergie libre de solvatation, il est démontré que le trans-OMCA est plus hydrophobe que le *cis*-OMCA. L'hydrophobie plus forte du *trans*-OMCA indique que le *trans*-OMCA reste associé aux micelles dans une plus large mesure. Au contraire, l'hydrophilie plus forte du *cis*-OMCA lui donne la possibilité de se déplacer vers la couche externe des micelles et même de s'échapper de les couches de micelles 12-2-12.2Br$^-$, et finalement induire la scission de la micelle.

Enfin, en calculant l'énergie d'interaction, les micelles contenant du *cis*-OMCA se révèlent moins stables. Après la photoisomérisation du *trans*-OMCA, pour obtenir un motif de tassement stable avec une énergie la plus faible, le *cis*-OMCA modifiera son motif de tassement, passant de l'incorporation du cycle aromatique dans la micelle à l'orientation de celui-ci à la surface de la micelle. Par conséquent, les longues micelles en forme de bâtonnets se diviseront en plusieurs micelles sphériques.

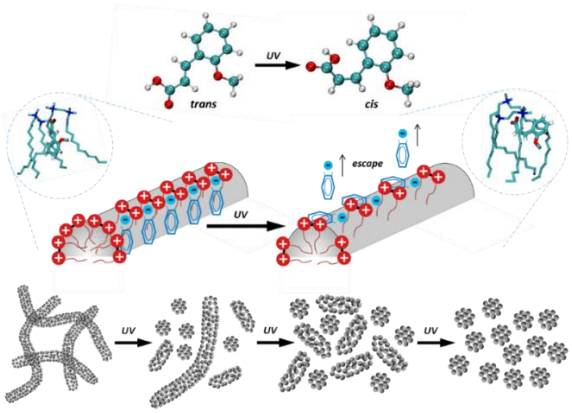

Fig. 2.1 Le mécanisme de la transition morphologique des micelles photosensibles 12-2-12.2Br$^-$/*trans*-OMCA.

3 Simulations de dynamique moléculaire et calcul quantitatif du comportement photosensible de micelles en forme de ver construites par des dérivés tensioactifs Gemini 12-3-12·2Br$^-$ et Cinnamate avec différents ortho-substituants

Sur la base de notre compréhension du mécanisme de transformation de la micelle vermiforme photosensible, nous avons sélectionné trois cinnamates ortho-substituants, le *trans*-o-méthoxy cinnamate (*trans*-OMCA), le trans-o-hydroxy cinnamate (*trans*-OHCA), et *trans*-cinnamate (*trans*-CA), pour construire des systèmes de micelles ressemblant à des vers photosensibles avec le tensioactif Gemini triméthylène-1,3-bis (bromure de dodécyldiméthylammonium) (12-2-12·2Br$^-$). Nous avons étudié le comportement

photosensible et la cinétique de réaction de photoisomérisation de la micelle vermiforme, combinés à une simulation de dynamique moléculaire et à des calculs quantitatifs pour étudier les effets de différents ortho-substituants dans les cinnamates sur la vitesse de réaction de photo-isomérisation et le comportement photosensible des micelles vermiformes.

Considérant les résultats expérimentaux, de simulation et de calcul de manière globale et systématique, les mécanismes sous-jacents de la transition photosensible des micelles vermiformes contenant *trans*-CA, *trans*-OHCA et *trans*-OMCA ont été spéculés et illustrés à la Fig. 3.1. La structure plane et l'encombrement stérique inférieur et l'hydrophilie des trans-cinnamates ainsi que le potentiel électrostatique plus élevé dans le carboxyle leur confèrent un motif d'emballage plus dense (les *trans*-cinnamates s'insèrent verticalement dans les couches hydrophobes du tensioactif.) avec des tensioactifs, formant ainsi des micelles vermiformes. Après irradiation UV, les *trans*-cinnamates se photo-isomérisent en *cis*-cinnamates. L'encombrement stérique et l'hydrophilie plus élevés ainsi que le potentiel électrostatique inférieur dans le carboxyle et la distribution électrostatique plus uniforme des *cis*-cinnamates conduisent à un motif de tassement lâche (les *cis*-cinnamates s'orientent à la surface des micelles.) Qui affaiblit l'interaction entre les tensioactifs et provoque finalement la fission des micelles.

Parmi les trois cinnamates, la présence d'ortho-substituants dans le cinnamate agrandit la différence entre l'encombrement stérique, la distribution électrostatique et l'hydrophilie des *trans/cis*-cinnamates. Ces différences plus importantes avant et après l'irradiation UV permettent au *cis*-OMCA et au *cis*-OHCA de s'échapper de la micelle et de rester en solution plus facilement que le *cis*-CA et conduisent à la transformation de la micelle. En outre, le taux de conversion de la réaction de photo-isomérisation est le facteur le plus important déterminant le degré de transition morphologique de la micelle vermiforme. L'existence des substituants ortho augmente la constante d'équilibre de la réaction de photo-isomérisation (l'OMCA augmente le plus.). Par conséquent, *trans*-OMCA est doté de la meilleure capacité photo-sensible.

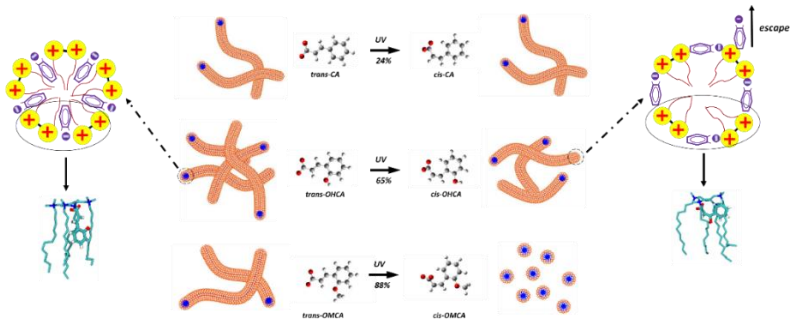

Fig. 3.1 Mécanisme de transition de la morphologie des micelles du 12-3-12·2Br⁻ et des dérivés cinnimates sous irradiation UV.

4 Simulations de dynamique moléculaire et calcul quantitatif du comportement photosensible de micelles en forme de ver construites par des dérivés tensioactifs Gemini 12-3-12·2Br⁻ et Cinnamte avec différentes positions méthoxy

Nous avons combiné des simulations de dynamique moléculaire avec des calculs quantitatifs pour étudier le comportement photo-réactif des systèmes de micelles en forme de ver contenant le tensioactif Gemini 12-3-12·2Br⁻ et trois trans-méthoxy-cinnimates avec groupe méthoxy en ortho-, méta- et para - position. Dans les simulations MD, nous avons simulé les micelles en forme de ver, en forme de bâtonnet et sphériques correspondant aux expériences et la transition entre elles avec succès avant et après irradiation UV. Ces morphologies micellaires ont été reconfirmées par la distribution de densité et les *P*. Les différents motifs de tassement entre les isomères 12-3-12·2Br⁻ et *trans/cis* ont été visualisés puis confirmés par $g(r)$ et SASA. L'énergie d'interaction entre 12-3-12·2Br⁻ et les isomères *trans/cis* illustre que la micelle contenant les isomères trans est plus stable.

Les calculs quantitatifs, y compris les distributions de potentiel électrostatique, l'énergie libre de solvatation, le volume de la molécule, l'angle et l'énergie d'interaction des modèles d'emballage typiques nous aident à explorer la différence de structure et de propriété entre les isomères *trans/cis*. Ces résultats indiquent que la présence d'ortho-substituant dans le cinnamate a un impact plus significatif sur le renforcement de la différence de l'encombrement stérique, de la distribution électrostatique et de l'hydrophilie des *trans/cis*-cinnamates avant et après l'irradiation UV et favorise davantage la capacité photo-réactive. de la micelle vermiforme correspondante.

Nous avons en outre utilisé les calculs quantitatifs pour prédire la photosensibilité de plusieurs acides cinnamiques. Compte tenu du volume molaire, de l'hydrophilie, de la distribution électrostatique, de l'équilibre de réaction constant globalement, la photosensibilité de l'OMCA est la meilleure.

5 Simulations de dynamique moléculaire et calcul quantitatif du comportement photosensible de micelles en forme de ver construites par des dérivés tensioactifs Gemini 12-3-12·2Br⁻ et Cinnamte avec différentes positions méthoxy

Nous avons exploré la montée des bulles dans des solutions micellaires de viscosité variable, avec des propriétés à la fois newtoniennes et d'amincissement par cisaillement. jusqu'à un saut de viscosité à des taux de cisaillement élevés, et des bulles plus grosses dans les fluides fluidifiants par cisaillement.

Comme le montre la Fig. 5.1, la montée des suspensions concentrées de bulles dans les fluides newtoniens est bien décrite en utilisant la description de Richardson et Zaki. Cependant, comme le montre la Fig. 5.2, dans les fluides fluidifiants par cisaillement, différents phénomènes peuvent être observés en fonction du taux de cisaillement autour des bulles, qui à son tour change avec la taille des bulles et la vitesse de montée. Si les bulles montent suffisamment lentement (bulles plus petites) de sorte que le taux de cisaillement se situe sur le plateau newtonien, la vitesse de montée des bulles est proche de celle attendue à partir de la vitesse de Stokes. Cependant, une fois que le taux de cisaillement autour des bulles est suffisamment élevé pour atteindre le régime d'amincissement par cisaillement, les bulles s'élèveront plus rapidement et la prédiction utilisant les taux de cisaillement locaux conduit à une sous-estimation de la vitesse de montée des bulles, probablement en raison de l'apparition de l'agrégation des bulles.La variation de la vitesse de montée des bulles en fonction de la fraction volumique des bulles est beaucoup plus faible que dans les fluides newtoniens. En effet, un exposant de $n = 1$ au lieu d'environ 4,5 dans l'expression de Richardson et Zaki décrit assez bien les données. Cela peut avoir implications importantes pour le processus de flottation dans les fluides fluidifiants par cisaillement, car nous montrons que le flux de surface maximal se produit à des fractions volumiques de gaz plus élevées que celles trouvées dans les fluides newtoniens.

Nos résultats donnent un aperçu de la montée des bulles de concentrations des solutions de bulles dans les fluides fluidifiants par cisaillement, qui ont été peu étudiées jusqu'à présent, malgré leur importance dans les applications. ce qui nécessite d'autres travaux expérimentaux et théoriques.

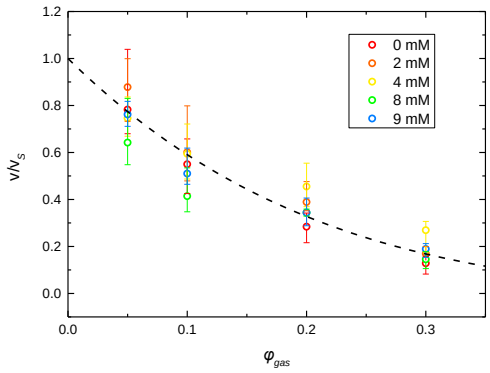

Fig. 5.1 La vitesse de montée de la bulle v normalisée en utilisant la vitesse de Stokes vs, en fonction de la fraction de gaz pour les solutions newtoniennes. La vitesse est mesurée en utilisant l'intensité I = 80. La ligne continue est la prédiction de Richardson et Zaki de l'équation avec n = 4,5.

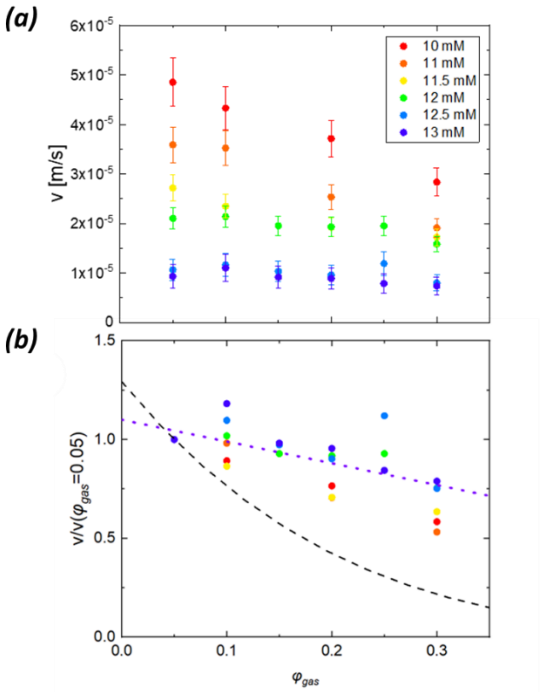

Fig. 5.2 (a) Vitesse de montée du front, v en fonction de gaz pour les solutions non newtoniennes, c'est-à-dire CTAB 20 mM avec NaSal 10-13 mM indiqué dans la légende. Les vitesses sont mesurées en utilisant I = 80. (b) Vitesse frontale normalisée par la vitesse à gas = 0,05, la ligne pointillée montre la prédiction de l'équation de Richardson et Zaki. La faible variation de la vitesse en fonction de peut être décrite en utilisant $\frac{v}{v(\varphi_{gas}=0.05)} = 1.1(1-\varphi_{gas})$ les pointillés (couleur) ligne

摘要

（该论文为中法联合培养项目，根据华东理工大学要求，论文主体以英文撰写，除正常摘要外，另附详细中文摘要一份）

在过去的几十年内，可以动态地响应外部环境刺激（包括电、光、磁、热、pH、CO_2等）的智能自组装材料一直是科研人员的研究热点。其中由表面活性剂参与构建的光响应自组装体引起了科学家们的广泛的关注。该刺激响应型自组装体系具有丰富的自组装形态和不同的自组装尺度，包括球形胶束、蠕虫状胶束、囊泡、凝胶、溶致液晶 (LC) 和双水相(ATPS)等。其中由表面活性剂构建的光响应自组装体有着无与伦比的优势，光的来源清洁无污染，是非干预的，不影响体系组分而且可以准确地控制调节时间和刺激位置。这些优势使其在药物释放、石油化工、可切换催化、表面改性、生物工程，智能光敏材料和光学系统等领域中脱颖而出，展现出有巨大的应用价值。在这些响应型自组装体中，光响应蠕虫状胶束具有多种可控胶束形态和大范围的可调流变特性，使其在光流变流体、光敏器件、减阻剂等实际应用中大放异彩。

向表面活性剂体系引入光敏小分子是最简单的获得光响应蠕虫状胶束体系的方法。该体系光响应能力的强弱取决于表面活性剂和光响应小分子的自组装能力。与传统的单链表面活性剂相比，相同浓度的 Gemini 表面活性剂的自组装能力远远强于常规表面活性剂。Gemini 表面活性剂优异的自组装能力和丰富的聚集行为，使得其与光敏小分子组成的光响应体系在工业应用中发挥更深远的作用。

光响应蠕虫状胶束的光响应能力的强弱，除了取决于体系表面活性剂的自组装能力以外，还取决于体系中光响应小分子的光敏效果。肉桂酸类分子结构中的碳碳双键在365nm 的紫外波长下的发生扭转，由反式变为顺式。这种光异构化反应会导致表面活性剂体系的自组装体发生排布方式上的转变，进而引起胶束构型的变化及宏观物理化学性质的变化。因为肉桂酸类分子本身具有一定的表面活性，溶解度和生物相容性较好，而且成本低廉，光敏效果优异。因此，由肉桂酸类光敏小分子和 Gemini 表面活性剂组成的光响应蠕虫状胶束成为目前炙手可热的研究对象。分子结构决定着分子的性质，肉桂酸类光敏小分子上不同的取代基，以及这些取代基所处的不同位置，都会对肉桂酸小分子的光异构化能力以及体系的光响应能力造成很大的影响。由于实验条件的限制，对于光响应蠕虫状胶束的光响应行为的微观机理的研究并不充分，同时因为合成的复杂困难程度和有限的人力物力，我们很难对种类繁多的肉桂酸类光敏小分子进行逐一实验，来验证和比较它们光响应能力的强弱。随着计算化学的发展，分子动力学模拟（MD）和量化计算为代表的计算机模拟计算方法正好可以帮助我们解决这些难题。

蠕虫状胶束的特殊的流变行为使它们成为一种典型的剪切稀化粘弹性流体。剪切稀化粘弹性流体中气泡的聚集上升行为在污水处理、石油提取和泡沫浮选等工业过程中非常常见。在工业过程中，气液两相的混合行为非常常见，相比于气相作为连续相出现的

液膜体系，其中更多的表现为气相作为分散相以气泡的形式分散在液相中。在许多工业应用中，如泡沫浮选、啤酒和碳酸饮料、污水提纯、两相分离等，气泡上升行为都起到非常重要的作用。由于气泡是可形变的，这导致其形状会随着上升速度以及连续相的流变行为的改变而发生变化，反之气泡的形状又影响着其上升速度以及连续相的流变行为。这种相互作用导致气泡的上升行为非常复杂，因此，目前对于气泡上升行为的研究多集中于牛顿流体和一些流变行为比较简单的流体如 Boger 流体和非弹性剪切变稀流体等。剪切变稀粘弹性流体是在工业应用上非常常见的流体，如聚合物溶液、聚合物溶体、油漆、涂料、稠油等。关于气泡在粘弹性剪切变稀流体中上升行为的研究少之又少，所以对于气泡在粘弹性剪切变稀流体中上升行为的研究非常有理论和实际应用价值。表面活性剂自组装成的蠕虫状胶束溶液是一种非常典型的具有粘弹性的剪切变稀流体，配制简单，成本低廉，并且随着表面活性剂或反离子盐浓度的改变，体系会呈现不同的流变特性，该体系非常适合用来研究气泡在粘弹性剪切变稀流体中上升行为。

本论文的主要内容如下：

第一章主要介绍了 Gemini 表面活性剂的分类、性质以及其自组装形态的种类、表面活性剂构建的不同类型的环境刺激响应型蠕虫状胶束、气泡在牛顿流体和非牛顿流体中上升行为的研究、以及分子动力学和密度泛函计算的理论基础。

1.1 Gemini 表面活性剂

Gemini 表面活性剂是由两个疏水尾链和两个亲水头基组成，通过联接基团连接的一种表面活性剂。Gemini 表面活性剂相比于传统的单链表面活性剂有着更加优异的界面活性，更丰富的聚集行为和更强的自组装能力，更复杂的流变学行为更优异的协同作用。如图 1.1，当表面活性剂在水溶液浓度达到临界胶束浓度（CMC）之上，由于其两亲性，表面活性剂分子会自组装成不同形态和尺度的自组装体。

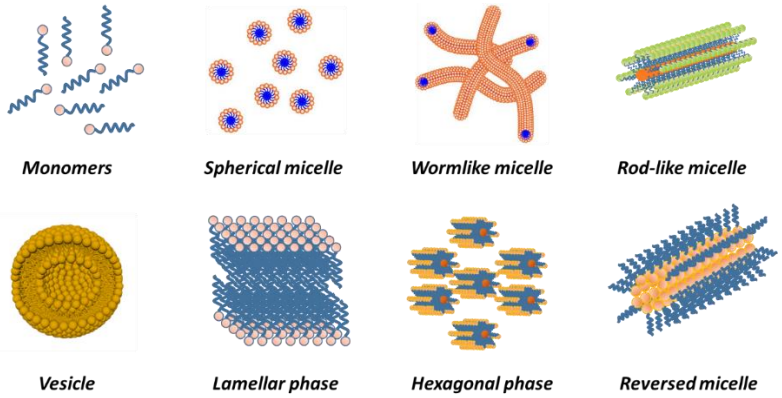

图 1.1　常见的表面活性剂自组装体种类

1.2　表面活性剂构建的智能响应型自组装体

外界环境的变化会导致表面活性剂自组装体的结构和形态发生改变，从而引起宏观

上的物理化学性质的改变。这些性质为其构建刺激响应型材料提供了理论和实验基础。通过刺激响应的类型，我们可以将刺激响应型自组装体分为两大类：物理信号类智能响应型自组装体（光、热、电、磁）和化学信号类智能响应型自组装体（CO_2、pH、氧化还原）。光响应自组装体有着诸多其他响应型所没有的优势：首先光刺激是一种干净的非接触性刺激，不改变系统的成分。其次，光易于获取，可操作性强。再者，光刺激的位点可以精确调节。因此，光响应自组装体在众多刺激响应性自组装体中脱颖而出。

如图 1.2 所示，常见的光敏小分子主要分为以下三种偶氮苯类、肉桂酸类和螺吡喃类。其中，肉桂酸类光敏小分子种类十分丰富，溶解性和生物相容性较好，可以与表面活性剂直接复配形成形态丰富的自组装体，成本更加低廉，是构建光响应表面活性剂自组装体的不二选择。

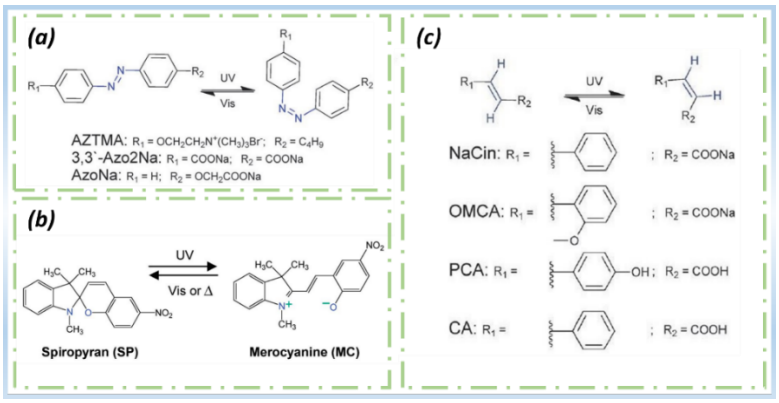

图 1.2　常见的光敏小分子种类：(a)偶氮苯类；(b)肉桂酸类；(c)螺吡喃类

1.4　气泡液

如图 1.3 所示，根据气相体积分数，气液混合物可分为单个气泡（$\varphi_{gas} \approx 0$）、气泡液（$\varphi_{gas} < 64\%$）、湿泡沫（$64\% < \varphi_{gas} < 85\%$）和干泡沫（$\varphi_{gas} > 95\%$）。当气相体积分数低于 64%时，各个气泡相互独立，不会相互接触发生变形。此时，它们通常被称为气泡液。气泡液是气泡在液体中极不稳定的分散体，随着气泡的粗化和聚结迅速上升，变成湿泡沫。

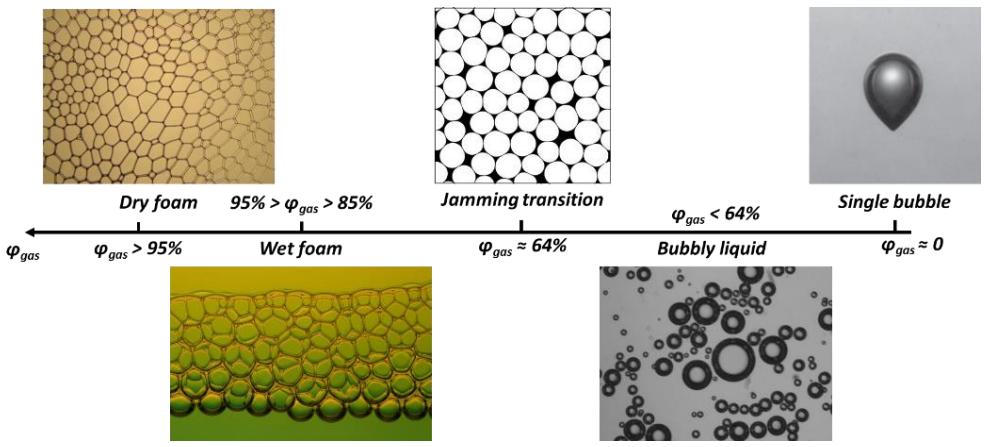

图 1.3　气泡作为分散相分布在液相中的分类

1.5 单个气泡在牛顿流体中的上升速度

当气泡处于静态流体中时，它受到的力如图 1.4 所示。当连续相为牛顿流体，分散相为气体。并且在气泡没有任何内部循环，边界处没有滑移，且气泡不发生形变的情况下，我们可以根据 Stokes 方程来计算牛顿流体中气泡的最终上升速度：

$$v_s = \frac{\rho_c g d_e^2}{18\eta_c} \tag{1-3}$$

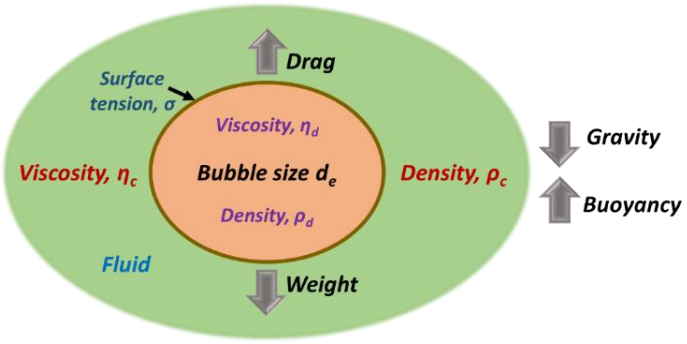

图 1.4　单个气泡在静止液体中上升受力分析

1.6 多气泡在牛顿流体中的上升速度

对于气体分数较大的气泡液体（气体分数大于 10^{-4}），如果气泡的分散程度不高，单个气泡引起的流动会影响其他气泡的运动。此时 Stokes 方程不再适用。在固定的气液总体积内，液体会通过向下移动以补偿气泡的上升带来的体积空缺。这种流体回流阻碍了气泡的上升，导致气泡平均上升速度小于单个气泡的上升速度。随着气体分数的增加，这种阻碍作用更加明显。为了校正这种阻碍效应，Richardson 和 Zaki 提出了一个关于多气泡在牛顿流体中上升的经验方程：

$$v_{RZ} = v_s \left(1-\varphi_{gas}\right)^n \tag{1-4}$$

其中 φ_{gas} 是气泡液的气体分数，n 是通过实验得到的常数，会随雷诺数变化而变化。对于低 Re，n 通常在 4.65 和 6.55 之间。Richardson-Zaki 方程已被证明与各种气体组分的实验数据非常吻合。当气体分数接近 0.60 时，气泡之间会产生接触挤压变形，上升速度开始偏离公式预测。

1.7 多气泡在非牛顿流体中的上升速度

对于非牛顿流体中气泡上升的研究主要集中在气体分数低于 1%的 Boger 流体和剪切变稀非弹性流体体系。对于更高的气体分数，由于气泡之间的相互作用更加复杂，相关的研究非常匮乏。粘弹性剪切稀化流体的粘度会随着气泡上升速度的增加而降低。由于液相粘度和气泡上升速度的不确定性，关于在剪切稀化粘弹性流体中气泡上升的理论研究少之又少。但又因为其在工业应用上的普遍性，所以对高气体分数下粘弹性剪切稀化流体中多气泡上升的实验和理论研究是非常有必要的。

1.8 分子动力学模拟和量化计算

二十一世纪来，随着计算机性能的飞速跃升，多数学科领域所遇到的复杂理论计算问题均可交由计算机解决。计算机模拟和理论计算已经和实验方法并列称谓已成为现代物理化学研究中最重要的三种方法。分子动力学模拟通过对牛顿运动方程积分来对由体系内所有粒子坐标和速度组成的相空间进行采样，再根据当前粒子的坐标和速度推算出下一个时间步长的坐标与速度。通过对每个粒子运动的统计分析，可以推断出系统的各种性质，包括分子构象和分子动态性质、系统的热力学性质，以及各种平衡态/非平衡态性质。分子动力学模拟优于其他模拟方法的地方在于系统中粒子的运动轨迹具有精确的物理推导依据，在获取系统热力学统计信息的同时，还可以获取系统的动态变化信息。

量子化学作为理论化学的一个分支，是化学与物理的交叉学科，是应用量子力学的基本原理和方法研究化学问题的基础科学。分子的结构和化学性质与分子的原子组成及其电子排列或运动状态密切相关。量子化学从电子运动的基本规律出发，描述系统中所有电子和原子的相对空间位置，从而实现对系统反应性和结构的研究。以量子化学为基础的量化计算非常强大，可以应用于许多不同的系统，例如研究稳定和不稳定分子的结构和性能，结构和性能之间的关系，分子之间的相互作用和分子间的相互碰撞和相互反应，为当前的化学研究提供了重要的理论工具。量子化学的计算方法主要有：从头计算法、半经验法和密度泛函理论（DFT）。

1.9 论文选题意义及设计思路

Gemini 表面活性剂与肉桂酸类光响应小分子构建的光响应蠕虫状胶束具有优异的光流变性质，在石油化工、日化护肤、光敏器件、光流变流体等领域都具有潜在的价值。但目前对于该体系光响应机理的研究仍未完善，且对于肉桂酸衍生物分子结构的差异对其光响应能力的影响仍未研究透彻。气泡上升行为有着巨大的工业应用价值，且目前对于气泡在剪切稀化粘弹性流体中上升行为的研究也非常匮乏，基于此：

（1）选择了 Gemini 表面活性剂二亚甲基-1,2-二（十二烷基二甲基溴化铵）（12-2-12·2Br^-）与肉桂酸类光敏小分子反式-邻甲氧基肉桂酸(*trans*-OMCA) 来构建光响应蠕虫状胶束体系。拟通过流变学与分子动力学、量化计算相结合的方法探讨该体系的光响应行为和自组装体形态转变的微观机理。

（2）基于以上的研究，挑选三种不同的邻位取代基的肉桂酸类光敏小分子反式肉桂酸（*trans*-CA），反式邻甲氧基肉桂酸（*trans*-OMCA），反式邻羟基肉桂酸（OHCA）和 Gemini 表面活性剂三亚甲基-1,3-二（十二烷基二甲基溴化铵）（12-2-12·2Br^-）进行复配来构建光响应蠕虫状胶束体系。通过反应动力学、流变学结合分子动力学模拟和量化计算来研究不同的肉桂酸衍生物邻位基团对光异构反应速率和蠕虫状胶束光响应行为的影响。

（3）基于前面两部分的研究，更进一步地研究由邻位、间位和对位甲氧基取代的肉

桂酸衍生物光敏分子（反式邻甲氧基肉桂酸（*trans*-OMCA）），反式间甲氧基肉桂酸（*trans*-MMCA）和反式对甲氧基肉桂酸（*trans*-PMCA））和 Gemini 表面活性剂 12-3-12·2Br⁻复配得到的光响应蠕虫状胶束体系，并通过分子动力学模拟和量化计算来研究不同取代基的位置对其光响应行为的影响。此外，拟计算几十种不同的肉桂酸衍生物的结构性质，为实验上构建光响应能力更强的蠕虫状胶束体系提供理论指导。

（4）拟选择了一种经典的粘弹性剪切变稀流体（CTAB/NaSal 蠕虫状胶束体系）来研究气泡在较高的气体分数下（5%-30%）的粘弹性剪切变稀流体中的上升速率，为其工业应用如泡沫浮选提供理论指导。

第二章主要介绍了由 12-2-12·2Br⁻和 *trans*-OMCA 构建的自组装体的光响应行为的分子动力学模拟和密度泛函理论计算。

2.1 12-2-12·2Br⁻和 *trans*-OMCA 蠕虫状胶束体系的光响应行为

2.1.1 微观结构

根据我们之前的研究，我们选择了浓度为 17mM 的 12-2-12·2Br⁻和 7mM 的 *trans*-OMCA 来构建蠕虫状胶束体系，并通过透射电镜观察其在不同紫外照射时间后自组装体的微观结构。图 2.1 展示了该体系在 25°C 经历不同紫外线照射时间下的 TEM 图像。如图 2.1 所示，该系统最初形成了一个交缠密集网络结构的蠕虫状胶束，在紫外线照射 40 分钟后，蠕虫状胶束开始变短，网络结构解体成短棒状胶束。当紫外线照射时间为 60 分钟时，棒状胶束完全转变为球形胶束。该体系呈现出了光响应性能，在紫外光照射后体系经历了蠕虫状胶束、棒状胶束、球状胶束三种胶束形态。

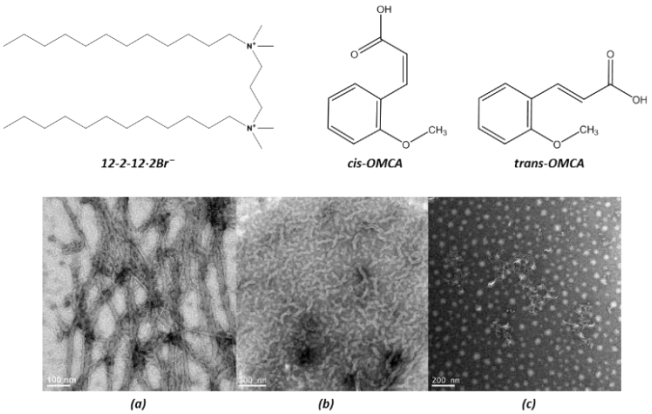

图 2.1 12-2-12·2Br⁻，*trans/cis*-OMCA 的化学结构式和 17 mM 12-2-12·2Br⁻/7 mM *trans*-OMCA 体系在 25°C 下随着紫外线照射变化的 TEM 图像 (a) 0 分钟；(b) 40 分钟；(c) 60 分钟

2.1.2 流变特性

图 2.2 展示了 17 mM 12-2-12·2Br⁻/7 mM *trans*-OMCA 混合溶液在不同紫外光照射时间下的流变特性。从图 2.2 (a)可以看出，在紫外光照前 17 mM 12-2-12·2Br⁻/7 mM *trans*-

OMCA 体系出现了零剪切粘度和剪切稀化现象，这表明了蠕虫状胶束的产生。当剪切速率较低时，网络结构难以被破坏，平台值出现（零剪切粘度，η_0）。当剪切速率相对较高时，致密的网络结构先解缠，然后被剪切破坏并转变为更短的胶束，剪切稀化行为出现。随着紫外光照射时间的延长到四十分钟，剪切稀化逐渐消失。系统的零剪切粘度（图 2(b)）在 40 分钟前迅速下降约 3 个数量级（从 2.7 ± 0.1Pa·s 到 7.3 ± 0.1mPa·s），并在之后几乎保持不变。这说明长的蠕虫状胶束历经 40 分钟的紫外线照射后逐渐转化为短的棒状胶束和球状胶束，并不再发生构型变化。此外，不同紫外线照射时间的动态频率扫描曲线(图 2.2(c)) 和 Cole-Cole 曲线(图 2.2(d)) 也再次证明了紫外线照射后，蠕虫状胶束转变为球形胶束。这些结果与之前的 TEM 结果一致。

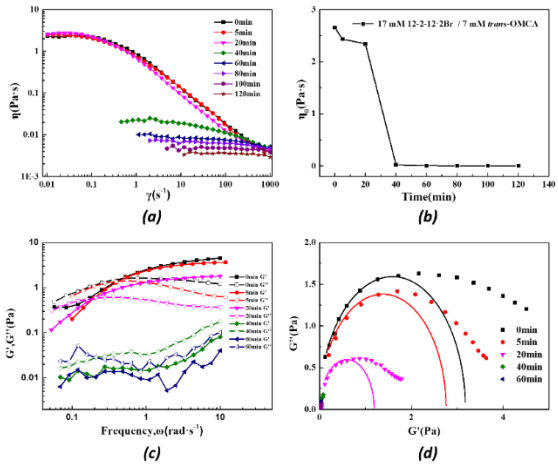

图 2.2　25°C 时不同紫外照射时间对 17 mM 12-2-12·2Br⁻/7 mM *trans*-OMCA 蠕虫状胶束流变特性的影响 (a) 稳定剪切粘度；(b) 零剪切粘度；(c) 动态频率扫描；(d) Cole-Cole 曲线

2.2　12-2-12·2Br⁻/*trans*-OMCA 蠕虫状胶束的光响应行为的分子动力学模拟

图 2.3 显示了模拟结果的快照。每个模拟体系都包含 216 个 12-2-12·2Br⁻分子和不同数量的 *trans*-OMCA 或 *cis*-OMCA 分子。我们定义 r_n 为模拟体系中 OMCA 和 12-2-12·2Br⁻的数量之比：

$$r_n = \frac{N_{OMCA}}{N_{Surfactant}} \tag{2-1}$$

随着 *trans*-OMCA 的加入，蠕虫状胶束首先出现($r_n = 0.75$)。当 *trans*-OMCA 浓度升高($r_n = 1$)时，形成了更致密的蠕虫状胶束。当 r_n 达到 1.25 时，蠕虫状胶束进一步增长，聚集成一条长蠕虫状胶束和几个球形胶束。最终，在 r_n = 1.5 时，该体系聚集为交织的网络结构。*trans*-OMCA 分子是两亲性的，具有表面活性，在被加入到 12-2-12·2Br⁻溶液中后，*trans*-OMCA 将与 12-2-12^{2+}一起参与胶束的构成，导致了更为致密的胶束形成。同时，由于 12-2-12^{2+}和 *trans*-OMCA^{-}的之间的强静电相互作用以及 *trans*-OMCA 的苯环和 12-2-12^{2+}带电头基之间的 π-阳离子相互作用，使得胶束的堆积密度增加，促进了长蠕

虫状胶束和网状结构的形成。

在紫外光照射下，*trans*-OMCA 异构化为 *cis*-OMCA。当 $r_n = 0.75$ 时，由 *trans*-OMCA 构成的短蠕虫状胶束在光照之后分裂成小的球形胶束。同样，长蠕虫状胶束会分裂成一个球形胶束和一条短蠕虫状胶束($r_n = 1$)。随着 r_n 增加到 1.25，长蠕虫状胶束破裂成一条短蠕虫状胶束。在最高的 OMCA 浓度(r_n = 1.5)下，致密的网络胶束破裂成长的蠕虫状胶束。从上述结果可以看出，12-2-12·2Br$^-$/*trans*-OMCA 胶束在此紫外光照射下表现出明显的光响应行为，这与我们 TEM 结果中交织的网状结构逐渐分解成较短的胶束形状一致。

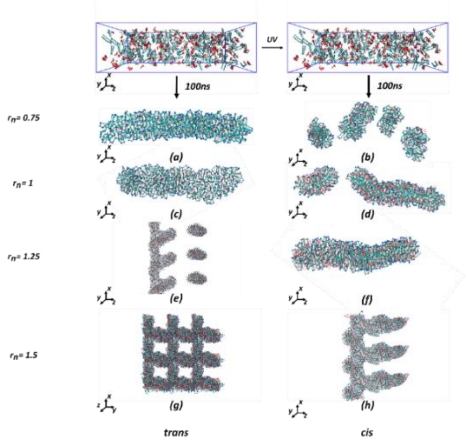

图 2.3　25℃ 时不同 r_n 下，12-2-12·2Br$^-$和 *trans*-OMCA 在盒子中的初始构型和 100ns 分子动力学模拟后的胶束形态快照。(a), (b), (c), (d), (f)包含一个周期。为了完全显示长蠕虫状胶束形态和网状形态，(e)和(h)包含三个周期，(g)包含九个周期。（青色离子为 12-2-12^{2+}；红色离子为 OMCA$^-$；为清楚起见，水和其他离子未显示。）

2.3　12-2-12·2Br$^-$/OMCA 在胶束中的排布方式

OMCA 和 12-2-12·2Br$^-$在胶束上的排布方式会直接影响胶束的形态。图 2.4 显示了从 $r_n = 0.75$ 模拟中最后一帧胶束上截取的 12-2-12·2Br$^-$/OMCA 两种代表性排布方式。我们可以很容易地观察到 *trans/cis*-OMCA 排布方式的差异：*cis*-OMCA 的苯环位于胶束表面，而 *trans*-OMCA 的苯环插入 12-2-12·2Br$^-$的疏水烷基链中；*trans/cis*-OMCA 的羧基均位于胶束表面，甲氧基嵌入胶束中。我们很难观察到 *trans*-OMCA 胶束表面的白色部分（*trans*-OMCA 中苯环上的氢原子）。这证实了 *trans*-OMCA 的苯环完全嵌入 12-2-12·2Br$^-$胶束中，而 *cis*-OMCA 的苯环位于胶束表面。

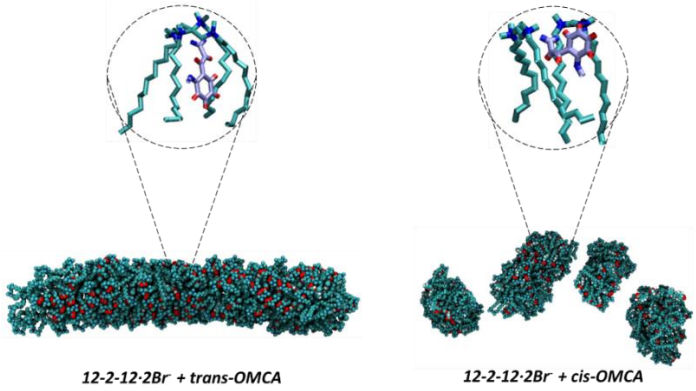

图 2.4　r_n = 0.75 时，12-2-12·2Br⁻和 OMCA 在胶束上的排布方式。(青色珠为 12-2-12^{2+}；红色珠和白色珠为 OMCA 中的氧原子和氢原子。)

2.4　胶束转变机理

2.4.1　分子结构

为了进一步探究紫外光照射后胶束转变的机理，我们采用了量化计算的方法计算了一系列参数。经过优化后的 *cis/trans*-OMCA 分子结构如图 2.5 所示。*trans*-OMCA 分子为平面结构。而 *cis*-OMCA 分子是一种三维结构，弯折程度更高，空间位阻较大，这同时也在我们计算得到的分子体积（表 2.1）中得到证实。因此，当插入胶束层时，平面结构的 *trans*-OMCA 分子更容易嵌入 12-2-12·2Br⁻胶束层形成更加稳定致密的胶束。紫外照射后，异构化产生的 *cis*-OMCA 分子则占据更多的空间，空间位阻增大，相互作用减弱，导致其与 12-2-12·2Br⁻之间的排布方式变得松散，最终胶束发生断裂。

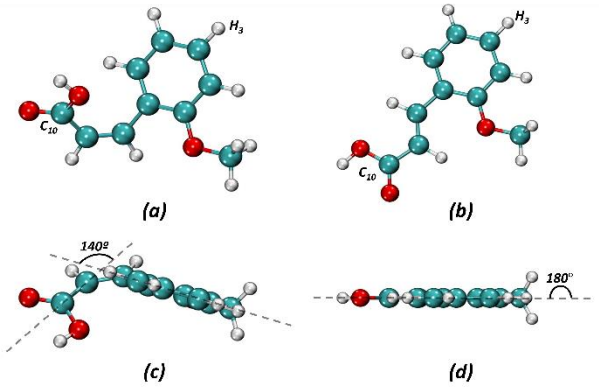

图 2.5　使用 M052X/6-31G*基组优化后的 *trans/cis*-OMCA 分子结构。

表 2.1　使用 Gaussian 09 在 SMD 水溶剂模型中以 M052X/6-31G*基组计算出的 *trans/cis*-OMCA 的溶剂化自由能、H_3 和 C_{10} 的原子距离以及分子摩尔体积

	溶剂化自由能 (kJ/mol)	C_{10}-H_3 距离 (Å)	分子摩尔体积 (cm^3/mol)
cis-OMCA	−40.56	6.46	125.16
trans-OMCA	−37.68	9.02	122.23

2.4.2 亲疏水性

溶剂化自由能的大小代表了分子亲疏水能力的强弱。如表 2.1 所示，*cis*-OMCA 和 *trans*-OMCA 的溶剂化自由能分别为−40.56 kJ/mol 和−37.68 kJ/mol。显然，*cis*-OMCA 亲水性更强，因此与 12-2-12·2Br⁻组成胶束以后，*cis*-OMCA 更容易逃离胶束表面到水中。为了验证这一推论，我们构建了一个由 26 个 12-2-12·2Br⁻分子（CMC 浓度）构成的空气/水界面层。添加过量的 OMCA 分子（52 个）以确保有 OMCA 分子可以从表面活性剂层中逸出。图 2.6 展示了该体系在 30 ns MD 模拟前后的快照。显然，逃逸出胶束层的 *cis*-OMCA 数远多于 *trans*-OMCA。这证实了我们的推论，较强的亲水性和较大的空间位阻驱使 *cis*-OMCA 从 12-2-12·2Br⁻胶束层中逃逸到水溶液中。一旦 *cis*-OMCA 脱离其位置，蠕虫状胶束随之断裂成棒状胶束甚至球形胶束。

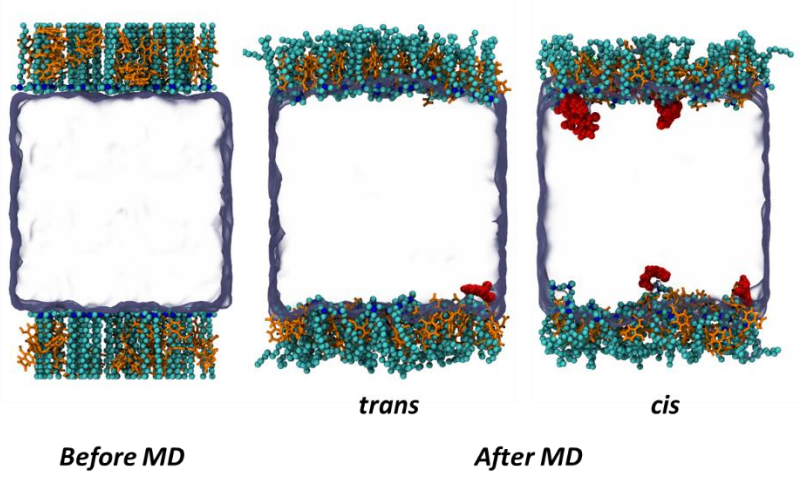

图 2.6　26 个 12-2-12·2Br⁻和 52 个 OMCA 的空气/水界面体系经过 30 ns MD 模拟前后的快照。（红色部分为从胶束中逸出的 OMCA 分子；黄色部分为嵌入到胶束中的 OMCA 分子；青色部分为 12-2-12·2Br⁻层。中间透明部分为水。）

2.4.3 能量

我们从 MD 模拟的最后一帧的胶束中截取了 12-2-12·2Br⁻和 *trans/cis*-OMCA 两种代表性的排布方式，一种是苯环嵌入到 12-2-12·2Br⁻烷基链层中，另一种是苯环位于胶束表面，并计算了这些排布方式相互作用能。为了方便比较，我们将(d)的相互作用能设为 0 kJ/mol，则(a) (b) (c) (d) 这四种排布方式的相对相互作用能分别为 35.5、3.1、8.5 和 0 kJ/mol。对于 *cis*-OMCA，苯环排布在胶束表面的结构更稳定，对于 *trans*-OMCA，苯环嵌入胶束内部的结构更稳定。这意味着在光照后排布方式由(d)变成(a)时，为了重新获得稳定的排布方式，先前稳定的排布方式(a)将会变为(b)。这种转变会导致胶束结构的松散和变形，最终引起胶束的裂变。

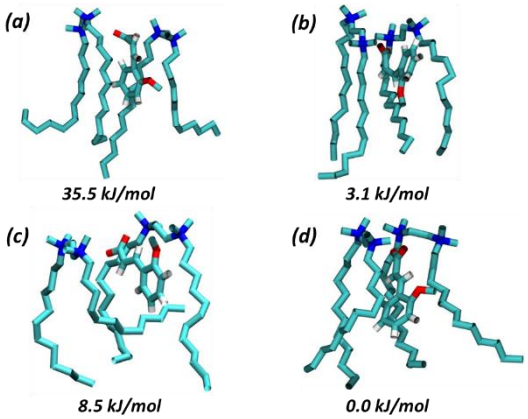

图 2.7　胶束上 12-2-12^{2+}和 OMCA^{-}之间特定排布方式的相对相互作用能(kJ/mol)。(a)和(d)的苯环嵌入胶束中，(b)和(c)的苯环出现在胶束表面。(a)和(b)是 *cis*-OMCA。(c)和(d)是 *trans*-OMCA。为清楚起见，氢原子未显示。为了方便比较，我们将(d)的相互作用能设为 0 kJ/mol

2.5　结论

本章使用了流变学、TEM 实验、分子动力学模拟和量化计算研究了 Gemini 表面活性剂 12-2-12·2Br^{-}和 *trans*-OMCA 的光响应行为。首先，*trans*-OMCA 与 12-2-12·2Br^{-}强烈的静电相互作用和 π-阳离子相互作用，导致蠕虫状胶束的形成。在紫外线照射下，*trans*-OMCA 光异构化为 *cis*-OMCA。蠕虫状胶束先裂解成棒状胶束，最后转化成球形胶束。图 2.8 展示了光响应 12-2-12·2Br^{-}/*trans*-OMCA 蠕虫状胶束形态转变机理。系统地研究了影响这些胶束转变过程的三个主要因素（几何形状、亲疏水性和能量差异）。*cis*-OMCA 的较大空间位阻削弱了其和 12-2-12·2Br^{-}之间的 π-阳离子相互作用和静电相互作用。其次，*cis*-OMCA 较强的亲水性导致 *cis*-OMCA 更容易从胶束层逃脱到溶液中。最后，*cis*-OMCA 与 12-2-12·2Br^{-}之间的相互作用能比 *trans*-OMCA 弱。这些因素的综合作用导致蠕虫状胶束的破裂和重排。

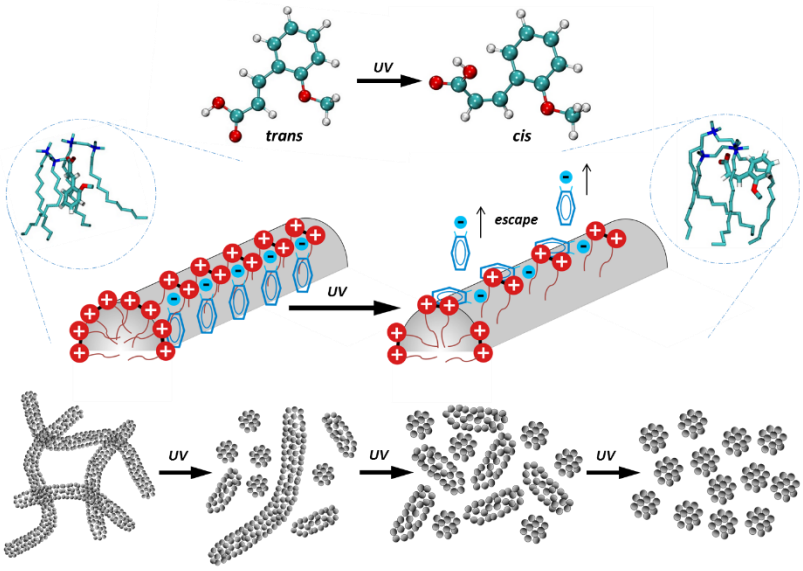

图 2.8　光响应 12-2-12·2Br^{-}/*trans*-OMCA 体系胶束形态转变机理

第三章主要介绍了由 12-2-12·2Br⁻和三种不同邻位取代基的肉桂酸衍生物(*trans*-CA, *trans*-OHCA 和 *trans*-OMCA)构建的蠕虫状胶束的光响应行为的分子动力学模拟和量化计算。

3.1 12-3-12·2Br⁻/肉桂酸衍生物混合体系的光响应行为

本章选取了三种不同邻位取代基团的肉桂酸衍生物，分别是反式肉桂酸(*trans*-CA)，反式邻羟基肉桂酸(*trans*-OHCA)和反式邻甲氧基肉桂酸(*trans*-OMCA)和季铵盐型 Gemini 表面活性剂 12-3-12·2Br⁻来构建光响应蠕虫状胶束体系。Gemini 表面活性剂 12-3-12·2Br⁻和三种不同邻位取代基团的肉桂酸衍生物的分子结构图如图 3.1 所示。

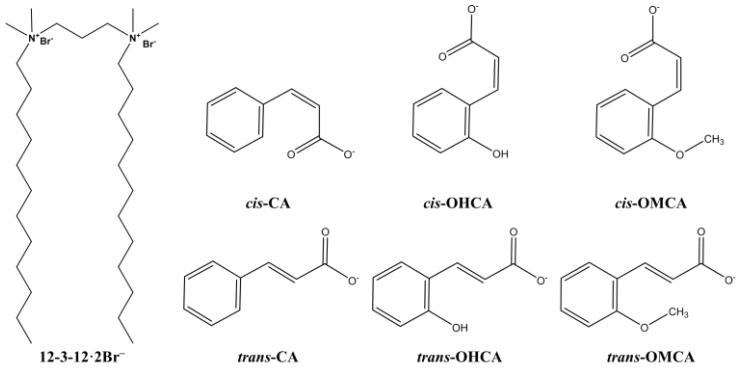

图 3.1 Gemini 表面活性剂 12-3-12·2Br⁻和肉桂酸衍生物 *cis/trans*-CA、*cis/trans*-OHCA 和 *cis/trans*-OMCA 的分子结构

图 3.2 展示了通过透射电镜结合负染色技术获得的不同紫外线照射时间后体系的微观结构图像。对于 40 mM 12-3-12·2Br⁻/24 mM *trans*-CA，该体系最初是互相缠绕的密集的蠕虫状胶束，在紫外线照射 160 分钟后，该结构基本不变。对于 40 mM 12-3-12·2Br⁻/24 mM *trans*-OHCA，该体系首先形成了蠕虫状网络结构，并在 160 分钟的紫外线照射下，交织的网络结构开始逐渐变稀疏，胶束长度逐渐变短。*trans*-OMCA 体系最初也形成了蠕虫状网络结构，在紫外线照射 160 分钟后，转变为短棒状胶束甚至球形胶束。

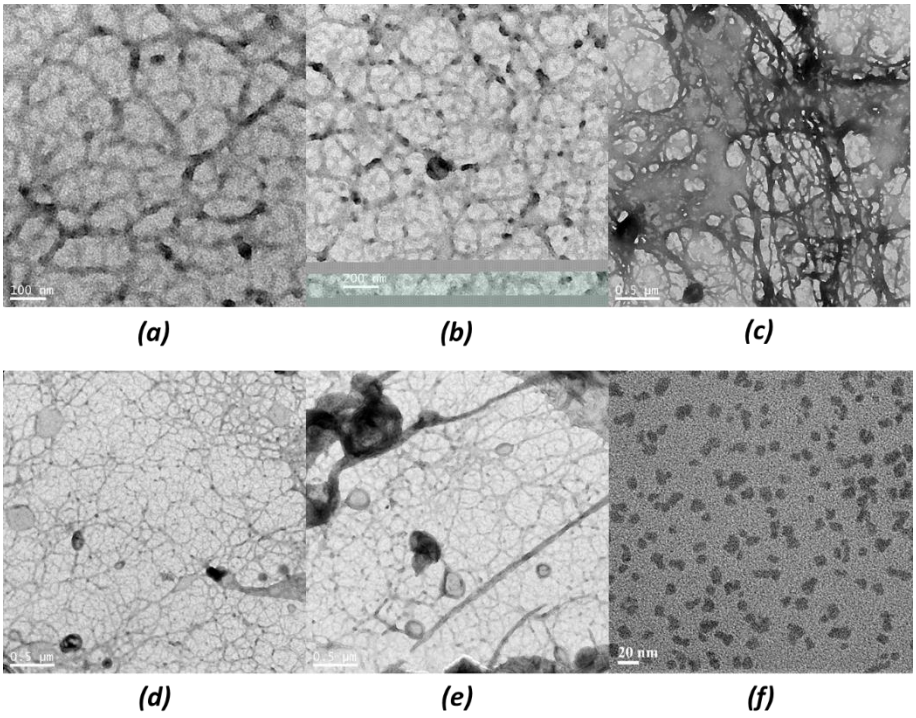

图 3.2　40 mM 12-3-12·2Br⁻和 24 mM 反式肉桂酸衍生物体系在 25°C 下经过不同紫外线照射时间的 TEM 图像 [(a) *trans*-CA，0 min; (b) *trans*-CA，160 min；(c) *trans*- OHCA，0min；　(d) *trans*-OHCA，160min；(e) *trans*-OMCA，0min；(f) *trans*-OMCA，160min]

3.2　12-3-12·2Br⁻与肉桂酸衍生物混合体系的流变特性

为了进一步研究紫外线照射后的 12-3-12·2Br⁻与肉桂酸衍生物混合体系流变行为的变化，我们测量了 40 mM 12-2-12·2Br⁻/24 mM 肉桂酸衍生物在不同的紫外线照射时间下的稳态剪切粘度和动态频率扫描曲线并展示在图 2.3 中。从图 2.3 (a)、(b)、(c)可以看出，这三种肉桂酸衍生物没有经过光照时均在低剪切速率下呈现平稳状态，而在高剪切速率区域则呈现剪切稀化现象，这说明了三个体系均形成了蠕虫状胶束。对于 12-3-12·2Br⁻/*trans*-CA 体系，在紫外光照射 160 分钟后，零剪切粘度几乎不变。从图 2.3 (d)中，我们可以看到 12-3-12·2Br⁻/*trans*-CA 的 *G'G"*曲线存在一个交点，证明了蠕虫状胶束的形成。在光照后，曲线和交点的位置几乎没有变化，表明蠕虫状胶束的粘弹性基本不变。这表明了 12-3-12·2Br⁻/*trans*-CA 蠕虫状胶束的光响应性基本可以忽略。对于 *trans*-OHCA 体系，在紫外线照射 160 min 后，剪切稀化现象仍然存在，η_0 从 19.7 Pa·s 降低到 2.63 Pa·s。此外，*G'G"* 的交点频率随着光照时间逐渐右移。很明显，驰豫时间的缩短表明了网络结构的强度减弱。对于含 *trans*-OMCA 的蠕虫状胶束，剪切变稀现象随着光照越来越弱，趋于消失，且 *G'G"*曲线的交点在 80 分钟后消失。这可能是因为含 *trans*-OMCA 蠕虫状胶束在紫外线照射后逐渐转变为短棒状胶束和球形胶束。

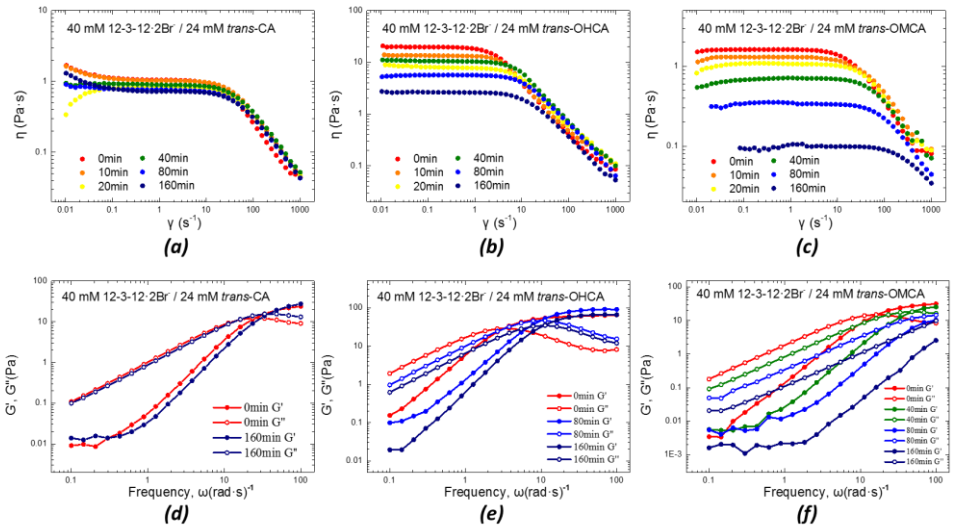

图 3.3　40 mM 12-2-12·2Br⁻和 24 mM 反式肉桂酸衍生物样品在 25°C 下的稳态剪切粘度曲线((a) *trans*-CA、(b) *trans*-OHCA、(c) *trans*-OMCA)和动态频率扫描曲线((d) *trans*-CA、(e) *trans*-OHCA、(f) *trans*-OMCA)

3.3　12-3-12·2Br⁻/肉桂酸衍生物混合体系的光响应动力学

为了探索三种肉桂酸衍生物光响应行为差异的深层原因，我们研究了这三种光异构化反应的动力学。为确保反式异构体尽可能的转化为顺式异构体，我们将 40 mM 12-3-12·2Br⁻/24 mM 反式异构体溶液稀释 1000 倍（40 μM 12-3-12·2Br⁻/24 μM 反式异构体），来进行光照实验至反应达到平衡。我们使用紫外可见吸收光谱和高效液相色谱(HPLC)来得到反应的转化率 f：

$$f = \frac{c_i - c_e}{c_i} \tag{3-1}$$

其中，c_i 是反式异构体的初始浓度，c_e 是反式异构体的平衡浓度。图 3.4 展示了三种肉桂酸衍生物在不同光照时间下的转化率曲线和动力学曲线。从之前的研究中可以获知，肉桂酸衍生物的光异构化反应一般为一级对峙反应。所以我们绘制了 $ln\frac{c_i-c_e}{c_i-c_e-c}$ 随时间变化的点图，并且发现这些点符合一级对峙反应。因此，我们使用线性拟合来获得直线斜率(k_1+k_{-1})，然后通过：

$$K_c = \frac{c_e}{c_i - c_e} \tag{3-2}$$

$$K_c = \frac{k_1}{k_{-1}} \tag{3-3}$$

计算反应平衡常数 K_c、正向速率常数 k_1 和逆向速率常数 k_{-1}。计算结果如表 3.1 所示，转化率和平衡常数的顺序为 *trans*-OMCA (f = 0.88, K_c = 7.33) > *trans*-OHCA (f = 0.65, K_c = 1.88) > *trans*-CA (f = 0.24, K_c = 0.31)，这和实验结果一致。

通过动力学曲线，我们可以看到 k_1 的大小顺序为 *trans*-OMCA (1.09) > *trans*-OHCA

(0.12) > *trans*-CA (0.006)，这说明了在相同浓度下，*trans*-OMCA 的光异构化速率是最快的。这和含 *trans*-OMCA 蠕虫状胶束转化速度最快的实验结果相一致。

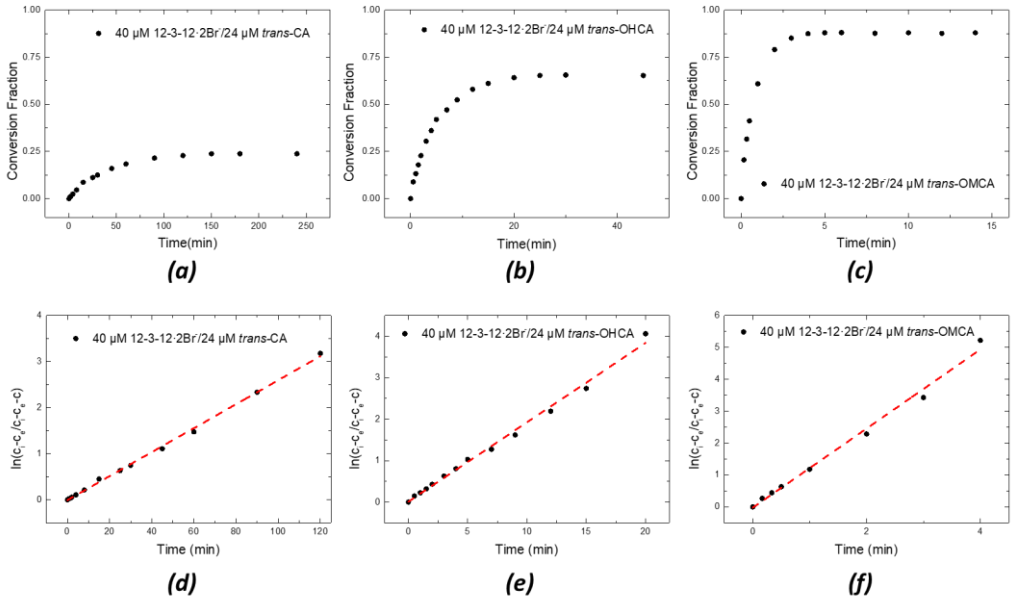

图 3.4　25°C 下 40 μM 12-3-12·2Br⁻和 24 μM 反式异构体体系随紫外光照时间的转化率曲线((a)、(b)、(c))和动力学曲线((d)、(e)、(f))。其中 (a)，(d)为 *trans*-CA；(b)，(e)为 *trans*-OHCA；(c)，(f)为 *trans*-OMCA

表 3.1　25°C 下三种肉桂酸衍生物 *trans*-CA、*trans*-OHCA 和 *trans*-OMCA 光异构化反应的转化率 *f*、动力学曲线的斜率(k_1+k_{-1})、反应平衡常数(K_c)、正向速率常数(k_1)和反向速率常数(k_{-1})

	trans-CA	*trans*-OHCA	*trans*-OMCA
f	0.24	0.65	0.88
k_1+k_{-1}	0.026	0.19	1.24
K_c	0.31	1.88	7.33
k_1	0.006	0.12	1.09
k_{-1}	0.020	0.07	0.15

3.4　12-3-12·2Br⁻与反式肉桂酸衍生物光响应行为的分子动力学模拟

图 3.5 展示了 12-3-12·2Br⁻和肉桂酸衍生物混合体系在不同转化率下的初始构型和 100 ns MD 模拟后的最终构型。从图 3.5 可以看出，经过 100 ns MD 模拟，三个体系均形成了蠕虫状胶束。在充足紫外光照射后，*trans*-CA 体系在 f = 0.24 时达到平衡。此时，蠕虫状胶束形态几乎没有变化。对于 *trans*-OHCA 体系，当 f = 0.24 时，蠕虫状胶束开始破裂。最终，体系在 f = 0.65 时达到平衡，转变为一个短棒状和一个球形胶束。对于 *trans*-OMCA 体系，在 f = 0.24 时，体系仍保持蠕虫状胶束。当 f 达到 0.65 时，蠕虫状胶束分

裂成两个短棒状胶束。在达到平衡时（$f = 0.88$），体系转变为 3 个球形胶束。光响应行为的模拟结果与我们的 TEM 实验结果非常吻合。

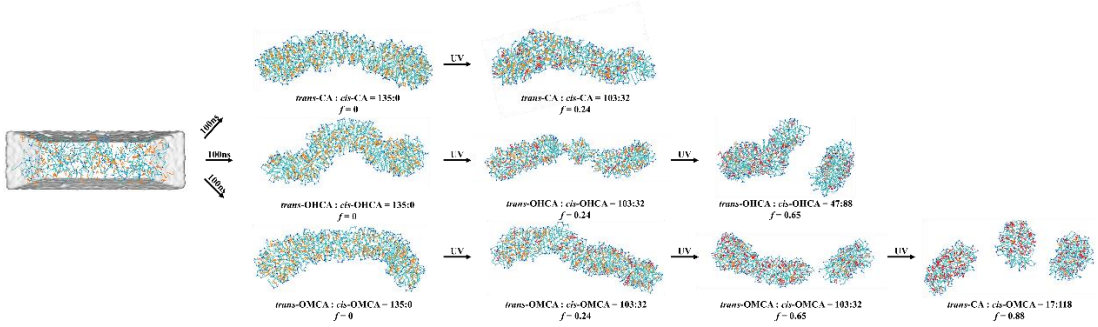

图 3.5　180 个 12-3-12^{2+}和 135 个肉桂酸衍生物混合体系在不同转化率下的初始构型和 100ns MD 模拟后最终构型的快照。（青色部分为 12-3-12^{2+}；橙色部分为反式异构体；红色部分为顺式异构体。为清楚起见，水、Br^{-}和 Na^{+}未显示。）

3.5　肉桂酸衍生物和 12-3-12^{2+}之间的排布方式

图 3.6 展示了从胶束表面截获的肉桂酸衍生物和 12-3-12^{2+}离子之间代表性的排布方式。我们可以看到顺式异构体横向分布在胶束表面，其苯环和羧基位于 12-3-12^{2+}的头基附近。而反式异构体的苯环垂直插入胶束内部，羧基仍旧靠近 12-3-12^{2+}的头基中心。因此，当反式异构体在紫外线照射后转化为顺式异构体时，苯环会从胶束内部逃出重排至胶束表面，导致胶束形态变化。

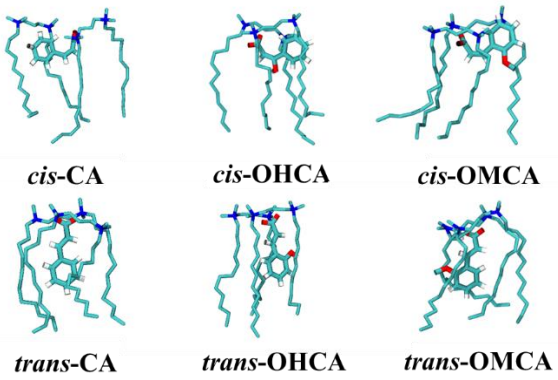

图 3.6　从 MD 模拟的胶束中截获的 12-3-12^{2+}和反式/顺式肉桂酸衍生物之间代表性的排布方式

3.6　三种肉桂酸衍生物分子的区别

3.6.1　分子结构

三种肉桂酸衍生物离子的优化结构在图 3.7 中展示。反式异构体具有平面结构，而顺式异构体具有三维结构。此外，从表 2.2 所示的摩尔体积中看出，OMCA 和 OHCA 反式异构体的摩尔体积小于顺式异构体的摩尔体积，而 CA 则相反。这表明在紫外线照射后，OMCA 和 OHCA 的空间位阻增加，导致胶束逐渐疏松甚至破裂，而 CA 保持蠕虫状胶束形态不变，这和我们实验上光响应胶束形态变化结果相符。摩尔体积差异证实

了对于肉桂酸衍生物，邻位取代基的存在会增强紫外线照射前后肉桂酸衍生物空间位阻的差异，导致其光响应能力的增强。

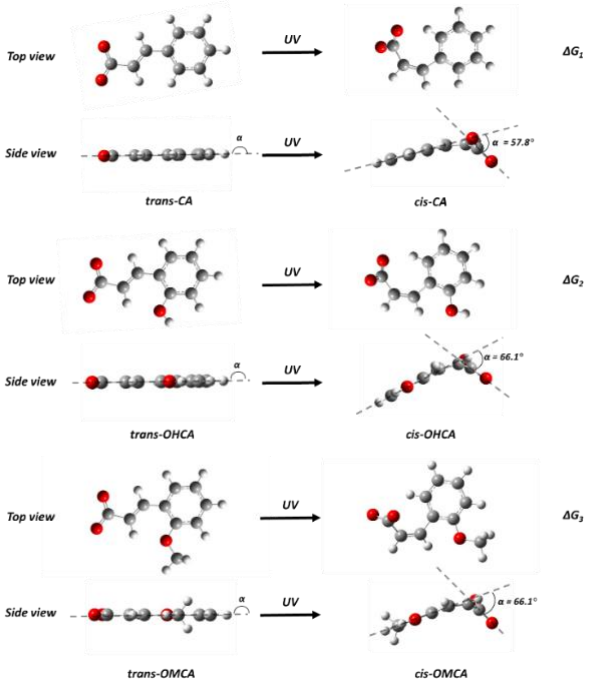

图 3.7　反式/顺式肉桂酸衍生物离子在 b3lyp/6-311+g (d, p)水平优化后的结构图

表 3.2　反式/顺式肉桂酸衍生物的溶剂化自由能、α 角、分子摩尔体积和溶剂化自由能

	trans-CA	*cis*-CA	*trans*-OHCA	*cis*-OHCA	*trans*-OMCA	*cis*-OMCA
溶剂化自由能 (kJ/mol)	-35.28	-37.16	-53.97	-56.39	-37.68	-40.56
α (°)	180	57.8	180	66.1	180	66.1
摩尔体积 (cm^3/mol)	116.16	104.50	107.35	110.60	122.23	125.16
Δ*E* (kJ/mol)	-1.88		-2.42		-2.88	

3.6.2　静电势

三种肉桂酸衍生物离子的静电势分布如图 2.10 所示。我们可以发现负电荷均集中在羧基上，而负电荷则集中在苯环上。由于羟基的存在，*trans*-OHCA 静电势分布最不均匀。*trans*-OHCA 具有最高的负电荷极值 (-7.36 eV) 和最不均匀的电荷分布。这表明 *trans*-OHCA 与 12-3-12^{2+}之间的静电相互作用最强，这也印证了含有 *trans*-OHCA 的蠕虫状胶束具有最致密的形态和最高的粘度。此外，在紫外线照射后，OHCA 和 OMCA 的静电势的极值下降得更显著，表明它们具有比 CA 更强的光响应能力。这也说明了在邻位引入羟基和甲氧基会增加肉桂酸衍生物中羧基的静电势，增强紫外线照射前后羧基上的静电势差，从而提高体系的光响应性。

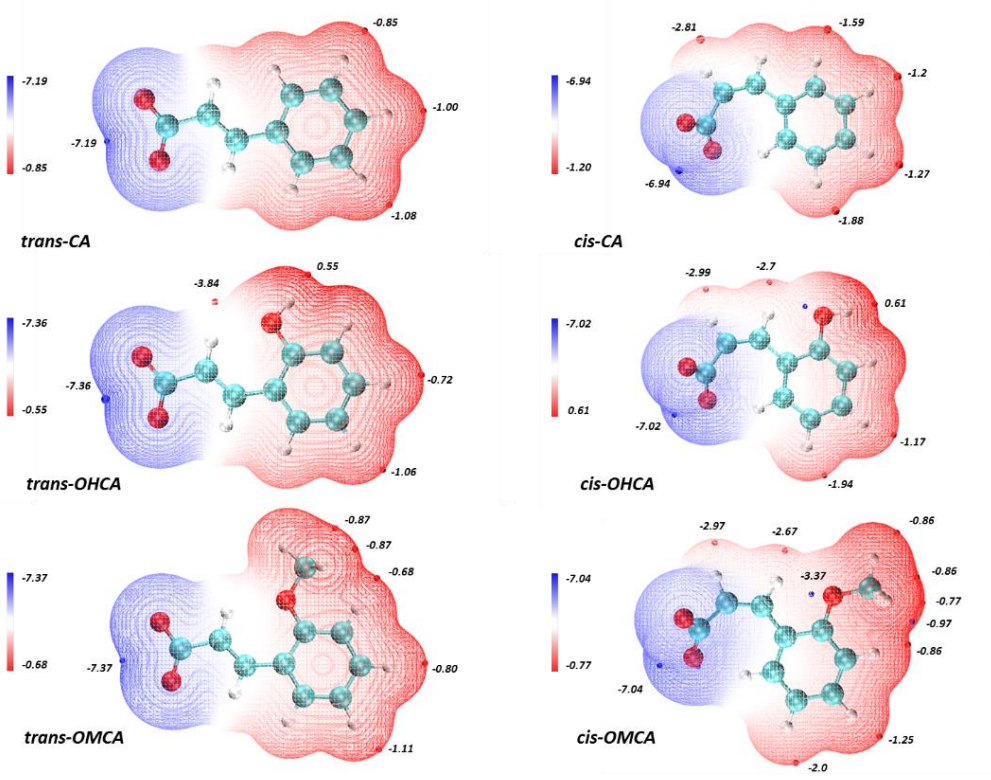

图 3.8　反式/顺式肉桂酸衍生物分子在 b3lyp/6-311+g (d, p)基组优化后的静电势分布 (eV)。红点为区域势能最高点，蓝点为区域势能最低点

表 3.2 列出了三种肉桂酸衍生物的溶剂化自由能。三种顺式异构体的溶剂化自由能均高于反式异构体，较高的亲水性使得顺式异构体更容易从胶束中逃逸出并进入溶液。ΔE 是反式和顺式异构体之间的溶剂化自由能差。可以看出，ΔE 的顺序是 OMCA > OHCA > CA，即在光异构化之后，OMCA 的亲疏水性变化程度最高，光响应效果最好。因此，亲水性邻位取代基羟基和甲氧基的存在会增强分子的亲水性和紫外线照射前后亲水性的差异，提高肉桂酸衍生物分子的光响应能力。

3.6.3　相互作用能

此外，我们反式/顺式异构体与 12-3-12^{2+}之间的两种典型的排布方式的相互作用能。一种是苯环嵌入到 12-3-12^{2+}烷基链中，另一种是苯环位于 12-3-12·2Br^{-}的头基附近。为方便比较，我们将(d) (h) (l)这三种的排布方式的相互作用能定义为 0 kJ/mol。如图 3.9 所示，显然，对于顺式异构体来说，苯环在胶束表面这种排布方式的相互作用能更小，说明了这种排布方式更加稳定。而对于反式异构体来说，苯环嵌入胶束中这种排布反式则更加稳定。以 CA 为例，苯环嵌入胶束中的 *cis*-CA 排布方式(a)和 *trans*-CA 排布方式（d）具有相似的排布方式，但顺式排布方式的相互作用能高于反式排布方式。这意味着当稳定的反式排布方式(d)在紫外线照射后转变为顺式排布方式(a)后，为了获得新的稳定排布方式，*cis*-CA 将改变其排布方式将嵌入胶束的苯环移动到胶束表面上。OHCA 和 OMCA 也是如此。

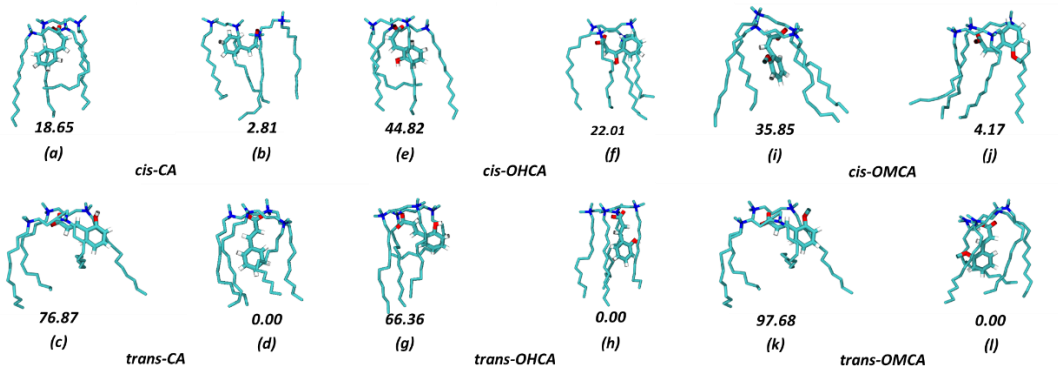

图 3.9　12-3-12·2Br⁻和反式/顺式肉桂酸衍生物在胶束上的不同排布方式及相应的相对相互作用能(kJ/mol)。(在(a)、(d)、(e)、(h)、(i)、(l)中，苯环嵌入胶束中。在(b)、(c)、(f)、(g)、 (j)、(k)中，苯环在胶束表面。为了清晰, 12-3-12²⁺上的氢原子没有显示，为了方便比较，将反式异构体苯环嵌入胶束的排布方式的相互作用能设置为 0 kJ/mol。）

3.7　结论

在本文中，我们利用流变学、透射电镜、反应动力学和高效液相色谱等实验方法，结合分子动力学模拟和量化计算，研究了含有 Gemini 表面活性剂 12-3-12·2Br⁻和三种不同邻位取代基肉桂酸衍生物的蠕虫状胶束的光响应行为。在实验中，我们观察到了由 12-3-12·2Br⁻和肉桂酸衍生物组成的蠕虫状胶束的初始形态和光照后的平衡形态，比较了不同紫外线照射时间下的蠕虫状胶束流变性能。此外，我们还研究了三种肉桂酸衍生物的光异构化反应动力学。结果发现 *trans*-OMCA 具有最高的异构化反应速度和转化率。在模拟方面，使用不同数量的反式/顺式异构体来模拟不同的转换率并成功模拟出了与 TEM 结果相对应的胶束形态，也观察到了 12-3-12·2Br⁻和反式/顺式异构体之间的不同排布方式。使用量化计算的方法计算了包括静电势分布、溶剂化自由能、分子体积、分子特殊二面角和相互作用能，分析了反式/顺式异构体之间结构和性质的差异。*trans*-OMCA 在光照前后具有最大的空间位阻变化、静电势分布变化和亲疏水性变化。这些因素的共同作用使 *trans*-OMCA 具有最强的光响应能力。此外，在邻位引入供电子基团会增加肉桂酸衍生物分子的光响应能力。

第四章主要介绍了由 12-2-12·2Br⁻和邻位、间位和对位甲氧基肉桂酸(*trans*-OMCA, *trans*-MMCA 和 *trans*-PMCA)构建的蠕虫状胶束的光响应行为的分子动力学模拟和量化计算。

4.1 12-3-12·2Br⁻与 *trans*-MCA 蠕虫状胶束的光响应行为

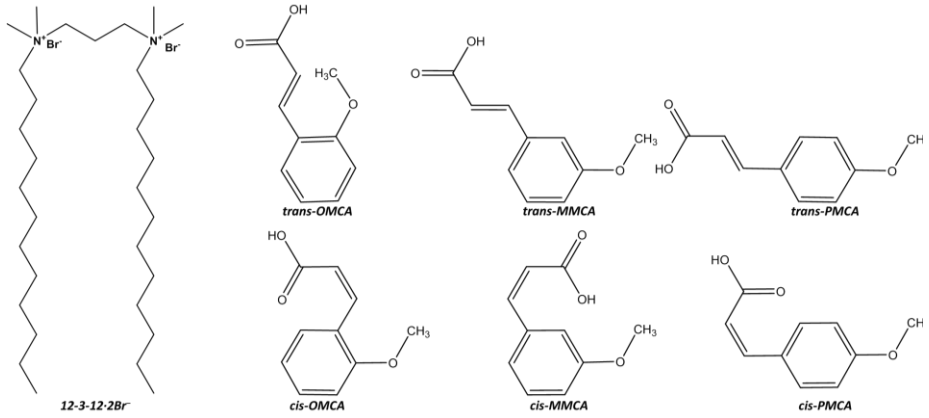

图 4.1 Gemini 表面活性剂 12-3-12·2Br⁻和肉桂酸衍生物 *trans/cis*-OMCA, *trans/cis*-MMCA 和 *trans/cis*-PMCA 的分子结构式

在之前的研究中，我们得到了三种肉桂酸衍生物分子的光异构转换率分别为 *trans*-OMCA(0.94)，*trans*-MMCA(0.91)，*trans*-PMCA(0.82)。图 4.2 展示了三种混合体系在初始状态和在平衡状态下分子动力学模拟的构型快照。如图 4.2 所示，在没有紫外线照射的情况下，12-3-12·2Br⁻/*trans*-MCA 系统在 100 ns MD 模拟后均自组装成蠕虫状胶束。经过足够的紫外线照射，达到反应平衡后，含有 *trans*-OMCA 的蠕虫状胶束转变为三个椭球形胶束。 *trans*-MMCA 和 *trans*-PMCA 蠕虫状胶束体系在平衡时则分解成短的蠕虫状胶束和棒状胶束。模拟结果与实验结果吻合良好。

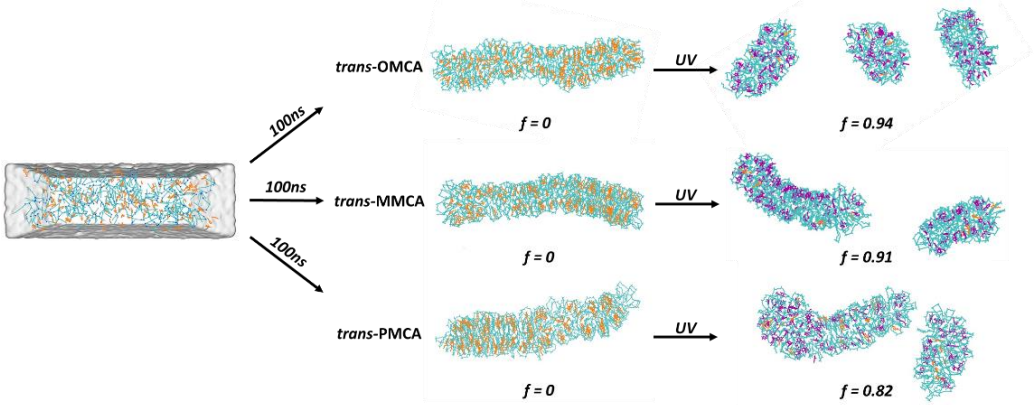

图 4.2 25℃下 180 个 12-3-12²⁺和 135 个 *trans*-OMCA, *trans*-MMCA, *trans*-PMCA 混合体系初始构型和在平衡转化率下经过 100 ns 分子动力学模拟后的最终构型的快照。（青色部分为 12-3-12²⁺；橙色部分为反式异构体；红色部分为顺式异构体。为清楚起见，水、Br⁻和 Na⁺未显示。）

4.2 12-3-12·2Br⁻与 *trans*-MCA 在蠕虫状胶束表面的排布方式

图 4.3 展示了在 MD 模拟中从最后一帧的胶束表面截获的 *trans/cis*-MCA 和 12-3-12²⁺离子之间的代表性的排布方式。可以看出，*trans*-MCAs 甲氧基和苯环完全插入到 12-3-12²⁺烷基链中。随着甲氧基位置从邻位向间位和对位移动，甲氧基则插入的越来越深。

相反，*cis*-MCAs 则水平排布在胶束表面，它们的苯环和羧基靠近 12-3-12^{2+}的头基。*cis*-OMCA 和 *cis*-MMCA 的甲氧基插入胶束内部，而 *cis*-PMCA 的甲氧基则位于胶束的表面。因此，当 *trans*-MCAs 在紫外线照射后光异构化为 *cis*-MCAs 时，苯环将从胶束内部脱离并在胶束表面重新排列。这个过程将导致 MCA 和 12-3-12^{2+}之间的堆积变的松散，进而使蠕虫状胶束裂变成短棒状或球形胶束。

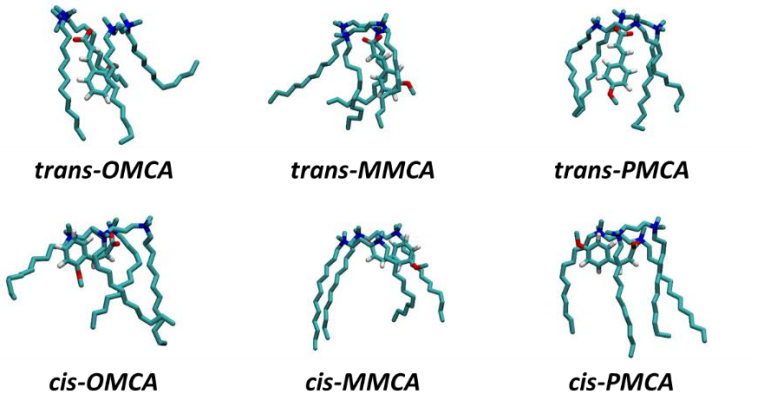

图 4.3　从 MD 模拟中最后一帧的胶束中截获的 OMCA，MMCA 和 PMCA 与 12-3-12^{2+}之间代表性的排布方式。

4.3　三种 MCA 分子的区别

为了进一步探索具有邻位、间位和对位 MCA 之间的构型和性质差异，我们使用了量化计算的方法来计算三种 MCA 分子的不同的参数。首先，我们使用了 b3lyp/6-311+g (d, p) 基组优化了 *trans/cis*-MCA 的结构并展示在图 4.4 中。如图 4.4 所示，*trans*-MCA 具有平面结构，而 *cis*-MCA 具有三维结构。计算得到的离子体积在表 4.1 中列出。在紫外线照射之前，随着甲氧基由邻位到间位到对位，*trans*-MCA 摩尔体积增加。UV 照射后，除了 *cis*-OMCA 体积急剧增加外，*cis*-MMCA 和 *cis*-PMCA 的离子体积显着降低。OMCA 在光照后弯曲程度和摩尔体积的上升增加了其空间位阻，因而导致胶束逐渐松散和破裂。对于 MMCA 和 PMCA，摩尔体积在光照之后降低，不利于相应的蠕虫状胶束发生构型转化。此外，间位和对位甲氧基的存在将反转紫外线照射前后肉桂酸衍生物离子摩尔体积的差异，导致体系的光响应能力下降。

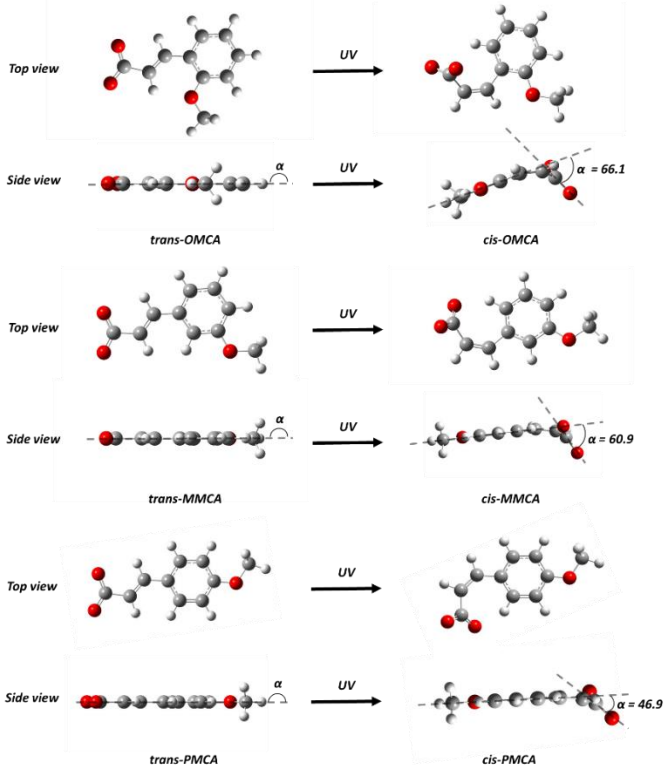

图 4.4　通过 b3lyp/6-311+g (d, p)基组优化后的 *trans/cis*-MCA 离子的结构

图 4.5 展示了三种 *trans/cis*-MCA 的静电势分布。MCA 离子的负静电势均集中在羧基和甲氧基上。*trans*-OMCA 离子的羧基处的负电势是最大的。UV 照射后，*cis*-MCA 的负电势随着离子结构的弯曲更多的转移到苯环上，负电势分布变得更加均匀，且羧基处的静电势分布减小，导致它们与 12-3-12^{2+}的静电相互作用变弱。其中，*cis*-OMCA 羧基处的负电势下降幅度最大，表明其光响应能力最强。

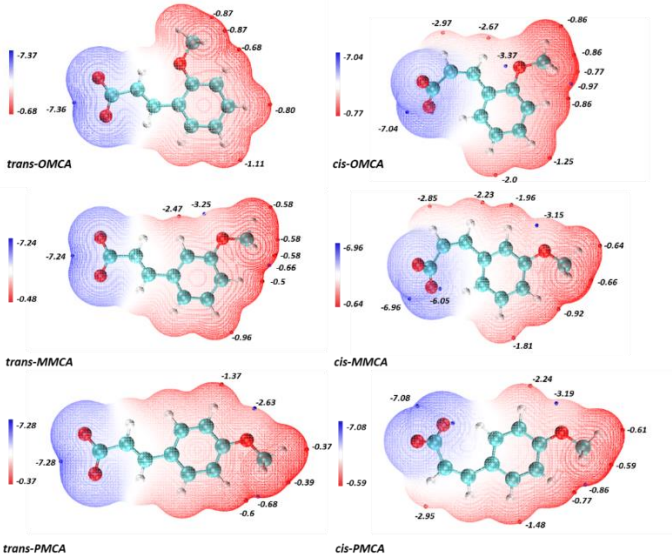

图 4.5　通过 b3lyp/6-311+g (d, p)基组优化后的 *trans/cis*-MCA 离子静电势分布图 (eV)。 蓝点代表附近区域静电势的最小值。红点代表附近区域静电势的最大值。

分子结构对分子的亲疏水性也有重要影响。表 4.1 中列举了顺反肉桂酸酯的溶剂化自由能。UV 照射前后，OMCA 和 PMCA 的溶剂化自由能增加，说明 *cis*-OMCA 和 *cis*-PMCA 相比反式构型更加亲水，更容易从胶束中逃逸出进入溶液。相反，MMCA 的溶剂化自由能略有下降，这说明 *cis*-MMCA 更有可能留在胶束层中而不是移动到溶液中，从而降低蠕虫状胶束光响应能力。

表 4.1　通过 Gaussian 09 计算得到的 *trans/cis*-MCA 分子的溶剂化自由能与 *trans/cis*-MCA 的离子体积

	trans-OMCA	*cis*-OMCA	*trans*-MMCA	*cis*-MMCA	*trans*-PMCA	*cis*-PMCA
溶剂化自由能 (kJ/mol)	-37.68	-40.56	-29.7	-27.7	-27.4	-30.4
离子体积 (cm^3/mol)	113.7	146.5	129	99.3	152.3	136.4

此外，我们截取了 MD 模拟中蠕虫状胶束上 *trans/cis*-MCA 与 12-3-12^{2+}的两种典型的排布方式，并计算了它们之间的相互作用能。其中一种是苯环嵌入到 12-3-12^{2+}烷基链中，另一种是苯环位于 12-3-12·2Br^-的头基附近。我们将(d) (h) (l)这三种的排布方式的相对相互作用能定义为 0 kJ/mol。如图 4.6 所示，对于 *trans*-MCA，苯环嵌入到胶束内部的排布方式相对作用能较低，较为稳定，而对于 *cis*-MCA，苯环位于胶束表面的排布方式相互作用能更低，较为稳定。这意味着当稳定的反式排布方式在紫外线照射后转变为顺式排布方式后，为了获得新的稳定排布方式，*cis*-MCA 将改变其排布方式将嵌入胶束的苯环移动到胶束表面上。这个排布方式变化的过程会导致胶束的松散和破裂。

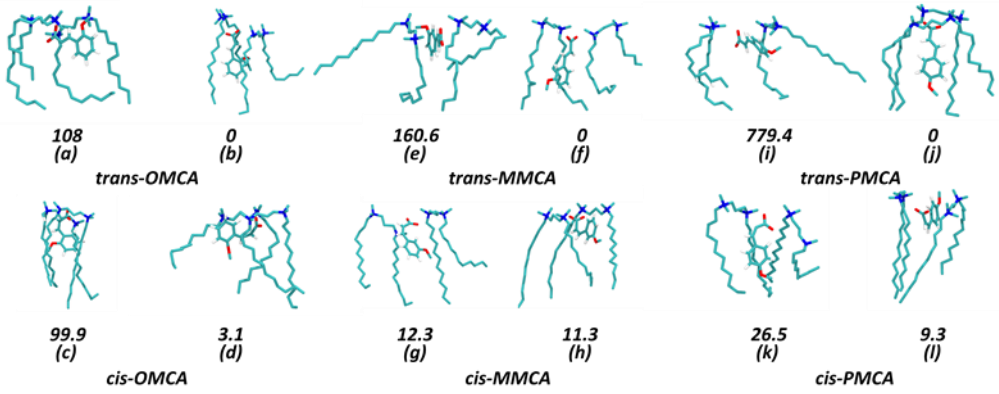

图 4.6　12-3-12^{2+}和 OMCA、MMCA、PMCA 在胶束上不同排布方式和相应的相互作用能 (kJ/mol) 。在(a)、(d)、(e)、(h)、(i)、(l)中，苯环分布在胶束表面。在(b)、(c)、(f)中， (g)、(j)、(k)中，苯环嵌入 12-3-12^{2+}的烷基链中。为清楚起见，未显示和甲氧基和 12-3-12^{2+}上的氢原子。为方便起见，将苯环嵌入胶束中的反式异构体排布方式的相互作用能设为 0 kJ/mol。）

为了筛选出光敏效果最好的肉桂酸衍生物，我们选择了二十四种在邻位、间位和对位具有不同供电子取代基的肉桂酸衍生物，并计算了摩尔体积(*V*)、溶剂化自由能(*E*)和

它们之间的差值(ΔV, ΔE)，电荷分布，吉布斯自由能，单线态和三线态下的反应平衡常数($K_{singlet}$, $K_{triplet}$)和吉布斯自由能($\Delta G_{singlet}$, $\Delta G_{triplet}$)等一系列参数。这些肉桂酸衍生物分别为间羟基肉桂酸（MHCA）、对羟基肉桂酸（PHCA）、邻巯基肉桂酸（OSCA）、间巯基肉桂酸（MSCA）、对巯基肉桂酸（PSCA）、邻甲硫基肉桂酸（OMTCA）、间甲硫基肉桂酸 (MMTCA)、对甲硫基肉桂酸 (PMTCA)、邻氨基肉桂酸 (OACA)、间氨基肉桂酸 (MACA)、对氨基肉桂酸 (PACA)、邻甲氨基肉桂酸 (OMACA)，间甲氨基肉桂酸 (MMACA), 对甲氨基肉桂酸 (PMACA), 邻二甲基氨基肉桂酸 (ODACA), 间二甲基氨基肉桂酸 (MDACA), 对二甲基氨基肉桂酸 (PDACA), 邻硝基肉桂酸 (ONCA), 间- 硝基肉桂酸（ONCA），对硝基肉桂酸（ONCA）。它们的化学结构如图 4.7 所示。

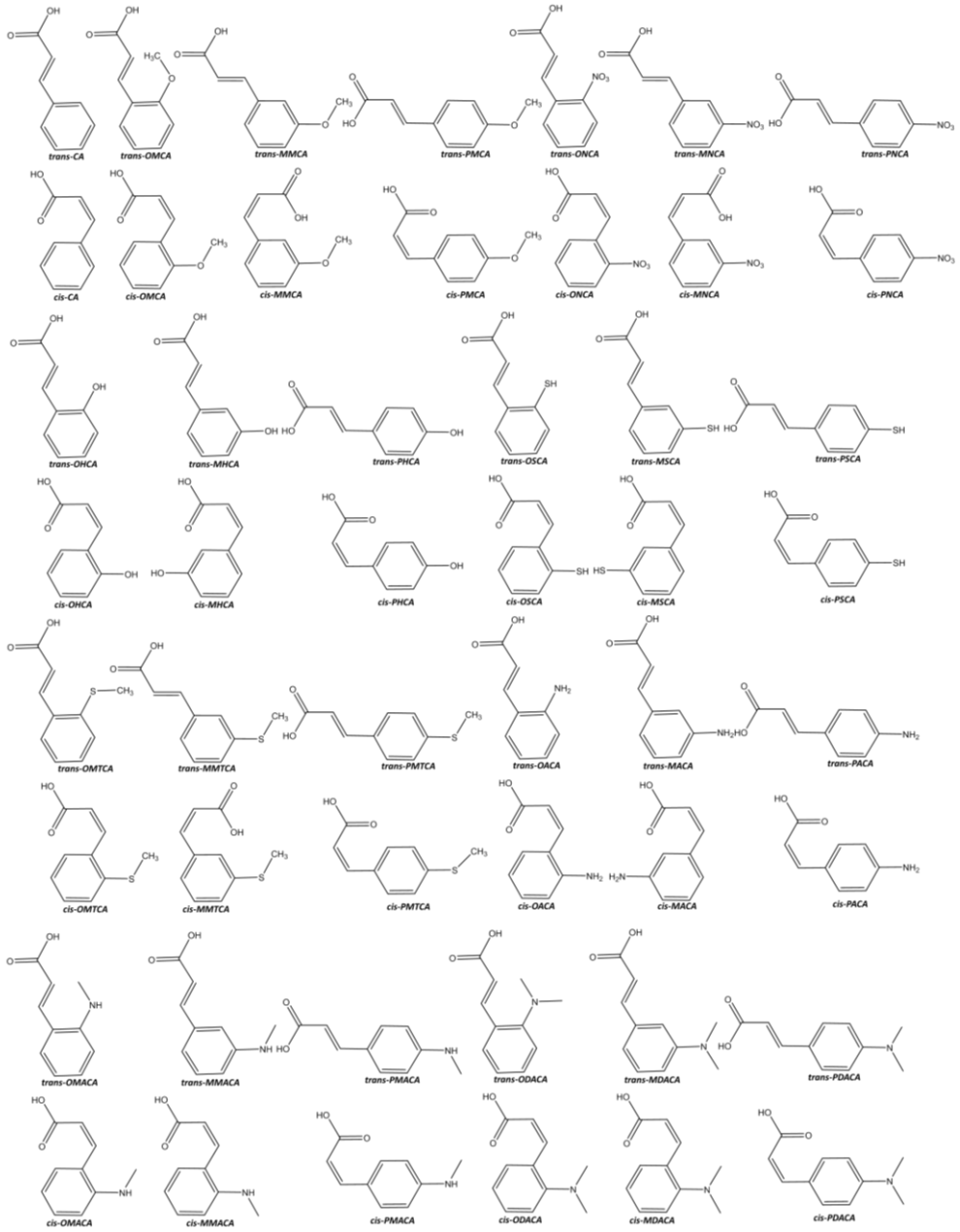

图 4.7　肉桂酸衍生物的分子结构式

计算结果如表 4.4 所示。图 4.14 显示了反式/顺式肉桂酸离子的离子摩尔体积（黑色柱形 Δ*V*）和反式/顺式肉桂酸分子之间的溶剂化自由能（红色柱形 Δ*E*）的差异。根据我们之前的工作，正 Δ*V* 和负 Δ*E* 值有助于促进相应蠕虫状胶束的光响应能力。从图 4.14 可以看出，满足这个条件的只有 OMCA、ODACA、PHCA 和 PNCA。在三重态下，OMCA、OHCA、OMCA、MMCA、PMCA 和 PMTCA 的 $K_{triplet}$ 值都大于 1000，这说明在足够长的紫外线照射后，这些肉桂酸衍生物的转化率比较高。OMCA、OHCA、OMTCA、OSCA、ONCA、MNCA、MSCA 和 PNCA 的 Δmax 均大于 0.3，表明 UV 照射后这些肉桂酸酯与表面活性剂的静电相互作用降低更为显着。综上，在所有肉桂酸衍生物中，OMCA 拥有最好的光敏效果。

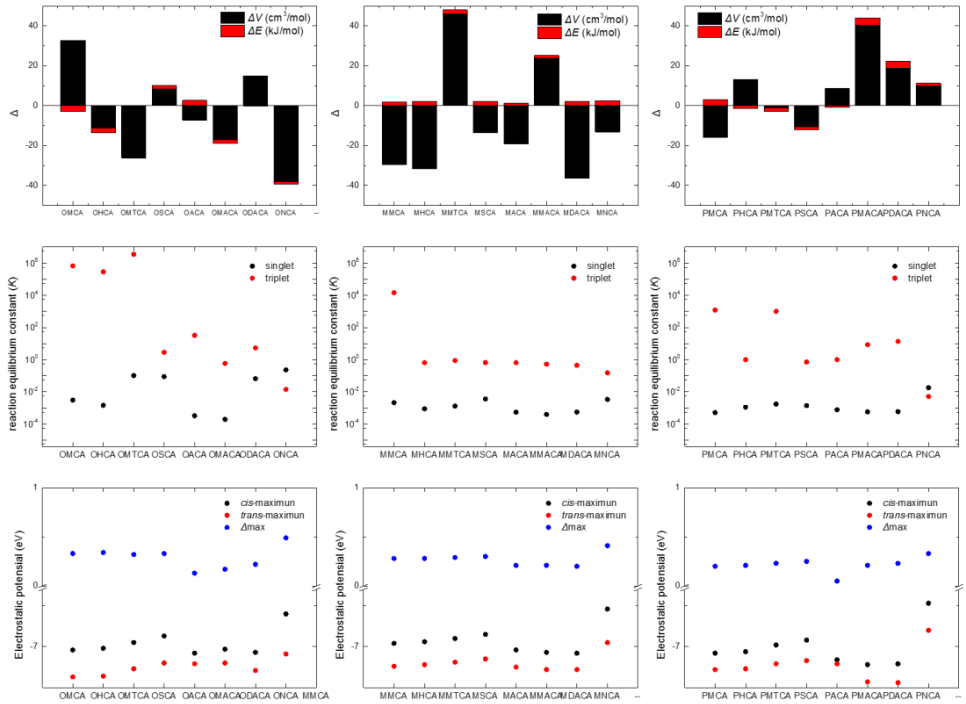

图 4.8　反式/顺式肉桂酸衍生物经紫外光照射后离子摩尔体积（黑柱 Δ*V*（cm³/mol））和溶剂化自由能（红柱 Δ*E*（kJ/mol））的差值，最大负静电势值（eV）*cis*-maximun, *trans*-maximun 以及它们的差值 Δmax，以及单线态和三线态下光异构反应的平衡常数 $K_{singlet}$，$K_{singlet}$。

4.4　结论

在本章中，我们使用分子动力学模拟和量化计算的计算方法，研究了含有 Gemini 表面活性剂 12-3-12·2Br⁻和邻位、间位、对位甲氧基肉桂酸所构建的蠕虫状胶束体系的光响应行为。使用了不同数量的 *trans/cis*-MCA 来模拟 *trans*-MCA 的光转换率，成功模拟出了与实验结果相对应的胶束形态变化，也观察到了 12-3-12·2Br⁻和 *trans/cis*-MCA 之间的不同排布方式。使用量化计算的方法计算了 *trans/cis*-MCA 的静电势分布、溶剂化自

由能、分子体积、二面角和相互作用能，讨论了 *trans/cis*-MCA 之间结构和性质的差异。结果发现 *trans*-OMCA 在光照前后具有强烈的空间位阻变化、静电势分布变化和亲疏水性变化。这些因素的共同作用使 *trans*-OMCA 蠕虫状胶束具有最强的光响应能力。此外随着甲氧基由邻位转移到对位和间位，顺反异构体的分子体积和亲疏水性会和 OMCA 存在相反的变化趋势，导致其光响应能力的减弱。

我们计算了二十四种肉桂酸衍生物的摩尔体积，亲疏水性，电势分布以及反应平衡常数，综合考虑以上所有因素，*trans*-OMCA 拥有最优异的光敏效果。

第五章主要介绍了气泡在不同浓度和气体分数下的 CTAB/NaSal 的溶液中上升速度的研究。

5.1 CTAB/NaSal 溶液的流变学

我们测量了 20 mM CTAB 和不同 NaSal 浓度的混合溶液的流动曲线，如图 5.1 所示。在低 NaSal 浓度下（0、2、4、8、9 mM），这些溶液表现出了牛顿流体性质。在高 NaSal 浓度下（10、11、11.5、12、12.5、13 mM）这些溶液表现出了剪切稀化粘弹性流体性质。

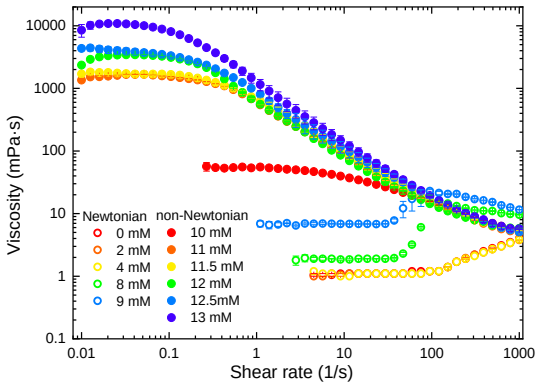

图 5.1 20 mM CTAB 和 0-13 mM NaSal 溶液在 22°C 时的流动曲线。

5.2 气泡尺寸

使用了双注射器法来制造气泡，气体体积分数控制在 5%到 30%之间。一旦气泡形成，立刻使用 Mastersizer 3000 测量它们的尺寸。图 5.2 显示了所有样品的 Sauter 半径 R_{32}。对于 NaSal 浓度较低的样品，气泡尺寸最小。当溶液向非牛顿流体过渡时（8 和 9 mM NaSal），气泡尺寸变大。对于牛顿流体而言，平均气泡半径介于 12 和 22 μm 之间（8 和 9 mM NaSal 时平均气泡半径要大一些）。气泡尺寸随着气体体积分数 φ 的增加而微弱地增加。在非牛顿流体溶液中，气泡尺寸更大，在 25 到 35 μm 之间，并且气泡尺

寸与气体分数没有关系。

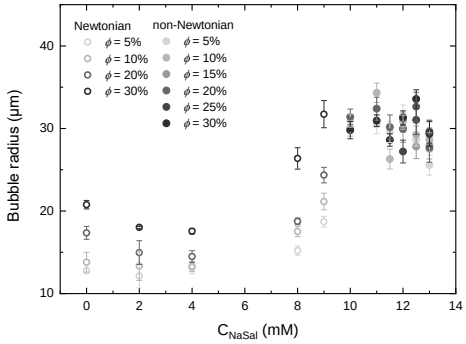

图 5.2　22°C 下 20 mM CTAB 和 0-13 mM NaSal 溶液中产生的气泡的 Sauter 半径

5.3. 气泡上升速度的测量

为了研究 CTAB/NaSal 溶液中气泡是如何上升的，我们拍摄了不同浓度和气体分数下气泡上升的照片。图 5.3 (a) 显示了 20 mM CTAB/4 mM NaSal 在 φ = 5%时气泡上升过程的照片。当样品瓶内填充满气泡液时，瓶身呈现黑色。气泡随着上升，气泡液和透明液之间的分界线变得清晰可见。分界线随着时间向上移动。我们使用 Image J 软件来处理图片并通过计算分界线的移动速度来计算气泡上升速度，并绘制了不同时间下，灰度随分界线高度变化的曲线图 5.3 (b)。

从图 5.3 (b)中，可以看出图像灰度在 0 到 160 之间变化，于是我们选择了三个灰度值 I = 40、80 和 120（较小的 I 表示较暗的区域）并从中截取出不同时间下的相同灰度对应的分界线高度，并绘制了图 5.3(c)。如图 5.3(c)所示，分界线高度随时间线性变化，且每个灰度值的分界线上升速度不同，分别为 0.31mm/s (I = 40)、0.23mm/s (I = 80)、0.18mm/s (I = 120)。这些气泡上升速度差异是由于气泡尺寸的多分散性引起的。在下文中，我们使用 I = 80（图像中的平均灰度）的高度值来定义气泡上升分界的位置。

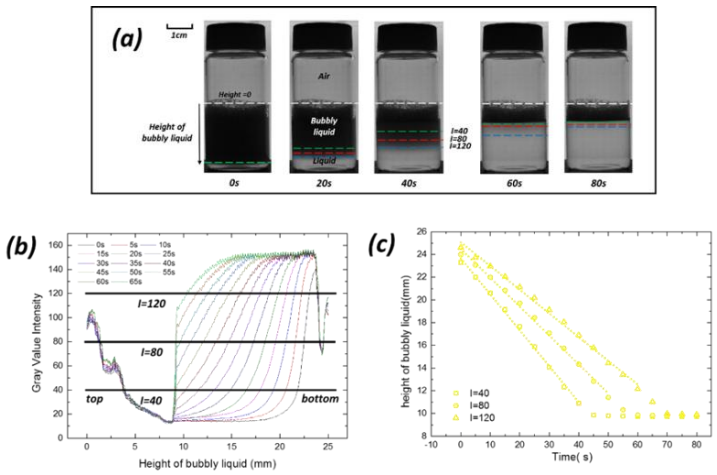

图 5.3　(a)不同时间 20 mM CTAB 和 4 mM NaSal 溶液在 φ = 5%的气泡液中气泡上升的图像。白线表示实验开始时气泡液顶部的位置。三条水平线（绿色、红色和蓝色）分别表示三个灰度级 I = 40、80 和 120 的位置。(b)不同分界线高度与灰度之间的关系。(c)不同灰度下的分界线高度与时间的关系

除了含有 13 mM NaSal 的样品外，所有样品的气泡上升速度都是恒定的。对于含有 13 mM NaSal 的溶液，其气泡上升速度随时间变化而变化。图 5.4 (a)展示了该溶液气泡上升过程不同阶段的照片，同时显示了不同灰度下的分界线位置（对于 I = 40、80 和 120）。图 5.3 (b)则展示了不同时间下，灰度随分界线高度变化的曲线。我们可以看到。在气泡上升后期，曲线更加不平滑，说明了气泡的分散性更强。在图 5.4 (c)中，在前 100 秒，气泡快速上升。此后，气泡上升速度显着减慢，完全转换为澄清溶液需要超过 15 小时。

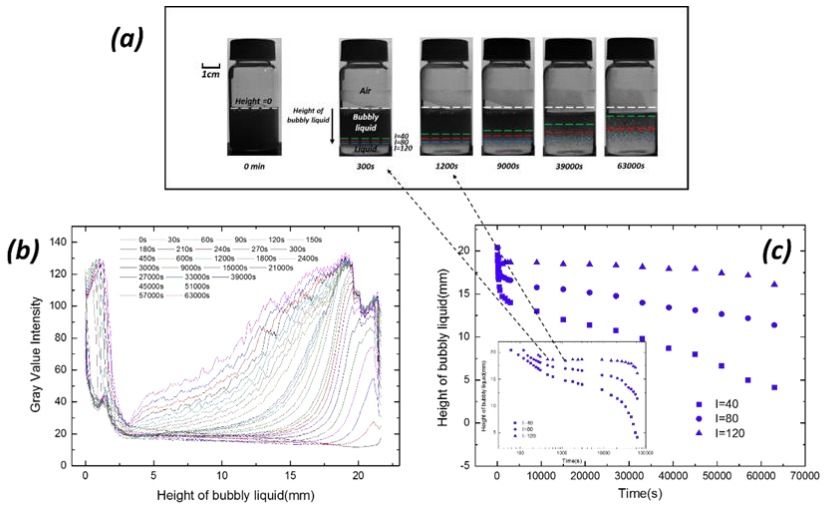

图 5.4　(a)不同时间 20 mM CTAB 和 13 mM NaSal 溶液在 φ = 5%的气泡液中气泡上升的图像。白线表示实验开始时气泡液顶部的位置。三条水平线（绿色、红色和蓝色）分别表示三个灰度级 I = 40、80 和 120 的位置。(b)不同分解界高度与灰度之间的关系。(c)不同灰度下的分界线高度与时间的关系。插图为半对数图

5.5 牛顿流体中泡沫的上升

图 5.5 显示了在 I = 80 时，不同浓度和气体分数下的气泡上升速度 v/v_s（由 Stokes 速度归一化后）。v_s 通过公式(5-1)计算得到，其中 R 为 Sauter 半径，η 为溶液的粘度。

$$v_s = \frac{2\Delta\rho g R^2}{9\eta} \tag{5-1}$$

我们可以看到正如牛顿流体所预期的，不同浓度和气体分数的速度都归于一条主曲线上。

$$v = v_s(1-\varphi)^n \tag{5-2}$$

使用(5-2)上计算得到的 Richardson-Zaki 曲线如图 5.5 中的黑色虚线所示。我们可以看到，在误差范围内，v/v_s 与 Richardson-Zaki 模型非常吻合。对 φ = 0 的外推值与用 Sauter 半径计算的 Stokes 速度一致，证明了在气泡上升过程中，气泡表现为固体颗粒。

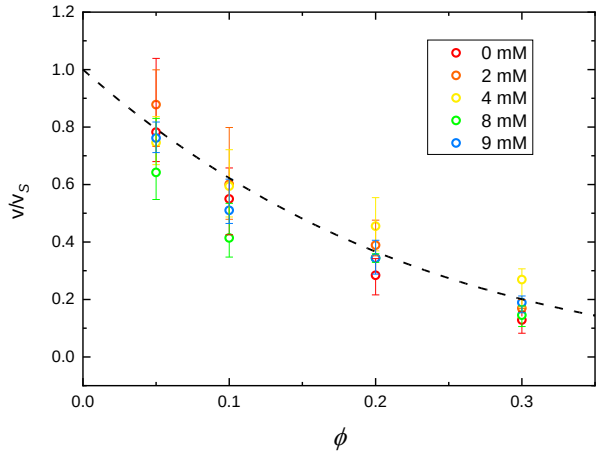

图 5.5　在牛顿流体中(20 mM CTAB 和 0-9 mM NaSal)，在不同气体分数下 I = 80 时气泡上升速度 v/v_s（由 Stokes 速度归一化后）。测量速度。虚线为 Richardson-Zaki 曲线，其中 n = 4.5

5.6 非牛顿流体中的气泡上升速度

对于非牛顿流体，不同气体分数下气泡上升速度如图 5.6 (a)所示。与在牛顿流体中一样，气泡上升速度随着 NaSal 浓度的增加而降低，即随着样品粘度的增加而降低。为了更好地比较气泡上升速度和 φ 之间的关系，我们用 φ = 0.05 处的速度将气泡上升速度归一化，如图 5.6 (b)所示，黑色虚线为 Richardson-Zaki 曲线。

可以看出，气泡上升速度随气体分数升高的降低程度比 Richardson-Zaki 方程预测出的结果要弱得多，并且在高 NaSal 浓度下，拟合程度非常差（见图 5.6 (b)）。因此，Richardson-Zaki 方程对于非牛顿粘弹性剪切稀化流体并不适用。对于最粘稠的样品（如 12.5 和 13 mM NaSal），在高气体分数下气泡上升速度比 Richardson-Zaki 方程预测值更高。此外，我们可以使用

$$\frac{v}{v(\varphi=0.05)} = 1.1(1-\varphi) \tag{5-3}$$

（紫色点线）来描述非牛顿流体中归一化的气泡上升速度随气体分数的变化趋势。

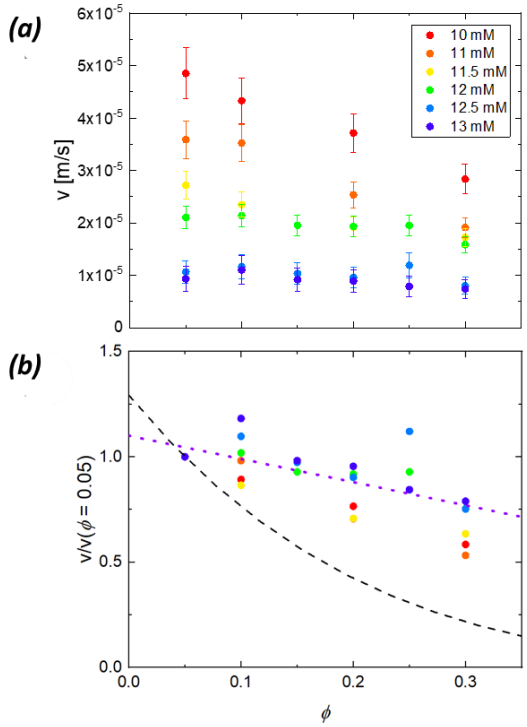

图 5.6 (a) I = 80 时，非牛顿流体（20 mM CTAB 和 10-13 mM NaSal）中，不同气体分数下气泡上升速度 v。(b) 由 φ = 0.05 处的速度归一化的气泡上升速度，黑色虚线显示了 Richardson-Zaki 方程预测的气泡上升速度。作为 φ 的函数气泡上升速度可以使用公式 (5-3) 紫色虚线来描述。

5.7 在非牛顿（剪切稀化）流体中的浮选

泡沫浮选用于从流体中净化和分离物质：物质附着在气泡表面上，气泡表面上升以进行分离。量化泡沫浮选的一个重要参数是气泡表面积通量$\dot{S}$，它表明每秒有多少表面积与泡沫接触，并且该参数与泡沫浮选的工作效率直接相关。在气泡柱中，$\dot{S}$由平均气泡上升速度 $v(\varphi)$和气泡数密度$N \propto \frac{\varphi}{R}$的乘积给出，

$$\dot{S}=v(\varphi)\frac{\varphi}{R} \tag{5-4}$$

由于 v 在牛顿流体和非牛顿流体中的变化非常不同，因此$\dot{S}$也会发生变化。在牛顿流体中，Richardson-Zaki 方程拟合效果很好，如公式(5-2)所示。对于非牛顿流体，我们看到气泡上升速度和 φ 的相关性较弱，如图 5.6 (b)中的虚线和公式(5-3)所示。因此，我们可以使用公式(5-2)和公式(5-3)来计算牛顿流体和非牛顿剪切稀化流体中的$\dot{S}$随 φ 变化的曲线。如图 5.9 所示，如果将气泡表面积通量最大化设为目标，那么在牛顿流体中，最佳的气体分数是 φ = 0.16，而在非牛顿流体中，更高 φ 会增加面积通量。但由于我们实验

的气体分数小于 0.3，我们无法推测更高的 φ 下会发生什么。我们的结果表明，当溶液为非牛顿流体时，最佳浮选的气体分数可能与牛顿流体的大不相同。

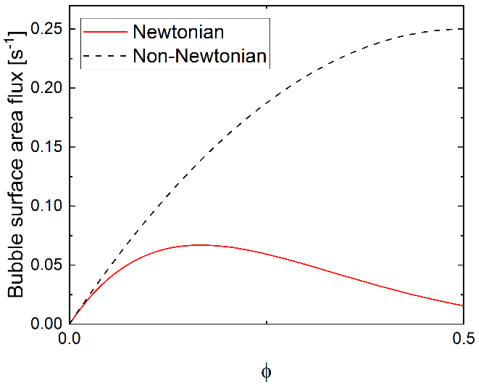

图 5.7　在牛顿流体和非牛顿流体中气泡表面积通量随气体分数的变化曲线

5.8　结论

我们研究了不同粘度的牛顿流体和剪切稀化的非牛顿流体蠕虫状胶束溶液中气泡上升行为。我们使用了双注射器法制造气泡，并测量了气泡的大小。当 NaSal 浓度较低时，溶液为牛顿流体，且在高剪切速率下，会出现剪切增稠现象。在这些溶液中，气泡的尺寸较小。当 NaSal 浓度较高时，溶液为剪切稀化的非牛顿流体，此时溶液中容易出现较大的气泡。

使用 Richardson-Zaki 方程可以很好地描述牛顿流体中气泡液的上升行为。在非牛顿流体中，气泡上升速度对于气体分数的敏感度较牛顿流体低。将 Richardson-Zaki 方程中的指数改为 1，可以很好地描述非牛顿流体的气泡上升速度。我们的结果表明非牛顿流体的最大面积通量的气体分数比在牛顿流体中更高，这对剪切稀化流体中的泡沫浮选过程具有重要意义。